

Retardation of radionuclides relevant to waste disposal in clay stone and saline systems - sub-project 1

Rückhaltung endlagerrelevanter Radionuklide im natürlichen Tongestein und in salinaren Systemen – Teilprojekt 1

Final Report

Karlsruher Institut für Technologie, Institut für Nukleare Entsorgung

Förderkennzeichen 02E10961

Nidhu Banik, Muriel Bouby-Laliron, Nicolas Finck, Katja Hinz, Tom Kupcik, Rémi Marsac, Andreas Schnurr, Christian Marquardt, Thomas Rabung

Das diesem Bericht zugrundeliegende Vorhaben wurde mit Mitteln des Bundesministeriums für Wirtschaft und Technologie unter dem Förderkennzeichen 02E10961 gefördert. Die Verantwortung für den Inhalt dieser Veröffentlichung liegt bei den Autoren.

Zusammenfassung

Das hier beschriebene Vorhaben lief in den Jahren 2011 bis 2015 in Rahmen des BMWi Förderprogramm „Entsorgung gefährlicher Abfälle in tiefen geologischen Formationen: Verbesserung von Instrumentarien für die Sicherheitsbewertung von Endlagern und Untertagedeponien“. Die Untersuchungen umfassten Sorptions-, Diffusions-, Komplexierungs- und Löslichkeitsexperimente mit dem Schwerpunkt auf Tonstein- und Salzsteinsysteme. Durch das Vorhaben wurde eine große Anzahl neuer experimenteller Daten als Schlüssel-Eingangsgroßen für die Bewertung des Quellterms (maximal erwartete Löslichkeit) der Actiniden (III, IV, V, VI) in Tonstein/Salzstein gewonnen. Durch die Wahl der experimentellen Bedingungen wurde ein breites Spektrum von Endlagerkonzepten und -szenarien abgedeckt.

Die Sorptionsuntersuchungen wurden mit dreiwertigen, vierwertigen, fünfwertigen und sechswertigen Actiniden untersucht: Cm(III)/Eu(III), Np(IV/V), Pu(IV/V) und U(VI); Eu(III) wurde als dreiwertiges chemisches Analogon für dreiwertige Actiniden eingesetzt. Die Sorption der Actiniden wurde untersucht an dem reinem Tonmineral Illit und an dem natürlichen Tonstein Opalinuston, bei variierenden Grundelektrolyt-Konzentrationen und –Gemischen unter Ausschluss von CO₂. Die Batch-Experimente wurden ergänzt durch Laserfluoreszenz-Untersuchungen, welche zwischen pH_c 3 und 12 (für MgCl₂-Lösungen wegen der Ausfällung von Mg(OH)₂ nur bis pH_c 9) durchgeführt wurden.

Die experimentellen Sorptionsdaten zeigen für Eu(III) einen nur kleinen Einfluss der Salinität auf den log K_D-Wert., speziell im neutralen bis basischen pH_c-Bereich. In saurem Medium wird die Sorption mit steigender NaCl-Konzentration verringert, da der Kationenaustausch-Prozess durch Erhöhung der Na⁺-Konzentration unterdrückt wird. Der gleiche Effekt wird auch in CaCl₂ und MgCl₂-Lösungen beobachtet. Bei pH_c-Werten größer als 8 wird in allen untersuchten Systemen eine beinahe vollständige Sorption mit log K_D ≥ 4.5 erhalten. Zeitaufgelöste Laserfluoreszenz-Spektroskopie (TRLFS)-Untersuchungen mit Cm(III) in salinen Lösungen zeigen, dass die erste Koordinations-Schicht von dem Metallion nicht signifikant verändert wird und damit die Cm(III)-Speziation durch die erhöhte Ionenstärke nicht beeinflusst wird. Für die Modellierung mit dem Oberflächenkomplexierungsmodell 2SPNE SC/CE wurden über den gesamten Ionenstärkebereich deshalb identische Spezies angenommen. Dieses Modell beschreibt die Eu(III)/Cm(III) Sorption über den gesamten pH- und Ionenstärkebereich recht gut. Die Aktivitätskoeffizienten und die Wasseraktivität wurden hierbei mit dem Pitzer-Modell angepasst.

Die Sorption der Aktinylionen Np(V) und U(VI) wird durch die Ionenstärke über den untersuchten pH_c-Bereich kaum beeinflusst. Wie erwartet ist die Sorption von Np(V) schwächer als für die anderen Kationen. Sie startet ab ca. pH_c 8 (>20 %) und erreicht bei pH_c > 10 eine quasi-quantitative Sorption. Die experimentellen Daten können mit

dem 2SPNE SC/CE-Sorptionsmodell gut beschrieben werden. Die Sorptionskanten der U(VI)-Sorptions ähneln der Sorptionskanten von Eu(III). Allerdings ist die pH-Kante für U(VI) ein wenig zu kleineren pH-Werten verschoben, da das U(VI) leichter hydrolysiert. U(VI) zeigt kaum Kationenaustausch und die pH-abhängige Sorption beginnt bei etwa pH_c 4. Die Sorption ist zwischen pH 6 und 11 quasi quantitativ. Bei höheren pH-Werten nimmt die Sorption ab, weil als dominierende Spezies $UO_2(OH)_4^{2-}$ gebildet wird und die zweifach negative Ladung dieser Spezies die Uran-Sorption stark verringert. Die Modellierung mit dem 2SPNE SC/CE-Sorptionsmodell beschreibt die experimentellen Daten recht gut bis $pH_c \sim 7$. Bei höheren pH-Werten werden mit dem Modell niedrigere K_d -Werte als im Experiment erhalten und es wird eine Ionenstärke-Abhängigkeit vorhergesagt, die nicht im Experiment beobachtet wurde.

Die Sorption von Np(V) wurde auch über längere Reaktionszeiten von bis zu 2 Monaten als Funktion des pH-Wertes (pH 3-10) und in 0.1 M NaCl-Lösungen unter Argonatmosphäre untersucht. Ab einer Reaktionszeit von einer Woche wurde keine weitere Veränderung der Sorption von Np beobachtet und das Erreichen eines Gleichgewichtszustand konnte damit vermutet werden. Unter anaeroben Bedingungen sind die Fest-Flüssig-Verteilungskoeffizienten (K_d oder R_d) der Np(V)-Sorptions an Illit allerdings größer als unter Luft. Die Beobachtung, dass R_d mit abnehmenden p_e -Wert ($p_e = -\log a_e$, negative dekadischer Logarithmus der Elektronenaktivität in Lösung) zunimmt, lässt auf eine Reduktion des fünfwertigen zu vierwertigem Np schließen. Über das in Lösung gemessene Redoxpotential wird auf einen ersten Blick das Np(V) als dominierende Redoxstufe vorhergesagt. Allerdings konnte eine Reduktion von Np(V) an der Illit-Oberfläche über XANES-Messungen (Röntgen-Nahkanten-Absorptionsspektroskopie) bestätigt werden. Die Np(IV/V)-Speziation in Gegenwart von Illit konnte konsistent mit dem 2SPNE SC/CE-Modell beschrieben werden. Die experimentell gemessenen p_e -Werte wurden für die Berechnung des Np-Redoxzustands verwendet, wobei die notwendigen Oberflächenkomplexierungskonstanten für das vierwertige Np (Np(IV)) an die experimentellen Daten angefügt wurde. Die so erhaltenen Konstanten sind konsistent mit Konstanten, die über einen „linear free energy relationship“ (LFER) abgeleitet wurden. Die vorliegende Studie zeigt hiermit, dass die Reduktion von Np(V) in der Gegenwart von sorbierenden Mineral-Oberflächen im Vergleich zur wässrigen homogenen Lösung ohne Festkörper thermodynamisch bevorzugt ist.

Die Pu-Sorption an Illit wurde ebenfalls untersucht in 0.1 M NaCl-Lösung und unter anaeroben Bedingungen. Im pH-Bereich 3 bis 10 ist die Sorption von Pu sehr stark ($\log R_d > 4 \text{ L kg}^{-1}$). Eine Mischung von Pu(III) und Pu(IV) wird bei $pH < 5$ beobachtet. Eine solche starke, pH-unabhängige Sorption wird im Modell unter Berücksichtigung der gemessenen Redoxpotential und damit abgeleiteten individuellen Redoxverteilung von Pu erhalten, wenn man für die unbekanntenen Pu(III)-Daten Eu(III)-Illit-Sorptionsdaten verwendet (Eu(III) gilt als chemisches Analogon für Pu(III)). Wie schon mit Eu(III) gezeigt wurde, wird die Pu(III,IV)-Sorptions durch die Anwesenheit von Calcit in Illit/Calcit-Suspensionen kaum beeinflusst. Die hier aus experimentellen Daten und Modellierungen erhaltenen Sorptions-Daten können gut verwendet werden um die Pu-Rückhaltung in reduzierenden calcit-haltigen Grundwässern, wie sie für nukleare Endlager durchaus zu erwarten sind, vorherzusagen.

Generell kann man als Ergebnis für die Sorptionsstudien hervorheben, dass die Vorhersagen mittels dem 2SPNE SC/CE-Modell ganz gut mit den experimentellen Daten übereinstimmen, wenn man Ionenstärke-Korrekturen für die Aktivitäten der gelösten Spezies mit dem Pitzer bzw. SIT-Modell vornimmt und dabei die Redoxgleichgewichte der Spezies in der Lösung berücksichtigt. Eine starke bis sehr starke Sorption der drei-, vier-, fünf- und sechswertigen Aktiniden an Tonmineralien wird erwartet unter salinen Bedingungen und Abwesenheit von Karbonat.

Im Rahmen der Arbeiten bezüglich der Rückhaltung von Radionukliden an Eisenkorrosionsprodukten wurde Grüner Rost-Chlorid und Magnetit, die dreiwertiges Neodym und Americium enthalten (Nd, Am), synthetisiert. Die Festkörper wurden charakterisiert mittels Röntgendiffraktometrie (XRD) und Raman-Spektroskopie. Zusätzlich wurden Informationen mittels Röntgen-Photoelektronen-Spektroskopie (XPS) bezüglich Speziation der Strukturelemente und den Dopant erhalten. Scanning-Elektronenmikroskopie (SEM) lieferte Informationen über die Größe und Form der Partikel. Grüner Rost (GR) wurde hergestellt, indem eine Mischung aus Fe(II) und Fe(III)-Ionen in Anwesenheit von Nd(III) direkt ausgefällt wurde. Der dotierte Nd(III)-GR wurde mit sauerstofffreien Wasser gewaschen, um die Umwandlung zu Magnetite zu starten und anschließend zu charakterisieren. Parallel dazu wurde Magnetit aus einer Fe(II)/Fe(III)-Lösung synthetisiert, die auch Tracer-Konzentrationen an Am(III) enthielt. Es ist schwierig die gesamten Ergebnisse der Raman, XRD und SEM-Untersuchungen in Einklang zu bringen. Aber in keinen der Proben beeinflusste der Dopant die entstandene Mineralphase und weder Nd(III) noch Am(III) bildeten eine separate Phase durch Ausfällung.

Die Diffusion von HTO, Cl⁻, Eu, Np(V) und Fulvinsäure in Illit wurde in „In“-Diffusions- oder „Through“-Diffusions-Versuchen untersucht. Hierzu wurden kompaktierte, zylindrische Na-Illit-Proben und NaCl als Grundelektrolyt verwendet. Die Diffusionsparameter von HTO und Cl⁻ wurden in 0.1 M und 0.5 M NaCl untersucht. Die Diffusionskoeffizienten (D_e) und die Porosität (ϵ) für HTO sind für beide Ionenstärken sehr ähnlich und zeigen, dass die Erhöhung der Ionenstärke kaum einen Einfluss auf die geometrischen Eigenschaften (Tortuosität (α), Konstriktivität) des Illits hat. Für das Anion Chlorid ist D_e und α in 0.5 M NaCl größer als in 0.1 M. Im Vergleich zu HTO ist D_e kleiner und kann mit einem reduzierten zugänglichen Porenraum für anionische Tracer erklärt werden. Anionen werden durch die negativ geladenen Tonoberfläche in den Poren abgestoßen. Der Diffusionsversuch mit Eu(III) zeigte ein stetiges Abnehmen der Eu(III)-Konzentration im Reservoir bis fast auf null über eine Zeitdauer von 1500 h. Eu(III) wird damit vollständig im Ton aufgenommen. Eine Desorption des Eu(III) mit einem Wasser/Alkohol-Gemisch Eu(III) wurde nicht beobachtet. Np(V)-Diffusion wurde in zwei „Through“-Diffusions-Experimente mit PEEK/Membran bzw. Edelstahlfilter durchgeführt. Nach 100 Tagen Reaktionszeit wurde ein Durchbruch von Np(V) beobachtet, wobei ein Steady State nicht erreicht wurde. Der Kurven-Verlauf des Diffusionsflusses als Funktion der Zeit, als auch die zeitliche Abnahme der Np(V)-Konzentration im Reservoir war in beiden Experimenten signifikant unterschiedlich. Eine schlüssige Erklärung für diese Unterschiede konnte bisher nicht gefunden werden. Fulvinsäure zeigt ebenfalls eine Diffusion durch kompaktierten Illit. Aus den experimentellen Daten wurde ein Diffusionskoeffizient mit $D_e = 1.51 \times 10^{-11} \text{ m}^2/\text{s}$ bzw. $1.70 \times 10^{-11} \text{ m}^2/\text{s}$ für 0.1 und

1.0 M NaCl ermittelt werden. Für α wurden Werte von -0.44 und 0.61 (0.1 und 1.0 M NaCl) abgeleitet. D_e für Fulvinsäure ist hierbei vergleichbar mit D_e -Werten für negativ geladene Tracer wie $^{36}\text{Cl}^-$. Auf der anderen Seite erscheint der negative Wert für α recht unrealistisch.

Die vorliegenden Untersuchungen der Np(V)-Komplexierung mit den niedermolekularen Tonorganika Propionat und Lactat zeigt, dass hauptsächlich jeweils ein 1:1-Komplex – Np(V)-Propionat- bzw. Np(V)-Lactat-Komplex gebildet wird. Die Komplexbildungskonstanten wurden zu $\log \beta_0 (25^\circ \text{C}) = 1.32 \pm 0.05$ für Np (V) Propionat und $\log \beta_0 (25^\circ \text{C}) = 2.07 \pm 0.01$ für Np (V) Lactat bestimmt. Beide Komplexbildungskonstanten nehmen mit der Ionenstärke ($0.5 < \text{NaCl} < 2.5 \text{ m}$) und der Temperatur ($20 < T < 60^\circ \text{C}$) zu. Die Komplexbildungsreaktion ist für die Propionat-Komplexierung endotherm und entropiegetrieben, gemäß der folgenden ermittelten Daten für $\Delta_r H_m^0 = 16.3 \pm 3.0 \text{ kJ mol}^{-1}$ and $\Delta_r S_m^0 = 77 \pm 9 \text{ J mol}^{-1} \text{ K}^{-1}$. Die Größe von $\Delta_r S_m^0$ ist konsistent mit einem zweizähligen Koordinationsmodus, was auch durch spektroskopische Ergebnisse bestätigt wird. Die Laktatkomplexbildungsreaktion ist dagegen exotherm und entropiegetrieben, was durch $\Delta_r H_m^0 = -5.4 \pm 1.4 \text{ kJ mol}^{-1}$ und $\Delta_r S_m^0 = 19 \pm 4 \text{ J mol}^{-1} \text{ K}^{-1}$ belegt wird. Dieses Verhalten wird vermutlich durch den Einfluss der α -Hydroxyl-Gruppe im Laktat verursacht.

Die Stabilität bei höheren Salinitäten von natürlichen kleinen organischen Komponenten (SSOM) und Fulvinsäure (FA) wurde in NaCl-, MgCl_2 - und CaCl_2 -Lösungen untersucht. Die ersten Ergebnisse zeigen eine hohe Stabilität des SSOM unter den vorliegenden Bedingungen: Der DOC variiert um weniger als 5-10%, und ein Einfluss ist bis zu 3 M NaCl nicht zubeobachten. Bei Ionenstärken (IS) von 5 M NaCl, sowie 3 M CaCl_2 , MgCl_2 und HCl zeigen sich bei den Absorptionsspektren einige Veränderungen. Eine detailliertere Auswertung der Absorptionsspektren mittels „Differential Spectroscopy“ lässt vermuten, dass die Erhöhung der IS spezifisch bestimmte Gruppen beeinflusst (Aromaten mit oder ohne Substitution wie $-\text{OH}$ oder $-\text{COOH}$ substituierete Benzolringe oder Carboxylphenole). Eine Veränderung der Konformation bzw. Größe der Komponenten wurde durch eine Kombination von Größenausschlusschromatographie (SEC) und UV-Vis-Absorptions-Spektroskopie identifiziert. Natürliche und synthetische FA zeigen bei steigender Ionenstärke mit NaCl ($> 3 \text{ M}$) eine Erhöhung des hydrodynamischen Radius (Molekulargewicht), während die Zugabe von CaCl_2 oder MgCl_2 eine Verkleinerung des Makromoleküls bewirkt. Der maximale hydrodynamische Radius wurde mittels SEC zu 2 nm, 1.7 nm und 3.8 nm für FA-573, FA-532 und SFA-1 bestimmt. Mit diesen Untersuchungen wurde gezeigt, dass die natürlichen Fulvinsäuren ihre Mobilität als Kolloide auch in natürlichen Grundwässern mit höheren Ionenstärken beibehalten.

Im Rahmen einer Promotion wurde der Einfluss von Borat auf die Komplexbildungsreaktionen, Löslichkeiten und Redoxreaktionen der Actiniden untersucht unter endlagerrelevanten Bedingungen. Die Untersuchungen erstreckten sich von verdünnten bis salinaren Lösungssysteme sowie von reduzierten (+III) bis zu oxidierten (+VI) Actinid-Redoxzuständen. Für die dreiwertigen Ln/An(III) und das fünfwertige Np(V) wurde der

größte Einfluss von Borat auf die Löslichkeiten beobachtet. Löslichkeitsdaten in Verbindung mit Festkörper- und Lösungs-Charakterisierung wurden beschrieben mittels der Gleichgewichtsthermodynamik der aquatischen Systeme und dem SIT-Formalismus für Ionenstärkekorrekturen. Die Bildung von schwerlöslichen Ln/An(III)- und An(V)-Borat-Festphasen stellt einen bisher unbekanntem Rückhalte Mechanismus für dreiwertige und fünfwertige Actiniden dar. Diese Art von Rückhaltung ist besonders für das mobile Np(V) relevant. Die erhaltenen Ergebnisse verdeutlichen, dass die Borat-Wechselwirkung für die korrekte Abschätzung der Actinidenverhaltens unter Endlagerbedingungen berücksichtigt werden muss.

Summary

This project was performed from 2011 to 2015 within the frame of the BMWi R&D program "Entsorgung gefährlicher Abfälle in tiefen geologischen Formationen: Verbesserung von Instrumentarien für die Sicherheitsbewertung von Endlagern und Untertage-deponien" The studies comprises sorption, diffusion, complexation and solubility experiments with focus on clay systems as well as salt rock systems. The investigations within the project generated new experimental data which provides key inputs for the assessment of the source term (maximum expected solubility) for actinides (III, IV, V, VI) covering a wide spectrum of waste disposal concepts and scenarios.

The sorption studies were performed with tri-, tetra-, penta-, and hexavalent actinides: Cm(III) and Eu(III) as trivalent analogon, respectively, Np(IV/V), Pu(IV/V) and U(VI). The sorption was investigated on pure clay mineral illite and the natural claystone opalinus clay by varying the background electrolyte concentration and composition ($[\text{NaCl}]_{\text{max}} = 4.0 \text{ M}$, $[\text{MgCl}_2]_{\text{max}} = 2.0 \text{ M}$ und $[\text{CaCl}_2]_{\text{max}} = 4.0 \text{ M}$) and with exclusion of CO_2 . The batch experiments and the laser fluorescence investigations were performed at pH_c between 3 and 12 (for MgCl_2 up to pH_c 9).

The experimental sorption data shows for Eu(III) a small influence of the salinity on the $\log K_D$ values, especially in the neutral up to the alkaline pH_c range. In acidic media the sorption is significantly diminished with increasing NaCl concentration, because the cation exchange reaction is suppressed with increasing Na^+ concentration in solution. This effect is also observed for CaCl_2 and MgCl_2 . Nevertheless, a almost quantitative sorption ($\log K_D \geq 4.5$) occurs for all systems at $\text{pH}_c > 8$. TRLFS investigations with Cm(III) in saline systems hints to no significant change of the first coordination sphere of the metal ion, meaning that the surface speciation of Cm(III) is not influenced by elevated ionic strength. Identical surface species were also assumed for the modelling of the experimental data with the 2SPNE SC/CE sorption model. This model describes the Eu(III)/Cm(III) sorption over the total pH_c and ionic strength range. For the adjustment of the activity coefficients of the solution species and the water activity the Pitzer approach was used.

The actinyl cations Np(V) and U(VI) shows no significant ionic strength influence of the sorption over the total pH_c range. As expected, the sorption of Np(V) is weaker than the other cations and starts at $\text{pH}_c \sim 8$ (>20%), but reaches quasi quantitative sorption at $\text{pH}_c > 10$. The experimental data can be described with the 2SPNE SC/CE model quite well. The sorption edges of U(VI) systems are comparable with the Eu(III) systems. Because of the slightly stronger hydrolysis the U(VI) pH edge is slightly shifted to lower pH_c values. No significant cation exchange is observed at the experimental conditions and the pH dependent sorption starts (<20%) at about $\text{pH}_c \sim 4$. The sorption is quasi quantitative (> 99,5%) between pH_c 6 and 11. At higher pH_c values the sorption decreases, because the two-fold negative charged species $\text{UO}_2(\text{OH})_4^{2-}$ dominates the aqueous speciation. The modeling with the 2SPNE SC/CE model describes quite well the experimental data up to $\text{pH}_c \sim 7$. At higher pH_c values the model predicts a lower

sorption and an ionic strength influence of the sorption that is not observed in the experiment.

The sorption of Np(V) onto illite was also intensively investigated over reaction times until two months as a function of pH (3-10) in 0.1M NaCl under Ar atmosphere. After about one week reaction time under ambient atmosphere, only an insignificant variation of Np sorption is observed and the establishment of reaction equilibrium can be assumed. Surprisingly, solid-liquid distribution ratios (R_d) are clearly higher than those measured for Np(V) sorption onto illite under aerobic conditions. The observation that R_d increases with decreasing p_e ($p_e = -\log a_{e^-}$, negative decadic logarithm of electron activity in solution) suggests partial reduction to Np(IV), although measured redox potentials (p_e values) at a first glance suggest the predominance of Np(V). Reduction to Np(IV) at the illite surface could indeed be confirmed by X-ray absorption near-edge spectroscopy (XANES). Np speciation in presence of the purified Na-illite under given conditions is consistently described by applying the 2SPNE SC/CE model. Measured p_e data are taken to calculate Np redox state; the necessary surface complexation constants for Np(IV) are derived by applying a data fitting procedure. These constants are very consistent with results obtained by applying an existing linear free energy relationship (LFER). The Np(V)/Np(IV) redox borderline of a Eh-pH diagram, calculated with the new Np(IV) surface complexation constants, is shifted in presence of illite surfaces by 3-5 p_e units (0.2-0.3 V) towards redox neutral conditions. Our study suggests that Np(V) reduction in presence of a sorbing mineral phase is thermodynamically favored in contrast to the solution without the solid.

We also investigated Pu sorption onto illite under anaerobic conditions in 0.1 M NaCl. In the pH range $3 < \text{pH} < 10$, Pu uptake is constantly high ($\log R_d > 4 \text{ L kg}^{-1}$). A mixture of Pu(III) and Pu(IV) occurs in solution for $\text{pH} < 5$. Using Eu(III)-illite uptake data (with Eu(III) as a chemical analogue of Pu(III)), adsorption models for the individual redox states and measured redox potentials, overall Pu uptake is accurately predicted for a mixture of redox states. As in previous sorption studies on Eu(III), results for Pu(IV) interaction with an illite:calcite mixture suggest that Pu(III,IV) uptake by illite is weakly affected by the presence of carbonate. Our experimental and modeling results can be used to predict Pu retention in the reducing, calcite saturated groundwaters expected for potential nuclear waste repository sites.

Generally, the model prediction with the 2SPNE SC/CE model agree quite well with the experimental values by using ionic strength corrections – Pitzer or SIT - for the activity of the aqueous species and including redox equilibria in solution. A strong sorption of trivalent, tetravalent, pentavalent and hexavalent actinides on clay minerals is expected under saline conditions and absence of carbonate.

Concerning the impact of iron corrosion products on radionuclide retention, the syntheses and characterization of green rust chloride and magnetite containing trivalent f-elements (Nd, Am) was performed. The bulk solids were characterized by X-ray diffraction (XRD) and Raman spectroscopy and X-ray photoelectron spectroscopy (XPS) was

used to obtain information on the speciation of the various structural elements and dopant. Finally, scanning electron microscopy (SEM) provided information on the size and shape of the particles. Green rust (GR) was synthesized by direct precipitation of a mixture of Fe(II) and Fe(III) ions in the presence of trace amounts of Nd(III) or Am(III). The doped GR were washed with deoxygenated water to initiate their transformation to magnetite, but only the Nd-containing sample was analyzed. Separately, magnetite was synthesized by direct precipitation from a solution containing Fe(II) and Fe(III) ions and trace amounts of Am(III). It is difficult to harmonise the results of Raman spectroscopy, XRD, and SEM data, but in none of the sample the dopant (Nd or Am) had an influence on the synthesis of iron phase and it does not precipitate as a separate phase.

The diffusion of HTO, Cl⁻, Eu, Np(V), and fulvic acid in illite was investigated in in-diffusion or through-diffusion experiments. The diffusion (“in” or “through” diffusion) experiments were performed with compacted, cylindrical Na-illite samples and in NaCl as background electrolyte. The diffusion parameters of HTO and Cl⁻ were determined in 0.1 M and 0.5 M NaCl. HTO diffusion coefficients (D_e) and values for the porosity (ϵ) are similar in 0.1 and 0.5 M NaCl, indicating that an increase in background electrolyte concentrations has no effect on the geometrical properties (tortuosity (α) or constrictivity). For the anion Cl⁻, D_e and α were deduced to be higher in 0.5 M NaCl. The lower D_e value for Cl⁻ compared to HTO can be related to a reduced accessible pore space for anionic tracers, as anions are repelled from the vicinity of the negatively charged clay surfaces. The diffusion experiment with Eu(III) showed a steadily decreasing Eu concentration in the reservoir for < 1500 h, and the Eu concentration dropped to almost zero. This result indicates a complete Eu uptake onto the Na-illite mineral. The Eu(III) was not released from the clay by replacing the reservoir solution with several water/alcohol mixtures. The Np(V) diffusion was investigated in two through-diffusion experiments with i) a PEEK/membrane set-up and ii) stainless steel filter set-up. A breakthrough of Np was observed after 100 days, but a steady state was not established. The time-dependent curves of the diffusion flux and the decrease of the Np concentration in the reservoir was different for both experimentals. These observations cannot be explained at the moment. Fulvic acid (FA) also shows diffusion in the compacted illite. The diffusion coefficients of $D_e = 1.51 \times 10^{-11} \text{ m}^2/\text{s}$ and $1.70 \times 10^{-11} \text{ m}^2/\text{s}$ were deduced for 0.1 and 1.0 M NaCl, respectively. For α , the calculated values were -0.44 and 0.61 (0.1 and 1.0 M NaCl, respectively). The D_e for FA are comparable to D_e values determined for negatively charged traces (i.e. ³⁶Cl⁻). On the other hand, the value for the rock capacity factors seems to be unrealistic.

The present studies of the Np(V) complexation with low-molecular weight clay organics propionate and lactate show that the 1:1-complex – Np(V)-propionate or -lactate complex - is mainly formed. The complex formation constants were determined to be $\log \beta_0 (25^\circ\text{C}) = 1.32 \pm 0.05$ for Np(V) propionate and $\log \beta_0 (25^\circ\text{C}) = 2.07 \pm 0.01$ for Np(V) lactate. Both complex formation constants increase with ionic strength ($0.5 < \text{NaCl} < 2.5 \text{ m}$) and temperature ($20 < T < 60^\circ\text{C}$). The complex formation reaction is endothermic for propionate complexation and entropy driven, as evidenced in the present work with $\Delta_r H_m^0 = 16.3 \pm 3.0 \text{ kJ mol}^{-1}$ and $\Delta_r S_m^0 = 77 \pm 9 \text{ J mol}^{-1} \text{ K}^{-1}$. The magnitude of $\Delta_r S_m^0$ is consistent with a bidentate coordination mode, which is also confirmed by spectroscopic

results. However, the lactate complex formation reaction is exothermic and entropy driven, evidenced by $\Delta_r H_m^0 = -5.4 \pm 1.4 \text{ kJ mol}^{-1}$ and $\Delta_r S_m^0 = 19 \pm 4 \text{ J mol}^{-1} \text{ K}^{-1}$. This might be caused by the influence of the α -hydroxy group in the lactate molecules.

The stability of small sized organic matter (SSOM) and fulvic acid (FA) was studied in NaCl, MgCl₂, and CaCl₂ solutions. The first results indicate a high stability of the SSOM under the present conditions: the DOC varies by less than 5-10% and no effect is noticeable up to 3 M NaCl. At 5 M NaCl or ionic strength (IS) of 3 M for CaCl₂/MgCl₂ and HCl some variations are noticeable on the absorption spectra. A refined analysis of the absorption spectra by differential spectroscopy suggests, that an increase of the ionic strength affects more specifically some kind of groups (aromatic with or without substitution like –OH and –COOH-substituted benzene rings or carboxyphenols). Conformation (size) changes are qualitatively evidenced by a combination of size exclusion chromatography (SEC) and UV-Vis absorption spectroscopy. For the fulvic acids, natural or synthetic, the NaCl addition (> 3 M) results in an expansion of the hydrodynamic volume (molecular weight) while the addition of CaCl₂ or MgCl₂ results in a compaction of the macromolecule. The maximum hydrodynamic diameter values estimated from SEC data are respectively 2 nm, 1.7 nm and 3.8 nm for FA-573, FA-532 and SFA-1 respectively. The natural fulvic acids can thus certainly preserve their mobility in high ionic strength natural media

In the frame of a PhD thesis the impact of borate on the chemical behaviour of actinides has been studied under repository-relevant conditions, with special emphasis on complexation reactions, solubility phenomena and partly also on redox processes. The study extends from dilute to concentrated saline systems and from reduced (+III) to oxidized (+VI) actinide redox states. The strongest impact of borate on the solubility was observed for the trivalent Ln/An(III) and the pentavalent Np(V). Solubility data in combination with solid and aqueous phase characterization have been described and quantified in terms of equilibrium thermodynamics of aqueous systems using the SIT formalism for ionic strength corrections. The formation of sparingly soluble Ln/An(III)- and An(V)-borate solid phases represents a so-far unknown retention mechanism for these redox states, and it is especially relevant for the highly mobile Np(V). These results highlight the need of accounting for borate interactions for the correct assessment of actinide behaviour under repository conditions.

This work was performed at the Karlsruhe Institute of Technology, Institute for Nuclear Waste Disposal (KIT-INE) by several colleagues contributing to the experiments, data evaluation, implementation and writing of the present report:

Nidhu Lal Banik contributed to sorption studies of neptunium and plutonium on OPA and illite, complexation of Np(V) with lactate and propionate.

Muriel Bouby-Laliron contributed to studies of the stability of humic and fulvic acid at high ionic strengths.

Nicolas Finck contributed to interaction studies of actinides with iron phases

Katja Hinze contributed within the frame of her PhD thesis to the studies of borate impact on the actinide solubilities

Tom Kupcik contributed to diffusion studies of europium, neptunium and fulvic acid.

Christian Marquardt contributed to the sorption and complexation studies and was the editor of the final report.

Remi Marsac contributed to sorption studies of neptunium and plutonium on OPA and illite, modelling of sorption with PREEQC, complexation studies with humic and fulvic acids.

Thomas Rabung contributed to the sorption studies.

Andreas Schnurr contributed within the frame of his PhD thesis to sorption studies of curium, europium, uranium with OPA and illite, modelling of the experimental studies with PREEQC

In the studies are also involved some bachelor, master and DAAD students: Sarah Waltz, Alexandre Diascorn, Alesandre Vasiliev.

Table of Contents

1	Introduction	1
2	Sorption of radionuclides on clay minerals and iron phases	2
2.1	Sorption onto Clay minerals	2
2.1.1	Trivalent actinides and lanthanides (Cm(III) and Eu(III)).....	2
2.1.1.1	Sorption of Eu(III) on illite (IdP) in the NaCl system	5
2.1.1.2	Sorption on Illit (IdP) in CaCl ₂ and MgCl ₂ systems.....	9
2.1.1.3	Curium (Cm(III)) sorption on illite (IdP).....	14
2.1.1.4	Sorption of Eu(III) on natural Opalinus clay mineral.....	18
2.1.2	Sorption of neptunium(V) onto illite in the NaCl system	19
2.1.2.1	Neptunium redox speciation on the illite surface.....	20
2.1.3	Plutonium	29
2.1.3.1	Plutonium sorption at the kaolinite surface	29
2.1.3.2	Plutonium sorption at the illite surface	34
2.1.4	Conclusion	44
2.1.5	U(VI) sorption on Illite at high ionic strengths.....	44
2.1.6	Conclusions.....	51
2.2	Iron phases	51
2.2.1	Green rust synthesized in the presence of Nd(III).....	52
2.2.2	Green rust and magnetite synthesized in the presence of Am(III)	53
3	Diffusion of radionuclides in clay minerals	56
3.1	Diffusion of Tritium and Chloride in Illite.....	57
3.2	Diffusion of Eu(III) in compacted illite	59
3.3	Diffusion of Np(V).....	59
3.4	Diffusion of fulvic acid in Illite	61
3.5	Conclusions.....	63
4	Clay organic compounds, fulvic and humic acid: interactions with radionuclides.....	64
4.1	Investigation of the Np(V) propionate and lactate complex formation.....	64
4.1.1	Spectroscopic study of the Np(V) propionate complex formation	65

4.1.2	Investigation of propionate and lactate complexation by Solvent extraction.....	72
4.1.3	Conclusions.....	82
4.2	Humic acid complexes at high ionic strengths	83
4.2.1	Stabilization of polynuclear plutonium(IV) species by humic acid	83
4.2.2	Conclusions.....	85
4.3	Investigations on the stability of humic substances at elevated ionic strengths	86
4.3.1	Material and methods.....	86
4.3.2	Results and discussion	89
4.3.3	Conclusions.....	101
5	Solubility of Actinides in presence of borate and at high ionic strengths	103
5.1	Experimental	104
5.1.1	Chemicals	104
5.1.2	pH measurement in saline solutions	104
5.1.3	Speciation of boron in aqueous saline solutions	106
5.1.4	Determination of total metal concentration and aqueous speciation techniques used for Ln(III) and An(III/IV/V/VI) in solution	106
5.1.5	Solid phase characterization (XRD, XPS, SEM-EDS, EXAFS).....	107
5.1.6	Ln(III)/An(III/IV/V/VI) solubility experiments.....	108
5.2	¹¹ B-NMR in NaCl, CaCl ₂ and MgCl ₂ solutions.....	110
5.2.1	¹¹ B-NMR studies in NaCl solutions.....	111
5.2.2	¹¹ B-NMR studies in CaCl ₂ and MgCl ₂ solutions.....	112
5.2.3	Conclusions.....	113
5.3	Interaction of Ln(III)/An(III) with borate.....	114
5.3.1	Solubility of Nd(III) in NaCl, CaCl ₂ and MgCl ₂ solutions	115
5.3.2	Cm(III) aqueous speciation in the presence of borate: TRLFS	119
5.3.3	Conclusions.....	123
5.4	Solubility of Th(IV) in the presence of borate	124
5.4.1	Conclusions.....	126
5.5	Interaction of Pu(III/IV) with borate.....	127

5.5.1	Conclusions.....	129
5.6	Solubility of Np(V) in the presence of borate.....	130
5.6.1	Solubility of Np(V) in NaCl and MgCl ₂ solutions	131
5.6.2	Conclusions.....	135
5.7	Solubility of U(VI) in the presence of borate.....	136
5.7.1	Solubility of U(VI) in NaCl and MgCl ₂ solutions	136
5.7.2	Solid phase characterization	139
5.7.3	Conclusions.....	139
List of Tables.....		141
List of Figures		145

1 Introduction

In the context of final disposal of radioactive waste in deep geological formations the sorption onto mineral phases and particularly onto surfaces of clay minerals represents an important retention mechanism for actinides. The sorption onto clay minerals was intensively investigated in the last decades. However, these investigations have mostly been performed at low back electrolyte concentrations ($I_{\max} = 0.1 \text{ M}$). In Jurassic and Cretaceous clay deposits in Northern Germany as well as in sediments in Canada, which are also discussed as host rocks for repositories, groundwaters with higher salt concentrations are expected. The geochemical modelling of radionuclide sorption in saline solutions has not been developed so far. Therefore, the application of the widely used sorption model for low ionic strengths (2SPNE SC/CE) are to be tested for high ionic strength ($I > 1 \text{ M}$) in the frame of this project. Relevant geochemical aspects were investigated regarding the retention of the actinides uranium, neptunium, plutonium, americium, curium as well as the lanthanide europium in clay stone. The lanthanide Eu represents a chemical analogon for trivalent actinides. The focuses in this project were on the sorption, diffusion, complexation and redox processes of the actinides at higher ionic strengths in clay systems. Some preliminary experiments were also performed at higher temperature, e.g. the complexation of Np(V) with clay organics propionate and lactate.

The opalinus clay (OPA) from the Mont Terri project (Switzerland) as a reference natural clay stone and, as one main component of the OPA, the pure clay mineral illite was taken for the studies. Additionally, aspects of the impact of organic compounds found in the OPA, small molecules like propionate and polyelectrolytes like fulvic acids, are included in the investigations. The canister as an important component of the waste generates corrosion products in case of water intrusion into the repository that can have a positive influence on the retention of radionuclides. First experiments in this project have been performed to elucidate the role of these corrosion products on the retention. Another aspect has been studied: the interaction of borate with lanthanides (III) and actinides (III, IV, V, VI) in dilute to concentrated saline solutions. Boron can be present as component of the emplaced waste in a nuclear waste repository. In certain rock salt formations, high boron concentrations can also occur in the intruding brine solutions. In this framework, it is very relevant to understand the impact of borate in the chemical behaviour of actinides (e. g. complexation, solubility phenomena or redox processes) under repository relevant conditions.

The work within the project proceeded in close cooperation with the Helmholtz Center Dresden-Rossendorf, the Universities of Mainz, Potsdam, Heidelberg, Köln, the Saarland, as well as the Technical Universities Dresden and Munich.

2 Sorption of radionuclides on clay minerals and iron phases

Actinide retention at clay mineral surfaces is a well-established process, which has been intensely investigated in the context of nuclear waste disposal. Up to now, however, almost no experimental data for actinide sorption at elevated ionic strength is available in the literature. In addition, also no mechanistic sorption model exists that reliably describes actinide uptake at elevated ionic strength ($I > 1 \text{ M}$). Such conditions are to be expected e. g. in the vicinity of a repository in rock salt formations, in the Jurassic and lower Cretaceous clay rock layers in Northern Germany and in sedimentary layers in Canada, which are identified as potential host rock for the disposal of high level nuclear waste. The results of these studies are presented in the first part of this chapter.

The clay barrier is not the only solid phase that can fix radionuclides. A second important retention phase in the near field is the iron from canister material that is converted into secondary iron phases during corrosion processes with ground water. These secondary phases might retain radionuclides by sorption and incorporation into the mineral structure. The relevance of such iron phases is elucidated in preliminary sorption experiments with the goal to help designing experiments for future projects. The second part of this chapter deals with the iron phases.

2.1 Sorption onto Clay minerals

Within the present study, the uptake of actinides (Cm(III) and the trivalent analogue lanthanide Eu(III), Np(V), Pu(IV/V) and U(VI)) onto illite and on an Opalinus clay sample was investigated in dilute to concentrated saline systems.

2.1.1 Trivalent actinides and lanthanides (Cm(III) and Eu(III))

The sorption of the trivalent actinide Cm(III) and the analogue element Eu(III) onto illite was investigated in NaCl, CaCl₂, and MgCl₂ solution. The investigated back electrolytes and their maximum concentrations were $[\text{NaCl}]_{\text{max}} = 4.0 \text{ M}$, $[\text{MgCl}_2]_{\text{max}} = 2.0 \text{ M}$ and $[\text{CaCl}_2]_{\text{max}} = 4.0 \text{ M}$. To avoid carbonate complexation, the experiments were performed in the absence of CO₂ in a glovebox with argon atmosphere. Eu(III) batch sorption experiments and Cm(III) time-resolved laser fluorescence spectroscopy (TRLFS) studies were carried out in the pH range 3 - 12 (for MgCl₂ solutions up to pH = 9).

Clay materials were obtained as aqueous suspensions from the Laboratory for Waste Management (LES) of the Paul Scherrer Institute (PSI), Switzerland. The preparation and pretreatment (Bradbury and Baeyens, 2009a) of the Illite du Puy along with details of the experimental methodologies have been described in much detail in a number of previous publications (Baeyens and Bradbury, 2004; Bradbury and Baeyens, 2002, 2009a; Poinssot et al., 1999). Relevant information such as N₂-BET surface area and

cation exchange capacity is available in these references and will not be repeated here. All suspensions were stored in the dark at 4 °C prior to use and utilized within one year after preparation.

All experiments were carried out under controlled argon atmosphere in glove boxes ($O_2 \sim 2$ ppm) at room temperature (25 ~ °C). Eu sorption measurements were carried out as a function of pH at constant ionic strength and solid to liquid ratio. Details of the experimental procedures, geochemical modelling and data evaluation are described in (Schnurr et al., 2015).

To simulate the clay/actinide/solution systems even at high ionic strengths, the computer program PHREEQC (Parkhurst and Appelo, 1999) was used, which has a built-in ability to handle both Pitzer equations and adsorption modeling. As we applied a non-electrostatic sorption model, there was no need to select a specific surface charge model to simulate surface. This program also has a built-in SIT option, but the SIT formalism is restricted to $I < 3-4$ m. SIT coefficients for the Cm/Eu species were taken from (Neck et al., 2009).

We verified that the calculations involving the Pitzer formalism and an adsorption model gave consistent results. To this end a code comparison was carried out. One set of model calculations was performed using the program ECOSAT 4.8 (Keizer and van Riemsdijk, 1999). Because of the fact that to our knowledge no previously published surface complexation modeling that involves the Pitzer formalism, such a cross check was deemed to be useful. There are no fundamental differences between the two ways of calculations.

Table 1: Formation constants for hydrolysis and chloride complexation at infinite solution used for Eu in the sorption modeling. Data are from the NEA-TDB (Guillaumont et al., 2003)

Complexation reaction	log K°
$Eu^{3+} + H_2O = Eu(OH)^{2+} + H^+$	-7.2
$Eu^{3+} + 2 H_2O = Eu(OH)_2^+ + 2 H^+$	-15.1
$Eu^{3+} + 3 H_2O = Eu(OH)_3 + 3 H^+$	-26.2
$Eu^{3+} + 4 H_2O = Eu(OH)_4^- + 4 H^+$	-40.7
$Eu^{3+} + Cl^- = EuCl^{2+}$	0.24
$Eu^{3+} + 2 Cl^- = EuCl_2^+$	-0.74

Eu sorption onto illite is modeled with the 2 site protolysis non-electrostatic surface complexation and cation exchange (2SPNE SC/CE) sorption model (Bradbury and Baeyens, 1997, 2002). The model considers two types of high surface density protolysable (W1 and W2) sites to simulate clay proton titration data. In the latest version of the model (Bradbury and Baeyens, 2009a), only strong sites, S, have been considered for modeling cation surface complexation data at trace metal ion concentrations.

Table 2: Cation exchange capacities (CEC) and surface hydroxyl group densities for SWy-2 and Illite du Puy (Bradbury and Baeyens, 2006, 2009a)

Site types	Na-SWy-2 Site capacity (mol/kg)	Na-illite Site capacity (mol/kg)
$\equiv\text{S}^{\text{S}}\text{OH}$	2.0×10^{-3}	2.0×10^{-3}
$\equiv\text{S}^{\text{W1}}\text{OH}$	4.0×10^{-2}	4.0×10^{-2}
$\equiv\text{S}^{\text{S2}}\text{OH}$	4.0×10^{-2}	4.0×10^{-2}
CEC (meq/100g)	87.7	22.5

Table 3: Protolysis of Eu(III) surface species to model Eu sorption on illite with the 2SPNE SC/CE model and SWy-2 for comparison reasons (Bradbury and Baeyens, 2006, 2009a)

Reactions	Na-SWy-2	Na-illite
Surface protolysis	Log $K_{\text{protolysis}}$	
$\equiv\text{S}^{\text{S}}\text{OH} + \text{H}^+ = \equiv\text{S}^{\text{S}}\text{OH}_2^+$	4.5	4.0
$\equiv\text{S}^{\text{S}}\text{OH} = \equiv\text{S}^{\text{S}}\text{O}^- + \text{H}^+$	-7.9	-6.2
$\equiv\text{S}^{\text{W1}}\text{OH} + \text{H}^+ = \equiv\text{S}^{\text{W1}}\text{OH}_2^+$	4.5	4.0
$\equiv\text{S}^{\text{W1}}\text{OH} = \equiv\text{S}^{\text{W1}}\text{O}^- + \text{H}^+$	-7.9	-6.2
$\equiv\text{S}^{\text{W2}}\text{OH} + \text{H}^+ = \equiv\text{S}^{\text{W2}}\text{OH}_2^+$	6.0	8.5
$\equiv\text{S}^{\text{W2}}\text{OH} = \equiv\text{S}^{\text{W2}}\text{O}^- + \text{H}^+$	-10.5	-10.5

Table 4: Cation exchange reaction of illite (IdP) and SWy at infinite dilution to model Eu sorption on illite with the 2SPNE SC/CE model and SWy-2 for comparison reasons (Bradbury and Baeyens, 2006, 2009a), (Schnurr, 2015).

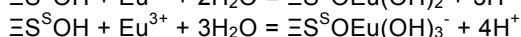
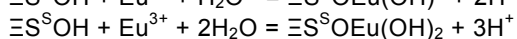
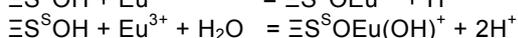
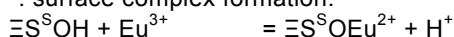
Cationic exchange reactions	Na-SWy-2	Na-illite
	Log $K_{\text{protolysis}}$	
$\text{NaX} + \text{H}^+ \rightarrow \text{HX} + \text{Na}^+$	4.5	4.0
$2 \text{NaX} + 2 \text{Ca}^{2+} \rightarrow \text{CaX}_2 + 2 \text{Na}^+$	-7.9	-6.2
$3 \text{NaX} + \text{Eu}^{3+} \rightarrow \text{EuX}_3 + 3 \text{Na}^+$	4.5	4.0
$3 \text{CaX}_2 + 2 \text{Eu}^{3+} \rightarrow 2 \text{EuX}_3 + 3 \text{Ca}^{2+}$	-7.9	-6.2

Table 5: Thermodynamic equilibrium parameters at infinite dilution to model Eu sorption on illite (IdP) with the 2SPNE SC/CE model (Bradbury and Baeyens, 2009b).

Surface complex [#] (log K _{SC})	Na-IdP	Na-IdP (p.w.)	Ca-IdP*	Ca-IdP (p.w.)
$\Xi\text{S}^{\text{S}}\text{O}\text{Eu}^{2+}$	1.9	1.9	0.4 (Δ -1.5)	0.4
$\Xi\text{S}^{\text{S}}\text{O}\text{Eu}(\text{OH})^+$	-4.6	-4.1	-5.4 (Δ -0.8)	-4.9
$\Xi\text{S}^{\text{S}}\text{O}\text{Eu}(\text{OH})_2$	-12.8	-12.0	-13.1 (Δ -0.3)	-12.3
$\Xi\text{S}^{\text{S}}\text{O}\text{Eu}(\text{OH})_3^-$	-24.0	-23.2	-24.3 (Δ -0.3)	-23.7
$\Xi\text{SSO}\text{Ca}_3\text{Eu}(\text{OH})_6^{2+}$	-	-	-	-55.5

*: the values accord to the analog $\Delta\log K_{\text{SC}}$ (values in parathesis) of Na-SWy to Ca-SWy in (Schnurr, 2015).

#: surface complex formation:



2.1.1.1 Sorption of Eu(III) on illite (IdP) in the NaCl system

Ionic strength has a small impact on $\log K_{\text{D}}$ values for Eu(III) in NaCl systems at near-neutral to alkaline pHc. Only under acidic pHc conditions where cation exchange is the dominating binding mechanism a significant decrease of Eu(III) sorption is observed with increasing NaCl concentration. Unlike to the NaCl system, a significant decrease in the uptake is observed in all solutions at elevated MgCl_2 and CaCl_2 concentrations. Nonetheless, $\log K_{\text{D}}$ values (K_{D} in $\text{L}\cdot\text{kg}^{-1}$) remain high ($\log K_{\text{D}} \geq 4.5$) for all systems in the pHc range 8 - 11. TRLFS studies do not indicate any significant change in the first coordination sphere of Cm(III) at a given pHc if ionic strength is increased. As a consequence, we do not expect any change in the surface speciation of Cm(III) at elevated ionic strength compared to previous studies at low background electrolyte concentration. Identical surface species are assumed and Eu(III) uptake data are sufficiently well described using the 2SPNE SC/CE model calibrated at lower ionic strength. The impact of elevated ionic strength on the activities of solutes and of water is taken into account by applying the Pitzer approach.

The uptake of Eu onto illite is presented as percentage sorbed (Figure 1) and $\log K_{\text{D}}$ (Figure 2) versus pH_m . The sorption edges include replicate measurements from two years apart (2010 and 2012) with two different clay batches. The data points obtained with the two batches are plotted together in Figure 1 and 2. They do not differ significantly. The general pH_m dependent sorption of trivalent metal cations onto clay minerals shows the usual features. At low pH_m values and $I = 0.09 \text{ m}$, Eu uptake is higher than 50% and reaches nearly 100% for $\text{pH} > 5-6$ (Figure 1). The uptake in the low pH region is reduced with increasing salt content. The amount of adsorbed Eu at $\text{pH}_m = 3-$

4 decreases from 50% to 70% for the lowest NaCl concentration (0.09 m) to nearly no sorption for higher NaCl concentrations (0.92 and 3.90 m). Also, a slight shift of the sorption edge to higher pH_m with increasing NaCl concentration is observed. Nevertheless, almost complete uptake of Eu ($\geq 99.5\%$) is observed for all investigated NaCl concentrations at $pH_m \geq 6.5$. The results for Eu sorption onto illite clearly show that for pH values relevant to nuclear waste disposal ($pH_m \sim 8$ for typical clay porewater conditions and $pH_m > 10$ in the presence of cementitious material), at least in pure NaCl solutions and in the absence of carbonate, no significant ionic strength effect is observed. Such a relationship might, however, simply be invisible due to large analytical uncertainties in this pH range. The shaded area in Figure 2 represents the region of very high $\log K_D$ values >6.2 corresponding to $>99.97\%$ sorption which corresponds to the calculated detection limit of our analytical method (based on the 3σ standard deviation of the background criterion).

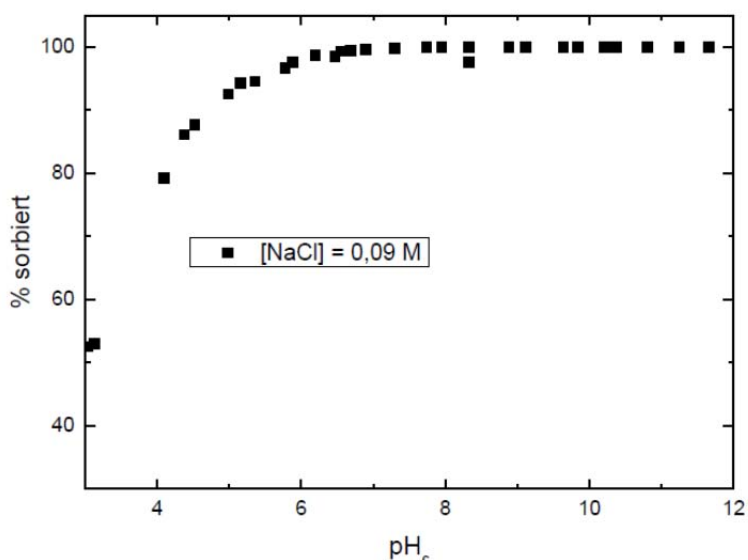


Figure 1: Eu(III) sorption on Illit du Puy (IdP) plotted as sorbed % against pH_c in NaCl (0.09 M) ; S :L = 2 g/L, $[Eu]_{total} = 2.0 \times 10^{-7}$ M.

Additionally, the $\log K_d$ values for Cm(III) sorption on IdP, deduced from the fluorescence emission spectra discussed later on (s. next chapter), are also plotted in Figure 2. All own data are faced to the data from Bradbury and Baeyens (Bradbury and Baeyens, 2009a, 2015).

The dependence of the ionic strength on the Eu(III) sorption significantly occurs in the lower pH_c range until 6.5. The sorption decreases with increasing NaCl concentration; the main sorption mechanism of cation exchange is suppressed with increasing Na^+ concentration in solution. In the range of the main sorption mechanism of inner sphere complexation – $pH_c > 6.5$ – the ionic strength effect is very weak. Small deviations of the data are in the range of the experimental uncertainties. At $pH_c \sim 8$ and higher, the range of quasi quantitative sorption is observed. The experimental data at $pH_c > 8.5$ in

the present work are near the scope of the detection limit, which was estimated to be $\log K_d \geq 6.25$ ($\geq 99.97\%$) with 3σ standard deviation. The data within this range shows relatively large uncertainties.

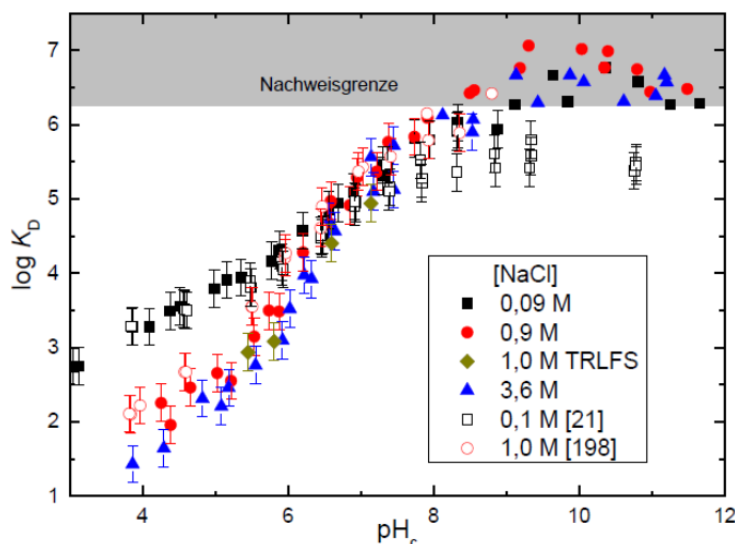


Figure 2: Eu(III) sorption on Illit du Puy (IdP) plotted as $\log K_D$ against pH_c at different NaCl concentrations (0.09, 0.90, 3.60 M); S :L = 2 g/L, $[Eu]_{total} = 2.0 \times 10^{-7}$ M. The data from TRLFS measurements of Cm(III) sorption and data from literature (Bradbury and Baeyens, 2009a, 2015) are additionally shown.

By comparison of data in diluted NaCl solution from the present work with data from literature, both data set show almost identical trend of the sorption edge until pH_c of ~ 8 . At $pH_c > 8$ the data of the present experimental work are about 0.5 – 0.8 $\log K_d$ units systematically larger than in previous work. The difference of about 0.5 $\log K_d$ units – this corresponds to a difference between 99.90 and 99.97 % sorption – occurs at very low Eu(III) concentration near the detection limit. The low metal concentration implies high requirements on the analytical methods for a reliable data evaluation. As a consequence, the difference among the individual data sets is not significant, equals the experimental uncertainties and is appraised as not relevant. Two possible reasons might explain the difference of the data sets, which only differ in the technique of the phase separation. Bradbury and Baeyens centrifuge the sample volumes at $g_{max} = 105000$ directly after reaching the equilibrium time and subsequently takes the supernatant for further investigations (Bradbury and Marques, 2013). In the present work the suspension was centrifuged after the equilibrium time with $g_{max} = 694000$ and finally the supernatant was conveyed by a syringe into a new vial. Either, the selection of the lower speed of centrifugation does not separate all particle sizes, especially nano-particles, and feigns lower sorption, or, an extra sorption of Eu(III) on the vial wall feigns higher sorption. The very small discrepancy of the results – percentual difference at the second decimal place - cannot be clarified because of the application of disparate tools.

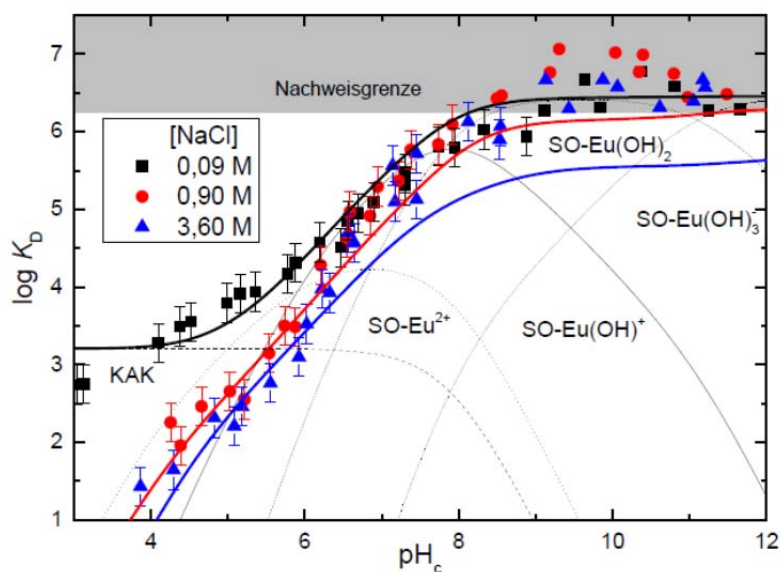


Figure 3: Modeling (solid lines) of the Eu(III) sorption data (symbols) plotted as $\log K_D$ against pH_c at different NaCl concentrations (0.09, 0.90, 3.60 M); S:L = 2 g/L, $[\text{Eu}]_{\text{total}} = 2.0 \times 10^{-7}$ M. The 2SPNE SC/NE model with detailed sorption species distribution at $I = 0.09$ M was used.

To demonstrate the analogy of Eu(III) and Cm(III), the Cm(III) data at 1.0 M NaCl, deduced from TRLFS spectra, are also shown in Figure 2. TRLFS cannot differentiate between uncomplexed and free Cm(III) aqua ion in solution and outersphere sorbed Cm(III) species. But at high ionic strength the outersphere complexation is totally suppressed and the free Cm(III) aqua ion and the Cm(III) surface species can be discriminated spectroscopically and a $\log K_d$ can be determined. The Cm(III) data deduced from the spectra fits very well to the Eu(III) data from (Bradbury and Baeyens, 2015) and from this work.

The results of the modelling of the Eu(III) sorption data with the 2SPNE SC/CE approach are shown in Figure 3. The corresponding constants used for the calculation are listed in Table 2 Table 5. The constants of the surface complexes slightly differ from literature constants ($\Delta \log K_{\text{SC}} \pm 0, +0.5, 0.8, 0.8$ for the surface complexes SO-Eu^{2+} to SO-Eu(OH)_3^-), and they were adjusted to get the best fit to the latest data diluted NaCl solution. The curves. These adaptation was necessary to minimize the deviation of the experimental data from the modelling curve using literature data and to describe the data correctly. This correct data set at dilute ionic strength ($I \leq 0.1$ M) for the modelling is a prerequisite to reliably describe the experimental data at saline conditions including the activity coefficients deduced by the Pitzer formalism. The modelling curve describes the experimental data at high ionic strengths quite well. The suppressed cation exchange at low pH values as well as the trend of the sorption edges is reflected correctly. Furthermore, the modelling of the probed systems specifies the quasi quantitative sorption (>99.5%; $\log K_d > 5.5$) at $\text{pH}_c > 8$, according to the experimental data. However, the modelling also predicts a general ionic strength dependence of the sorption in the mid to high pH_c range, that is not observed in the experiments. Either, the relatively large uncertainties in the band of the detection limit because of the

analytical restrictions mask such a ionic strength dependence, or the model is inadequately parameterized. The approach of a non-electrostatic surface complexation model might also be inadequate for the application at very high ionic strengths. The implementation of an additional species like in the uranyl system (Schnurr, 2015), the mixed surface complex $\Xi\text{SO-Eu-Cl-OH}$, could correct the deviation in the model. Such a species that occurs in only small concentrations could not be detected by spectroscopy and, hence, is not considered, here. Nonetheless, the modelling with the 2SPNE SC/CE model produces quite well results and can predict the Eu(III) sorption onto illite over a broad pH_c range at high saline NaCl solutions.

2.1.1.2 Sorption on Illit (IdP) in CaCl_2 and MgCl_2 systems

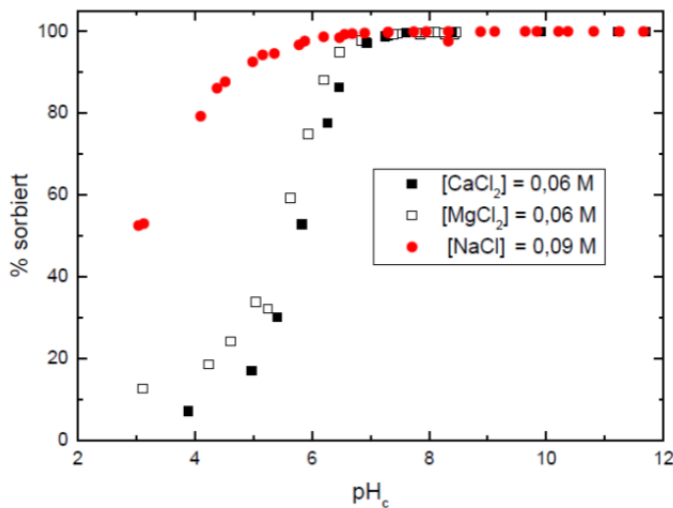


Figure 4: Comparison of Eu(III) sorption on Illite in NaCl (0.09 M), CaCl_2 (0.06 M) and MgCl_2 (0.06 M) solutions.

The results of Eu(III) sorption on illite in diluted CaCl_2 und MgCl_2 (0,06 M) solutions and for comparison reasons in NaCl (0.09 M) solution are shown in Figure 4. Because the $\text{Mg}(\text{OH})_2$ precipitates at $\text{pH}_c > 9$, the investigation stops for the Mg^{2+} system at pH_c 9 (Altmaier et al., 2003a). Figure 4 clearly demonstrates, that even in diluted solutions of CaCl_2 and MgCl_2 the cation exchange reaction is suppressed in contrast to NaCl solutions. At low pH_c values no significant sorption of Eu(III) is observed. The sorption edge is found in the pH_c range 5 – 7 and quasi full sorption is observed above $\text{pH}_c \sim 7$. There is no difference in the influence on the sorption between Mg^{2+} and Ca^{2+} . This behavior becomes clearer when the concentration of Ca and Mg is increased up to 2 M as shown in Figure 5. The sorption edges of each cation at the same concentration are almost superimposed. Differences in the sorption data between both cations are within the experimental error margin.

It stands out that the sorption edge shifts to higher pH_c values with increasing ionic strength at pH_c values below 9. At higher pH_c values no difference in the sorption is visible, because the sorption is quasi quantitative, and it maintains independent of the ionic strength up to pH_c 12, the maximum pH value in the experiment.

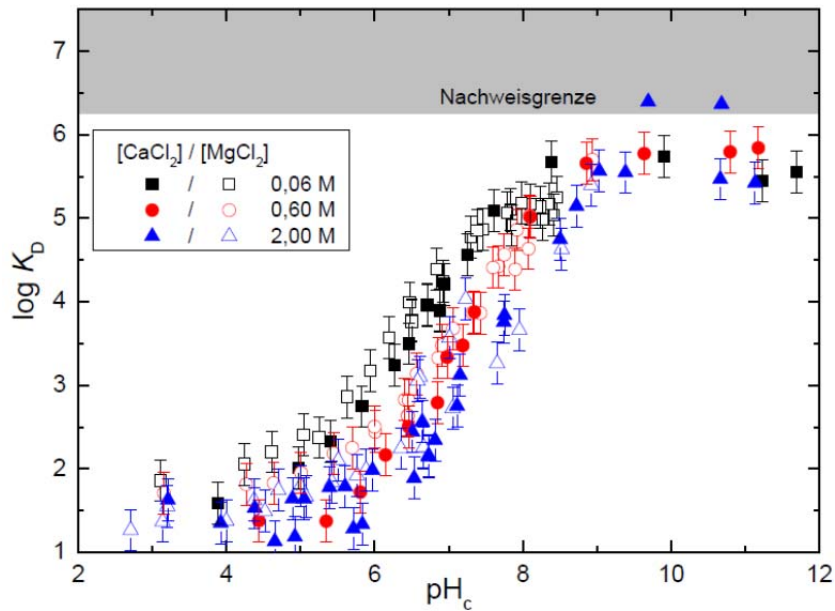


Figure 5: Distribution coefficients $\log K_d$ of Eu(III) sorption on illite ($[\text{Eu}]_{\text{total}} = 2,0 \cdot 10^{-7}$ M, solid:liquid = 2 g/L) as a function of pH_c in MgCl_2 and CaCl_2 solutions with various concentrations (0.06, 0.60, 2.00 M).

Up to now, no surface complexation constants $\log K_{\text{sc}}$ are published for the Ca-illite and Mg-illite surface complexes. As basis for an estimation of a parameter set for the illite sorption, the information from studies of the Eu(III) montmorillonite sorption has been taken. For montmorillonite, a parameter set of $\log K_{\text{sc}}$ values are given in the literature (Bradbury and Baeyens, 2006; Schnurr, 2015) for the Eu(III) sorption on Na-montmorillonite and Ca-montmorillonite (Na-SWy and Ca-SWy) at background electrolyte concentrations of $[\text{NaCl}] = 0.1$ M and $[\text{CaCl}_2] = 0.06$ M. For the illite only $\log K_{\text{sc}}$ values of the Na-illite are available. Analog to the montmorillonite system, the differences in the surface complexation constants between Eu(III) sorption on Na-SWy and Ca-SWy are taken to establish a new parameter set for Eu(III) sorption on Ca-illite (Ca-IIdP). That means that the $\log K_{\text{sc}}$ values from the Eu(III)/illite/NaCl system were diminished by the same amount as found for the montmorillonite system ($\Delta \log K_{\text{sc}}$ -1.5, -0.8, -0.3, -0.3 for the surface complex $\equiv \text{SO-Eu}^{2+}$ to $\equiv \text{SO-Eu}(\text{OH})_3^-$) (Table 5). The modeling of Eu(III) sorption on $\text{CaCl}_2/\text{MgCl}_2$ solution by the 2SPNE SC/CE including the new parameter set is shown in Figure 6.

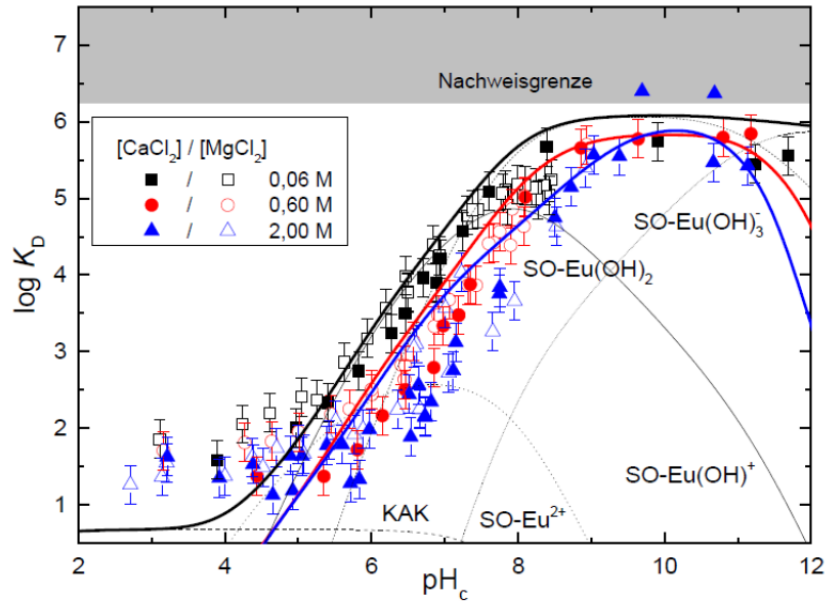


Figure 6: Eu(III) sorption ($[Eu]_{total} = 2.0 \cdot 10^{-7} \text{ M}$) an IdP (S:L = 2 g/L) plotted as $\log K_D$ against pH_c values at various MgCl_2 and CaCl_2 concentrations (0.06, 0.60, 2.00 M). The lines are the modelled values by 2SPNE SC/CE modell including detailed sorption speciation at $I = 0.18 \text{ M}$.

The experimental are described quite well with the modelled results for the diluted electrolyte solutions. The cation exchange reaction in the acidic pH_c range (< 5) is slightly underestimated, but has only minor relevance in the range of 10% total sorption. The increase of the sorption edge in the near neutral pH_c range (5 – 8) and the quasi quantitative sorption in the alkaline range ($\text{pH}_c > 8$) describes the observed behavior of the Eu sorption. The sorption edges in saline solution are also simulated quite well, but slightly overestimates the Eu(III) sorption in the middle pH_c range. But the deviation between modelled and experimental results is insignificant larger than the experimental error. At $\text{pH}_c > 11$, the simulated curves of $\log K_d$ abruptly drops down. This suppression of the sorption can be explained by the generation of a mixed Ca-Eu-OH species in solution, the dominant solution species at higher Ca concentrations and pH_c values Figure 7.

In summary we establish, that the pure NaCl system as well as the pure CaCl_2 (MgCl_2) system is described quite well from diluted to saline conditions by geochemical modelling with the certain parameter set. Consequently the question arises whether the sorption in mixed Na-Ca/Mg-Cl electrolyte systems, which is the general situation in natural ground waters, shows the same behavior and can also be described with the same quality.

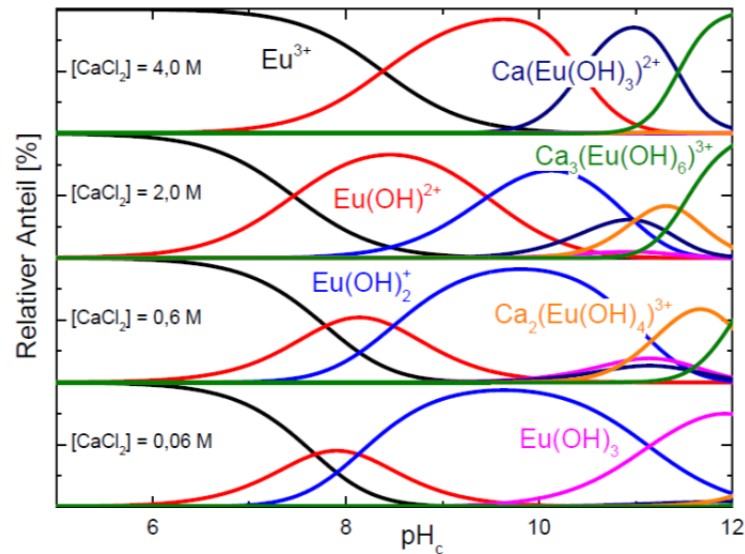


Figure 7: Speciation of Eu(III) in aqueous CaCl_2 solutions ($[\text{Eu}]_{\text{total}} = 2,0 \cdot 10^{-7} \text{ M}$) in CaCl_2 ($[\text{CaCl}_2] = 0.06, 0.6, 2.0$ and 4.0 M).

First investigations in a mixed electrolyte system are shown in Figure 8. Batch experiments of Eu(III) and Illite at two pH_c values ($\text{pH } 6.1$ and 7.3) were investigated at various concentration ratios of NaCl and CaCl_2 . The ionic strength was kept constant at $I = 1.0$, to minimize the effect of the ionic strength. The chosen pH_c values correspond to conditions where inner-sphere complexation mainly occur. It is observed, that the Eu(III) sorption decreases with increasing CaCl_2 concentration at both pH_c values. However, the effect is quite small. The data are within the experimental error margin ($\text{max. } \Delta \log K_D = 0.5$) for $\text{pH}_c 6.1$. The effect is slightly larger at $\text{pH}_c 7.3$ with $\Delta \log K_D = 0.8$. The experimental uncertainty is certainly larger because of the stronger sorption. Still, a significant influence of the CaCl_2 on the Eu(III) sorption occurs, which is definitely not caused by an ionic strength effect.

For the modelling of mixed Na-Ca-Cl systems the relative portion of the ion exchange sites occupied by Na^+ and Ca^{2+} ions must be known. The fractions can be calculated by the selectivity coefficient based on the reaction $2 \text{Na-X} + \text{Ca}^{2+} = \text{CaX}_2 + 2 \text{Na}^+$. The relative occupation of the sites by Na^+ and Ca^{2+} is listed in Table 6. The concentration of all available ionic exchange sites used in the modelling is divided into the clay fraction NaX and CaX_2 . The Eu(III) sorption is described by surface complexation with the parameter set ($\log K_{\text{sc}}$) for Na- and Ca-IdP. In a first approach, each of both clay mineral fractions are considered as single and independent illite fractions, the sodium form NaX and the calcium form CaX_2 . The capacity of the available ion exchange sites is estimated from the cation exchange capacity. The sorption on both IdP fractions is estimated by the corresponding surface complexation constants of each surface species.

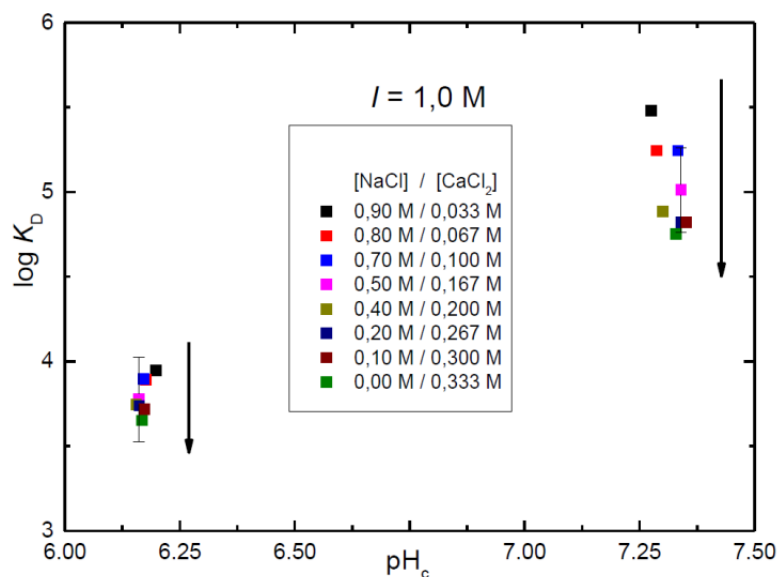


Figure 8: Eu(III) sorption ($[\text{Eu}]_{\text{gesamt}} = 2.0 \cdot 10^{-7} \text{ M}$) on IdP ($S : L = 2 \text{ g/L}$) plotted as $\log K_D$ against the pH_c in different NaCl – CaCl_2 mixtures ($I = 1 \text{ M}$).

Table 6: Calculation of the relative occupation of cation exchange sites ($[\text{X}_{\text{gesamt}}] = 4.5 \times 10^{-4} \text{ M}$) in experiments with various NaCl/ CaCl_2 ratios in solution (Bradbury and Baeyens, 2009a), (Schnurr, 2015).

[NaCl]	[CaCl ₂]	[NaX]	[CaX ₂]	NaX (%)	CaX ₂ (%)
0.9	0.033	$3.80 \cdot 10^{-4}$	$3.50 \cdot 10^{-5}$	84.38	15.62
0.8	0.067	$3.21 \cdot 10^{-4}$	$6.41 \cdot 10^{-5}$	71.44	28.56
0.7	0.100	$2.72 \cdot 10^{-4}$	$8.89 \cdot 10^{-5}$	60.42	39.58
0.5	0.167	$1.85 \cdot 10^{-4}$	$1.33 \cdot 10^{-4}$	41.03	58.97
0.4	0.200	$1.45 \cdot 10^{-4}$	$1.52 \cdot 10^{-4}$	32.26	67.74
0.2	0.267	$7.06 \cdot 10^{-5}$	$1.90 \cdot 10^{-4}$	15.70	84.30
0.1	0.300	$3.50 \cdot 10^{-5}$	$2.07 \cdot 10^{-4}$	7.79	92.21
1×10^{-5}	0.333	$1.53 \cdot 10^{-7}$	$2.25 \cdot 10^{-4}$	0.03	99.97

The result of the modelling at conditions (Na^+ to Ca^{2+} ratios) depicted from Table 6 is shown in Figure 9. The simulation demonstrates a significant influence of the Ca^{2+} on the sorption. In the low pH_c range, the difference between low and high Ca^{2+} content is especially pronounced. In general, the difference increases with decreasing pH_c value. At pH_c values 8.5 and higher, the data between almost pure NaCl and CaCl_2 solutions differ only in ~ 0.3 log units; they can be regarded as constant considering the error margin. This observation follows the trend of the difference in the $\log K_{\text{sc}}$ values of both

clay fractions with 1.5 and 0.8 log units for surface species $\equiv\text{SO-Eu}^{2+}$ and $\equiv\text{SO-Eu(OH)}^+$, respectively, in the acidic and neutral pH_c range. In the alkaline pH_c range the difference is only 0.3 log units between the $\log K_{sc}$ of $\equiv\text{SO-Eu(OH)}_2$ und $\equiv\text{SO-Eu(OH)}_3^-$.

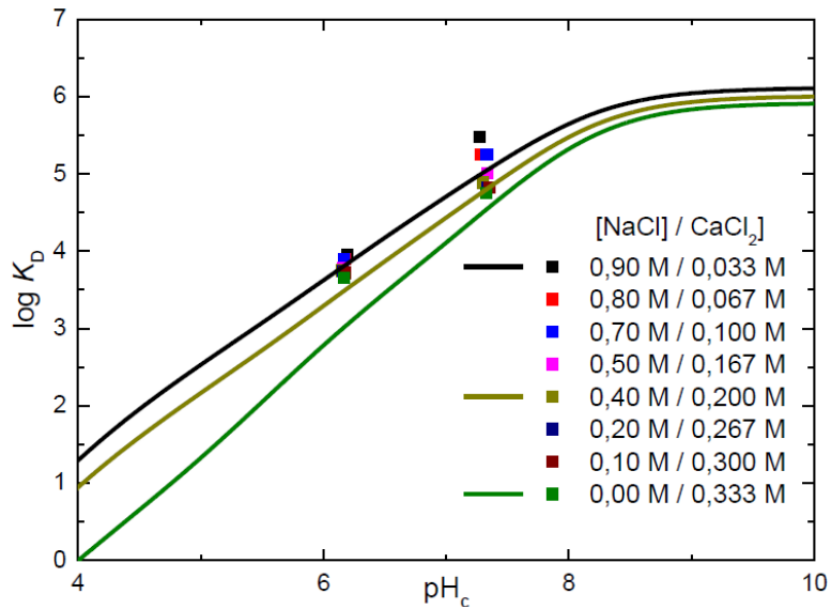


Figure 9: Eu(III) sorption ($[\text{Eu}]_{\text{total}} = 2,0 \cdot 10^{-7} \text{ M}$) on illite (IdP) (S:L = 2 g/L) plotted as $\log K_D$ against the pH_c value in various NaCl - CaCl₂ mixtures (I = 1 M). The curves were generated by predictions with the 2SPNE SC/CE model.

Because of the limited number of data and relative high experimental error, the model approach could not completely be verified. This model approach needs to be proven by additional investigations. Nevertheless, the modelling reflects the general trend of the experimental data.

2.1.1.3 Curium (Cm(III)) sorption on illite (IdP)

TRLFS investigations of Cm(III) on SWy in NaCl and CaCl₂ electrolyte systems showed that the chloride as back electrolyte does not affect the innersphere surface species of Cm(III) (Schnurr et al., 2015; Schnurr, 2015). The spectroscopic investigations was performed to demonstrate whether the sorption of Cm(III) on illite differs from the sorption on montmorillonite. A comparison of the results of the batch sorption experiments between Eu(III) sorption on SWy and IdP showed very similar behavior (Schnurr et al., 2015). Figure 10 exhibits the fluorescence emission spectra on the Cm-IdP system ($m_{\text{Cm}} = 2 \cdot 10^{-7} \text{ m}$, S:L ratio = 0.25 g/L) exemplary at ionic strength of 0.1 M NaCl. Parallel to this series, spectra were also recorded for ionic strengths of 1 and 4 M NaCl but they are not shown here. In comparison to the fully hydrated $\text{Cm}^{3+}_{\text{aquo}}$ ion ($\text{pH}_c = 1$) the concentration of the aquatic Cm(III) species decreases with increasing pH_c value according to

increasing sorption. The band maxima simultaneously shifts to higher wavelengths. The emission spectra demonstrate that several species (surface and aqueous species) have to be considered and that the spectra are similar to the fluorescence spectra in the Cm(III)-SWy system (NaCl).

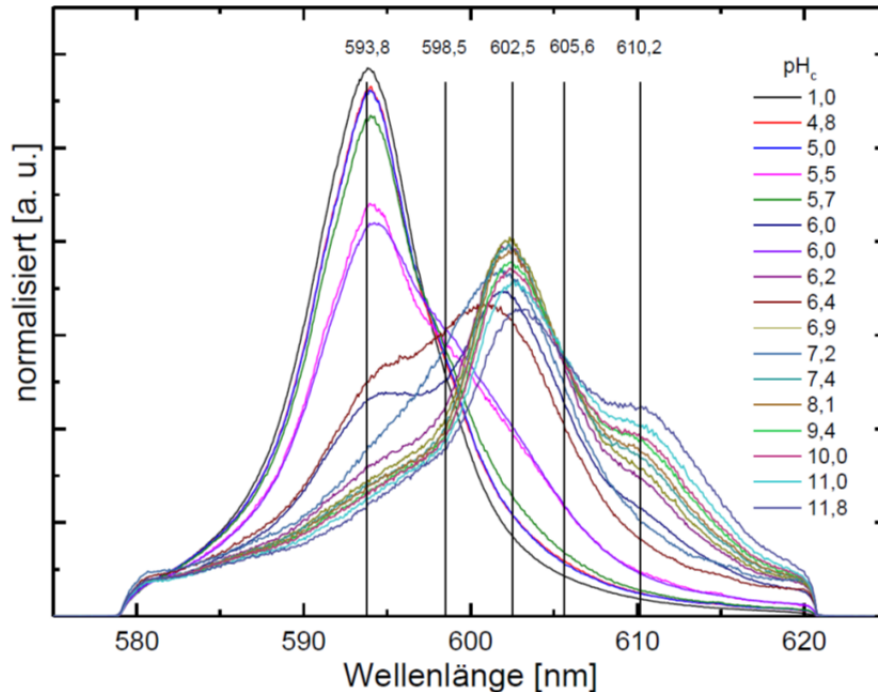


Figure 10: pH_c dependence of the TRLFS spectra (peak area normalized) $[\text{Cm}]_{\text{Total}} = 2.0 \cdot 10^{-7} \text{ M}$, $[\text{NaCl}] = 0.1 \text{ M}$, IdP , $\text{S:L} = 0.25 \text{ g/L}$.

Peak deconvolution of the spectra for each ionic strength results in a minimum of single compounds of four inner-sphere surface species. They exhibit emission band peak-maxima for illite (in brackets for montmorillonite) at approximate 598.5 (598.5), 602.5 (602.4), 605.6 (605.8) and 610.2 (610.4) nm ($\pm 0.2 \text{ nm}$) (Figure 10). The first three inner-sphere complexes can be assigned to the same surface species that had been previously reported for illite and montmorillonite (Rabung et al., 2005): $>\text{SOCm}(\text{H}_2\text{O})_5^{2+}$, $>\text{SOCm}(\text{OH})(\text{H}_2\text{O})^{4+}$, $>\text{SOCm}(\text{OH})_2(\text{H}_2\text{O})_3$. An additional inner-sphere surface species with a higher peak shift was observed at high pH_m . From the compilation of all pure component spectra of the different electrolyte solutions (Figure 11) no significant influence of NaCl background electrolyte concentration on Cm surface speciation exists. Even at $m\text{NaCl} = 4.37 \text{ m}$, peak deconvolution results in the four inner-sphere surface species with approximately the same emission band positions. This corroborates our modeling assumptions in having identical surface species independent of NaCl ionic strength.

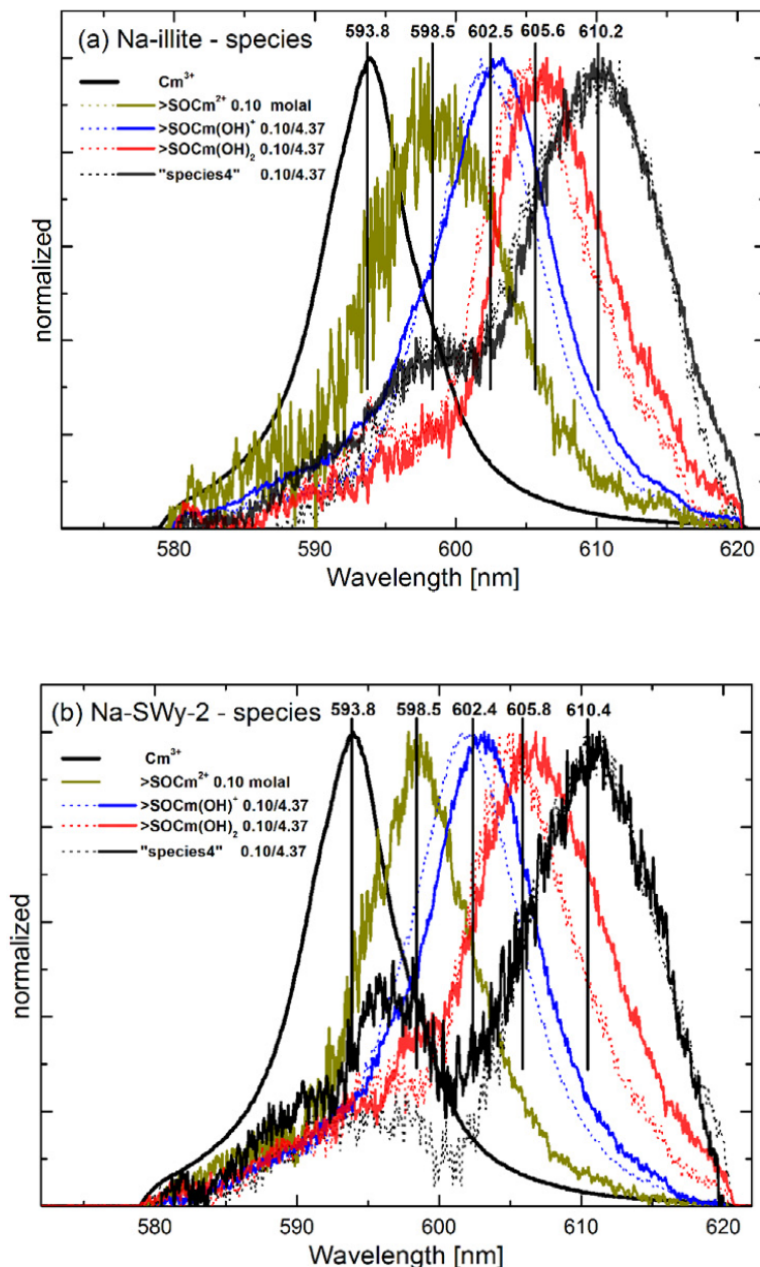


Figure 11: (a) Na-illite, (b) Na-SWy-2: Pure component spectra derived from peak deconvolution of measured fluorescence spectra obtained at each ionic strength (0.10, 4.0 M (0.10 and 4.37 m))

The measurements of fluorescence life times in the Cm(III)–IdP systems yield in $\tau_0 = 68 \pm 2 \mu\text{s}$ for $\text{Cm}^{3+}_{\text{aquo}}$ ion and $\tau_1 = 113 \pm 10 \mu\text{s}$, corresponding to a species with 4.8 ± 0.3 $\text{H}_2\text{O}/\text{OH}^-$ units in the first coordination sphere of the Cm(III). The 4th species at high pH_c values has a significant longer life time with $\tau_2 = 165 \pm 15 \mu\text{s}$. These results agree quite well with earlier results in the montmorillonite system from (Rabung et al., 2005)

The lifetime measurements support the results and interpretations based on the fluorescence emission spectra that there is no ionic strength dependency for the different inner-sphere sorption species. Additional inner-sphere coordinated chloride would lead

to a further increase of the fluorescence lifetime. In view of the decreasing H₂O activity at high NaCl concentrations, the unchanged number of water molecules in the first Cm coordination sphere is certainly remarkable and points to a strong binding to the central metal ion.

The nature of the species causing the fluorescence band at 610 nm was examined in additional experiments concerning silicate in solution. Based on findings from (Huittinen et al., 2012), where a similar Cm species in their sorption studies with kaolinite was found from the fluorescence spectra, this species was assigned to a mixed clay mineral / curium / silicate surface complex. The occurrence of silicate in solution can be explained by dissolution of the clay material at alkaline conditions (pH_m > 10).

According to (Huittinen et al., 2012), Cm(III) illite samples were prepared at pH_c 9 and 0.1 M NaCl (TRIS buffer for pH fixation) and various amount of dissolved Si(IV) were added to the samples. The pH of 9 was chosen because no dissolution of the clay and, hence, no release of Si occurs and no absorption of any Si species is expected at 610 nm.

The spectra of the four samples with Si(IV) concentrations of 0, 1·10⁻⁵, 1·10⁻⁴, 1·10⁻³ M are shown in Figure 12. Addition of small amount of Si(IV) has no effect on the Cm spectra. The shift of the maximum to 602.5 nm is not influenced by Si(IV) but is rather a consequence of the sorption to the illite resulting in the inner sphere species >SO-Cm(OH)(H₂O)₄⁺. At Si(IV) concentrations of ≥ 10⁻³ M, which is below the solubility of amorphous silica, a change in the spectra accompanied by a significant peak shift (~604 nm) is observed. This supports the above mentioned hypothesis that with increasing silicate concentration in solution additional inner-sphere surface species involving silicate can be formed. A possible stoichiometry for the species at pH_m = 9 could be >SOCm(OH)_x(SiO₄)_y(H₂O)_{4-x} (with x, y = 1, 2).

Based on this result, the 610 nm species in the illite sorption study might be assigned to a clay/curium/silicate/ hydroxo surface complex as the measured aqueous silica concentration is m_{Si} = 7·10⁻³ m at pH_m > 11 (Bradbury and Baeyens, 2009a). The increased lifetime of τ = 165 ± 15 μs at higher pH values supports the hypothesis of a silicate containing Cm surface complex. Similar lifetime values have been reported by (Huittinen et al., 2012). The lifetime would be compatible with a >SOCm(OH)_x(SiO₄)_y(H₂O)_{3-x} (with x, y = 1, 2) species with silicate binding in a bidentate mode. However, additional studies are required to obtain more information on the exact stoichiometry and structure of this surface complex.

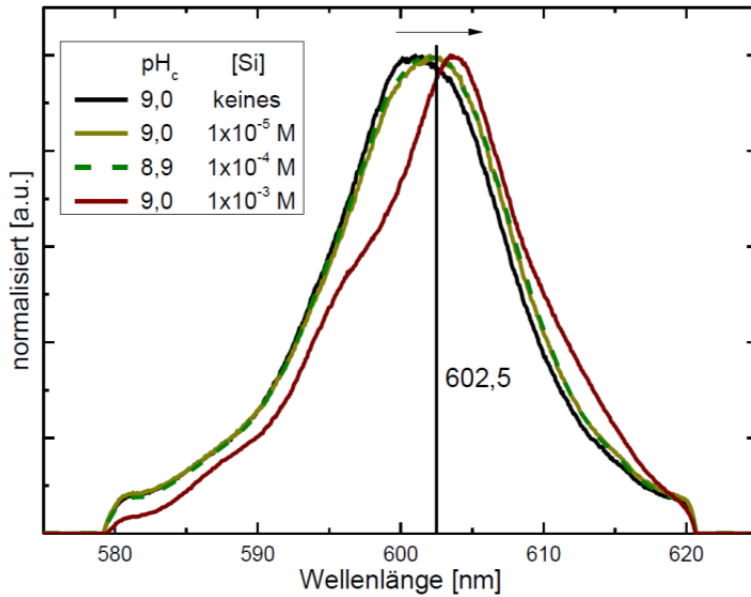


Figure 12: Cm(III) fluorescence spectra of solution containing IdP (0.25 g/L), different amounts of Si(IV) (0, $1 \cdot 10^{-5}$, $1 \cdot 10^{-4}$, $1 \cdot 10^{-3}$ M), and 0.1 M NaCl at $\text{pH}_c = 9$.

2.1.1.4 Sorption of Eu(III) on natural Opalinus clay mineral

Finally, the results of the sorption of the pure illite mineral have to be compared with a natural claystone. For that, the Opalinus clay (OPA) has been chosen, as one of the most investigated claystone originating from the Mont Terri underground facility. Because the OPA is a heterogenous compound containing many various minerals, we decide to use only the fraction of the clay minerals of the OPA. The Opalinus claystone was purified and minor components like organic compounds, calcite and quartz, were removed. The thus purified clay sample is named OPA-CF (OPA clay fraction) and consisted mainly of illite/smectite mixed phases, kaolinite and minor amounts of calcite. With OPA-CF batch sorption experiments similar to the former sorption experiments were performed. The experimental results are shown in Figure 13 together with data from the pure Eu-illite system in NaCl and CaCl_2 solutions. Following the “bottom up” approach from Bradbury and Baeyens, the mixed illite/smectite mix phases is handled like the pure illite mineral. That means that the sorption behavior of the OPA is governed by the illite, whereas minor components like kaolinite and chlorite are considered as not relevant. The results of the Eu(III) sorption experiments with OPA-CF are faced with those of the pure Eu(III) illite, without any corrections or assumptions.

Figure 13 (on the left, a, b, c) shows the comparison of both systems in NaCl solutions with various concentrations (0.09, 0.9, and 3.6 M). The Eu(III) sorption edge on illite and OPA-CF is for all NaCl concentrations quite similar and the increase of the sorption is nearly the same. The K_d values in the quasi quantitative sorption range with $> 99.5\%$

Eu(III) sorption ($\text{pH}_c > 8$) is for OPA somehow lower as the very high values for the pure illite system. But both systems show with $\log K_d$ values > 5 very strong sorption. In the pH_c range 9 – 10 the OPA-CF system shows a slightly diminished sorption at all ionic strengths. This is caused by a small amount of carbonate in solution released from the OPA-CF, because of dissolution of calcite as a component of OPA that could not be removed during the purification. Finally, we can state that the illite in the OPA-CF is the clay mineral fraction that dominates the sorption of Eu(III).

Figure 13 (on the right) shows also the comparison between Eu(III) sorption on OPA-CF and illite in CaCl_2 solutions. The sorption results show a slightly stronger sorption in the range of the sorption edge for OPA-CF at 0.06 M and partly at 0.6 M CaCl_2 . However, this distinction is with < 0.5 log units within the margin of the experimental uncertainty. At pH_c and higher, both systems behave identically. The experimental data at 2.0 M CaCl_2 are also identical over the whole pH_c range, consistent with the Eu-Na-OPA system. The small difference in the Eu-Na-OPA system caused by the carbonate in solution at $\text{pH}_c \sim 9 - 10$, can not be observed in the Ca system. The reason could be the small carbonate concentration and the precipitation of calcite in the Ca containing solution. Analog to the NaCl system, the illite dominates the Eu(III) sorption in the OPA-CF and can be regarded as the main clay mineral fraction in the OPA responsible for the sorption of trivalent actinides.

2.1.2 Sorption of neptunium(V) onto illite in the NaCl system

Studies of the sorption of neptunium are somehow more complex than the trivalent lanthanides and actinides, because it is a redox sensitive element and can exist in two different oxidation states, the tetravalent and pentavalent oxidation state. Thus, the chemical behavior can change from weak to strong interactions and vice versa. The trivalent and the hexavalent neptunium has no relevance at environmental and reducing conditions like in a deep geologic formation. The studies were started with pentavalent neptunium (Np(V)) and the results of these sorption studies with illite are published in (Marsac et al., 2015a).

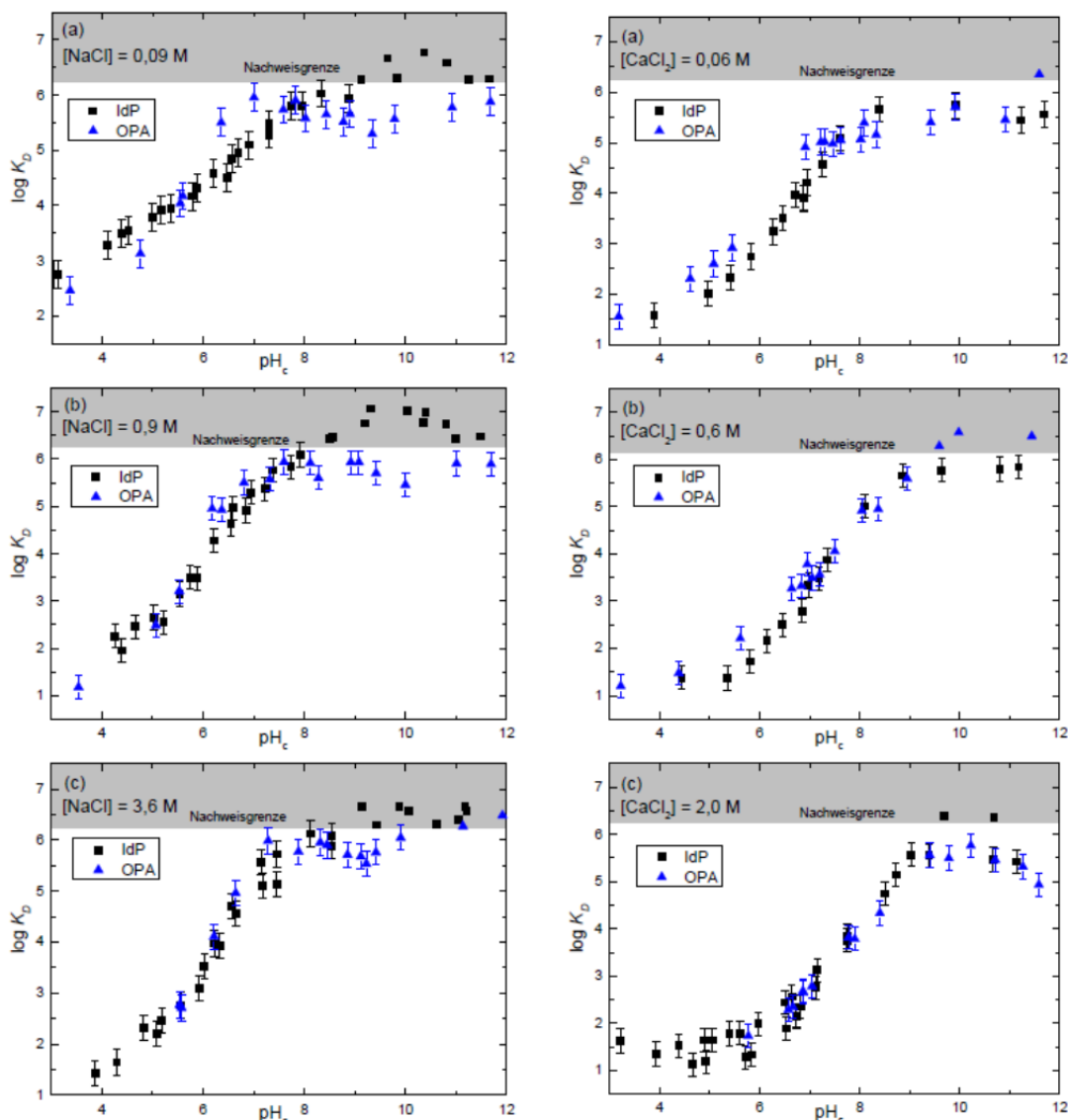


Figure 13: Eu(III) sorption on OPA clay fraction (OPA-CF) and IdP in NaCl (0.09, 0.90 und 3.60 M) and in CaCl₂ (0.06, 0.6, and 2.00 M) plotted as log K_d against pH_c ([Eu]_{total} = 2.0 · 10⁻⁷ M, S:L = 2 g/L).

2.1.2.1 Neptunium redox speciation on the illite surface

Purified Na-illite was used in this work and was provided within the EC project CP CatClay (www.catclay.org). The purification process is described in detail in (Marsac et al., 2015a). Despite intensive purification, the illite contains 7 wt.% Fe₂O₃.

All sorption experiments were performed as batch type experiments at initial Np(V) concentrations in the range of 3x10⁻⁸ to 10⁻⁴ M. Maximum Np concentration is below the solubility limit of relevant Np(V)-bearing solids (Guillaumont et al., 2003). The batch experiments were carried out at room temperature in an argon glove box (<1 ppm O₂,

absence of CO₂). At a solid to liquid ratio of 2 g/L, the suspensions were preconditioned in 0.1 M NaCl by shaking continuously for 4–5 days. To achieve a given target pH value 0.1 M HCl or 0.1 M NaOH were added. After 7, 21, 35 and 63 days, pH and Eh were measured in the suspension and an aliquot of each sample was centrifuged in a Ultracentrifuge at 90,000 rpm for 1 h. The supernatant and all other solutions were analyzed for Np by liquid scintillation counting (LSC). The oxidation state of Np in solution were determined by liquid-liquid extraction with HDEHP and PMBPA (Bertrand and Choppin, 1982; Nitsche et al., 1994).

Results obtained in batch experiments will be expressed throughout as distribution coefficients (R_d in L/kg), calculated by the following equation:

$$R_d = ([\text{Np}]_{\text{tot}}/[\text{Np}]_{\text{aq}} - 1) \times V/m$$

where $[\text{Np}]_{\text{aq}}$ and $[\text{Np}]_{\text{tot}}$ (mol/L) are the dissolved (final) equilibrium and total (initial) concentrations of Np in solution, respectively. The term V/m corresponds to the aqueous solution volume to illite mass ratio (L/kg). An uncertainty of ± 0.3 is commonly associated with $\log R_d$ determination for radionuclide sorption to clay minerals (Bradbury and Baeyens, 2009a), although for low $[\text{Np}]_{\text{tot}}$ and high uptake, the uncertainty on $\log R_d$ might be higher.

Figure 14 presents the Np sorption to illite (R_d in L/kg) as a function of pH (i.e. pH-edge). Only the highest and the lowest Np total concentrations investigated in the present study at various pH are presented here: $[\text{Np}]_{\text{tot}} = 10^{-6}$ M (Figure 14a) and 3×10^{-8} M (Figure 14b). Results obtained for intermediate $[\text{Np}]_{\text{tot}}$ are consistent with those data. The complete dataset is provided within the supplementary file of (Marsac et al., 2015a). R_d values determined after different reaction times (7, 21, 35 and 63 days) are presented.

After about one week reaction time, only an insignificant variation of Np sorption is observed and the establishment of reaction equilibrium can be assumed. Surprisingly, solid–liquid distribution ratios (R_d) are clearly higher than those measured for Np(V) sorption onto illite under aerobic conditions.

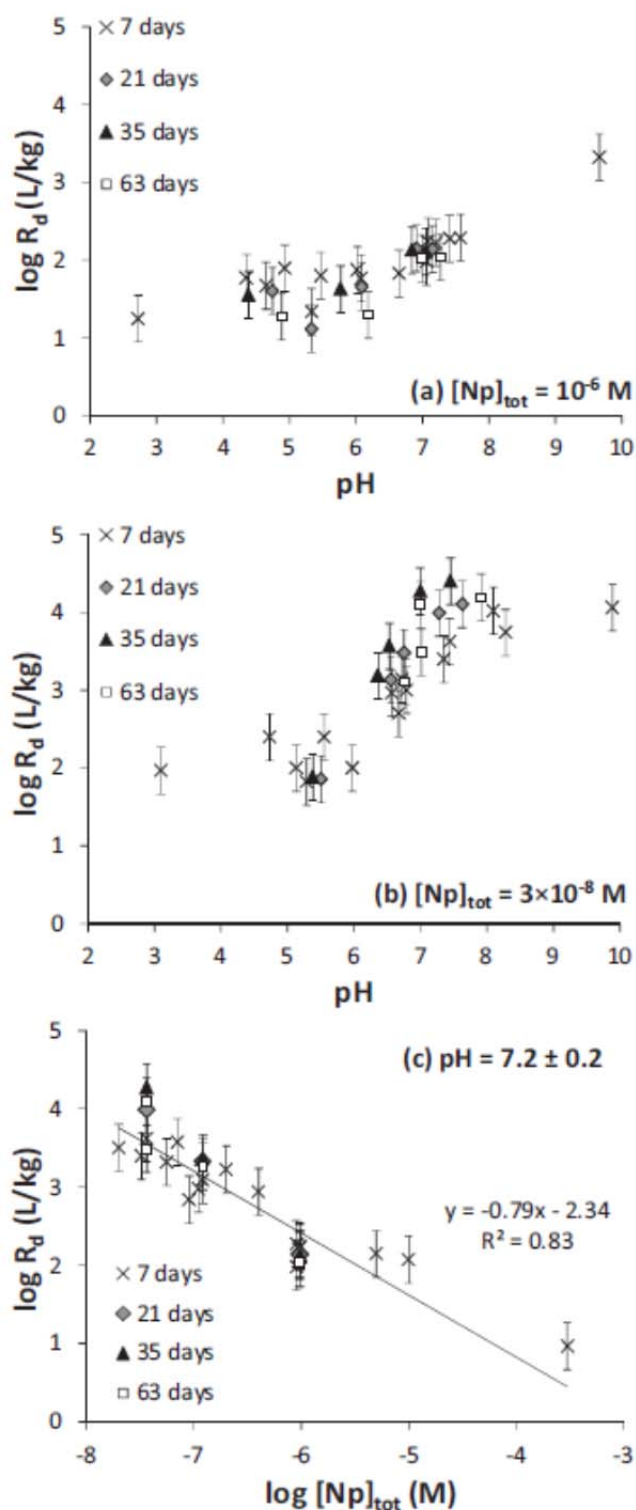


Figure 14: Np sorption to illite (R_d , in L/kg) versus pH measured for different reaction times (7, 21, 35, 63 days) and a Np total concentration of (a) $10^{-6} M$ and (b) $3 \times 10^{-8} M$. (c) Results obtained for $pH = 7.2 \pm 0.2$ are plotted as $\log R_d$ versus $[Np]_{tot}$.

For $[Np]_{tot} = 10^{-6} M$ (Figure 14a), most of the data being recorded for $pH < 8$ show only a small increase of R_d with pH, which is consistent with the weak surface complexation

of Np(V) at the edges of clay particles. For $[\text{Np}]_{\text{tot}} = 3 \times 10^{-8}$ M (Figure 14b) and $\text{pH} < 6$, R_d values are relatively similar to those measured at higher metal ion concentration. However, a significant increase of R_d is observed for $\text{pH} > 6$ with values being 1 to 2 orders of magnitude higher than for experiments with $[\text{Np}]_{\text{tot}} = 10^{-6}$ M. Slightly more scattering R_d values are observed for $[\text{Np}]_{\text{tot}} = 3 \times 10^{-8}$ M but the sorption results are reproducible within an experimental uncertainty for $\log R_d$ of about ± 0.5 . When increasing $[\text{Np}]_{\text{tot}}$, pH-edges are shifted to higher pH, i.e. a decrease of R_d with increasing $[\text{Np}]_{\text{tot}}$ is observed at a given pH. This is consistent with non-ideal sorption behavior of Np. Sorption data for $\text{pH} = 7.2 \pm 0.2$ are plotted as $\log R_d$ versus $\log [\text{Np}]_{\text{tot}}$ in Figure 14c, which further illustrates the non-ideal sorption behavior.

The observation that R_d increases with decreasing p_e ($p_e = -\log \text{activity}(\text{e}^-)$) suggests partial reduction to Np(IV), although measured redox potentials (p_e values) at a first glance suggest the predominance of Np(V). A redox state analysis applied to one of the samples ($\text{pH} = 7.0$; $[\text{Np}]_{\text{tot}} = 10^{-5}$ M; $[\text{NaCl}] = 0.1$ M; $m/V = 2$ g/L) also corroborates the partial reduction of Np(V) to Np(IV) on the illite surface. After one week contact time, only Np(V) is found in solution ($93 \pm 10\%$). After re-suspending the illite in 1M HCl for 2 days, a significant amount of the desorbed Np is found to be Np(IV) ($41 \pm 10\%$).

Np redox speciation at the illite surface is further investigated by XANES. The Np L_3 -XANES measured at $\text{pH} = 7.4$ and 9.6 , $m/V = 20$ g/L and 3×10^{-4} M of Np (initially introduced as NpO_2^+) is presented in Figure 15. These samples contain the highest $[\text{Np}]_{\text{tot}}$ and exhibits as well the highest p_e ($p_e = 6.8 \pm 0.8$). At $\text{pH} 7.4$, 15 % of the total Np is sorbed onto illite (i.e. 2.3×10^{-3} mol/kg). XANES spectra of the NpO_2^+ and Np^{4+} aquo ions in 0.1 M HClO_4 from (Gaona et al., 2012) are used as references for Np(V) and Np(IV). The Np-illite XANES for $\text{pH} = 7.4$ shows significant differences compared to a Np(V) reference, especially an increase in WL intensity. Reduction to Np(IV) at the illite surface could indeed be confirmed by X-ray absorption near-edge spectroscopy (XANES). By fitting the Np-illite XANES with a linear combination of Np(V) and Np(IV) reference samples, 14 % of the adsorbed Np is determined to be Np(IV). In the sample at $\text{pH} = 9.6$, the measured p_e does not significantly differ from that obtained at $\text{pH} = 7.4$ ($p_e = 6.8 \pm 0.8$), reflecting more oxidizing conditions. Due to the higher pH, 90 % of Np is sorbed to the illite surface (1.3×10^{-2} mol/kg). The Np L_3 -XANES at $\text{pH} 9.6$ shows a less intense WL compared to $\text{pH} 7.4$. The LCF using the XANES spectra of NpO_2^+ and Np^{4+} aquo-ion shows that only 5 % of the adsorbed Np at the illite surface is Np(IV).

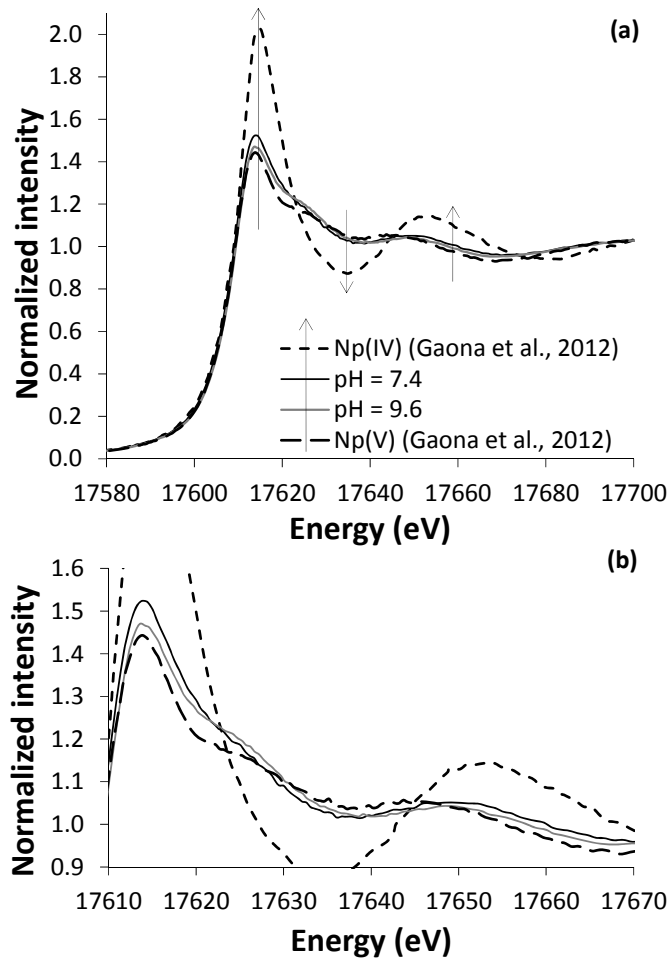


Figure 15: (a) Np L3-XANES measured for a Np-illite sample prepared at pH = 7.4 and 9.6 ($[\text{Np}]_{\text{tot}} = 3 \times 10^{-4} \text{ M}$, $m/V = 20 \text{ g/L}$, $E_h = 0.40 \pm 0.05 \text{ V}$). Reference XANES of aqueous Np(IV) and Np(V) in 1M HClO_4 from (Gaona et al., 2012) are shown for comparison. Arrows highlight a Np(V) reduction to Np(IV) process in the present study. The area between 17610 and 17670 eV is enlarged in (b).

Np speciation in presence of the purified Na-illite under given conditions is consistently described by applying the two sites protolysis non-electrostatic surface complexation and cation exchange model (2SPNE SC/CE). Only strong sites at the illite surface were considered and only sorption data with experimentally determined p_e are considered. The last is necessary because p_e is needed to calculate Np redox speciation according to the first equation in Table 7. The Np redox state and surface complexation constants for Np(IV) are derived by applying a data fitting procedure. Constants are very consistent with results obtained by applying an existing linear free energy relationship (LFER).

Table 7: Reactions and respective thermodynamic constants used in the present modeling section.

Reaction	log K (I = 0)
$\text{NpO}_2^+ + 4 \text{H}^+ + \text{e}^- = \text{Np}^{4+} + 2 \text{H}_2\text{O}$	10.21
$\text{NpO}_2^+ + \text{H}_2\text{O} \equiv \text{NpO}_2\text{OH} + \text{H}^+$	-11.3
$\text{NpO}_2^+ + 2 \text{H}_2\text{O} \equiv \text{NpO}_2(\text{OH})_2^- + 2 \text{H}^+$	-23.6
$\text{Np}^{4+} + \text{H}_2\text{O} = \text{NpOH}^{3+} + \text{H}^+$	0.55
$\text{Np}^{4+} + 2 \text{H}_2\text{O} = \text{Np}(\text{OH})_2^{2+} + 2 \text{H}^+$	0.35
$\text{Np}^{4+} + 3 \text{H}_2\text{O} = \text{Np}(\text{OH})_3^+ + 3 \text{H}^+$	-2.3 (Pu)
$\text{Np}^{4+} + 4 \text{H}_2\text{O} = \text{Np}(\text{OH})_4 + 4 \text{H}^+$	-8.3
$\text{NpO}_{2(\text{am})} + 2 \text{H}_2\text{O} = \text{Np}^{4+} + 4 \text{OH}^-$	-56.7
$\text{X-Na} + \text{NpO}_2^+ = \text{X-NpO}_2$	0 ^f
$\equiv\text{SOH} + \text{H}^+ = \equiv\text{SOH}_2^+$	4 ^f
$\equiv\text{SOH} = \equiv\text{SO}^- + \text{H}^+$	-6.2 ^f
$\equiv\text{SOH} + \text{NpO}_2^+ = \equiv\text{SO-NpO}_2 + \text{H}^+$	-2.0 ^f
$\equiv\text{SOH} + \text{NpO}_2^+ + \text{H}_2\text{O} = \equiv\text{SO-NpO}_2\text{OH}^- + 2 \text{H}^+$	-10.3 ^f
$\equiv\text{SOH} + \text{Np}^{4+} = \equiv\text{SO-Np}^{3+} + \text{H}^+$	nd (8.4 ± 0.6)
$\equiv\text{SOH} + \text{Np}^{4+} + \text{H}_2\text{O} = \equiv\text{SO-NpOH}^{2+} + 2 \text{H}^+$	nd (8.2 ± 0.7)
$\equiv\text{SOH} + \text{Np}^{4+} + 2 \text{H}_2\text{O} = \equiv\text{SO-Np}(\text{OH})_2^+ + 3 \text{H}^+$	6.4 ± 1.2 (6.0 ± 0.7)
$\equiv\text{SOH} + \text{Np}^{4+} + 3 \text{H}_2\text{O} = \equiv\text{SO-Np}(\text{OH})_3 + 4 \text{H}^+$	0.7 ± 1.3 (1.0 ± 1.1)
$\equiv\text{SOH} + \text{Np}^{4+} + 4 \text{H}_2\text{O} = \equiv\text{SO-Np}(\text{OH})_4^- + 5 \text{H}^+$	-5.7 ± 1.2 (nd)

Aqueous reaction constants and the solubility product of $\text{NpO}_{2(\text{am})}$ are taken from (Guillaumont et al., 2003). The missing $\text{Np}(\text{OH})_3^+$ formation constant is taken from the analogue $\text{Pu}(\text{OH})_3^+$. “f” denotes fixed parameters during the fitting procedure, taken from (Bradbury and Baeyens, 2009b). Np(IV) surface complexation constants are fitted from the present experimental results associated with their uncertainty. Calculated values using a LFER are shown for comparison between parentheses. “nd” refers to values that could not be determined.

The results are presented in Figure 16 for the complete dataset used to fit the surface complexation constants for Np(IV).

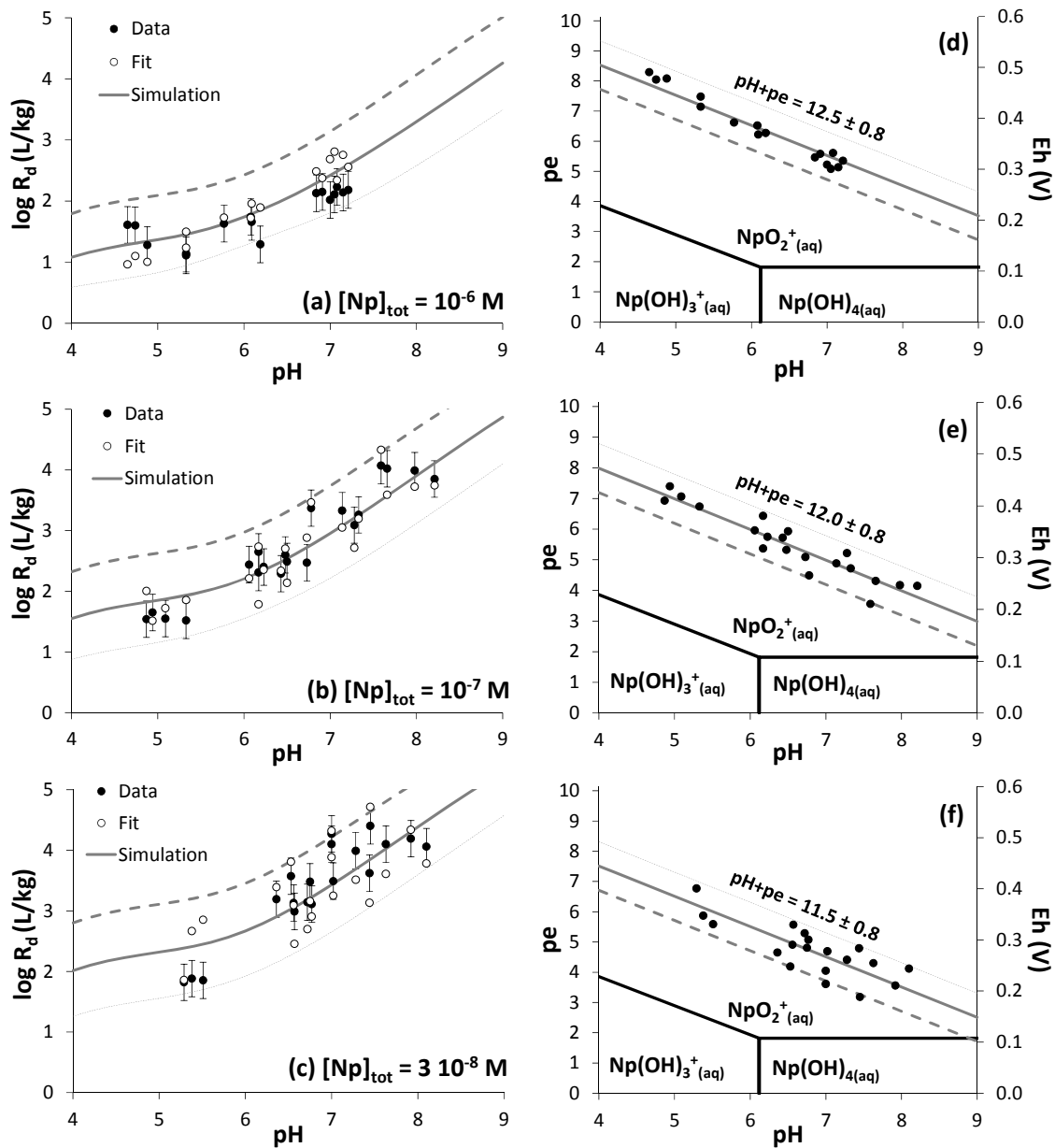


Figure 16: Experimental $\log R_d$ (black circles) and the corresponding calculated values (white circles) with the fitted surface complexation constants for Np(IV) with illite versus pH for $[\text{Np}]_{\text{tot}} = 10^{-6}$ (a), 10^{-7} (b) and 3×10^{-8} M (c). The corresponding redox (pH-pe/Eh plot) conditions are shown on the right side with the predominance diagram for aqueous Np species (d) (e) (f). Lines represent calculations made for constant pH+pe (bold line) ± 0.8 (lower limit: bold dashed line; upper limit: thin dashed line).

Figure 16 a, b, and c show $\log R_d$ versus pH for the three series of experiments with $[\text{Np}]_{\text{tot}} = 10^{-6}$, 10^{-7} and 3×10^{-8} M, respectively. Experimental $\log R_d$ and the corresponding calculated values with the fitted constants are shown, respectively, as black and white symbols. Figure 16 c, d, and e show the corresponding redox conditions for each series on a pH-pe(Eh) diagram. In addition, calculations with constant redox conditions

(i.e. constant pH+pe values) for each series in the range of the expected experimental uncertainty (i.e. ± 0.8 pe units / ± 50 mV) illustrate the coupled effect of pH and pe on Np sorption to illite. The increase of $\log R_d$ with decreasing $[\text{Np}]_{\text{tot}}$ is well described. More detailed explanation regarding simulation and the used data are given in (Marsac et al., 2015a).

Taking Np(IV) surface complexation constants into account, the calculated Np(V)/Np(IV) redox borderline shifts in presence of illite surfaces by 3–5 pe units (0.2–0.3 V) towards redox neutral conditions. From this observation we suggest that Np(V) reduction in presence of a sorbing mineral phase is thermodynamically favored resulting in an Np(IV) surface species.

Based on constants given in Table 7: Reactions and respective thermodynamic constants used in the present modeling section., a predominance diagram for Np surface speciation are constructed for the pH range $4 < \text{pH} < 10$ (Figure 17; grey lines). The pe-pH diagram is superimposed by the respective predominance diagram for aqueous species (Figure 17; black lines). When Np(V) sorption is weak ($\text{pH} < 8$) reduction to Np(IV) at the surface is thermodynamically highly favored due to the strong sorption of Np(IV) even at relatively high pe. The redox boundary for the Np(V)/Np(IV) couple for Np illite surface species is by approximately 4.6-5 pe units (0.27-0.30 V) higher than for the corresponding dissolved Np species at $\text{pH} < 8$. For $\text{pH} > 8$, Np(V) surface complexation to illite edge sites increases, via the formation of $\equiv\text{SO-NpO}_2\text{OH}^-$ species according to the 2SPNE SC/CE model. Consequently, reduction to Np(IV) at the illite surface becomes less favorable and the redox boundary surface species is only approximately 3 pe units (0.18 V) higher as compared to the respective solute species at $\text{pH} = 10$. Figure 17 clearly demonstrates that despite the fact that all data lie within the predominance field of aqueous Np(V) species (black lines), reduction to Np(IV) becomes thermodynamically favored in the presence of illite (grey lines). The high R_d values measured under the given experimental conditions can be explained by the strong sorption of Np(IV) species at the illite surface being in equilibrium with Np(V) species in solution.

Still the question arises, how the Np(V) is reduced to Np(IV). In absence of oxidizing or reducing agents experimentally determined pe-pH values should follow the “redox neutral” line with $(\text{pe} + \text{pH}) = 13.8$ (dashed line in Figure 17, (Neck et al., 2007)). Apparently, our data lie below this line, i.e. a reductant is needed for the reduction. Fe(II) is known as an efficient redox partner (Marsac et al., 2015a). Although the illite sample investigated in our studies was purified under aerobic conditions, the presence of traces of structural Fe(II) or adsorbed Fe(II), possibly formed via partial dissolution of the clay under anaerobic conditions, cannot be ruled out. A spectroscopic identification of Fe(II) in our experimental system, however, appears to be hardly possible. A maximum of 6.8×10^{-4} mol Np/kg illite was found to be reduced Np(IV). The corresponding amount of Fe(II) required for Np(V) reduction then corresponds to about 0.08 % of the total amount of Fe contained in the illite (7wt.% as Fe_2O_3 gives 0.88 mol of Fe per kg of illite). Such small fractions are very likely below the detection limit of available experimental techniques. Presently, we are unable to determine precisely the nature of the

redox reaction on a molecular scale. Nevertheless, the fact that sorption data can be consistently described by using pe values as a relevant master parameter clearly demonstrates the applicability of the thermodynamic equilibrium approach to simulate coupled redox sorption processes in clay mineral systems.

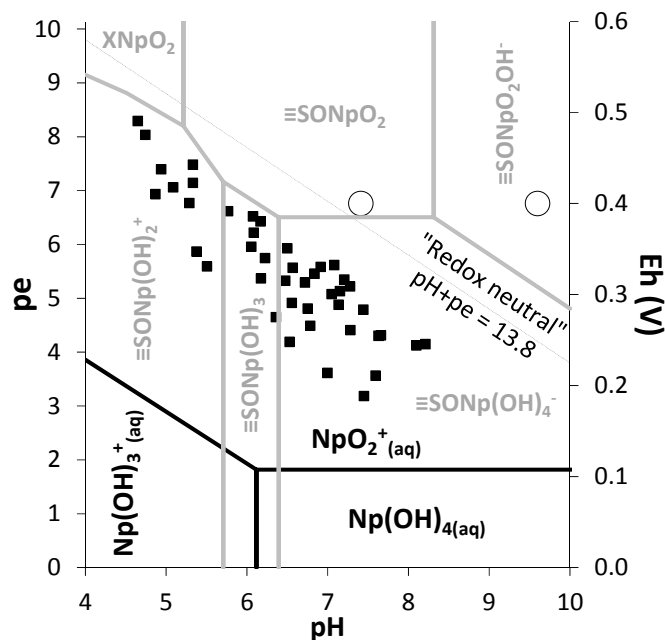


Figure 17: pH-pe (or Eh on the secondary scale) diagram of Neptunium in 0.1 M NaCl solution (black lines) and superimposed Np predominance diagram calculated at the illite surface (grey lines). It shows that the Np(V)/Np(IV) borderline at the illite surface is between 3 and 5 pe units (0.18-0.30 V), depending on the pH, higher than the corresponding one in solution. Experimental pH-pe values are also plotted (without error bars for clarity, s. also (Marsac et al., 2015a)), showing that in the present batch experiments, Np(V) prevails in solution whereas and Np(IV) prevails at the surface, explaining the stronger Np-illite sorption observed compared with literature, under aerobic condition.

Conclusions

The unusually high Np(V) sorption to illite observed in the present study can be explained by partial reduction and concurrent formation of stable Np(IV) surface species. We found a clear relationship of measured pe with Rd values: Np sorption increases with decreasing redox potential. Our combined batch sorption, spectroscopic and geochemical modeling study suggests that the predominance field of reduced Np(IV) species in a pe-pH diagram expands significantly due to the thermodynamically favored formation of Np(IV) surface complexes in a wide pH range. The retention of redox sensitive Np species is thus much more efficient under pe conditions only slightly below redox neutrality in presence of mineral surfaces than expected. Scoping geochemical

estimations of radionuclide redox states at given p_e and pH values but neglecting surface complexation reactions can thus be misleading. The result that measured p_e values can be taken as a master parameter to simulate complex redox processes including surface reactions is encouraging, even though the determination of redox potentials is flawed by relatively high analytical uncertainties. Nevertheless, by using the measured p_e as an input parameter, Np(IV) surface complexation constants for the 2SPNE SC/CE model could be fitted to the experimental data which are very comparable to those values estimated by applying an established LFER approach. The complete sorption dataset can be numerically described assuming surface mediated reduction of Np(V) to Np(IV) based on the strong affinity of Np(IV) for the illite surface.

The exact mechanism of Np(V) reduction, however, could not be clarified within the present study due to the apparently limited concentration of reductant species. The fact that redox and sorption equilibria establish relatively fast, points to a surface mediated process. Electron transfer from adsorbed or structurally bound Fe(II) to surface bound Np(V) is considered as a plausible mechanism for the observed coupled redox/sorption reaction. The presented modeling approach, however, predicts reduction also in absence of an explicit reductant in the solid. The thermodynamical stability of Np(IV) surface species alone is sufficient to shift the redox borderline and to induce partial Np(V) reduction.

The presented modeling concept might be applicable as well to describe the behavior of other redox-sensitive elements in the geosphere.

2.1.3 Plutonium

2.1.3.1 Plutonium sorption at the kaolinite surface

Plutonium with its particularly complex redox chemistry may be thermodynamically stable in the states +III to +VI depending on the redox conditions in the environment. Mineral surfaces can also affect Pu redox speciation. Therefore, the interpretation of Pu sorption data becomes particularly challenging, even for simplified laboratory experiments with simple mineral phases.

The present study focuses on the Pu sorption to kaolinite. Am(III), Th(IV), Np(V) and U(VI) literature sorption data are used as analogues for the corresponding Pu redox states to calibrate a simple surface complexation model, and the Nernst formalism is applied. (Marsac et al., 2015b)

The data used for this work and the simulation curves are shown in Figure 18.

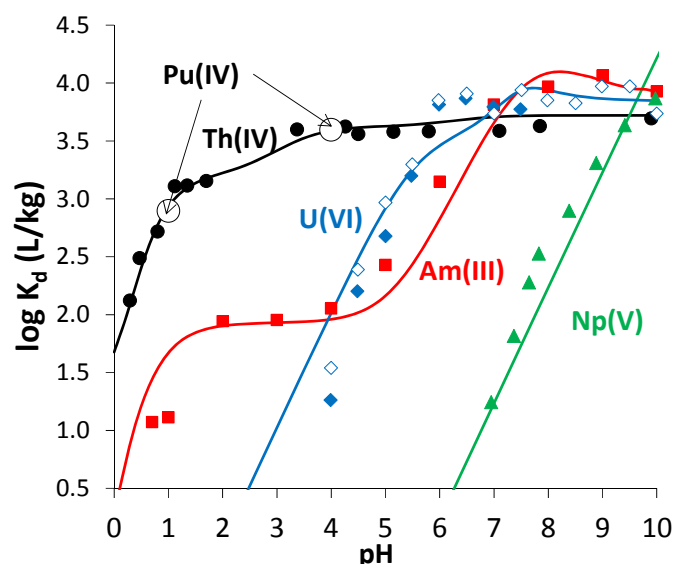


Figure 18: Experimental sorption data (K_d , in L/kg) on kaolinite versus pH for actinides with different redox states (Am(III)/Th(IV)/Np(V); data from (Amayri et al., 2011; Banik et al., 2007; Buda et al., 2008) for 0.1 M NaClO₄. Data for U(VI) are taken from (Křepelová, 2007) for 0.1 M NaClO₄ in the presence of CO₂ (closed diamonds; pH < 8) and 0.01 M NaClO₄ in the absence of CO₂ (open diamonds). The elements are considered as chemical analogues for Pu(III/IV/V/VI). Pu(IV) data are recalculated from the sorption data and Pu redox state analysis of (Banik, 2006) using eq. 17 (two large white circles). Curves represent the modeled result for each Pu redox state.

Two independent pH–pe diagrams, one for the kaolinite surface and another for the aqueous phase, are constructed and superimposed. This allows visualization of the prevalent Pu redox state in both phases. The model suggests that the stability field of the most strongly adsorbing redox state is larger at the surface than in solution. Because Pu(V) weakly sorbs to kaolinite, it never prevails at the surface. Within the stability field of Pu(V) in 0.1M NaClO₄ solution, Pu(VI) and Pu(IV) prevail at the kaolinite surface under oxidizing and slightly reducing conditions, respectively. By contrast, the Pu(III)/Pu(IV) boundary is hardly affected because both redox states strongly sorb to kaolinite, especially for pH < 6. The present method is applied to literature data for Pu sorption to kaolinite.

Our model is applied to the experimental data of (Banik et al., 2007) where 6.6×10^{-9} M of Pu(IV) was contacted with 4 g/L kaolinite in 0.1 M NaClO₄. The experimental percentage of Pu uptake reported by (Banik et al., 2007) in air (only for pH < 8) and in argon atmosphere are shown in Figure 19a together with Th(IV) data ($[^{234}\text{Th}]_{\text{tot}} = 6.6 \times 10^{-13}$ M). Pu overall uptake is systematically lower than Th(IV). Overall Pu uptake increases from 10 to 80% for $0 < \text{pH} < 3$, decreases down to ~60% for pH around 4 and reaches again ~80% above pH = 7. The dip at intermediate pH is unusual and cannot be explained by Pu(IV) alone, which becomes clear from a redox state analysis of Pu in the aqueous phase.

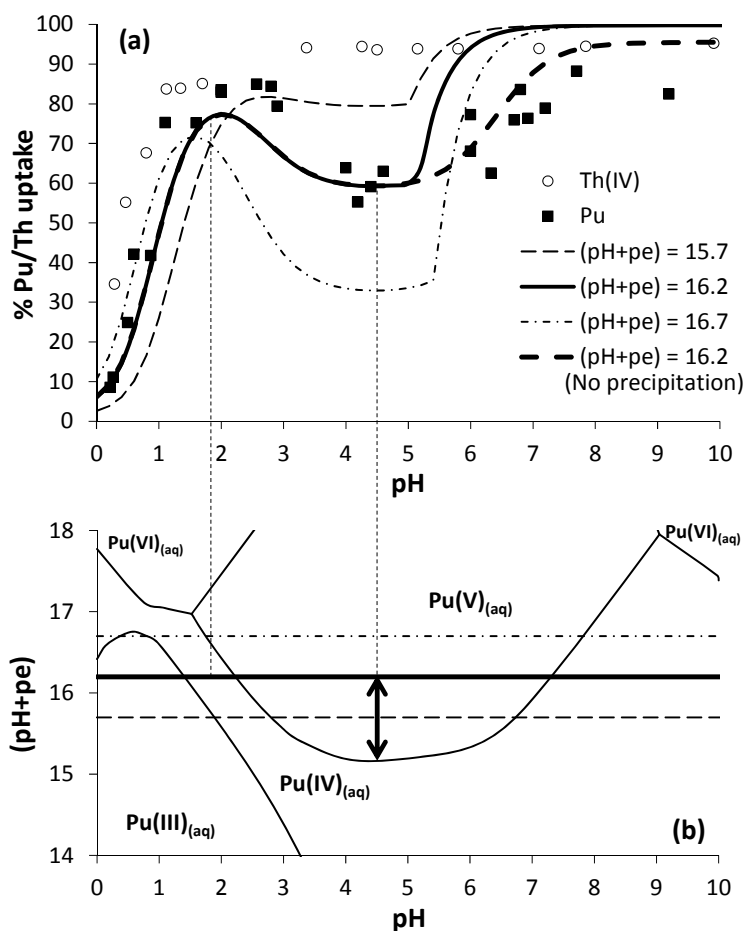


Figure 19: (a) Percentage uptake of Pu and Th by kaolinite ($[Pu]_{tot} = 6.6 \times 10^{-9} \text{ M}$ / $[Th]_{tot} = 6.6 \times 10^{-13} \text{ M}$; 0.1 M NaClO_4 ; $S/V = 4 \text{ g/L}$; either under ambient air below $\text{pH} = 8$ or argon atmosphere) experimentally obtained by (Banik et al., 2007) and calculated for $\text{pH}+\text{pe} = 16.2$, considering (bold line) or not (bold dashed line) the precipitated $\text{PuO}_{2(am)}$ to be removed from the aqueous phase with the kaolinite. The model sensitivity to pe is illustrated applying ± 0.5 uncertainty on the pe : $\text{pH}+\text{pe} = 15.7$ (dashed line) and 16.7 (dashed-dotted line); precipitated $\text{PuO}_{2(am)}$ is considered to have been removed with kaolinite. (b) Predominance diagram for the aqueous solution plotting $\text{pH}+\text{pe}$ versus pe to visualize constant redox conditions horizontally. The legend is valid for (a) and (b).

The present approach allows the description of overall Pu uptake on kaolinite, by applying thermodynamic concepts and by simultaneously taking into account the complete Pu redox chemistry and the respective sorption behavior. The calculations are very sensitive to pe , as illustrated in Figure 19 by considering $\text{pe} \pm 0.5$ (corresponding to $\pm 0.03 \text{ V}$). This result clearly shows that without any information concerning the redox conditions in the experiment, it is almost impossible to predict Pu uptake by kaolinite.

Above $\text{pH} = 5$, information about pe is not available. Simulations are made assuming $\text{pH}+\text{pe} = 16.2$ as before. Because of the strong assumption, the simulations and discussions should be considered with caution. For $\text{pH} = 9$, Pu(IV) is the dominant redox

state in solution (see Figure 19b), consistent with redox state analysis. For pH > 5, the solution is oversaturated with respect to $\text{PuO}_{2(\text{am,hyd})}$: total aqueous $[\text{Pu(IV)}]_{\text{tot, aq}}$ equals approximately 10^{-9} M for pH = 9, whereas the Pu(IV) solubility limit is $10^{-10.4 \pm 0.5}$ M (Neck et al., 2007). This circumstance implies a lot of problems like Pu-colloid formation that is discussed in (Marsac et al., 2015b). Unfortunately, the sorption of Pu-colloids to kaolinite cannot be simulated yet using a mechanistic model without making additional assumptions. However, the sorption of Pu(IV)-colloids to minerals needs to be studied in further experiments.

Table 8: Thermodynamic constants at zero ionic strength used in the present study (Guillaumont et al., 2003). The missing hydrolysis constants for Pu are taken from the corresponding analogues (in brackets). Surface complexation constants for Pu(III, IV, V, VI) are obtained assuming that the experimental uptake data of Am(III), Th(IV), Np(V) and U(VI) by kaolinite are representative for the uptake of the corresponding Pu redox states. (*) Exchange and surface complexation constants have been determined by (Tertre et al., 2008). Some constants could not be determined since no appropriate experimental data were available. According to (Tertre et al., 2006; Tertre et al., 2008), the surface area of kaolinite is 10 m²/g, site density for ≡SOH and exchange sites are 1.66 and 3.70 μmol/m², respectively.

	Reaction	Log K (I = 0)	
Solubility	$\text{PuO}_{2(\text{am,hyd})} + 2 \text{H}_2\text{O} = \text{Pu}^{4+} + 4 \text{OH}^-$	-58.33	
Redox	$\text{PuO}_2^{2+} + \text{e}^- = \text{PuO}_2^+$	15.82	
	$\text{PuO}_2^{2+} + 4 \text{H}^+ + 2 \text{e}^- = \text{Pu}^{4+} + 2 \text{H}_2\text{O}$	33.27	
	$\text{PuO}_2^+ + 4 \text{H}^+ + \text{e}^- = \text{Pu}^{4+} + 2 \text{H}_2\text{O}$	17.45	
	$\text{Pu}^{4+} + \text{e}^- = \text{Pu}^{3+}$	17.69	
Hydrolysis	$\text{PuO}_2^{2+} + \text{H}_2\text{O} = \text{PuO}_2\text{OH}^+ + \text{H}^+$	-5.50	
	$\text{PuO}_2^{2+} + 2 \text{H}_2\text{O} = \text{PuO}_2(\text{OH})_2 + 2 \text{H}^+$	-13.20	
	$\text{PuO}_2^{2+} + 3 \text{H}_2\text{O} = \text{PuO}_2(\text{OH})_3^- + 3 \text{H}^+$	-20.25 (U)	
	$\text{PuO}_2^{2+} + 4 \text{H}_2\text{O} = \text{PuO}_2(\text{OH})_4^{2-} + 4 \text{H}^+$	-32.40 (U)	
	$\text{PuO}_2^+ + \text{H}_2\text{O} = \text{PuO}_2\text{OH} + \text{H}^+$	-11.30 (Np)	
	$\text{PuO}_2^+ + 2 \text{H}_2\text{O} = \text{PuO}_2(\text{OH})_2^- + 2 \text{H}^+$	-23.60 (Np)	
	$\text{Pu}^{4+} + \text{H}_2\text{O} = \text{PuOH}^{3+} + \text{H}^+$	0.60	
	$\text{Pu}^{4+} + 2 \text{H}_2\text{O} = \text{Pu}(\text{OH})_2^{2+} + 2 \text{H}^+$	0.60	
	Continuation Table 8		
	$\text{Pu}^{4+} + 3 \text{H}_2\text{O} = \text{Pu}(\text{OH})_3^+ + 3 \text{H}^+$	-2.30	
	$\text{Pu}^{4+} + 4 \text{H}_2\text{O} = \text{Pu}(\text{OH})_4 + 4 \text{H}^+$	-8.50	
	$\text{Pu}^{3+} + \text{H}_2\text{O} = \text{PuOH}^{2+} + \text{H}^+$	-6.90	
	$\text{Pu}^{3+} + 2 \text{H}_2\text{O} = \text{Pu}(\text{OH})_2^+ + 2 \text{H}^+$	-15.10 (Am)	
	$\text{Pu}^{3+} + 3 \text{H}_2\text{O} = \text{Pu}(\text{OH})_3 + 3 \text{H}^+$	-26.20 (Am)	

Exchange	$2 \text{ X-Na} + \text{PuO}_2^{2+} = \text{X}_2\text{-PuO}_2 + \text{Na}^+$	nd
	$\text{X-Na} + \text{PuO}_2^+ = \text{X-PuO}_2 + \text{Na}^+$	nd
	$3 \text{ X-Na} + \text{Pu}^{3+} = \text{X}_3\text{-Pu} + \text{Na}^+$	1
	$4 \text{ X-Na} + \text{Pu}^{4+} = \text{X}_4\text{-Pu} + \text{Na}^+$	nd
	$\text{X-Na} + \text{H}^+ = \text{X-H} + \text{Na}^+$	-1 ^(*)
Surface complexation	$\equiv\text{SOH} + \text{PuO}_2^{2+} = \equiv\text{SO-PuO}_2^+ + \text{H}^+$	0.2
	$\equiv\text{SOH} + \text{PuO}_2^{2+} + \text{H}_2\text{O} = \equiv\text{SO-PuO}_2\text{OH} + \text{H}^+$	-6.9
	$\equiv\text{SOH} + \text{PuO}_2^{2+} + 2 \text{ H}_2\text{O} = \equiv\text{SO-PuO}_2(\text{OH})_2^- + 3 \text{ H}^+$	-14.5
	$\equiv\text{SOH} + \text{PuO}_2^+ = \equiv\text{SO-PuO}_2 + \text{H}^+$	-4.0
	$\equiv\text{SOH} + \text{Pu}^{4+} = \equiv\text{SO-Pu}^{3+} + \text{H}^+$	nd
	$\equiv\text{SOH} + \text{Pu}^{4+} + \text{H}_2\text{O} = \equiv\text{SO-PuOH}^{2+} + 2 \text{ H}^+$	6.0
	$\equiv\text{SOH} + \text{Pu}^{4+} + 2 \text{ H}_2\text{O} = \equiv\text{SO-Pu}(\text{OH})_2^+ + 3 \text{ H}^+$	3.2
	$\equiv\text{SOH} + \text{Pu}^{4+} + 3 \text{ H}_2\text{O} = \equiv\text{SO-Pu}(\text{OH})_3 + 4 \text{ H}^+$	-3.0
	$\equiv\text{SOH} + \text{Pu}^{3+} = \equiv\text{SO-Pu}^{2+} + \text{H}^+$	-0.5 ^(*) (Eu)
	$\equiv\text{SOH} + \text{Pu}^{3+} + \text{H}_2\text{O} = \equiv\text{SO-PuOH}^+ + 2 \text{ H}^+$	-9.3

It is well known that Pu redox speciation has a strong impact on its mobility in the environment. Various experimental studies have shown that mineral surfaces affect Pu redox speciation. In the present study, Pu redox speciation at the kaolinite surface is interpreted based on the thermodynamic stability of the respective Pu redox state at the surface. To overcome difficulties in the interpretation of results related to the sensitivity of Pu to redox conditions, uptake data on kaolinite of the more redox-stable Am(III), Th(IV), Np(V) and U(VI) - chemical analogues for Pu(III,IV,V,VI) - are used to calibrate a surface complexation model. To fully understand Pu redox chemistry in the aqueous kaolinite suspension, the system is treated separately for the aqueous solution and the kaolinite surface, and the two resulting Pu predominance diagrams are superimposed. This method visualizes how the prevailing Pu redox states can differ between solution and surface for given pH/pe conditions. Notably, the kaolinite surface has no impact on the Pu(IV)/Pu(III) distribution in neutral to alkaline conditions, in the absence of aqueous ligands other than OH⁻. Therefore, the study of Pu(III) sorption to minerals is relevant for the reducing conditions encountered in deep geological nuclear waste repository sites. Under slightly oxidizing conditions, Pu(IV) can be stabilized at the kaolinite surface within the stability field of Pu(V) in solution, which significantly increases overall Pu uptake. The present model predicts overall experimental Pu uptake when the Pu(V)/Pu(IV) redox couple is involved. This suggests that Pu-mineral interaction is strong, even under slightly oxidizing condition. Also Pu(VI) can be stabilized at the kaolinite surface within the stability field of Pu(V) in solution, under oxidizing conditions. Its impact on overall Pu uptake is limited to redox conditions in equilibrium with ambient air atmosphere (O₂), by the weak Pu(VI) sorption to kaolinite for pH < 5 and the strong Pu(VI)-carbonate (due to atmospheric CO₂) complexation in alkaline conditions. Inde-

pendent experimental data for other minerals with Pu and with Np corroborate our approach. The derived equations are of rather generic form making them easily applicable yet to other adsorbant/adsorbat systems.

Based on the thermodynamic stability of the sorbed Pu species, the exact redox mechanism does not need to be explicitly considered but the redox potential of the system must be known. Measurement of redox potential is rarely simple and often bears large uncertainties, but the p_e (or E_h) strongly affects overall Pu uptake by kaolinite. A redox state analysis of aqueous Pu can provide information on p_e , when a steady state is reached. The determination of p_e from Pu redox state analysis heavily relies on the accuracy of the available thermodynamic database for aqueous complexes, i.e. their capability to describe the speciation of the different Pu redox states in presence of various ligands. This fact becomes more important for natural samples that are more complex than the systems considered in this work.

2.1.3.2 Plutonium sorption at the illite surface

As already shown before, the geochemical behavior of Pu strongly depends on its redox speciation. In this study we investigated Pu sorption onto Na-illite, a relevant component of potential host rocks for high-level nuclear waste repositories, under anaerobic conditions. More details about experimental conditions as well as about the methods used in this study are described in (Banik et al., 2016).

The purified Na-illite was provided within the EC project CP CatClay (www.catclay.org). The source material derives from lacustrine continental sediments deposited at the Upper Eocene (~ -35 Ma) in the basin of Le Puy en Velay (Massif Central, France). The purification procedures and the characterization of the purified illite were given in detail in (Marsac et al., 2015a) and will not be repeated here.

A ^{238}Pu stock solution was used. The concentration of the Pu stock solution was 3.9×10^{-5} M in 0.1M HClO_4 . The ^{238}Pu stock solution contained 85% Pu(IV), 11% Pu(V) and 4% Pu(III). A diluted solution ($[\text{Pu}] = 7.8 \times 10^{-7}$ M) in 0.1 M HClO_4 was prepared from the main stock solution to perform experiments at low Pu(IV) concentration. The concentrations of ^{238}Pu in solution were determined by LSC. In addition, the stock solution of ^{238}Pu was checked by ICP-MS measurements and the results are in excellent agreement with LSC measurements. Pu redox state distribution in the stock solution was determined by liquid-liquid extraction with HDEHP and PMBP (Marquardt et al., 2004; Nitsche et al., 1994).

All sorption experiments were performed as batch type experiments. The effect of pH was investigated at an initial Pu concentration ($[\text{Pu}]_{\text{tot}}$) of 8×10^{-11} M. In addition the effect of $[\text{Pu}]_{\text{tot}}$ is investigated for $8 \times 10^{-11} < [\text{Pu}]_{\text{tot}} < 10^{-8}$ M and $\text{pH} = 4.3, 6.2$ and 9.3 . A first series of batch experiments was carried out at room temperature in an argon glove box (< 1 ppm O_2 , absence of CO_2). At a solid to liquid ratio of 2 g L^{-1} , the suspensions

were preconditioned in 0.1 M NaCl under continuous shaking for 4-5 days. pH was adjusted by adding 0.1 M HCl or 0.1 M NaOH. The samples were closed and shaken end-over-end. After one week, pH and Eh were measured in the suspension and an aliquot of each sample was centrifuged in a Beckman L7 Ultracentrifuge at 90000 rpm for 1 h. The supernatant was analyzed for dissolved Pu by LSC. The same procedure was repeated after one year contact time.

Eu(III) is investigated as a chemical analogue of Pu(III). A radiotracer solution from Amersham International was used with a total Eu concentration of 6.0×10^{-4} M. Batch Eu sorption experiments were performed with $[\text{Eu}]_{\text{tot}} = 3 \times 10^{-9}$ M applying the same protocol as for Pu except that, because no redox reaction is involved, (i) one week contact time was chosen and (ii) the Eh measurement was not recorded. After ultracentrifugation, the supernatant was analyzed for dissolved Eu by γ -spectrometry.

Batch Pu sorption experiments involving an illite/calcite mixture were also performed under same conditions mentioned before. The calcite was purchased from Merck, Germany. On the basis of a previous study on Eu(III) sorption to a smectite:calcite mixture (Hartmann et al., 2008) and to avoid the potential release of $\text{CO}_{2(\text{g})}$ during long-term equilibration of the sample (e.g. one year), Pu uptake was measured one week after the addition of Pu. Two series of experiments were conducted at $\text{pH} \approx 8.5$ and 10, respectively, with $[\text{Pu}]_{\text{tot}} = 0.5, 0.8$ and 1×10^{-9} M. An additional (“control”) series of experiments is performed in the absence of calcite for $\text{pH} \approx 10$, the same range of $[\text{Pu}]_{\text{tot}}$ and one week equilibration time.

The modelling of the data was performed with the geochemical speciation program PHREEQC (Parkhurst and Appelo, 1999) and the results were visualized by PHREEPlot (Kinniburgh D. G. and Cooper D. M., 2009). Thermodynamic constants for Pu and Eu/Am aqueous speciation are taken from the NEA thermodynamic database (Guillaumont et al., 2003). The specific ion interaction theory (SIT) (Ciavatta, 1980) is used for the calculation of the activity coefficients of aqueous species. In case of gaps in the Pu database, data from analogue species are chosen (i.e. Eu/Am(III), Np(IV), Np(V) and U(VI) for the respective Pu redox states). The formation constant of $\text{Pu}(\text{OH})_2(\text{CO}_3)_2^{2-}$ selected in THEREDA (Release 2013-08-02) is also used.

Auxiliary reactions and constants are taken from the SIT database provided by PHREEQC (sit.dat file). Again, the 2SPNE SC/CE model is used to simulate Pu and Eu sorption to illite. For the calculations in the presence of calcite, the total dissolved inorganic carbon concentration ([DIC]) is assumed to be in equilibrium with calcite in a closed system with no gas phase. A summary of the thermodynamic database, SIT coefficients and parameters for the 2SPNE SC/CE model is given in in Table 9, Table 10, and Table 11.

Table 9: Relevant aqueous reaction for the calculations of Pu sorption and speciation in the present study. Thermodynamic constants are taken from the NEA-TDB¹ and refer to the value at infinite dilution. Ternary Pu(IV)-hydroxo-carbonato complexes formation constants are taken for THEREDA². In case of gaps in the available database for Pu, data for analogues are used (i.e. Eu/Am(III), Np(IV), Np(V) and U(VI) for the respective Pu redox states). Although available for Pu, the formation constants for PuOH²⁺ and Pu(OH)_{4(aq)} are taken from Eu/Am(III) and Np(IV) to ensure the consistency between aqueous speciation and surface complexation modeling, i.e. to avoid additional corrections of the literature parameters for the 2 SPNE SC/CE model.

	Reaction	Available for Pu	Value used	Analogue
Redox	$\text{PuO}_2^{2+} + \text{e}^- = \text{PuO}_2^+$	15.82		
	$\text{PuO}_2^{2+} + 4 \text{H}^+ + 2 \text{e}^- = \text{Pu}^{4+} + 2 \text{H}_2\text{O}$	33.27		
	$\text{PuO}_2^+ + 4 \text{H}^+ + \text{e}^- = \text{Pu}^{4+} + 2 \text{H}_2\text{O}$	17.45		
	$\text{Pu}^{4+} + \text{e}^- = \text{Pu}^{3+}$	17.69		
Hydrolysis	$\text{AnO}_2^{2+} + \text{H}_2\text{O} = \text{AnO}_2\text{OH}^+ + \text{H}^+$	-5.50	-5.50	
	$\text{AnO}_2^{2+} + 2 \text{H}_2\text{O} = \text{AnO}_2(\text{OH})_2 + 2 \text{H}^+$	-13.20	-13.20	
	$\text{AnO}_2^{2+} + 3 \text{H}_2\text{O} = \text{AnO}_2(\text{OH})_3^- + 3 \text{H}^+$		-20.25	U(VI)
	$\text{AnO}_2^+ + \text{H}_2\text{O} = \text{AnO}_2\text{OH} + \text{H}^+$		-11.30	Np(V)
	$\text{An}^{4+} + \text{H}_2\text{O} = \text{AnOH}^{3+} + \text{H}^+$	0.60	0.60	
	$\text{An}^{4+} + 2 \text{H}_2\text{O} = \text{An}(\text{OH})_2^{2+} + 2 \text{H}^+$	0.60	0.60	
	$\text{An}^{4+} + 3 \text{H}_2\text{O} = \text{An}(\text{OH})_3^+ + 3 \text{H}^+$	-2.30	-2.30	
	$\text{An}^{4+} + 4 \text{H}_2\text{O} = \text{An}(\text{OH})_4 + 4 \text{H}^+$	-8.50	-8.30	Np(IV)
	$\text{An}^{3+} + \text{H}_2\text{O} = \text{AnOH}^{2+} + \text{H}^+$	-6.90	-7.20	Am/Eu(III)
	$\text{An}^{3+} + 2 \text{H}_2\text{O} = \text{An}(\text{OH})_2^+ + 2 \text{H}^+$		-15.10	Am/Eu(III)
	$\text{An}^{3+} + 3 \text{H}_2\text{O} = \text{An}(\text{OH})_3 + 3 \text{H}^+$		-26.20	Am/Eu(III)
Chloride	$\text{AnO}_2^{2+} + \text{Cl}^- = \text{AnO}_2\text{Cl}^+$	0.23	0.23	
	$\text{AnO}_2^{2+} + 2 \text{Cl}^- = \text{AnO}_2\text{Cl}_2$	-1.15	-1.15	
	$\text{An}^{4+} + \text{Cl}^- = \text{AnCl}^{3+}$	1.80	1.80	
	$\text{An}^{3+} + \text{Cl}^- = \text{AnCl}^{2+}$		0.24	Am/Eu(III)
	$\text{An}^{3+} + 2 \text{Cl}^- = \text{AnCl}_2^+$		-0.74	Am/Eu(III)
Carbonate	$\text{An}^{4+} + 2 \text{H}_2\text{O} + 2 \text{CO}_3^{2-} =$	18.24	18.24	
	$\text{An}(\text{OH})_2(\text{CO}_3)_2^{2-} + 2 \text{H}^+$			

(1): Guillaumont, R.; Fanghänel, Th.; Fuger, J.; Grenthe, I.; Neck, V.; Palmer, D. A.; Rand, M. H. Update on the Chemical Thermodynamics of Uranium, Neptunium, Plutonium, Americium and Technetium; Elsevier: Amsterdam, 2003. (2): THEREDA, Thermodynamic Reference Database. Release 2013-08-02. www.thereda.de.

Table 10: Surface complexation and cation exchange parameters for the 2 SPNE SC/CE model are taken from the literature^{3,4,5} and for Pu(IV) (determined in the present study). The surface complexing site density is $[\equiv S]_{\text{tot}} = 2 \times 10^{-3}$ mol/kg. The cation exchange capacity is $[X]_{\text{tot}} = 0.225$ eq/kg. “na” refers to non-available values. Only the relevant reactions and constants for the present calculations are tabulated.

	Reaction	Np	Pu	Am	Value used
Surface	$\equiv\text{SOH} + \text{H}^+ = \equiv\text{SOH}_2^+$				4.00
	$\equiv\text{SOH} = \equiv\text{SO}^- + \text{H}^+$				-6.20
	$\equiv\text{SOH} + \text{An}^{4+} = \equiv\text{SO-An}^{3+} + \text{H}^+$	na	na		
	$\equiv\text{SOH} + \text{An}^{4+} + \text{H}_2\text{O} = \equiv\text{SO-AnOH}^{2+} + 2 \text{H}^+$	na	9.9 ± 0.5		9.9
	$\equiv\text{SOH} + \text{An}^{4+} + 2 \text{H}_2\text{O} = \equiv\text{SO-An(OH)}_2^+ + 3 \text{H}^+$	6.4 ± 1.2	5.9 ± 0.5		5.9
	$\equiv\text{SOH} + \text{An}^{4+} + 3 \text{H}_2\text{O} = \equiv\text{SO-An(OH)}_3 + 4 \text{H}^+$	0.7 ± 1.0	0.1 ± 0.5		0.1
	$\equiv\text{SOH} + \text{An}^{4+} + 4 \text{H}_2\text{O} = \equiv\text{SO-An(OH)}_4^- + 5 \text{H}^+$	-5.7 ± 1.2	-6.4 ± 0.5		-6.4
	$\equiv\text{SOH} + \text{An}^{3+} = \equiv\text{SO-An}^{2+} + \text{H}^+$			3.1	3.1
	$\equiv\text{SOH} + \text{An}^{3+} + \text{H}_2\text{O} = \equiv\text{SO-AnOH}^+ + 2 \text{H}^+$			-4.4	-4.4
	$\equiv\text{SOH} + \text{An}^{3+} + 2 \text{H}_2\text{O} = \equiv\text{SO-An(OH)}_2 + 3 \text{H}^+$			-12.7	-12.7
	$\equiv\text{SOH} + \text{An}^{3+} + 3 \text{H}_2\text{O} = \equiv\text{SO-An(OH)}_3^- + 4 \text{H}^+$			-24.3	-24.3
	Exchange	$2 \text{X-Na} + \text{Ca}^{2+} = \text{X}_2\text{-Ca} + 2 \text{Na}^+$			
$3 \text{X-Na} + \text{An}^{3+} = \text{X}_3\text{-An} + 3 \text{Na}^+$					1.9
$4 \text{X-Na} + \text{An}^{4+} = \text{X}_4\text{-An} + 4 \text{Na}^+$					na

(3): Bradbury, M. H.; Baeyens, B. Sorption modelling on illite Part I: Titration measurements and the sorption of Ni, Co, Eu and Sn. *Geochim. Cosmochim. Acta* **2009**, *73*, 990-1003. (4): Bradbury, M. H.; Baeyens, B. Sorption modeling on illite Part II: actinide sorption and linear free energy relationships. *Geochim. Cosmochim. Acta* **2009**, *73*, 1004-1013. (5): Marsac, R.; Banik, N. L.; Diascorn, A.; Kupcik, T.; Lützenkirchen, J.; Marquardt, C. M.; Schäfer, T.; Schild, D.; Rothe, J.; Dardenne, K.; Geckeis, H. Neptunium redox speciation at the illite surface. *Geochim. Cosmochim. Acta* **2015**, *152*, 39-51.

Table 11: SIT parameters ($\epsilon(i,k)$) used in the present study, taken from the NEA-TDB¹ for Pu or the corresponding analogue (as in Table S1). “na” refers to non-available values (set equal to 0).

i	k	$\epsilon(i,k)$
H ⁺	Cl ⁻	0.12
Na ⁺	Cl ⁻	0.03
Na ⁺	OH ⁻	0.04
PuO ₂ ²⁺	Cl ⁻	0.22
PuO ₂ OH ⁺	Cl ⁻	na
PuO ₂ (OH) ₃ ⁻	Na ⁺	-0.09
PuO ₂ Cl ⁺	Cl ⁻	0.22
PuO ₂ ⁺	Cl ⁻	0.09
Pu ⁴⁺	Cl ⁻	0.4
PuOH ³⁺	Cl ⁻	0.2
Pu(OH) ₂ ²⁺	Cl ⁻	0.1
Pu(OH) ₃ ⁺	Cl ⁻	0.05
Pu(OH) ₂ (CO ₃) ₂ ²⁻	Na ⁺	na
PuCl ³⁺	Cl ⁻	0.62
Pu ⁺³	Cl ⁻	0.23
PuOH ²⁺	Cl ⁻	-0.04
Pu(OH) ₂ ⁺	Cl ⁻	-0.06
Pu(OH) ₃	Cl ⁻	0
Pu(OH) ₃	Na ⁺	-0.17
PuCl ²⁺	Cl ⁻	0.191
PuCl ₂ ⁺	Cl ⁻	0.129

(1): Guillaumont, R.; Fanghänel, Th.; Fuger, J.; Grenthe, I.; Neck, V.; Palmer, D. A.; Rand, M. H. *Update on the Chemical Thermodynamics of Uranium, Neptunium, Plutonium, Americium and Technetium*; Elsevier: Amsterdam, 2003.

Results and Discussion

Figure 20 presents Pu sorption to illite (R_d in L/kg) as a function of the pH (i.e. pH-edge) after 1 week and 1 year contact time for $[Pu]_{tot} = 8 \times 10^{-11}$ M. While Pu uptake by illite is always high, R_d values are significantly lower after 1 week for $4 < \text{pH} < 7$: about 5-10% of Pu remained in solution. For pH = 4, aqueous redox state analysis of Pu was performed on contact with illite after ultracentrifugation ($[Pu]_{tot} = 10^{-8}$ M). About 90% of

Pu in the aqueous phase was Pu(V), which weakly sorbs to clays, by analogy with Np(V) (Bradbury and Baeyens, 2006; Gorgeon, 1994). Because the Pu stock solution contains ~10% of Pu(V), the lower uptake after 1 week compared to 1 year contact time is attributed to slow reduction kinetics of Pu(V) to Pu(IV), in agreement with previous studies on montmorillonite (Begg et al., 2013; Zavarin et al., 2012) or other minerals (Hixon et al., 2013; Hixon and Powell, 2014; Powell et al., 2005). For pH > 7, log R_d values increase with the pH. For pH = 10, aqueous redox state analysis of Pu showed only the presence of Pu(IV) after 1 week. This might be attributed to an increasing reduction rate of Pu(V) to Pu(IV) with the pH, as observed for hematite and goethite (Powell et al., 2005). Between 1 week and 1 year, for pH < 7, Pu uptake by illite increases. However, for pH > 7, Pu uptake does not significantly evolve with time.

The log R_d slightly increases from approximately 4 to 5.3 L kg⁻¹ with increasing pH from 3 to 5 and remain constant at log R_d = 5.3 ± 0.5 L kg⁻¹ (2σ) for pH > 5. The Pu-illite sorption isotherms for pH = 4.3, 6.2 and 9.3 are shown on Figure 20b as log R_d versus log [Pu]_{aq} (i.e. the final aqueous Pu concentration in solution after ultracentrifugation). Log R_d does not vary significantly with log [Pu]_{aq} for the pH values investigated, with more scatter in the data for pH = 4.3. The measured log [Pu]_{aq} values in the presence of illite are close or below to the solubility limit of Pu(IV), i.e. log [Pu]_{aq} ≈ -9 (for pH = 4.3) and -10.4 M (for pH > 6) (Neck et al., 2007). No effect of PuO_{2(am,hydr)} precipitation on Pu uptake is observed at the highest [Pu]_{aq} investigated.

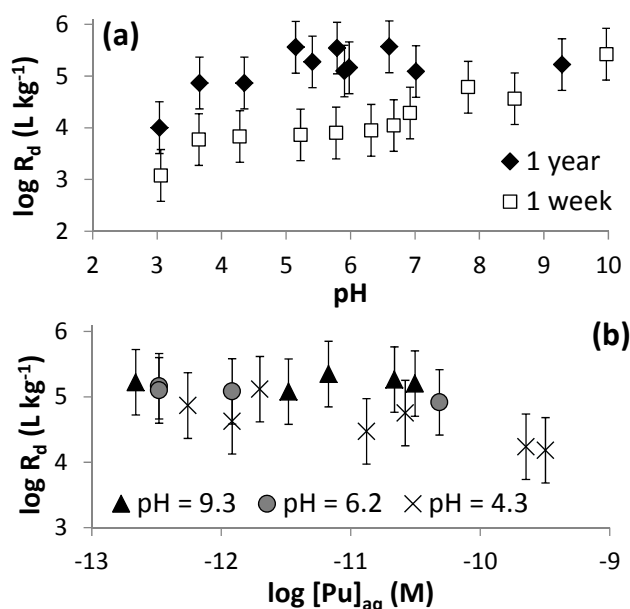


Figure 20: (a) Pu sorption to illite (R_d in $L\ kg^{-1}$) in 0.1 M NaCl as a function of the pH for $[Pu]_{tot} = 8 \times 10^{-11}$ M after 1 week and 1 year contact time. (b) Pu-illite sorption isotherms for pH = 4.3, 6.2 and 9.3 after 1 year contact time.

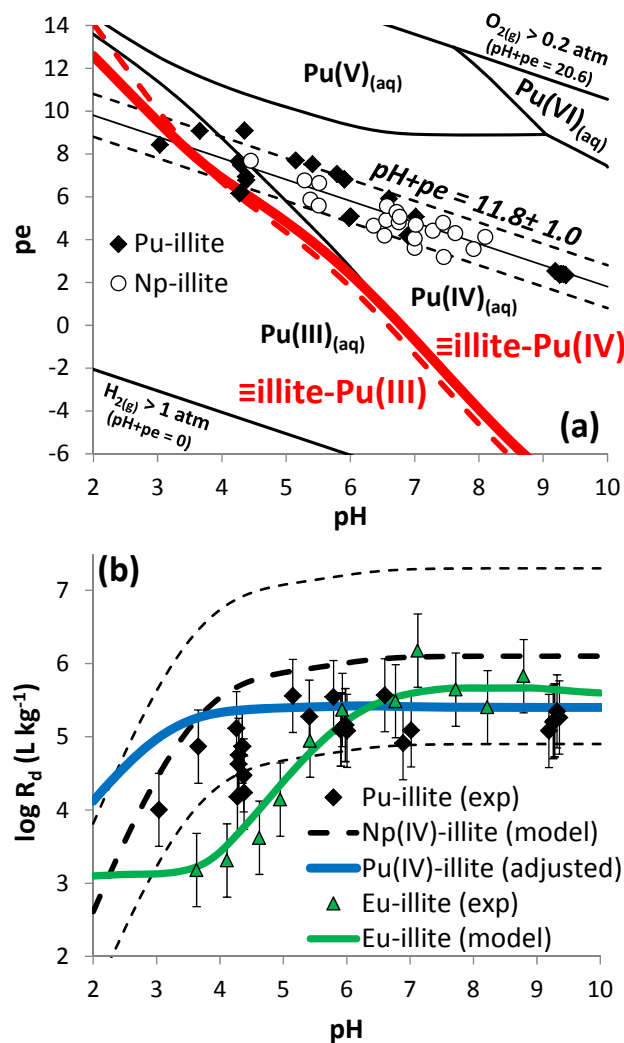


Figure 21 (a) Predominance pH-pe diagram for Pu in 0.1 M NaCl. Measured pH-pe values in the Pu-illite (present work) and Np-illite (Marsac et al., 2015a) suspensions in 0.1 M NaCl are shown as symbols. The bold red lines show the estimated (on the basis of chemical analogues; dashed line) and presently determined (solid line) Pu(IV)/Pu(III) borderline at the illite surface (see text for more details). (b) Pu and Eu(III) uptake data on illite (R_d in $L\ kg^{-1}$) as a function of pH compared with the predicted Eu/Am(III) (green bold line), Np(IV) (dashed black line) and the present model for Pu(IV) (blue bold line) based on the 2 SPNE SC/CE framework. Thin dashed lines correspond to the uncertainty associated to the surface complexation constants for Np(IV).

In Figure 21a, the experimental pH-pe values are compared to those reported for the Np-illite system (Marsac et al., 2015a) after contact times from 7 to 63 days. Only the data for the lowest $[Np(V)]_{tot}$ are shown (3×10^{-8} M) because higher $[Np(V)]_{tot}$ affected the pe. This is likely due to the limited redox capacity of the illite. Although the experimental pe involves large uncertainties, pH-pe measurements from both studies agree well, which suggests that the redox conditions of the 0.1 M NaCl illite suspension can be described relatively well by $pH + pe = 11.8 \pm 1.0$. Figure 21 also includes the predominance pH-pe diagram for Pu in 0.1 M NaCl solution. According to the calculations and the uncertainty in pe, significant amounts of Pu(III) are expected in the aqueous

phase below $\text{pH} \approx 5$. This is confirmed by aqueous Pu redox state analysis, i.e. after illite removal by ultracentrifugation ($[\text{Pu}]_{\text{tot}} = 10^{-8} \text{ M}$). For $\text{pH} = 4.3$, $22 \pm 10\%$ of Pu(III) and $85 \pm 10\%$ of Pu(IV) are detected. Pu(IV) is expected to prevail in solution above $\text{pH} \approx 5$. For $\text{pH} = 6.9$, aqueous redox state analysis of Pu shows that the amount of Pu(III) is insignificant ($5 \pm 10\%$) and only Pu(IV) is found.

The redox speciation of actinides may differ between the aqueous and adsorbed states (Marsac et al., 2015b; Marsac et al., 2015a). With a simple equation the stability field of different Pu redox states at a mineral surface (Marsac et al., 2015b), regarding only the relevant oxidation states Pu(IV) and Pu(III):

$$\{\text{Pu(IV)/Pu(III)}\}_{\text{surf}} = \{\text{Pu(IV)/Pu(III)}\}_{\text{aq}} + (\log R_d(\text{Pu(III)}) - \log R_d(\text{Pu(IV)}))$$

where $\{\text{Pu(IV)/Pu(III)}\}_{\text{aq}}$ involves the Nernst equation and describes the Pu(IV)/Pu(III) borderline in the aqueous phase shown on Figure 21a, and $\{\text{Pu(IV)/Pu(III)}\}_{\text{surf}}$ relates to the illite surface. The $\log R_d(\text{Pu(III)})$ and $\log R_d(\text{Pu(IV)})$ values in the above equation represent the individual uptake of the two redox states under the same physico-chemical conditions. Because the individual R_d values are not currently available for the two redox states of Pu, Eu(III) and Np(IV) are taken as analogues of Pu(III) and Pu(IV), respectively.

In order to accurately estimate the sorption behavior of Pu(III) to our illite, Eu(III) sorption experiments in 0.1 M NaCl ($[\text{Eu}]_{\text{tot}} = 3 \times 10^{-9} \text{ M}$) are carried out for $3 < \text{pH} < 10$ and the results are shown on Figure 21b. Predictions by the 2SPNE SC/CE model are in good agreement when using the set of surface complexation constants determined for Am(III) (Bradbury and Baeyens, 2009b). For $\text{pH} < 4$, Eu uptake is controlled by cation exchange. For $\text{pH} > 4$, Eu uptake increases with pH before reaching a plateau (ca. $\text{pH} > 7$) at nearly 100% uptake due to surface complexation. No experimental data for Np(IV) sorption to illite in the absence of Np(V) are available, but Figure 21b shows the pH-edge of Np(IV) in 0.1 M NaCl predicted with the 2 SPNE SC/CE model (Marsac et al., 2015a). The simulated $\log R_d$ values for Np(IV) are constant for $\text{pH} > 4$. The predicted decrease in $\log R_d$ with decreasing pH below pH 4 must be considered with caution, because the model for Np(IV) was only calibrated for $4 < \text{pH} < 10$, as discussed later. Since experimental pe values were required to calibrate of the model for Np(IV), the predicted $\log R_d$ values for Np(IV) involve relatively large uncertainties (ca $\pm 1.1 \log R_d$ units, dotted lines on Fig. 2b). Using the above equation, $\{\text{Pu(IV)/Pu(III)}\}_{\text{surf}}$ can now be calculated (Figure 21a, bold red dotted line). For $\text{pH} < 7$, Eu sorption to illite is weaker than Np(IV). The stability field of Pu(IV) is enlarged at the illite surface and overlaps with the stability field of Pu(III) in the aqueous phase. For $\text{pH} > 7$, Eu(III) and Np(IV) uptake are almost equal: the Pu(IV)/Pu(III) borderline at the illite surface coincides with the one in solution. Given the measured pH-pe values, Pu(IV) is expected to prevail (or, at least, to be present in significant amounts) at the illite surface in all samples. For $\text{pH} > 5$, Pu(III) is negligible and Pu uptake by illite is controlled by Pu(IV). For $\text{pH} < 5$, overall Pu uptake by illite is expected between Eu(III) and Np(IV).

At this point, it appears possible to provide a more accurate description of Np/Pu(IV) sorption to illite with the 2SPNE SC/CE model than previously possible (Marsac et al., 2015a). Given the similar chemical behavior of Np and Pu, their uptake on illite is not expected to differ by more than $\pm 0.5 \log R_d$ units. Because Pu(IV) prevails at the illite surface and in solution for $\text{pH} > 6$, the predicted overall Pu uptake is insensitive to small pe variations. Figure 21b shows that our Pu data are in the range of expected $\log R_d$ values but in the lower range defined by the confidence interval on complexation constants for Np(IV). Therefore, the surface complexation constants for Pu/Np(IV) in the 2SPNE SC/CE model can be slightly adjusted and the associated uncertainty confidently reduced to the experimental error on $\log R_d$. For $\text{pH} < 4$, the predicted decrease in $\log R_d(\text{Np(IV)})$ values are in contrast to the available Th(IV) and Sn(IV) data, where $\log R_d$ values remain constant down to $\text{pH} < 3$ (Bradbury and Baeyens, 2009a, 2009b). This follows from the fact that the formation constant for $\equiv\text{SONpOH}^{2+}$ is not known, because experimental data are not available at $\text{pH} < 4$ (Marsac et al., 2015a). The formation of $\equiv\text{SOPuOH}^{2+}$ is included in the present model and an adjusted thermodynamic constant extends the sorption plateau down to $\text{pH} = 3$. The predicted independent uptake of Pu(IV) is shown on Figure 21b. As shown in Figure 21a (bold grey line), $\{\text{Pu(IV)/Pu(III)}\}_{\text{surf}}$ is weakly affected by these adjustments and our previous conclusions remain valid.

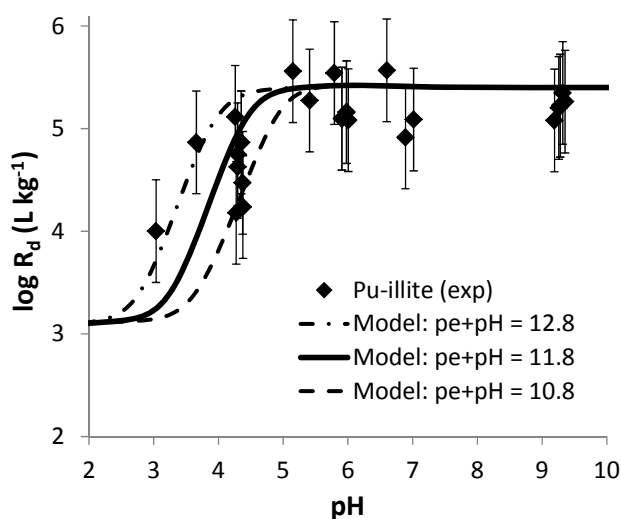


Figure 22: The experimental results for Pu sorption to illite (R_d in L kg^{-1}) as a function of pH are compared with overall $\log R_d$ calculated for $\text{pH} + \text{pe} = 11.8 \pm 1.0$ (bold line; lower and upper values: dashed and dashed-dotted lines, respectively).

The surface complexation parameters for Am(III) are used for Pu(III) and the overall $\log R_d$ for Pu (i.e. accounting for the presence of both Pu(III) and Pu(IV) in the suspension) is calculated for $\text{pH} + \text{pe} = 11.8 \pm 1.0$ with the 2 SPNE SC/CE model. Experimental and model results are compared Figure 22. For $\text{pH} > 5$, Pu(IV) prevails both at the surface and in solution, and overall $\log R_d$ for Pu equals $\log R_d(\text{Pu(IV)})$. For $\text{pH} < 5$, model and experiment are in agreement, and Figure 22 illustrates the effect of pe on the overall $\log R_d$ values. These results suggest that the modeling approach previously developed for Pu sorption to kaolinite (Marsac et al., 2015b), with focus on the Pu(V)/Pu(IV) cou-

ple, can be directly applied to illite even when the Pu(IV)/Pu(III) redox couple is involved. The model can be used to predict Pu uptake by illite in more reducing conditions than those investigated here.

Pu sorption to illite in the presence of calcite.

Natural clay rocks such as OPA and COx contain significant amounts of calcite and the effect of dissolved carbonate on Pu retention must be taken into account. Here, we report the first Pu(IV)-illite uptake data in the presence of carbonate from an illite-calcite mixture under inert atmosphere. In the absence of calcite, the experimental Pu uptake by illite for pH = 10 after only one week contact time agrees with the data obtained after one year, as shown on Figure 23. Therefore, Pu uptake data after 1 week contact time represents a steady-state, at least at alkaline pH. In the presence of calcite, $p_e = 4.4$ and 0.8 is measured for pH = 8.5 and 9.8, which is within the stability field of aqueous Pu(IV). The experimental $\log R_d$ values in the presence of calcite are plotted in Figure 23, together with model predictions for Pu uptake on illite and for the total dissolved inorganic carbon concentration ([DIC]). The model predicts $[DIC] = 1.2 \times 10^{-3}$ and 4.3×10^{-4} M for pH = 8.5 and 9.8, respectively. For pH = 8.5, $\log R_d = 5.3 \pm 0.5 \text{ L kg}^{-1}$ is measured, suggesting that Pu sorption to illite is weakly affected by the presence of carbonates in our experimental conditions, in agreement with the model. The observation is consistent with Th uptake on MX-80 bentonite at pH = 7.6 and OPA at pH = 8, with and without carbonate ($[DIC] = 4.2 \times 10^{-4}$ M and 1.8×10^{-4} M) (Bradbury and Baeyens, 2005, 2009b, 2011). For pH = 9.8, Pu uptake ($\log R_d = 4.5 \pm 0.5 \text{ L kg}^{-1}$) is slightly lower on average than in the absence of calcite, which might suggest a slight effect of carbonate, unlike what the model predicts. Pu uptake by calcite could not be modeled accurately above pH = 9 by others (Zavarin et al., 2005) and our modeling results also suggest that aqueous Pu-carbonate complexation is not accurately described with the current thermodynamic database for alkaline and low [DIC] conditions. However, this has little impact in the present study, which shows that Pu sorption to illite is only weakly affected by carbonate complexation in a calcite saturated solution. The model is used to predict Pu uptake by illite down to pH = 7, to mimic natural clay rock porewaters conditions such as in OPA or COx, which exhibit pH ≈ 7.5 . The range of modeled [DIC] in equilibrium with calcite in the presence of Na-illite (i.e. accounting for the Ca^{2+} - Na^+ exchange reaction) for $7 < \text{pH} < 8$ (i.e. 1.5-5 mM) is similar to OPA porewater (≈ 3 mM) (e.g. (Pearson et al., 2011)). The model predicts minor decrease of $\log R_d$ down to 4 L kg^{-1} for pH = 7, where $[DIC] = 5 \text{ mM}$. Because the formation of ternary Eu(III)- or U(VI)-carbonato surface complexes occurred in the case of smectite (Marques Fernandes et al., 2008; Marques Fernandes et al., 2012), a similar uptake mechanism cannot be excluded for Pu(IV) and illite. Further studies on tetravalent actinide sorption to clay minerals as a function of [DIC] are required to more accurately predict Pu(IV) sorption in natural clay rock-porewater systems.

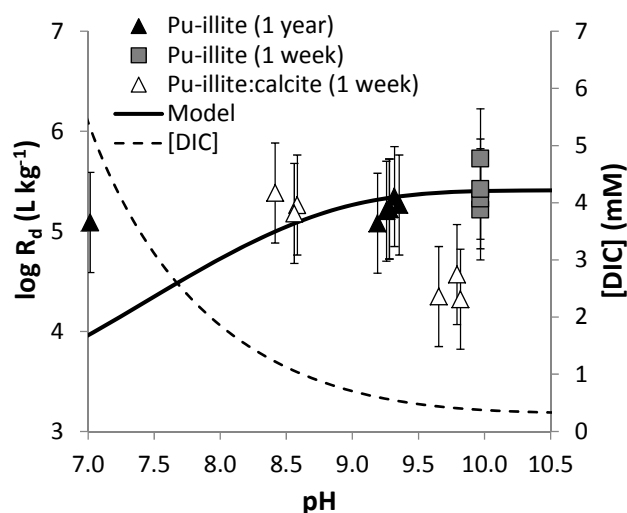


Figure 23: Experimental results for Pu sorption to illite (R_d in $L\ kg^{-1}$) versus pH after 1 year and 1 week (for pH = 10) in the absence of calcite, and after 1 week in the presence of calcite. The lines are model predictions of log R_d values for Pu (bold line) and the total inorganic carbon concentration ([DIC], in mM; dashed line) in the case of the Na-illite in contact equilibrium with calcite.

2.1.4 Conclusions

The results of our Np and Pu studies - Pu(IV)/Pu(III) transitions in presence of illite, the outcome of studies of the Pu(V)/Pu(IV) redox reactions in aqueous kaolinite suspensions, or the Np(V)/Np(IV) transitions in presence of illite - demonstrate the applicability of the approach to describe actinide redox reactions in presence of mineral surfaces over a wide range of possible redox conditions (i.e. when Pu(III), Pu(IV) and Pu(V) occur). A more accurate simulation of redox sensitive element behavior in near surface soil systems and deep geological formations becomes possible by implementing measured pe values of a given system into geochemical surface speciation calculations. Therefore, this study may allow more accurate prediction of Pu mobility in the geosphere. Because natural systems can be much more complex, containing e.g. carbonates and natural organic matter, further studies are required to verify the applicability of the present approach to a wider range of geochemical conditions and other redox sensitive elements (e.g. cerium, technetium, arsenic, chromium).

2.1.5 U(VI) sorption on Illite at high ionic strengths

The sorption of hexavalent uranium (U(VI), UO_2^{2+}) onto illite was investigated in the NaCl system as well as in the $CaCl_2$ and $MgCl_2$ system. In these experiments the Illite de

Puy (IdP) was used and its purification and characterization is described in detail in (Schnurr et al., 2015; Schnurr, 2015).

U(VI) sorption in the NaCl system

The sorption data ($\log K_D$) of U(VI) sorbed onto IdP (Illite de Puy) are shown Figure 24 at different NaCl solutions. The sorption is quasi quantitative over a broad pH range. At a pH > 11, a significant decreasing of the sorption is observed. The experimental data agree well with data of U(VI) sorption on illite from the literature (Bradbury and Baeyens, 2009b). The differences at high $\log K_D$ values might be caused by different different phase separation as mentioned for the Eu(III) sorption studies onto illite. A slight portion of colloidal clay minerals remaining in solution after centrifugation or filtration can affect result at such low uranium concentration in solution. The ionic strength effect is not significant in NaCl solution with concentrations between 0.1 and 4.0 M. At pH values below pH_c , no difference is observed at the different ionic strengths. At $\text{pH}_c > 7$, the $\log K_D$ seemingly depends slightly on the ionic strength.

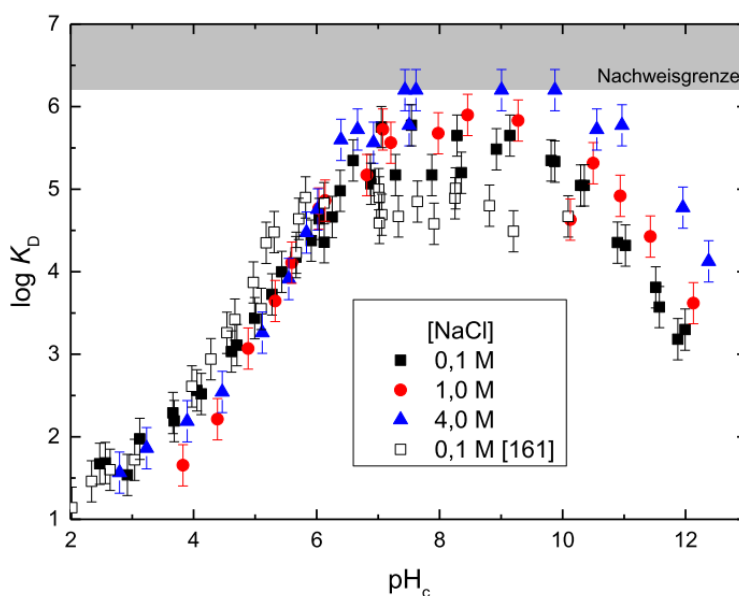


Figure 24: U(VI) sorption on IdP (S:L = 2 g/L) plotted as $\log K_D$ versus pH_c values at different NaCl concentrations. Opened quadratic symbols are data from (Bradbury and Baeyens, 2009b). $[\text{U}]_{\text{total}} = 4.0 \times 10^{-7}$ M.

Because of the fact that the uranium concentration in this pH range is near the detection limit of the ICP-MS and, hence, the experimental error is rather high, the observed ionic strength effect mustn't be over-interpreted. However, because of the rather low scattering of the data, the ionic strength dependence is obvious. At $\text{pH}_c > 10$, the uranium concentration in solution becomes higher, the experimental error becomes smaller and these data might confirm a ionic strength effect at higher pH_c values.

For the modelling with the surface complexation model 2SPNE SC/CE the parameter set of (Bradbury and Baeyens, 2009b) was used. The experimental results from literature slightly differ from the present experimental data. Because of this observation, the inner-sphere complexation constants ($\log K_{SC}$) were slightly modified and adapted to the new experimental data. The difference of the modified $\log K_{SC}$ values to the original ones is rather small ($\Delta \log K_{SC}$ 0, 0.1, 0.4, 0.5 for the four surface species, Table 12) and lie within the uncertainty of the published constants as well as the experimental error margin. The modelling with the adapted parameter set is shown in Figure 25. The modelling results agree well with experimental data at all ionic strengths at lower pH_c values up to pH_c 7. At higher pH_c values a significant difference occurs and the trend between modelling and experiments exhibits an opposing trend. Especially at high ionic strength of $[NaCl] = 4$ M the modelling underestimates the experimental data.

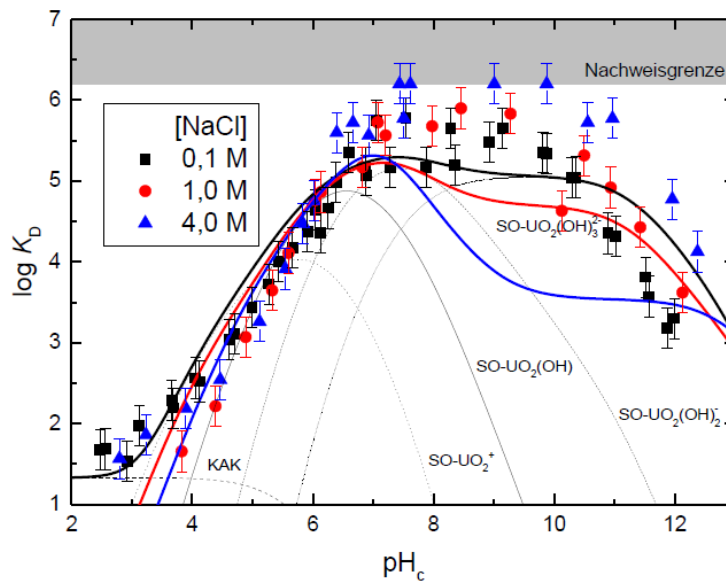


Figure 25: U(VI) sorption on IdP: Comparison between experimental data (symbols) and modelling by the 2SPNE SC/CE model (curves). The species distribution is exemplary shown for 0.1 M NaCl. $[U]_{total} = 4.0 \times 10^{-7}$ M; IdP: S/L = 2 g/L.

A second adjustment of the model is shown in Figure 26. An additional inner-sphere sorption species is included, which enhances the part of the sorbed uranium with increasing chloride concentration: $SO-UO_2Cl(OH)_2^{2-}$. Modelling with this species significantly improves the description of the experimental data at higher ionic strengths and higher pH_c values. Particularly, the ionic strength dependences at $pH_c > 11$ is satisfactorily reflected. The species $SO-UO_2Cl(OH)_2^{2-}$ is not mentioned in the literature and cannot definitively be confirmed in this work. But several findings hint to the existence of such a species. Fuger could identify a mixed solid phase of uranium: $UO_2ClOH \cdot 2H_2O$ (Fuger et al., 1983). Additionally, spectroscopic investigations by Runde show that mixed U(VI) complexes with Cl-OH and Cl-CO₃ are possible (Runde, 2011).

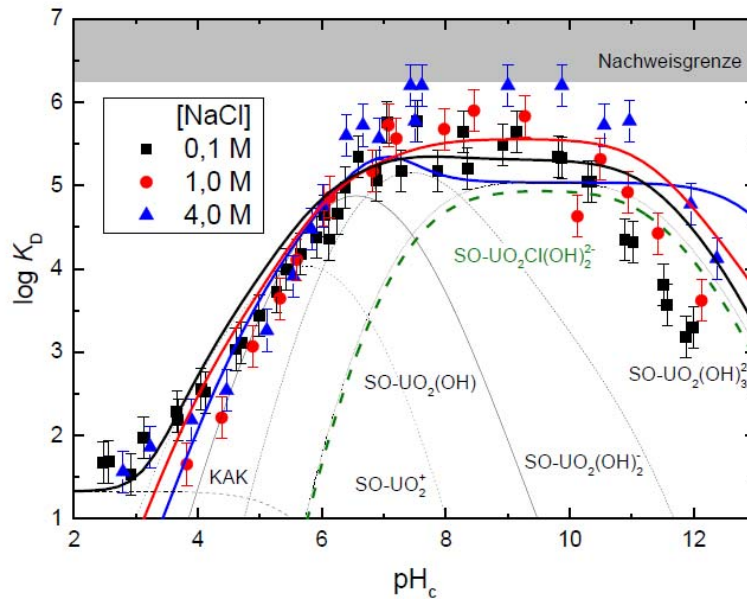


Figure 26: U(VI) sorption on IdP in NaCl solution: Comparison between experimental data (symbols) and modelling (lines) by the 2SPNE SC/CE model including the species $\text{SO-UO}_2\text{Cl}(\text{OH})_2^{2-}$ (green dashed curve). The species distribution is exemplary shown for 0.1 M NaCl. $[\text{U}]_{\text{total}} = 4.0 \times 10^{-7}$ M; IdP: S/L = 2 g/L.

U(VI) sorption in the MgCl_2 and CaCl_2 system

Further investigations were performed to elucidate the influence of the background electrolyte on the U(VI) sorption on illite. For this sorption batch experiments in MgCl_2 and CaCl_2 were made. The sorption edges of both electrolytes are very similar at low ionic strengths ($I = 0.18$ M). For MgCl_2 the sorption experiment stops at $\text{pH}_c \sim 9$, because at higher pH_c the $\text{Mg}(\text{OH})_2$ starts to precipitate. Comparison with the NaCl system at comparable ionic strength ($I = 0.1$ M) shows a very congruent sorption behavior. Only at very high pH_c values ($\text{pH}_c > 11$) the U(VI) sorption decreases stronger in the NaCl system. Nevertheless, the U(VI) is quasi quantitatively sorbed on the illite surface in the relevant pH_c range of 6 – 11.

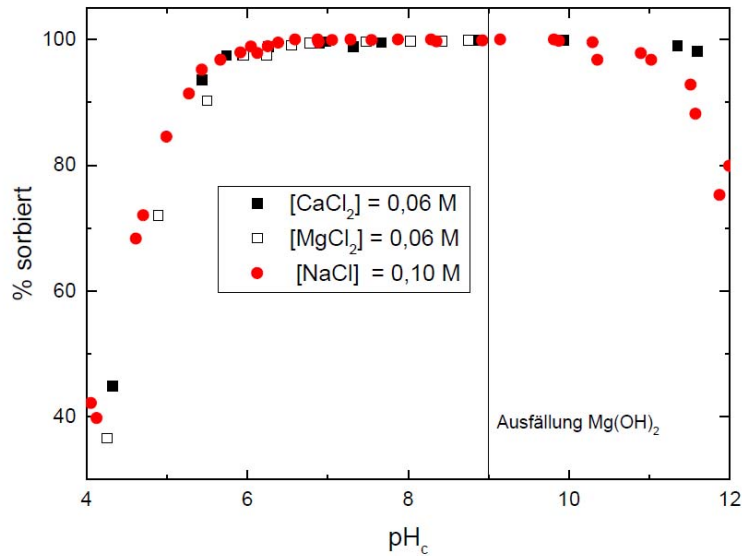


Figure 27: U(VI) sorption ($[U]_{\text{total}} = 4.0 \cdot 10^{-7} \text{ M}$) on IdP (S:L = 2 g/L) plotted as % sorbed against pH_c value in MgCl_2 (black, open), CaCl_2 (black, closed, 0.06 M) and NaCl (red, 0.10 M) solutions.

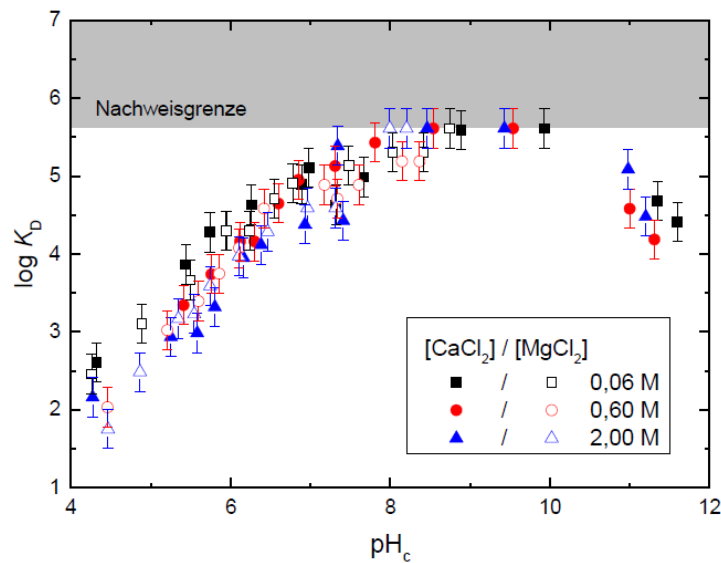


Figure 28: U(VI) sorption on IdP (S:L = 2 g/L) in Ca/MgCl_2 solution plotted as $\log K_D$ versus pH_c values at different MgCl_2 (open symbols) and CaCl_2 (closed symbols) concentrations.

A very similar sorption behavior of U(VI) on illite is also observed at elevated ionic strength as it is demonstrated in Figure 28. In the pH_c range 4.5 – 7 only a small ionic strength dependence is observed; the pH_c sorption edge is slightly shifted to higher pH_c values with increasing ionic strength ($< 0.5 \log K_D$ units per 1 M electrolyte). At $\text{pH}_c > 8$ the sorption is quasi quantitative ($\log K_D > 5$) and no significant change is obvious with increasing ionic strength. The radionuclide concentrations in solution of all systems reach the experimental detection limit and the sorption gains a maximum at $\log K_D =$

5.5 (99.95% sorption). Only at very high pH_c values (>12) the $\log K_D$ lessens to $\log K_D > 4$ (95%).

As mentioned before, different data set for modelling of the radionuclide sorption exist in the literature, especially for Eu(III) on Na- and Ca-clays. For the Ca-IdP no data sets of the inner sphere surface complexation constants for U(VI) are available in the literature. Therefore, the constants from the Na-IdP system were used to deduce the constants for the Ca-IdP system. The $\log K_{SC}$ of the U(VI) sorption on Na-IdP were corrected by the same difference values ($\Delta \log K_{SC}$) that were observed between the Eu(III) sorption on Na- and Ca-montmorillonite system (details see (Schnurr, 2015)). The result of the modelling by using the deduced $\log K_{SC}$ parameter set is shown in Figure 29 for 0.06 M CaCl_2 . Neither the published $\log K_{SC}$ of the Na-IdP, nor the deduced $\log K_{SC}$ for the Ca-IdP can describe correctly the experimental data. It is obvious that the difference between the Na and Ca system is not so much pronounced for U(VI) such as for Eu(III). Therefore, it can be assumed that the difference in $\log K_{SC}$ of U(VI) sorption between the Na and Ca system is not as large as in case of Eu(III) and that a new dataset is required. For a new modelling the $\log K_{SC}$ parameter set for the Ca-IdP was slightly elevated (Table 12), to describe the experimental data at 0.06 M CaCl_2 correctly.

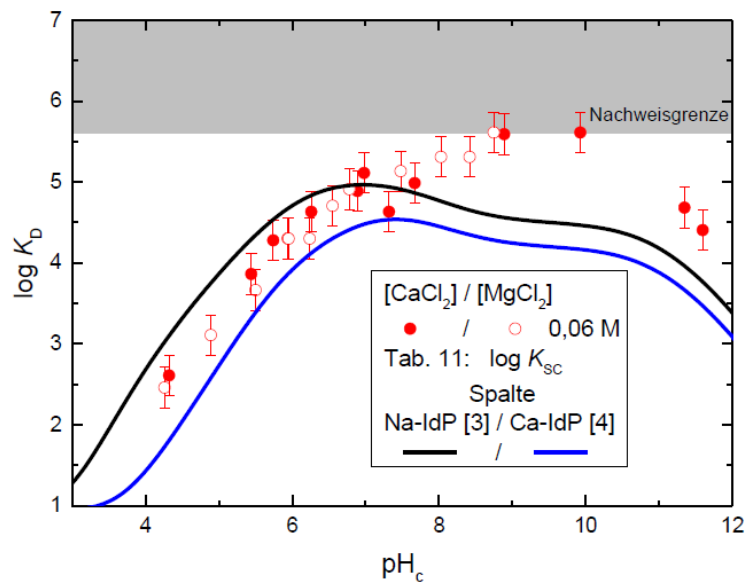


Figure 29: U(VI) sorption on IdP (S:L = 2 g/L) in 0.06 M Ca/MgCl_2 solution; comparison between experimental $\log K_D$ values (symbols) and calculation (curves) by the 2SPNE SC/CE model using the $\log K_{SC}$ for Na-IdP (black) and Ca-IdP (blue) from Table 12 (column 2 and 4).

Even at higher ionic strength the modified parameter set describes quite well the range around the edge. However, the decreasing sorption with increasing ionic strength at $\text{pH}_c > 8$ does not match with the experimental data, but not so distinct like in the Na system.

Table 12: Thermodynamic equilibrium parameters ($\log K_{SC}$) at infinite dilution to model U(VI) sorption on illite (IdP) with the 2SPNE SC/CE model (Bradbury and Baeyens, 2009b)

Surface complex [#] ($\log K_{SC}$)	Na-IdP	Na-IdP (p.w.)	Ca-IdP*	Ca-IdP (p.w.)
SSOUO ₂ ⁺	2,0	2,0	0,5 (Δ -1,5)	0,7
SSOUO ₂ (OH)	-3,5	-3,4	-4,3 (Δ -0,8)	-4,0
SSOUO ₂ (OH) ₂ ⁻	-10,6	-10,2	-10,9 (Δ -0,3)	-10,3
SSOUO ₂ (OH) ₃ ²⁻	-19,0	-18,5	-19,3 (Δ -0,3)	-18,2
SSOUO ₂ Cl(OH) ₂ ²⁻	-	-17,5	-	-17,5

*: the values accord to the analog $\Delta \log K_{SC}$ (values in parathesis) of Na-SWy to Ca-SWy in (Schnurr, 2015)

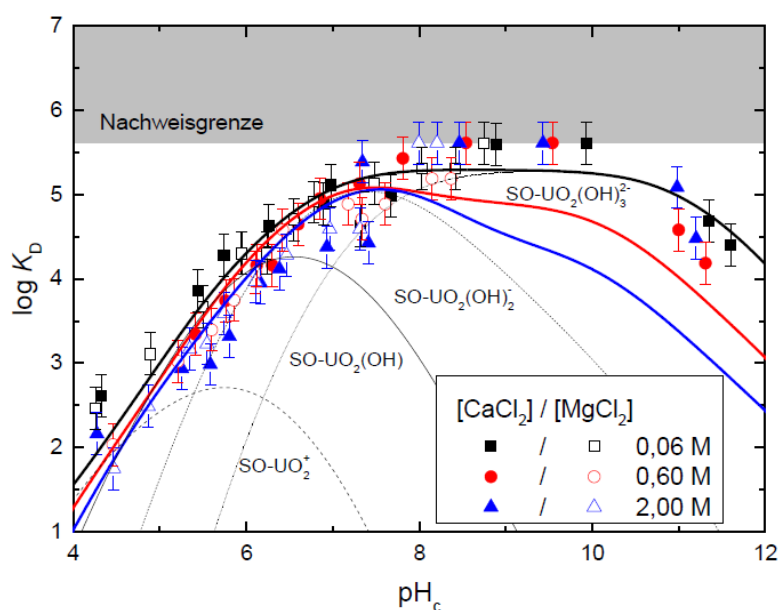


Figure 30: U(VI) sorption on IdP (S:L = 2 g/L) in Ca/MgCl₂ solution at various concentrations; comparison between experimental $\log K_D$ values (symbols) and calculation (curves) by the 2SPNE SC/CE model including sorption species distribution at 0.18 M salt concentration. The $\log K_{SC}$ used for the modelling is listed in Table 12 (column 5).

Figure 31 shows the modelling analog to the NaCl system by introducing a further inner sphere sorption species (SO-UO₂Cl(OH)₂²⁻). This species is regarded as one of several possible species in the CaCl₂ system. Especially in solutions with higher Ca²⁺ concentrations other species like SO-UO₂-Ca_xCl_y(OH)_z are also feasible. Also in presence of carbonate very stable Ca complex with UO₂ are described in the literature, like Ca-(UO₂)₂-CO₃-species (Dong and Brooks, 2006; Guillaumont et al., 2003). However, the addition of species that are definitely not characterized would over-parametrise the modelling and such species are neglected here. As shown in Figure 31, the experimental data are well described by regarding the new U(VI) surface species over the whole pH_c and ionic strength range.

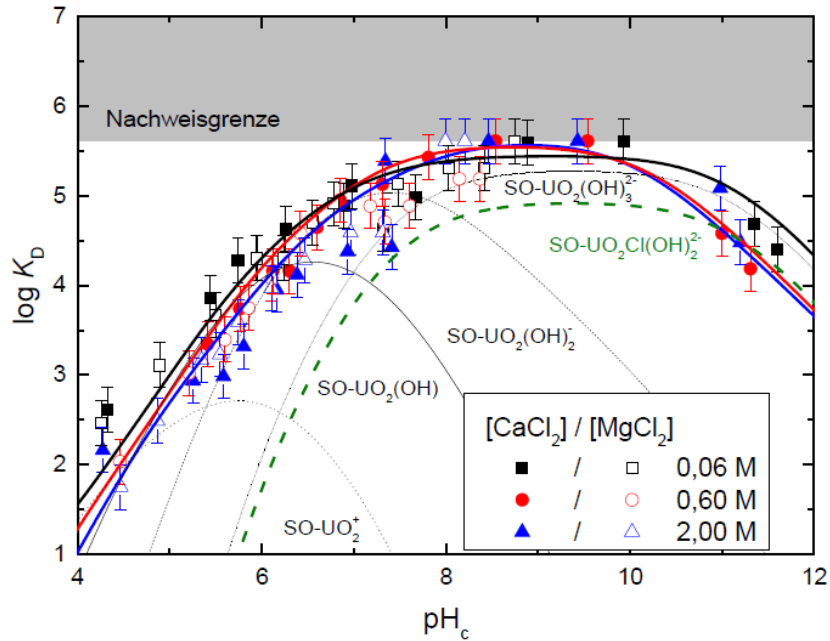


Figure 31: U(VI) sorption on IdP (S:L = 2 g/L) in Ca/MgCl₂ solution at various concentrations; Calculation of the sorption including the surface species SO-UO₂Cl(OH)₂²⁻ (green dashed curve). Modelling with the 2SPNE SC/CE model and log K_{SC} listed in Table 12 (column 5).

2.1.6 Conclusions

The U(VI) shows only a minimal cation exchange at lower pH_c values, which is not observable at higher pH_c values and inner-sphere complexation takes place. The 2SPNE SC/CE model can describe the experimental data at pH_c ≤ 7 for NaCl and pH_c ≤ 8 for the Ca/MgCl₂ system. At higher pH_c values (>8), the modelling predicts for the sorption an influence of the ionic strength that is not observed in the experiment. By introducing a additional possible surface species (SO-UO₂Cl(OH)₂²⁻), the experimental data are described quite well over the whole pH_c and ionic strength range. However, the existence of this species could definitely not confirmed in the present work and is one of the main task for future investigations.

2.2 Iron phases

Corrosion processes of final disposal container made of iron in contact with ground water transforms the iron into new iron phase. These secondary phases can interact with radionuclides and might immobilize them. In this work package first experiments with secondary products like Green Rust (GR) or magnetite (MAG) have been performed to get more insight into their behaviour with respect to the actinides. To keep the condi-

tions as simple as possible and to exclude redox reactions of the radionuclide of interest, the redox stable trivalent lanthanide neodymium and the trivalent actinide americium were probed. The GR and the MAG were synthesized in presence of both metal ions and the state of them in the matrix were characterized by XRD, XPS and SEM.

The results obtained for the green rust (GR) chloride synthesized in the presence of Nd(III) are presented first. The results obtained for GR and magnetite (MAG) prepared by direct precipitation in the presence of Am(III) are presented in the second section.

2.2.1 Green rust synthesized in the presence of Nd(III)

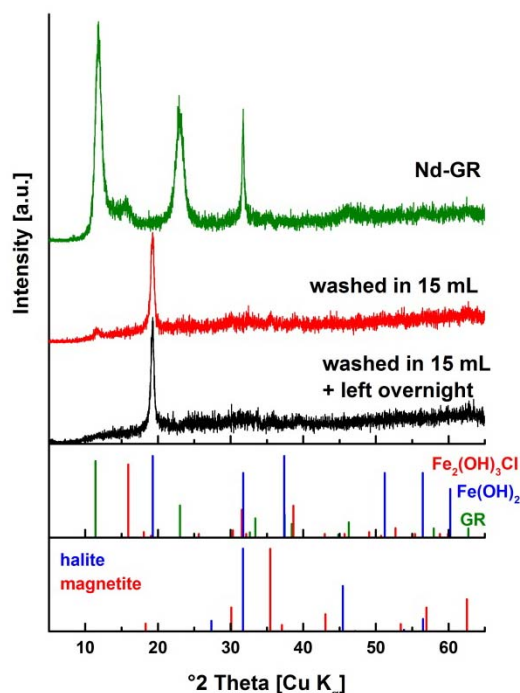


Figure 32: X-ray diffractogram of the sample Nd-GR and of the sample after different washing procedures, with comparison to the database.

Green rust was precipitated by addition of NaOH to a solution containing Fe(II), Fe(III) and trace amounts of Nd(III) ions (molar ratios Fe(II)/Fe(III) = 5/1 and $Fe_{tot}/Nd = 3000/1$, sample Nd-GR) under Ar (glove box). The pH (7.4(1)) and E_h (-535(20) mV vs Ag/AgCl) were recorded. The X-ray diffractogram indicated the formation of GR and minor amount of a by-product identified as $Fe_2(OH)_3Cl$, together with halite due to the high salt content (Figure 32). SEM micrographs revealed a layered structure, as expected for GR, and some aggregates that could possibly correspond to $Fe_2(OH)_3Cl$ (Figure 33). XPS was used to obtain information on the speciation of the elements. The position and the shape of the elemental line are governed by the immediate chemical environment. Data were collected at different positions on the sample: at the edge, at the center and at an intermediate position. The O 1s line indicated an increased oxide compo-

nent from the edge (~30 %) to the middle (~60 %) of the sample and at the same time, the proportion of Fe(III) increases concomitantly, based on the intensity of the Fe 2p satellite peak. This deprotonation of hydroxyl groups occurring simultaneously with an increase in ferric iron has already been reported (Mullet et al., 2008) and correspond to the ferrous iron oxidation within the GR structure. Obviously, the sample is not homogeneous, at least to a certain depth where information can be obtained by XPS (~3 nm). No Nd(III) could be detected. Finally, the sample was analyzed by Raman spectroscopy. Measurements were performed by placing the sample in a thin quartz cuvette closed with a septum screw cap. The detection of GR corroborates the XRD data, and magnetite was also detected by Raman but not by XRD. Magnetite is an oxidation product of GR: the best explanation is a diffusion of air into the cuvette followed by a wet oxidation. In contrast, XRD data were collected on dried sample where GR is less reactive toward oxygen.

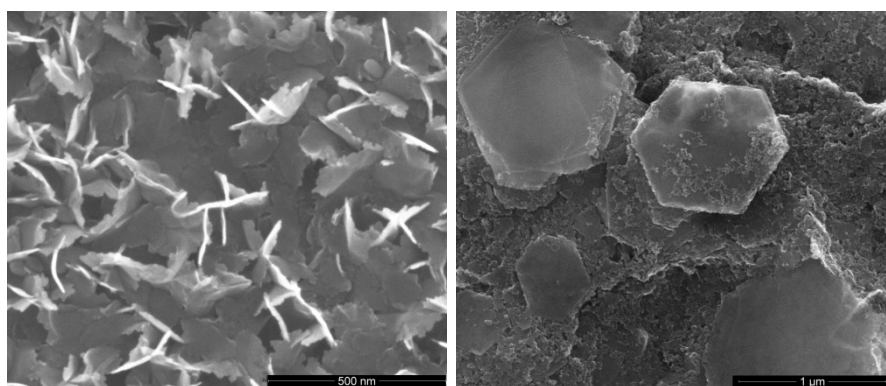


Figure 33: SEM micrographs of the sample Nd-GR before (left) and after (right) washing and aging overnight. Both samples exhibit a layered structure.

Part of this Nd-GR suspension (1.5 mL) was washed by centrifuging and replacing the supernatant by deoxygenated water (15 mL). The solid phase was analyzed by XRD shortly after this washing procedure and after additionally allowing to react overnight. No difference due to the longer reaction time could be detected. XRD data evidenced the formation of $\text{Fe}(\text{OH})_2$ (Figure 32), but no Fe(III)-bearing phase could be detected. However, a substantial part of the small particles exhibited magnetic properties, suggesting the formation of small sized magnetite particles. SEM revealed the presence of large hexagonal platelets, as for Nd-GR, together with fine grained particles (Figure 33). These aggregates represent a small fraction of the sample, possibly magnetite, but could not be detected/identified by XRD.

2.2.2 Green rust and magnetite synthesized in the presence of Am(III)

Green rust was precipitated in the presence of Am(III) following a procedure identical to that for Nd(III) (molar ratios $\text{Fe}(\text{II})/\text{Fe}(\text{III}) = 5/1$ and $\text{Fe}_{\text{tot}}/\text{Am} = 1500/1$, sample Am-GR). The final pH and E_h were, respectively, 7.3(1) and -486(20) mV vs Ag/AgCl. Separately, magnetite was precipitated in the presence of Am(III) by drop wise addition of a

Fe(II)/Fe(III) solution containing Am(III) (molar ratios Fe(II)/Fe(III) = 1/2 and $Fe_{tot}/Am = 1500/1$, sample Am-Magn) to a NaOH solution. Here, the final pH and E_h were, respectively, 12.3(1) and -685(20) mV vs Ag/AgCl. Only the sample Am-GR was analyzed by XRD: it contains green rust and the by-product $Fe_2(OH)_3Cl$, similarly to Nd-GR. SEM micrographs indicated that Am-GR exhibits a layered structure, as can be expected for GR compounds, and Am-Magn consists of aggregates of fine grained particles (10-20 nm).

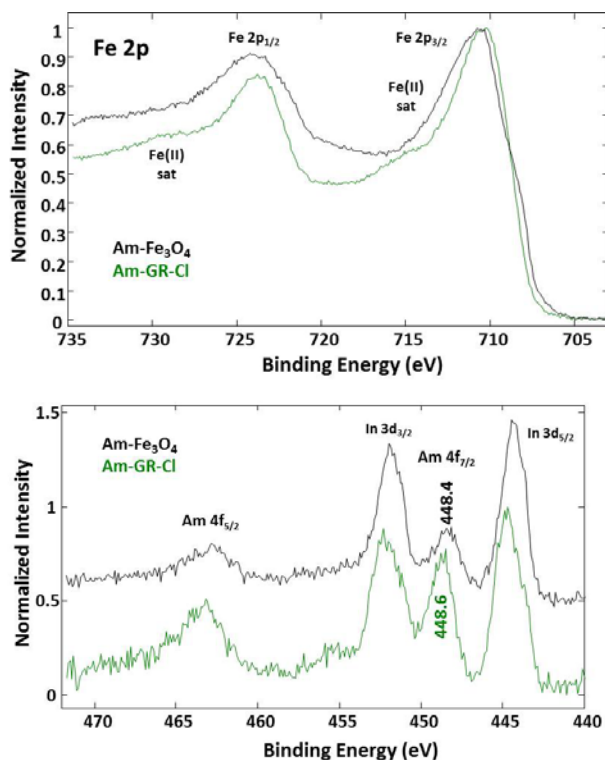


Figure 34: XPS Fe 2p (left) and Am 4f (right) spectra of the GR and magnetite containing Am(III). The indium line comes from the substrate

XPS data were collected for both samples. The Fe 2p narrow spectrum of Am-GR and Am-Magn (Figure 34) match with literature data (Huber et al., 2012; Mullet et al., 2008). The O 1s spectra indicate an equal proportion of oxide and hydroxide in Am-GR and a dominant oxide component in Am-Magn. Am-GR certainly underwent a partial oxidation similarly to Nd-GR. Despite the low content, Am(III) spectra could be recorded. The elemental line is within uncertainty located at similar energy in Am-GR and in Am-Magn, between that of the metal and that of the oxide (Gouder et al., 2005).

The samples were also analyzed by Raman spectroscopy: only magnetite could be detected in both samples. This is contradictory to the XRD and SEM data. No GR could be detected in Am-GR, meaning that the sample must have undergone a transformation. To prepare the Am-GR sample, part of the suspension was centrifuged and the supernatant removed. A small amount of water was used to dilute the wet paste and introduce the sample in the septum screw capped quartz cuvette. The sample Nd-GR was washed with a large amount of water and only $Fe(OH)_2$ could be detected by XRD: the

Am-GR sample preparation can thus not have led to the observed sample transformation. In contrast, it may rather be the diffusion of air in the cuvette followed by a wet oxidation. The same effect was observed for Nd-GR, but to a lesser extent. Part of the Am-GR suspension (1.5 mL) was washed with deoxygenated water (15 mL) similarly to Nd-GR and left in contact. This sample is not analyzed yet.

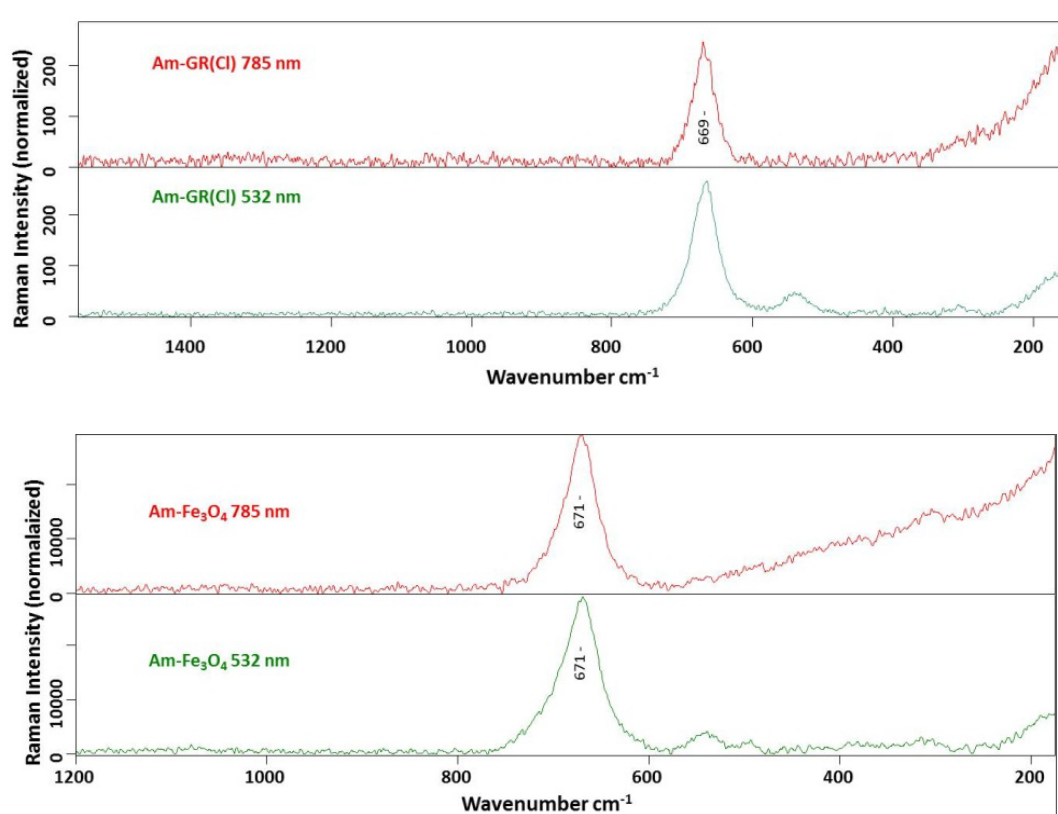
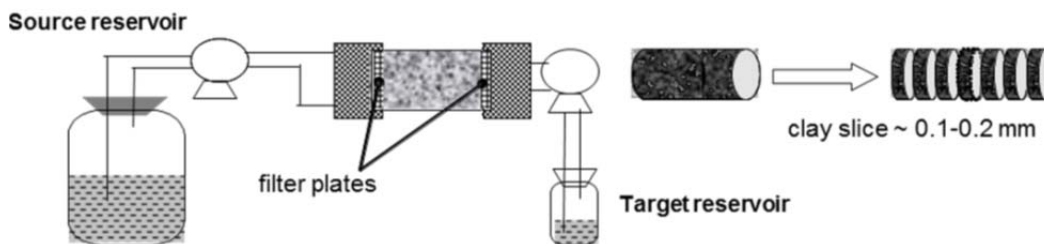


Figure 35: Raman spectra of Am-GR (top) and Am-Magn recorded at two wavelengths. Only magnetite is detected.

3 Diffusion of radionuclides in clay minerals

The main process responsible for possible transport of radionuclides in clay formations is molecular diffusion. Understanding the diffusion properties of radionuclides in clay formation is one key issue in performance assessment of repositories. Clay can be used as host rock or as buffer material to establish a repository. Natural clay rock possesses a heterogeneous composition and therefore heterogeneous diffusion properties. To ease the experiment, the diffusion of radionuclides was investigated with a single clay mineral. The illite was chosen as a main component of opalinus clay, like described in the sorption section. The non-swelling illite should exhibit only interparticle porosity and no intraparticle porosity.



Schematic illustration of the through-diffusion method

Illite de Puy used in this study was purified according to a procedure agreed on within the EC project CP CatClay (www.catclay.org). The diffusion (“in” and “through” diffusion) experiments with a compacted, cylindrical Na-illite sample (8.18 – 8.72 g, diameter = 2.54 cm, thickness = 1 cm, compaction factor = 1.61 g/cm³) were performed with

NaCl as background electrolyte. The experimental set-up (s. above) consists of a diffusion cell made of PEEK material or stainless steel.

3.1 Diffusion of Tritium and Chloride in Illite

Breakthrough curves for HTO and ^{36}Cl in 0.1 M NaCl, as well as the activity/concentration decrease in the source reservoir, are presented in Figure 36 a and b. The data are also representative for the higher ionic strength. For both tracers, a steady state (indicated by a constant flux) is achieved after ~ 3 days and remained more or less constant to the end of the experiment. In case of ^{36}Cl , the values for the diffusive flux are observed to scatter, which can be related to a low activity in the downstream solution. The results are presented in Table 13. It should be kept in mind, that the activity in the high-concentration reservoir decreased during the course of the experiment to $\sim 91\%$ of the initial concentration in case of HTO (the decrease in case of ^{36}Cl was only 2%). As constant boundary conditions were thus not fulfilled, the diffusion parameters calculated hereby may be inaccurate.

Table 13: Summary of D_e ($\text{m}^2 \text{s}^{-1}$) and α (-) values for HTO and ^{36}Cl in Na-illite at a bulk dry density (ρ_{db}) of $\sim 1700 \text{ kg m}^{-3}$ together with literature data ((Glaus et al., 2010), unpublished data from SCK-CEN and PSI).

Tracer	NaCl (M)	D_e ($\times 10^{-10}$) ($\text{m}^2 \text{s}^{-1}$)	α	Performed by
HTO	0.1	1.95 ± 0.04	0.53	This work
	0.5	1.97 ± 0.05	0.43	This work
^{36}Cl	0.1	0.67 ± 0.04	0.18	This work
	0.1	$0.28 \pm 0.03^{\text{a}}$	$0.12 \pm 0.03^{\text{a}}$	(Glaus et al., 2010)
	0.5	1.00 ± 0.05	0.25	This work
	0.5	$0.53 \pm 0.07^{\text{a}}$	$0.18 \pm 0.04^{\text{a}}$	(Glaus et al., 2010)

^a $\rho_{\text{db}} = 1900 \text{ kg m}^{-3}$

HTO diffusion coefficients and values for rock capacity factor α (Glaus et al., 2010) (or the porosity ε , respectively) are similar in 0.1 and 0.5 M NaCl, indicating that an increase in background electrolyte concentrations has no effect on the geometrical properties (tortuosity or constrictivity) on the compacted clay mineral. However, an increase in ionic strength affected the transport parameters in case of ^{36}Cl , where D_e and α are observed to be higher in 0.5 M NaCl. The lower D_e value for ^{36}Cl compared to HTO can be related to a reduced accessible pore space for anionic tracers (anion accessible porosity ε_{acc}), as anions are repelled from the vicinity of the negatively charged clay sur-

faces. On the other hand, the increase in D_e at higher ionic strength can be linked to an enhanced electrostatic shielding of this negative surface charge, increasing the fraction of anion accessible pore space (Glaus et al., 2010). In case of ^{36}Cl , available diffusion coefficients and α values in the literature are only reported for a higher bulk dry density (ρ_{db}) of $\sim 1900 \text{ kg m}^{-3}$

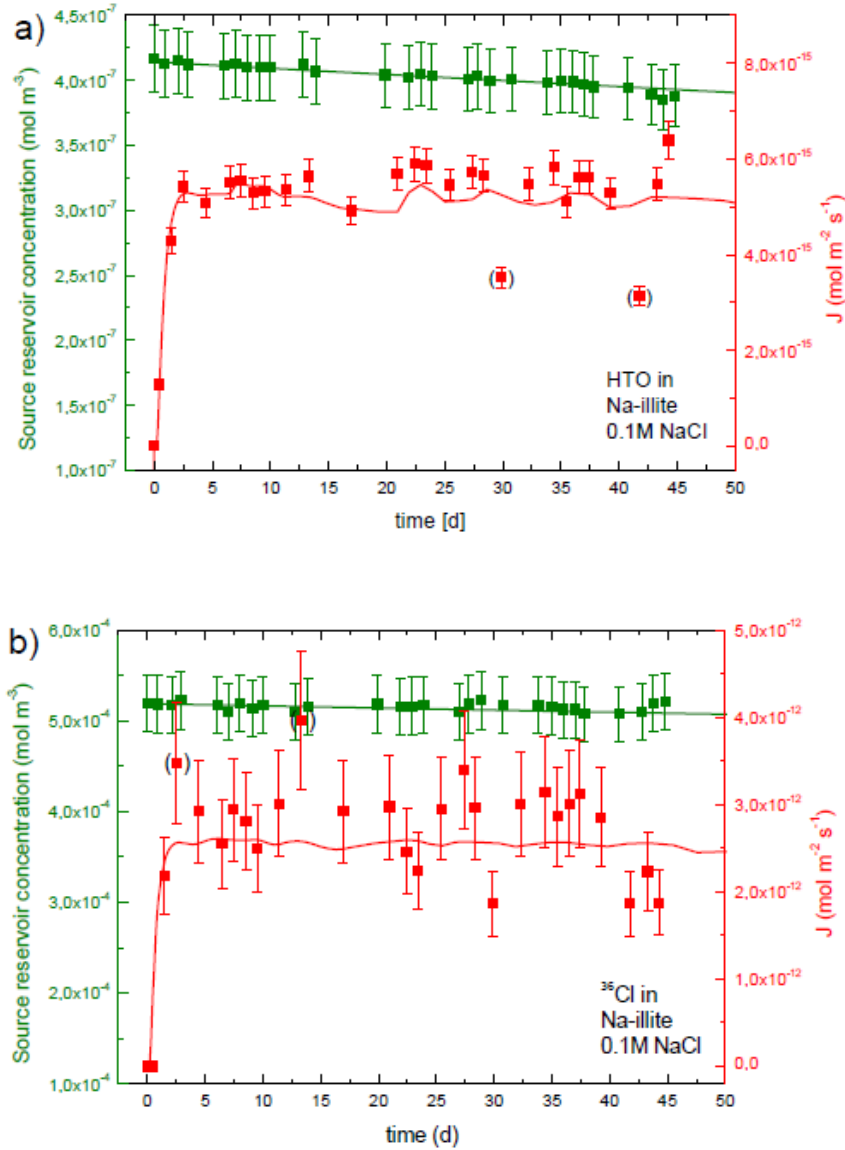


Figure 36: Diffusion of HTO (a) and ^{36}Cl (b) in compacted Na-illite ($\rho_{db} \sim 1700 \text{ kg m}^{-3}$) at pH 5.5 and 0.1 M NaCl as mass flux in the low concentration reservoir (J) and evolution of the source reservoir concentration.

Consequently, D_e and α are lower compared to the present set of experiments at $\rho_{db} \sim 1700 \text{ kg m}^{-3}$, but are also observed to increase with increasing background electrolyte concentration (Table 13).

3.2 Diffusion of Eu(III) in compacted illite

The experimental set-up comprises a diffusion cell made of PEEK material, a peristaltic pump and a reservoirs containing a Eu solution (Eu: 1E^{-6} M). The starting pH of the solutions was 5.3, but drifted to 6.4 during the experiment as no buffer was added. The solutions were circulated through the end plates with a total running time of 152 days (3650 hours).

The diffusion experiment result show a steadily decreasing Eu concentration for < 1500 h, reaching very low Eu(III) concentrations at the detection limit. This result indicates an almost complete Eu uptake onto the Na-illite mineral, which can be due to an increase of pH from 5.3 to 6.4. The Eu ions are not sorbed onto potential colloidal phases in the reservoirs, as the Eu concentration remained unchanged before and after phase separation by ultracentrifugation (90000 rpm for 1h).

After the in-diffusion experiment, the contact solution was exchanged by different methanol/water ratios followed by full methanol diffusion and consecutive LR white (epoxy resin) impregnation. As the analysis of the various alcohol/water mixtures and the epoxy resin revealed no mobilization of Eu during this preparation steps, this procedure opens a way for post-processing procedures (microstructure analysis including spatial resolved laser fluorescence studies).

The results of the in-diffusion experiments indicate a quantitative uptake of Eu onto Illite, which correlates with an increasing solution pH. In addition, an exchange of the electrolyte solution against an epoxy resin for impregnation purposes does not mobilize the tracer used, therefore being an appropriate way to preserve the illite microstructure, facilitating post-processing analysis.

3.3 Diffusion of Np(V)

The diffusion of Np(V) in compacted Na-illite at $\text{pCO}_2 = -3.5$ (atmospheric conditions) in 0.1 M NaCl is investigated by through-diffusion technique. Two experiments (NP1 and NP2) have been performed: 1. for the first experiment a diffusion cell with stainless steel filters at the in- and outlet was used; 2. for the second experiment a diffusion cell with PEEK supporting plates and filter membranes was applied instead of steel. A schematic illustration of the setup is given in Figure 37.

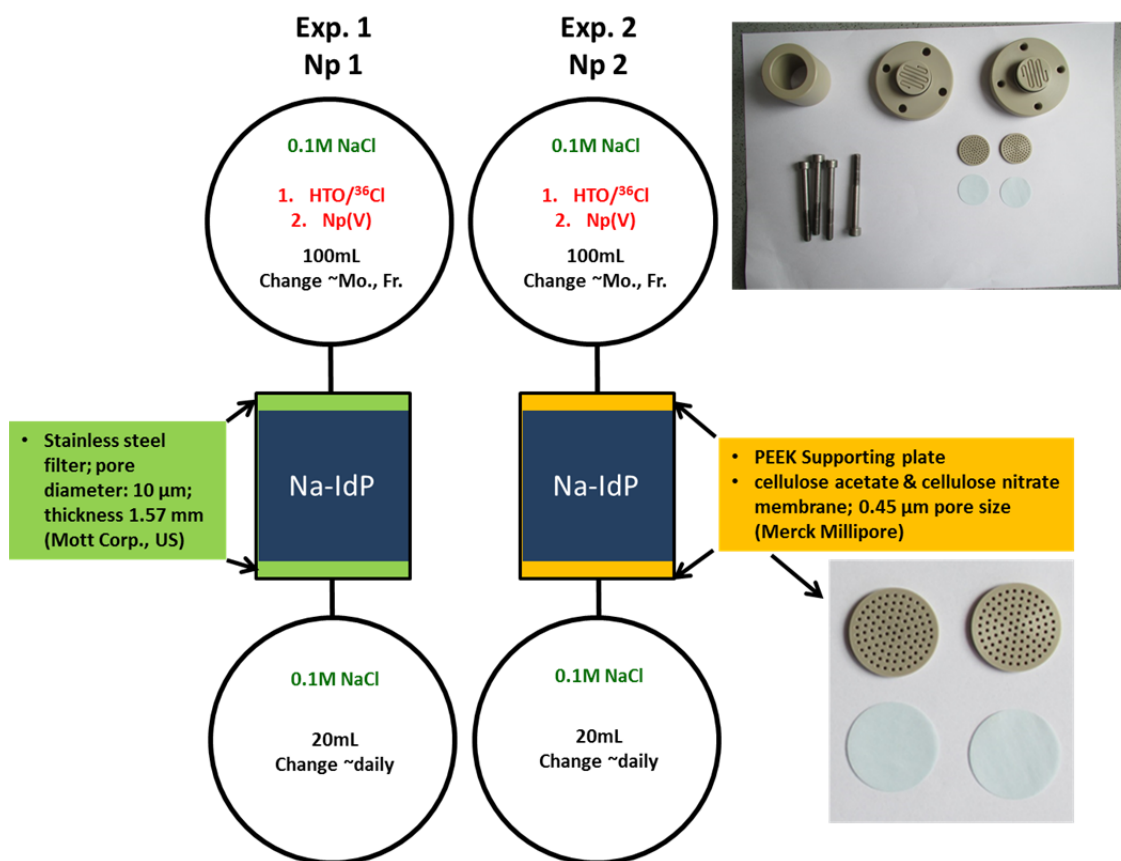


Figure 37: Schematic illustration of the two Np diffusion experiments NP1 and NP2.

The pH of the solution was pH 4.6 in experiment 1 (NP1) and pH 4.8 in experiment 2 (NP2). The Na-illite was compacted to an illite core with a bulk dry density of $\sim 1600 \text{ kg m}^{-3}$. In NP1, the core was sandwiched between stainless steel filters (Stainless steel: 316L, pore diameter: 10 mm, diameter = 0.0254 m, thickness = 0.0016 m; MOTT industrial division, Farmington, USA) and closed with two end-pieces. In NP2, a PEEK supporting plate with cellulose acetate and nitrate filters (0.45 μm pore size, Merck Millipore) was used. The samples were pre-equilibrated with 0.1 M NaCl solutions from both sides. After one month the solutions were replaced against new ones. The solution in one reservoir was spiked with $1.6 \times 10^{-5} \text{ M } ^{237}\text{Np}$ ($\sim 100 \text{ Bq cm}^{-3} \text{ V} = 100 \text{ mL}$), while the other one contained the background electrolyte solely ($\text{V} = 20 \text{ mL}$), representing the high (HCR)- and low-concentration (LCR) reservoir, respectively. The solution in the LCR is replaced daily, in order to keep the concentration of the tracer in this reservoir as low as possible (Van Loon et al. 2003). Samples from the HCR are being taken periodically (every 2-3 days). The activities in both reservoirs are measured by liquid scintillation counting (TRICARB 3110TR, Perkin-Elmer).

The results of the diffusion experiments are shown in Figure 38. It is obvious, that a difference exist between experiment NP1 and NP2. A plausible explanation could not be found, but might be related to sorption phenomena and texture of the filter material.

A breakthrough was observed after 100 days. Unfortunately, both experiments have not achieved a steady state. After reaching a maximum, the diffusive flux decreased and this behavior cannot be explained at the moment. Maybe neptunium could not reach the low concentration reservoir because of blocked tubings. The Np(V) experiment could not be completed within the project term, but it will be further examined in the frame of subsequent projects. As next steps, the clay cores must be characterized by HTO diffusion, and then, after stopping the experiment, post-mortem analysis of the cores must be performed by autoradiography, spectroscopic methods, and abrasive peeling. Additionally, modeling of the experiments can help to interpret the diffusion behavior of Np(V) in illite.

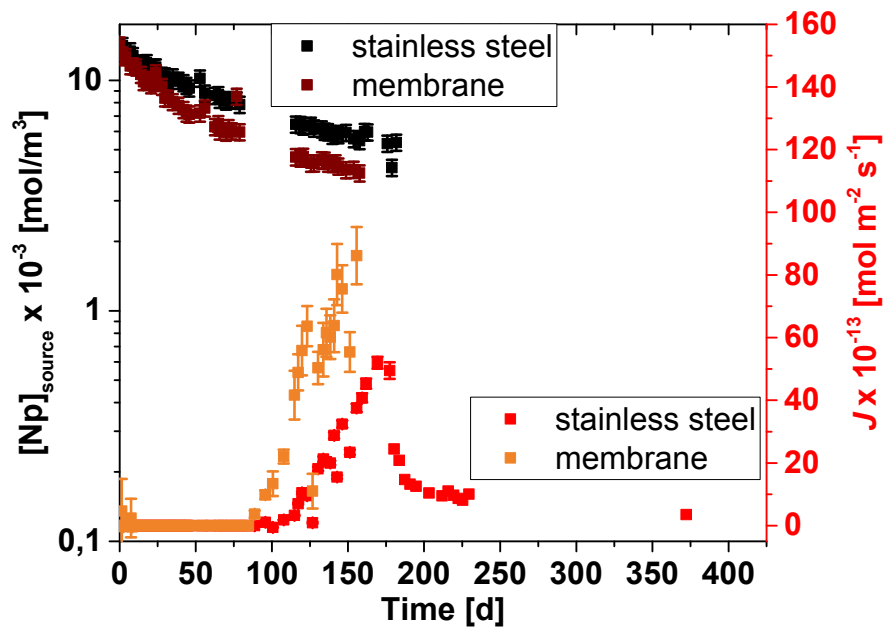


Figure 38: Np flux and break through cumulated activity of experiment Np1 (stainless steel filter, black and red points) and Np2 (peek supporting plate plus filter membrane, dark and light brown points) as a function of time.

3.4 Diffusion of fulvic acid in Illite

Natural clay stone very often contains organic fractions (dissolve organic matter, DOM) of various composition from small low molecular weight molecules up to large polyelectrolytes with colloidal behavior. The colloidal organics can complex radionuclides very strong and might facilitate radionuclide migration as DOM nanoparticle borne transport. Whether such colloid organics can migrate via diffusion processes through a compacted clay like illite is one key question for performance assessment. The diffusive transport in these systems was observed to be higher for cations and lower for anions, compared to neutral species. While the reduced mass transport for anionic tracers is generally explained by a reduced accessibility of the total pore space due to a repulsive interaction of the equally charged surfaces and solutes (anion exclusion effect), the reason for the enhanced transport of cationic species (surface diffusion) is under inten-

sive discussion. Here, the experiment should show, whether tritiated fulvic acid ($^3\text{T-FA}$), as an analogue for DOM, has diffusive properties in compacted Na-illite.

Na-illite with the same properties like in the Eu and Np experiment was used in this study. In contrast to the metal cation experiments, the volume on the low concentration side was increased to 500 mL and the container was not replaced regularly. The experiments were performed at two ionic strengths (0.1 and 1 M NaCl), while the pH was fixed at 5 with an organic buffer (5×10^{-3} M MES). Samples were taken in regular intervals and the activities in both compartments were determined by liquid scintillation counting. The experimental results are illustrated in Figure 39.

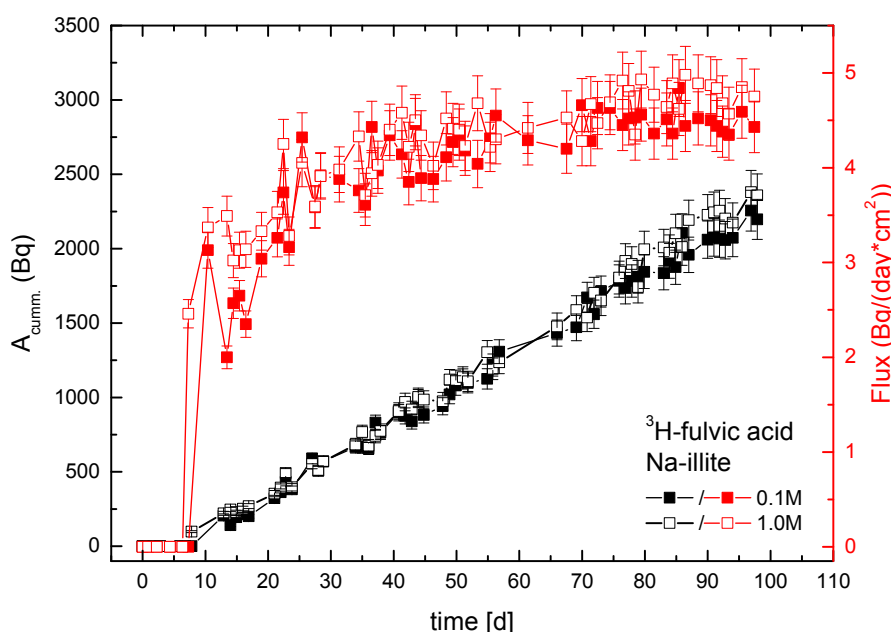


Figure 39: Diffusion of fulvic acid (FA) in compacted Na-illite at pH 5 and NaCl as back electrolyte: cumulated activity of $^3\text{H-FA}$ in LCR and flux of FA as a function of time.

During the experimental time the activity in the low concentration reservoir increased gradually, with a steady state (constant flux) observed after ~ 70 d. Due to the fact, that the decrease in activity in the high concentration compartment as well as the increase in the low concentration reservoir exceeded 1% of the initial concentration on the high concentration side, the boundary conditions used in the analytical solution are not fulfilled and the diffusion coefficient (D_e) as well as the rock capacity factor (α) can only be estimated by linear regression analysis. Taking these uncertainties into account, diffusion coefficients of $D_e = 1.51 \times 10^{-11} \text{ m}^2/\text{s}$ and $1.70 \times 10^{-11} \text{ m}^2/\text{s}$ can be calculated for 0.1 and 1.0 M NaCl, respectively. For α , the calculated values were -0.44 and 0.61 (0.1 and 1.0 M NaCl, respectively). The diffusion coefficients for FA are comparable to D_e values determined for negatively charged traces (i.e. $^{36}\text{Cl}^-$). However, these values should be

taken with care (and seems to be unrealistic for the rock capacity factors). More reliable data for D_e and α can be obtained by fitting the data in numerical (2-D) simulations, which will be applied in the future.

3.5 Conclusions

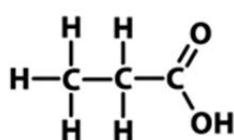
The diffusion of non and weak absorbing ions can be described quite well and the results from different studies show a good match. However, the experiments with strong absorbing metal cations, fulvic acid, as well as with redox sensitive metal ions exhibits some experimental difficulties. The boundary conditions for an unambiguous evaluation are mostly not given. Hence, the results have large uncertainties und are sometimes inconsistent. On these grounds well designed experiments shall be performed in future projects to give more insight into the diffusion of strong absorbing ions.

4 Clay organic compounds, fulvic and humic acid: interactions with radionuclides

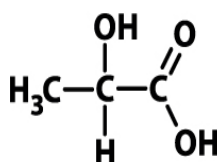
Natural clay rock formations, considered as a potential host rock for nuclear waste disposal, can contain a significant amount of organic matter. This organic matter can be low molecular organic (LMWO) (Courdouan et al., 2007a), as well as fulvic acid-like organic compounds (Schäfer et al., 2003). Additionally, humic acids were also included as a significant component of ground waters found in the cover deposits of salt rock formations and the Jurassic and lower Cretaceous clay rock layers in Northern Germany. To what extent these organic components might have an impact on the geochemical behavior of selected actinides is the aspect of the following chapter.

4.1 Investigation of the Np(V) propionate and lactate complex formation.

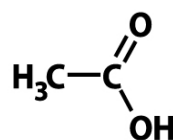
Low molecular weight organics (LMWO; e.g. acetate, propionate, lactate) might significantly impact the speciation and mobility of radionuclides in aqueous media. There are less thermodynamic data reported for the complexation of pentavalent actinides with LMWO, especially under elevated temperature conditions, relevant for assessing the long-term safety of disposal options for heat-producing high-level nuclear waste. The complexation of pentavalent neptunium aquo ion with propionate and lactate was studied by absorption spectroscopy, EXAFS, and with solvent extraction. The structural formula of propionic acid, lactic acid, and acetic acid for comparison reasons are given here:



Propionic acid



Lactic acid



Acetic acid

The complexation of Np(V) with the propionate ligand has not been studied so far, and hence, neither complex formation constants are available. The lactate complexation of Np(V) were described in a few studies using extraction methods and absorption spectroscopy. Most of the works give only conditional complex formation constants at various ionic strengths and only at room temperatures. A complex formation constant at ionic strength zero is only given in one publication. The Pitzer formalism was used to extrapolate to $I = 0$. An overview of the available complex formation constants of Np(V) lactate complexation is given in Table 17.

4.1.1 Spectroscopic study of the Np(V) propionate complex formation

In the present chapter, the complexation of Np(V) with propionate by using absorption spectroscopic is described. In the experiments the impact of ionic strength, ligand concentration and temperature was probed. The results are published in (Vasiliev et al., 2015).

The concentration of Np(V) was held between 2×10^{-5} and 6×10^{-5} M for UV-Vis/NIR experiments. Samples were usually equilibrated for 1–2 days prior to the measurement. Complexation of Np(V) with propionate in NaCl solution was studied by two independent series of measurements. A first set of samples was prepared at different NaCl concentrations ($I = 0.5\text{--}4.0$ M) with total propionate concentration ($[\text{Prop}]_{\text{tot}}$) being varied from 0.03 to 0.1 M to determine the ionic strength dependence of Np(V)-propionate complexation at room temperature. The ionic strength was adjusted with solid NaCl and the pH_c was adjusted to 5 with aliquots of 0.01 M HCl. A second set of samples was prepared at a constant $I = 0.5$ M, $[\text{Prop}]_{\text{tot}}$ varying from 0.03 to 0.1 M and T varying from 20 to 85 °C using a constant temperature circulator (Thermo Haake DL30-W45/BOpen-Bath, Germany) to determine the temperature dependence of Np(V)-propionate complexation. pH_c was adjusted to 5 at room temperature, before raising T . In addition, two experimental series at various $[\text{Prop}]_{\text{tot}}$ with $I = 0.5$ M, $T = 23$ and 85 °C were prepared at pH_c = 7 to confirm the results obtained at pH_c = 5. For pH measurements at $I > 0.1$ m, an empirical correction term was applied to correct the measured operational pH-values (pH_{exp}) to thermodynamically well-defined quantities (Vasiliev et al., 2015).

For EXAFS measurements, the samples were prepared at four different NaCl concentrations (from 0.5 to 4.37 m) with a constant propionate concentrations of 0.48 M and constant Np(V) concentration of 7.7×10^{-4} mol L⁻¹ (pH_c = 5.5–5.1).

pH measurements

The measurements of operational pH values were performed with an Orion 2 Star Benchtop pH meter using an Orion 8103SC combination pH electrode. Commercial pH Titrisol buffer concentrates (Merck p.a.) were used to calibrate the setup at room temperature. For pH measurements at $I > 0.1$ m NaCl, an empirical correction term was applied for the measured operational pH-values (pH_{exp}) to obtain thermodynamically well-defined quantities. An empirical correction coefficient (A) that depends on background electrolyte composition and concentration and that has been accurately determined in our laboratories for aqueous NaCl systems and at room temperature (Altmaier et al., 2003a) was used to correct the operational pH_{exp} values according to equations

$$\text{pH}_c = \text{pH}_{\text{exp}} + A_{\text{NaCl}}$$

and

$$A_{\text{NaCl}} = 0.0013 (m_{\text{NaCl}})^2 + 0.1715 m_{\text{NaCl}} - 0.0988$$

where m_{NaCl} is the molality of the background electrolyte. The pHc is a measurement of the molality of the proton ($-\log [H^+]$) and is only made here at room temperature.

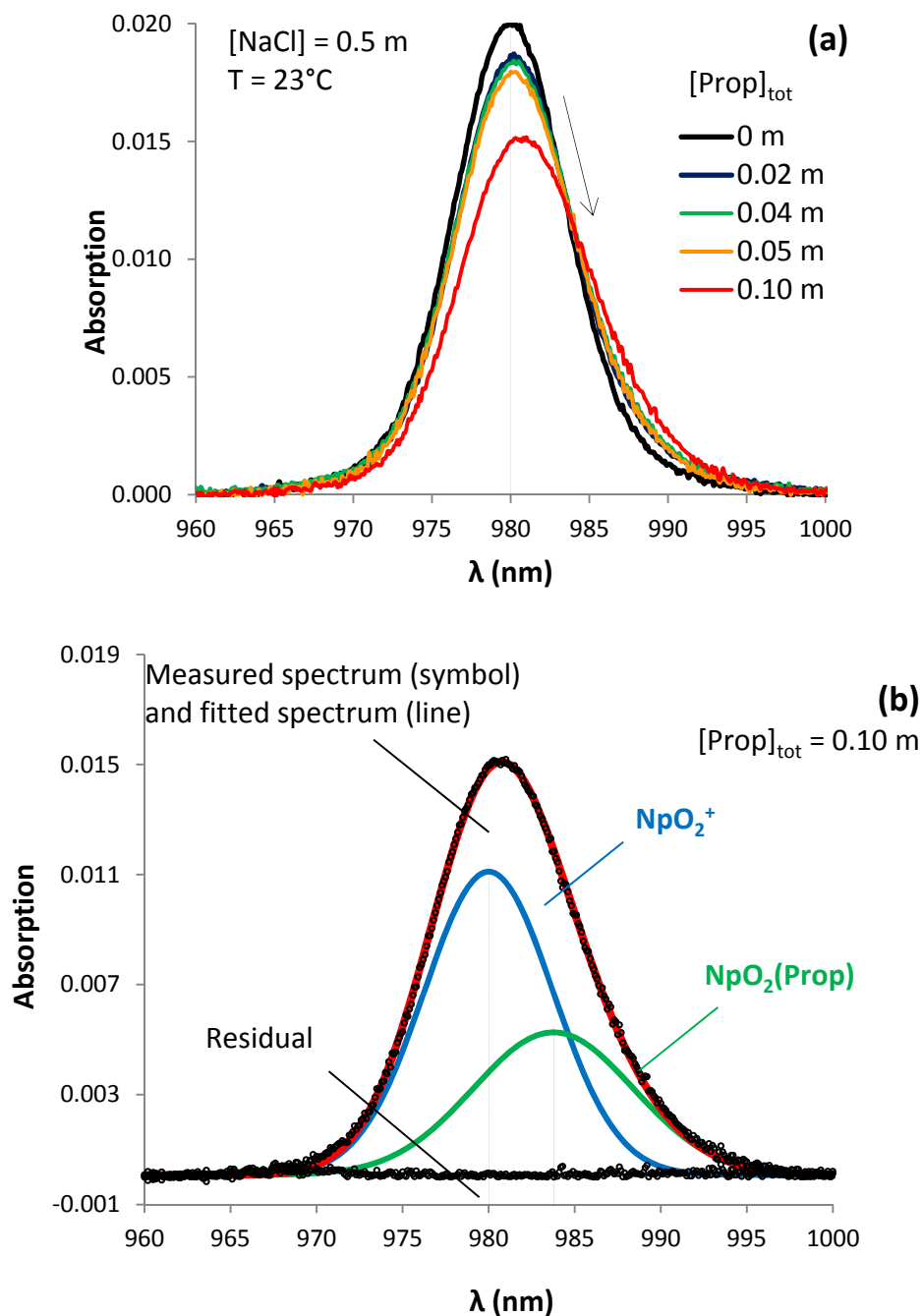


Figure 40: (a) Np(V) absorption spectra for various propionate concentrations (0–0.1 M) at $[Np(V)]_{\text{tot}} = 5.94 \times 10^{-5} \text{ M}$, $I = 0.51 \text{ m}$; $T = 23 \text{ }^\circ\text{C}$. (b) Example of a deconvoluted spectrum ($[Prop] = 0.1 \text{ m}$; $I = 0.51 \text{ m}$; $\text{pHc} = 5.0$, $T = 23 \text{ }^\circ\text{C}$.)

Results and Discussion

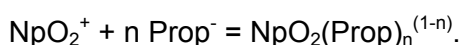
Figure 40a - the absorption spectra of Np(V) in the presence of propionate in [NaCl] = 0.51 m for T = 23 °C and pHc = 5 – exemplarily shows the spectrophotometric results of the Np(V)-propionate complex formation in [NaCl] solution and at T = 23 °C. Generally, as the concentration of propionate increases, the intensity of the absorption band of free NpO_2^+ at 980 nm decreases and the maximum of the absorption band is shifting to higher wavelengths. This is an indication that the NpO_2^+ ion is complexed by forming a new absorption band at higher wavelengths caused by the Np(V) propionate complex. Peak deconvolution of the spectra allows the determination of a single complex, as shown in Figure 40 for one spectrum. According to the peak deconvolution performed within the present study, the absorption band of the Np(V)-propionate complex has its maximum at ~984 nm, similar to the 1:1 Np(V) acetate complex (Pokrovsky and Choppin, 1997; Seibert et al., 2001). The absorption spectra shows very similar changes with increasing propionate concentration at different temperature while keeping I constant.

Effect of ligand concentration

The experimental data are plotted in Figure 41 according to the following equation for three different titration series:

$$\log \frac{[\text{NpO}_2(\text{Prop})_n^{(1-n)}]}{[\text{NpO}_2^+]} = \log \beta + n \times \log [\text{Prop}^-]_{\text{eq}}$$

consistent with the following reaction:



Results for T = 23 °C and 85 °C are faced (both in [NaCl] = 0.51 m solution) to show the effect of temperature on the complexation reaction. A comparison of the results at [NaCl] = 0.5 m and 3.20 m at T = 23 °C demonstrates the effect of ionic strength. The slopes ($n = 1.05 \pm 0.05$ at 23 °C; 0.99 ± 0.11 at 85 °C; 1.04 ± 0.15 for I = 3.2 m) confirm the formation of an 1:1 NpO_2 -propionate complex. The y-intercept, $\log \beta$, is determined as 1.04 ± 0.06 at 23 °C and increases with temperature (1.36 ± 0.13 at 85 °C) and with ionic strength (1.34 ± 0.15 at 3.2 m). The same stoichiometry is found at ionic strengths varying from 0.51 to 3.2 m (constant T, pHc = 5 and 7) or varying T from 20 to 85 °C (constant I, pHc = 5 and 7).

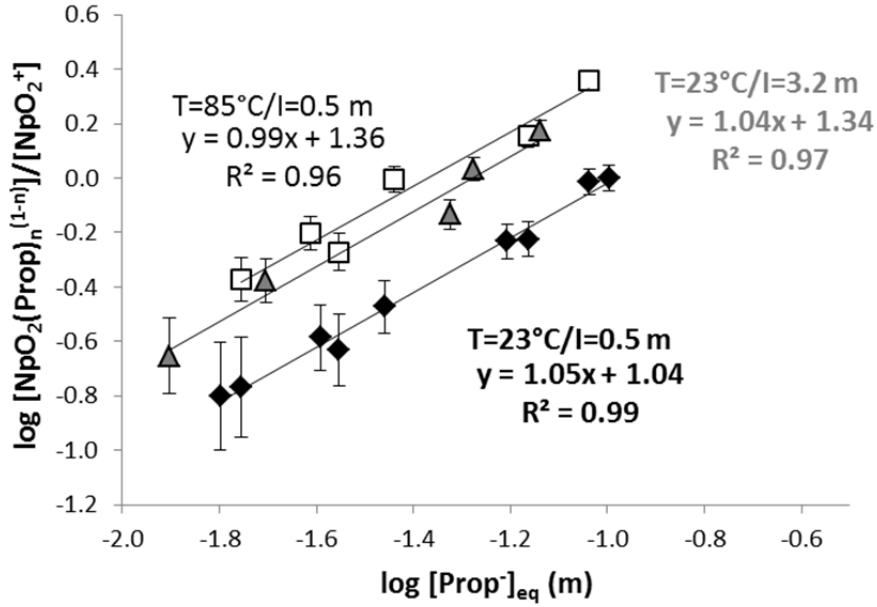


Figure 41: Slope analysis of the Np(V) propionate complex formed at 23 and 85 °C for [NaCl] = 0.51 m, and 23 °C for [NaCl] = 3.2 m. Slopes ≈ 1 (1.05 ± 0.05 and 0.99 ± 0.11 for both T, respectively, 1.04 ± 0.15 for $I = 3.2$ m) indicate the formation of the 1:1 complex. Log β (conditional) increases both with the temperature and the ionic strength (from 1.04 ± 0.06 to 1.36 ± 0.13).

Effect of ionic strength

This procedure allows evaluation of equilibrium constants (β_0) at infinite dilution:

$$\beta_0 = \beta \times \frac{\gamma(\text{NpO}_2\text{L})}{\gamma(\text{NpO}_2^+) \cdot \gamma(\text{L}^-)}$$

In SIT, activity coefficients can be expressed as:

$$\begin{aligned} \log \gamma_i &= -z^2 \frac{A(T)\sqrt{I}}{1+1.5\sqrt{I}} + \sum_k \varepsilon(i,k) \cdot m_k \\ &= -z^2 D + \sum_k \varepsilon(i,k) \cdot m_k \end{aligned}$$

where m_k is the molality of the aqueous species k ; $\varepsilon(i,k)$ is the specific ion interaction coefficient between species i and k ; D is the Debye-Hückel term; $A(T)$ is the limiting Debye-Hückel equation slope, that depends on temperature:

$$A(T) = e^3 \sqrt{\frac{2\pi N\rho}{100(K\varepsilon_d T)^3}}$$

where N is the Avogadro number, e stands for absolute electronic charge, ϵ_d is here the dielectric constant of water at the given temperature, ρ is the pure water density, k is the Boltzman constant, and T is temperature (K).

By systematically varying the NaCl background electrolyte concentration at constant T and applying an appropriate model for activity coefficients (γ) it is possible to extrapolate the conditional equilibrium constants β to the standard equilibrium constant (β_0) at zero ionic strength.

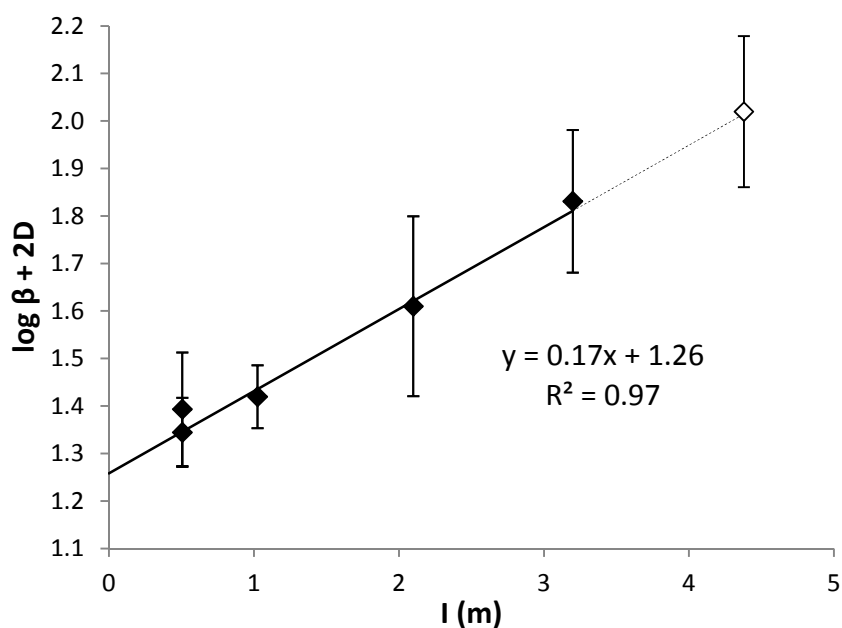


Figure 42: SIT plot of the equilibrium reaction $\text{NpO}_2^+ + \text{Prop}^- \rightleftharpoons \text{NpO}_2(\text{Prop})$ in NaCl, yielding $\log \beta_0 = 1.26 \pm 0.03$. The white symbol ($[\text{NaCl}] = 4.37 \text{ m}$) shows data outside the recommended applicability of the SIT (data not used in the regression). The dotted line shows the extrapolation of the results obtained for lower I to 4.37 m.

This was done with the equation

$$\text{Log } \beta - \Delta Z^2 \times D = \text{log } \beta_0 - \Delta \epsilon \times I$$

where $\Delta Z^2 = \sum Z^2(\text{products}) - \sum Z^2(\text{adducts}) = -2$ for the formation reaction above, and $\Delta \epsilon = \epsilon(\text{Na}^+ + \text{Cl}^-; \text{NpO}_2(\text{Prop})) - \epsilon(\text{Na}^+; \text{Prop}^-) - \epsilon(\text{Cl}^-; \text{NpO}_2^+)$.

Experimental data are plotted according to the equation as $\log \beta + 2D$ versus I in Figure 42, resulting in a linear relationship as expected. From the slope, $\Delta \epsilon$ is obtained as -0.17 ± 0.03 and the y-intercept ($\log \beta_0$) equals to 1.26 ± 0.03 . $\log \beta_0$ and $\Delta \epsilon$ are in agreement with previously determined values for NpO_2 -acetate complexation at 25 °C.²⁵ Using $\epsilon(\text{Cl}^-; \text{NpO}_2^+) = 0.09 \pm 0.05$ and assuming $\epsilon(\text{Na}^+; \text{Prop}^-) = 0.08 \pm 0.01$ by analogy with acetate, $\epsilon(\text{Na}^+ + \text{Cl}^-; \text{NpO}_2(\text{Prop}))$ would not be significantly different from

zero, which is expected for a non-charged species in accordance with SIT. Note that we have investigated Np(V)-propionate complexation up to 4.37 m, which is outside the recommended validity range of SIT. Therefore, these data are not used for the regression as indicated by the dotted lines in Figure 42. However, in this case it is obvious that the SIT approach remains applicable even above its usually accepted applicability limit.

Effect of temperature

The temperature effect on the NpO₂⁺ complexation by propionate was investigated between 20 and 85 °C, for [NaCl] = 0.51 m at pH_c = 5 and 7. Log β(T) is corrected to I = 0 for each temperature by applying the SIT as described in the previous section to obtain log β₀(T). As a first approach, heat capacity was hypothesized to be zero as observed, for instance, in recent Cm(III) propionate/acetate and uranyl acetate complexation studies (Fröhlich et al., 2013; Fröhlich et al., 2014; Sladkov, 2014). I.e. the molal standard reaction enthalpy Δ_rH_m⁰ and entropy Δ_rS_m⁰ do not vary with temperature between 20 and 85 °C. Following this simplification, Δ_rH_m⁰ and Δ_rS_m⁰ can be obtained from an Arrhenius plot on the basis of the van't Hoff equation

$$\log \beta_0(T) = -\frac{\Delta_r H_m^0}{RT \ln(10)} + \frac{\Delta_r S_m^0}{R \ln(10)}$$

where R is the ideal gas constant. Figure 43 shows the plot of log β₀(T) versus 1/T.

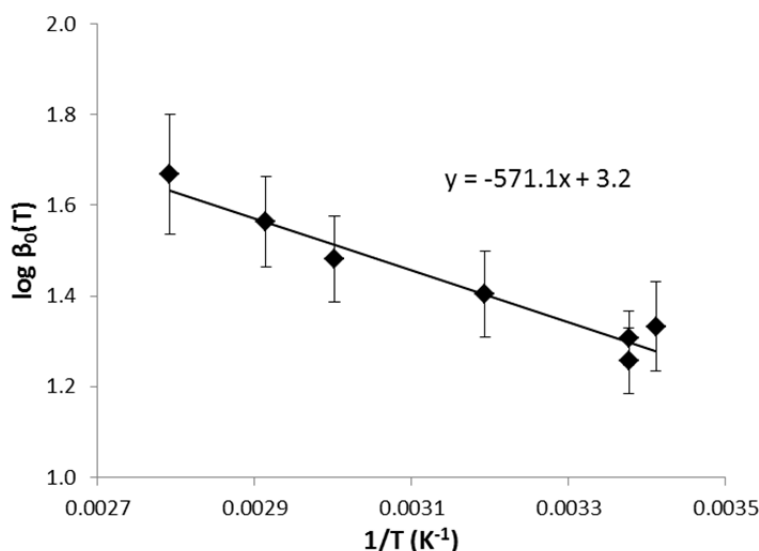


Figure 43: Np(V)-propionate complexation constant extrapolated to zero ionic strength (log β₀) versus the reciprocal of the temperature (K⁻¹).

The NpO₂(Prop) complex formation reaction significantly increases over about half an order of magnitude when increasing the temperature from 20 °C to 80 °C. A linear relationship is observed, confirming the initial hypothesis of zero heat capacity. Δ_rH_m⁰ and

$\Delta_r S_m^0$ are calculated as $10.9 \pm 1.2 \text{ kJ mol}^{-1}$ and $62 \pm 4 \text{ J mol}^{-1} \text{ K}^{-1}$, respectively. Both values are positive, showing that the formation of the $\text{NpO}_2(\text{Prop})$ complex is endothermic and entropy driven. Positive $\Delta_r H_m^0$ and $\Delta_r S_m^0$ are likely due to dehydration effects of NpO_2^+ and Prop^- ions.

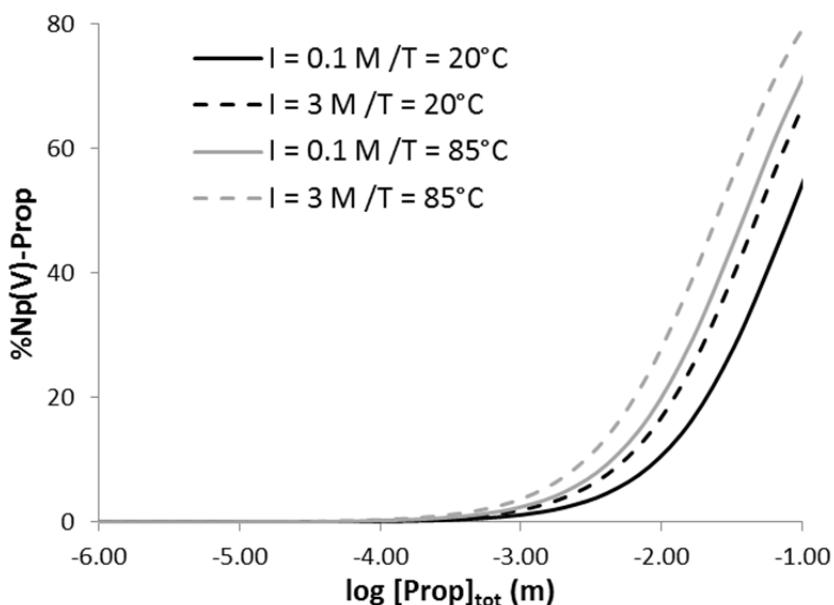


Figure 44: Calculated percentage of the Np(V)-propionate complex ($[\text{Np(V)}]_{\text{tot}} = 10^{-10} \text{ m}$) versus $\log[\text{Prop}]_{\text{tot}}$ for $\text{pHc} = 7$ and $I = 0.1$ or 3 m and $T = 20$ or $85 \text{ }^\circ\text{C}$ using thermodynamic parameters determined in this study.

Np(V)-propionate complexation at environmentally relevant propionate concentrations. Simulations are made for $\text{pHc} = 7$, with 0.1 and 3 m NaCl and $T = 20$ and $85 \text{ }^\circ\text{C}$ using the presently obtained Np(V)-propionate complexation parameters in order to test the impact of propionate on Np speciation under more environmentally relevant conditions than the present laboratory study. The percentage of Np(V), in aqueous solutions at $\text{pHc} = 7$ present as the NpO_2^+ cation, complexed to propionate versus $\log[\text{Prop}]_{\text{tot}}$ is shown in Figure 44 ($[\text{Np(V)}]_{\text{tot}} = 10^{-10} \text{ m}$). Although Np(V)-propionate complexation increases with I between 0.1 and 3 m for a given T , or with T between 20 and $85 \text{ }^\circ\text{C}$ for a given I , propionate remains a relatively weak ligand for Np(V) under these conditions: only 1 – 5% of Np(V) is bound to propionate for $[\text{Prop}]_{\text{tot}} = 10^{-3} \text{ m}$. In natural clay rocks porewater (e.g. OPA/COx), where propionate is present at lower concentration ($127 \text{ } \mu\text{M}$, (Courdouan et al., 2007a; Courdouan et al., 2007b)) and where Np(V) is in competition with other cations, propionate complexation is expected to have a minor impact on Np(V) speciation.

The present study shows that the stability constant for the formation of the $1:1 \text{ NpO}_2^+$ -propionate complex, with $\log \beta^0(25 \text{ }^\circ\text{C}) = 1.26 \pm 0.03$, increases both with the ionic strength ($0.5 < \text{NaCl} < 4.37 \text{ m}$) and temperature ($20 < T < 85 \text{ }^\circ\text{C}$). The complex formation reaction is endothermic and entropy driven, as evidenced by $\Delta_r H_m^0 = 10.9 \pm 1.2 \text{ kJ mol}^{-1}$ and $\Delta_r S_m^0 = 62 \pm 4 \text{ J mol}^{-1} \text{ K}^{-1}$, determined in this work. The magnitude of $\Delta_r S_m^0$ is consistent with a bidentate coordination mode, which is also shown by EXAFS

analysis, leading to the replacement of two water molecules in the first coordination shell of NpO_2^+ by the propionate ligand (Vasiliev et al. 2015). The newly derived thermodynamic data ($\Delta_r H_m^0$, $\Delta_r S_m^0$, $\log \beta^0(T)$) for the Np(V) -propionate complexation are a valuable contribution to the thermodynamic databases which are the basis of a reliable safety assessment for nuclear waste disposal scenarios. Using the comprehensive modeling tools and the thermodynamic data derived in this work, it becomes possible to predict the potential impact of the propionate (including respective ionic strength and temperature effects) on the geochemical behavior of Np(V) . Our predictions indicate that propionate has a minor impact on Np(V) speciation in environmentally relevant propionate concentrations.

Table 14: Thermodynamic data and interaction parameters according SIT for Np(V) propionate complex formation in NaCl solution determined in the present study. Uncertainties are reported at $\pm 1\sigma$ confidence level. Individual $\varepsilon(i,k)$ values are estimated based on $\varepsilon(\text{Na}^+; \text{acetate}^-)$ value.

Parameter	$\text{NpO}_2^+ + \text{Prop}^- \rightleftharpoons \text{NpO}_2(\text{Prop})$
$\log \beta_0(25 \text{ }^\circ\text{C})$	1.26 ± 0.03
$\Delta\varepsilon$ (in NaCl)	-0.17 ± 0.03
$\varepsilon(\text{NpO}_2^+; \text{Cl}^-)^{23}$	0.09 ± 0.05
$\varepsilon(\text{Na}^+; \text{Prop}^-)^{23}$	0.08 ± 0.01
$\varepsilon(\text{Na}^+ + \text{Cl}^-; \text{NpO}_2\text{Prop})$	0.00 ± 0.06
$\Delta_r H_m^0$ (kJ M^{-1})	10.9 ± 1.2
$\Delta_r S_m^0$ ($\text{J K}^{-1} \text{M}^{-1}$)	62 ± 4

4.1.2 Investigation of propionate and lactate complexation by Solvent extraction

In this work a solvent extraction technique was applied to determine the thermodynamic parameters of the Np(V) propionate and lactate complexation at varying NaCl concentration, ligand concentration, and temperature. The specific ion interaction theory (SIT) was used for correlation of ionic strength effects and the temperature dependent thermodynamic stability constants as well as $\Delta_r H_m^0$ and $\Delta_r S_m^0$ of the complexation reactions are determined.

Complexation experiment

All concentrations given in mol L^{-1} (molarity, M) were corrected to $\text{mol kg}^{-1} \text{H}_2\text{O}$ (molality, m) for later calculations to avoid changes in the concentration because of changes

in solution density by temperature and ionic strength. The concentration of Np(V) was held at 3×10^{-6} M in all extraction experiments. A first set of samples was prepared at different NaCl concentrations ($I = 0.5\text{--}2.5$ M) with total propionate ($[\text{Prop}]_{\text{tot}}$) being varied from (0.005–0.15 M) and lactate concentration ($[\text{Lac}]_{\text{tot}}$) (0.01–0.13 M) to determine the ionic strength dependence of Np(V) propionate and lactate complexation at room temperature. Furthermore, additional series were prepared at a constant ionic strength of 0.5 m with varying the ligand concentration in the same ranges and different temperatures from 22°C up to 60 °C. For maintaining of a constant temperature a water thermostat was used. The ligand (Prop, Lac) concentrations were obtained by adding of aliquots of a 1.0 M solution of propionic acid, 0.5 M and solution of sodium lactate. The pH_c in each experimental batch was adjusted to a desired value of 7.0 ± 0.1 at room temperature with 0.01 M HCl or NaOH and stabilized by introducing buffer of $5 \cdot 10^{-3}$ mol/L piperazine-N,N'-bis(2-ethanesulfonic acid) (PIPES). 2-thenoyltrifluoroacetone (TTA) and 1,10-phenanthroline were used without purification. A $1 \cdot 10^{-3}$ M TTA + $5 \cdot 10^{-4}$ M of 1,10-phenanthroline solution in isoamyl alcohol (Inoue and Tochiyama, 1982) was prepared and used as an organic phase for the extraction of NpO_2^+ .

Solvent extraction

For the extraction 2 mL of $1 \cdot 10^{-3}$ M of TTA with $5 \cdot 10^{-4}$ M of 1,10-phenanthroline in isoamyl alcohol and 2 mL of the sample solution were mixed in tubes. The tubes were inserted into the holes of the temperature-controlled shaker for 3 hours at desired temperature. Afterwards the tubes were centrifuged at the same temperature and 0.5 ml aliquots were taken from both phases to measure ^{237}Np content using Beckman Liquid Scintillation Counter (LSC) by mixing aliquots of the samples with 10 ml Ecolite scintillator. No quenching effects were observed either in aqueous or organic phases under the experimental conditions. In the remaining aqueous phase pH_{exp} was determined and pH_c was calculated as described below. The hydrolysis of NpO_2^+ is insignificant when $\text{pH}_c < 8$ at the present temperature range of 20–60 °C (Rao et al., 2004). At room temperature Np(V)-carbonate complexation is negligible for $\text{pH} < 7.5$. To our knowledge, there is no study on Np(V) carbonate complexation at elevated temperature. Since this work was carried out at $\text{pH}_c = 7.0 \pm 0.3$, the hydrolysis and carbonate complexation reactions are not taken into account.

pH measurements

In the present study, measurements of operational pH values were performed with an Orion 2 Star Benchtop pH meter using an Orion 8103SC combination pH electrode. Commercial pH Titrisol buffer concentrates (Merck p.a.) were used to calibrate the set-up at room temperature. For pH measurements at $I > 0.1$ m NaCl, an empirical correction term was applied for the measured operational pH-values (pH_{exp}) as described in chapter 4.1.1. The pH_c is a measurement of the molality of the proton ($-\log [\text{H}^+]$) and is only made here at room temperature. The apparent proton dissociation constant of propionate/lactate (pK_a) remains below 5 within the range of $[\text{NaCl}]$ and T investigated. For $\text{pH}_c = 7$ (i.e. $> \text{pK}_a + 2$), both ligands can be considered as fully unprotonated.

PIPES was chosen as a buffer for its maximum water solubility, minimum solubility in all other solvents (i.e. during the extraction experiment), minimal salt effects and minimal change in pKa with temperature (Good et al., 1966). Hence, pHc is not expected to be significantly affected when varying the temperature and the total ligand concentration ($[Prop]_{tot}$ or $[Lac]_{tot}$) is considered equal to the free ligand concentration ($[prop]_{eq}$ or $[Lac]_{eq}$) for the calculations.

Determination of the distribution ratio (D_0) in absence of a ligand

The complexation reaction of Np(V) with ligand L^- can be expressed as:

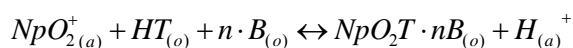


with the conditional stability constant (β , in $kg \cdot mol^{-1}$) defined as:

$$\beta = \frac{[NpO_2L_n^{(1-n)}]}{[NpO_2^+] \times [L^-]^n}$$

We used Neptunium(V) extraction by synergetic extraction with the mixture of 2-thenoyltrifluoroacetone (TTA) and 1,10-phenanthroline (Phen). The method was successfully applied for complexation studies of Np(V) complexes with organic acids by Inoue and Tochiyama (Inoue and Tochiyama, 1982, 1983).

The extraction could be presented by the reaction:



where (o) and (a) refers to the species in the organic and aqueous phases, and HT and B represents TTA and Phen, respectively.

Extraction is characterized by a distribution ratio (D) that depends on the species of extracting ions, pH and other factors:

$$D(pH, T, I) = \frac{\Sigma[M]_o}{\Sigma[M]_a}$$

where $\Sigma[M]_o$ is the total concentration of metal ion in the organic phase and $\Sigma[M]_a$ is the total concentration of metal ion in the aqueous phase. Assuming the presence of various species in the aqueous phase and D_0 as a distribution ratio in the absence of a ligand, it can be written:

$$D_0^k / D^k = 1 + \Sigma \beta_n \cdot [L_n]^n$$

where k is a serial number of a particular experiment.

In case of a 1:1 Np-ligand complexation - we have observed in our spectroscopical study of both propionate and lactate - the above equation can be simplified to:

$$D_0^k / D^k = 1 + \beta[L^-]$$

and the slope of the graph $[L^-]$ versus D_0^k/D^k is equal to the conditional stability constant. For application of liquid-liquid extraction it is necessary to obtain D_0 (distribution ratio in the absence of a ligand) values for all changing conditions namely pH_c , ionic strength and temperature at fixed concentrations of extractants (TTA and 1,10-phenanthroline) and Np(V) ions.

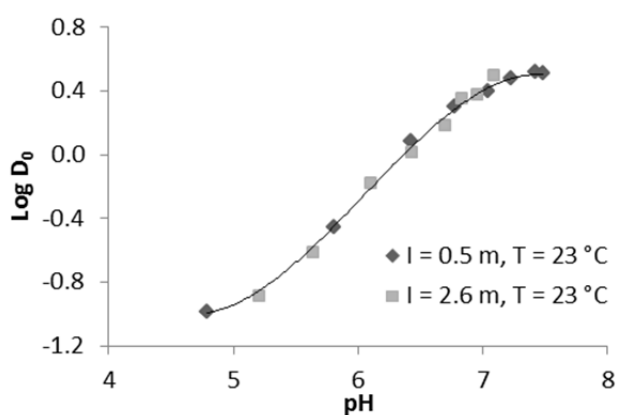


Figure 45: Distribution ratios of Np(V) upon extraction by $1 \cdot 10^{-3}$ M TTA and $5 \cdot 10^{-4}$ M 1,10-phenanthroline in the absence of complex forming ligands at 23°C with two ionic strength 0.5 m and 2.6 m NaCl.

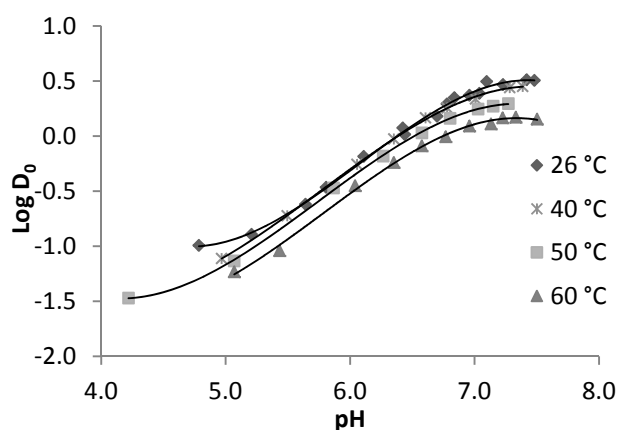


Figure 46: Distribution ratios of Np(V) upon extraction by $1 \cdot 10^{-3}$ M TTA and $5 \cdot 10^{-4}$ M 1,10-phenanthroline in the absence of complex forming ligands at varying temperature and at 0.5 m NaCl.

Figure 45 shows the results of synergistic extraction of Np(V) as a function of pH_c in the absence of complexation agents at two ionic strengths 0.5 m and 2.5 m. The slope of the linear part of this curve is equivalent to 0.74 that well fits to the literature data (In-

oue and Tochiyama, 1982). No significant influence of ionic strength on D_0 values was observed. Otherwise by increasing the temperature of the system distribution ratios slightly decrease as demonstrated in Figure 46. The data from Figure 45 and Figure 46 were used to determine D_0 at the measured pH_c values.

The effect of TTA complexation with Np(V) in the aqueous phase as well as Np(V)-Cl complex formation was found to be negligible under all presented conditions (Inoue and Tochiyama, 1982).

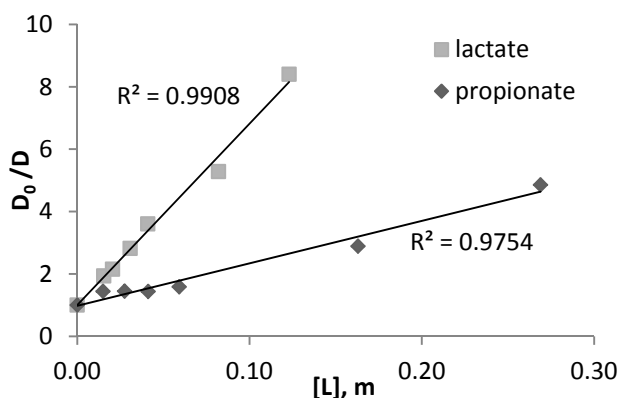


Figure 47: Representative plot of D_o/D versus free ligand concentration. Aqueous phase: 0.5 m NaCl. Organic phase: 0.001 m TTA + 0.0005 m 1,10-phenanthroline.

Figure 47 shows typical plots of the experimental values of D_o/D as a function of free propionate, lactate concentrations. Distribution ratios of Np(V) in organic and aqueous phases were found to decrease with increasing concentration of all investigated ligands. The decrease in D is caused by the increase in concentration of Np(V)-L complexes in the aqueous phase with increasing ligand concentration and pH that are not extracted into the organic phase by TTA+Phen. The linear dependences of D_o/D from the concentration of the ligands indicate the formation of only 1:1 complexes for Np-propionate and Np-lactate complexes. The slope of the straight lines (Figure 47) is equal to the conditional complex formation constants (β_c). Each value of β_c was calculated from six to eight experimental data points for each graph.

Table 15 summarizes the experimental results and published data for the conditional complex formation constants of Np(V) and the clay organics acetate, propionate, and lactate. No dependence of the conditional complex formation constants on pH_c in the 6-8 pH_c region is established indicative that only the unprotonated complexes NpO_2L are present. Therefore for simplification in this study the pH_c was chosen to be high enough

for complete dissociation of the propionic and lactic acids. The tendency in the variation of conditional complex formation constants with ionic strength is similar to the literature data obtained for the ionic strength from 0.3 m to 5.0 m (Table 15).

Effect of ionic strength

SIT is applied to extrapolate the complex formation constant at given ionic strength to zero ionic strength. As mentioned before the equation

$$\log \beta - \Delta z^2 \cdot D = \log \beta_0 - \Delta \varepsilon \cdot I$$

was used with $\Delta z^2 = -2$ to obtain the ions interaction coefficient $\Delta \varepsilon$. Figure 48 presents the plot of $\log \beta + 2D$ on I (m). The intercept of the linear approximation equals to the stability constant at zero ionic strength and the slope to ions interaction coefficient ($\Delta \varepsilon$). The conditional complex formation constants $\log \beta_c$ at given ionic strength used for the extrapolation are listed in Table 15. For all studied ligands we obtained a slight increase of $\log \beta_c$ with ionic strength. The complex formation constants for Np(V)-propionate at zero ionic strength $\log \beta_0$ was obtained from intercept of the linear regression analysis: $\log \beta_0 = 1.32 \pm 0.03$.

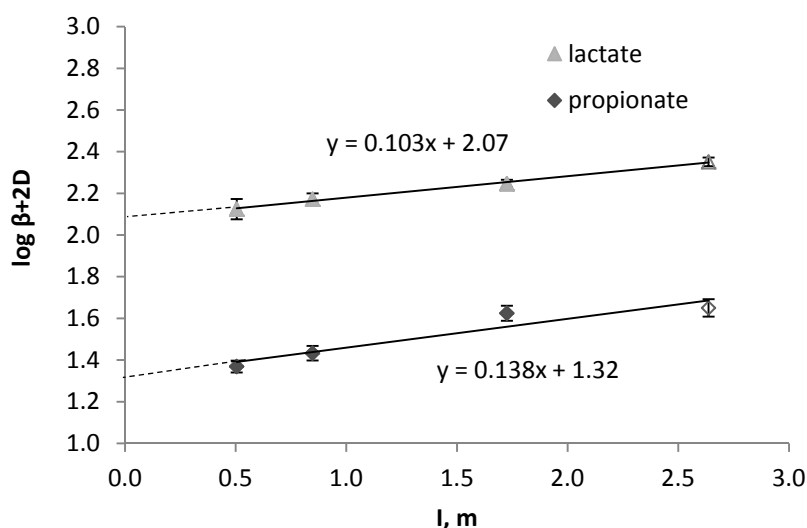


Figure 48: SIT plot of the equilibrium reaction $\text{NpO}_2^+ + \text{L}^- \rightleftharpoons \text{NpO}_2(\text{L})$ in NaCl, yielding $\log \beta_0 = 1.32 \pm 0.03$ for propionate and $\log \beta_0 = 2.07 \pm 0.03$ for lactate. The white symbol ($[\text{NaCl}] = 2.5 \text{ m}$) shows data outside the recommended applicability of the SIT (data not used in the regression). The dotted line shows the extrapolation of the results obtained for lower I to 2.5 m.

Table 15: Conditional complex formation constants of neptunium (V) acetate, propionate, and lactate formation at 25±1 °C.

Reaction	Medium	pH range	Method	log β_c	Reference
$\text{NpO}_2^+ + \text{Acet}^- \leftrightarrow \text{NpO}_2\text{Acet}$	0.30 m NaCl	6.0-7.2	LLE	1.05±0.04	A
	1.00 m NaCl	6.0-7.2	LLE	1.13±0.05	A
	2.00 m NaCl	6.0-7.2	LLE	1.25±0.05	A
	3.00 m NaCl	6.0-7.2	LLE	1.55±0.05	A
	4.00 m NaCl	6.0-7.2	LLE	1.70±0.20	A
	5.00 m NaCl	6.0-7.2	LLE	1.80±0.02	A
	1.05 m NaClO ₄	7.0	LLE, cal	0.74±0.04	B
	$\text{NpO}_2^+ + \text{Prop}^- \leftrightarrow \text{NpO}_2\text{Prop}$	0.51 m NaCl	7.0±0.5	LLE	0.99±0.03
0.83 m NaCl		7.0±0.5	LLE	1.01±0.03	present work
1.67 m NaCl		7.0±0.5	LLE	1.14±0.03	present work
2.50 m NaCl		7.0±0.5	LLE	1.14±0.04	present work
$\text{NpO}_2^+ + \text{Lact}^- \leftrightarrow \text{NpO}_2\text{Lact}$	0.51 m NaCl	7.0±0.5	LLE	1.75±0.05	present work
	0.83 m NaCl	7.0±0.5	LLE	1.75±0.03	present work
	1.67 m NaCl	7.0±0.5	LLE	1.76±0.02	present work
	2.50 m NaCl	7.0±0.5	LLE	1.84±0.02	present work
	0.30 m NaCl	6.0-7.2	LLE	1.78±0.03	A
	1.00 m NaCl	6.0-7.2	LLE	1.43±0.04	A
	2.00 m NaCl	6.0-7.2	LLE	1.48±0.05	A
	3.00 m NaCl	6.0-7.2	LLE	1.76±0.02	A
	4.00 m NaCl	6.0-7.2	LLE	1.93±0.06	A
	5.00 m NaCl	6.0-7.2	LLE	1.95±0.04	A

*LLE – liquid-liquid extraction, spec – absorption spectroscopy, cal – calorimetry. A: (Moore et al., 1999); B: (Rao et al., 2010).

A further experimental problem arises in comparing complex formation constants obtained by different techniques (Choppin, 1997). Solvent extraction is a technique from which log β_0 is calculated by using the total complexed metal species, i.e. outer and inner sphere complexes. Spectroscopic technique takes into account only inner sphere species and that is expressed in a slightly lower value with log $\beta_0 = 1.26 \pm 0.03$ (Vasiliev et al., 2015). It is noticeable that the log β_0 of Np(V)-acetate (literature data) and Np(V)-propionate are similar and equal to ca. 1.3. This could be explained by the fact that only the carboxyl group participates in complex formation. An increase of the chain length by one –CH₂ group has no significant impact on the complexation process and hence on log β_0 .

Effect of temperature

Effect of the temperature on the complexation was investigated at T = 25, 40, 50 and 60 °C and c (NaCl) = 0.51 m (Table 16). The log β_c was corrected to complex formation constant log $\beta(T)$ at infinite dilution for each temperature using SIT approach as described above. With the assumption that molal standard reactions enthalpy $\Delta_r H_m^0$ and entropy $\Delta_r S_m^0$ do not change with temperature – the heat capacity does not change

significantly with T - under the experimental conditions, it is possible to estimate these thermodynamic parameters from an Arrhenius plot on the basis of the van't Hoff equation:

$$\log \beta(T) = \frac{\Delta_r H_m^0}{RT \ln 10} + \frac{\Delta_r S_m^0}{R \ln 10}$$

where R is the ideal gas constant. Figure 49 plots $\log \beta(T)$ versus the reciprocal temperature ($^{\circ}\text{K}$) $1/T$. The linear dependences of the complex formation constants as a function of temperature confirms the assumptions, that $\Delta_r H_m^0$ and $\Delta_r S_m^0$ do not significantly change with temperature.

Table 16: Conditional stability constants of neptunium (V) complex formation at different temperatures.

Reaction	Method	Medium	T, $^{\circ}\text{C}$	$\log \beta_c$	Reference
NpO₂⁺+Acet⁻↔	spec, cal	1.04 m NaClO ₄	25	1.05±0.04 (SIT) *	a
NpO₂Acet	spec, cal	1.04 m NaClO ₄	40	1.11±0.03 (SIT)*	a
	spec, cal	1.04 m NaClO ₄	55	1.19±0.03 (SIT)*	a
	spec, cal	1.04 m NaClO ₄	70	1.34±0.05 (SIT)*	a
NpO₂⁺+Prop⁻↔	LLE	0.51 m NaCl	25	0.99±0.03	p. work
NpO₂Prop	LLE	0.51 m NaCl	40	1.15±0.01	p. work
	LLE	0.51 m NaCl	50	1.29±0.10	p. work
	LLE	0.51 m NaCl	60	1.36±0.06	p. work
NpO₂⁺+Lact⁻↔	LLE	0.51 m NaCl	25	1.75±0.05	p. work
NpO₂Lact	LLE	0.51 m NaCl	40	1.77±0.03	p. work
	LLE	0.51 m NaCl	50	1.71±0.02	p. work
	LLE	0.51 m NaCl	60	1.69±0.02	p. work

* In this work $\log \beta(T)$ at zero ionic strength was deduced with SIT approach.

References: a: (Rao et al., 2010).

It should be noted that in case of propionate complexation the $\log \beta$ significantly increases with temperature, whereas for lactate the $\log \beta$ slightly decreases. The values of $\Delta_r H_m^0$ and $\Delta_r S_m^0$ are listed in the Table 17 together with literature data for comparison reasons. The standard reaction enthalpy $\Delta_r H_m^0$ for propionate and acetate are positive indicating that complexation of Np(V) is an endothermic reaction. The dehydration energy of the metal ion or ligand (positive enthalpy) preponderates the metal-ligand interaction (negative enthalpy). The positive entropy of the reaction signals an entropy driven reaction where the degree of disorder is enhanced by removing a water molecule from the first hydration sphere of entropy. It was pointed out from Choppin (Choppin, 1997) that the 1:1 complexes of Ln(III) with monocarboxylate ligands are predominantly outer sphere in character if pK_a of ligand acid is < 2 and predominantly inner sphere if the $\text{pK}_a > 3$. The $\Delta_r H_m^0 > 0$ indicates that dehydration energy is required for complexes formation and supports the model of inner-sphere binding of Np(V)-propionate complexes with only one carboxylate group. Relatively high value of entropy

factor could be connected with bidentate coordination mode of Np-OOC binding for acetate and propionate both $75 \pm 6 \text{ J} \cdot \text{M}^{-1} \text{K}^{-1}$ (Rao et al., 2010) and $77 \pm 9 \text{ J} \cdot \text{M}^{-1} \text{K}^{-1}$, respectively) with replacement of two water molecules from the inner sphere of Np.

For lactate $\Delta_r H_m^0$ is slightly negative and the value of -5.4 ± 1.4 is comparable with literature data. In case of lactate no stability constants at elevated temperature is available for Np(V) in literature, only data for lactate complexation of Nd^{3+} was found (Tian et al., 2010). They explain the results in the way that the Ln(III) lactate complexation is more favored by enthalpy - less dehydration energy is required to form the coordination bond - probably because the R-hydroxyl group is less hydrated than the carboxylate group. Additionally, the Ln(III) lactate interaction is stronger than the Ln(III)-acetate or propionate interaction so that more energy is gained in the former. The same can be assumed for Np(V). Due to the participation of the hydroxyl groups there is a stronger Np-ligand interaction and ordering of the system which expressed in negative enthalpy and in 2 times lower entropy value than for propionate and acetate complexation.

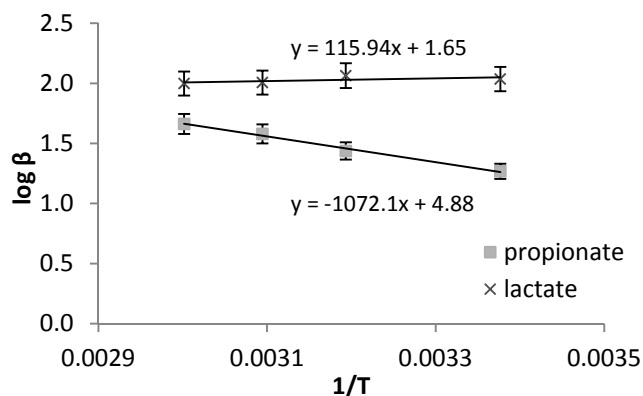


Figure 49: Np(V) complexation constants corrected to zero ionic strength ($\log \beta_0$) versus the reciprocal of the temperature (K^{-1})

Comparison of thermodynamic data with literature data

The thermodynamic parameters of the complex formation reaction between Np(V) and ligands obtained in this study and comparison to literature data are summarized in Table 17.

Recently published data (Vasiliev et al., 2015) for the spectroscopic studies of Np(V)-propionate at elevated temperature and ionic strength are available and are faced to the present studies by the extraction method (see Table 17). Data available in literature for highly analog chemical systems were published by (Rao et al., 2010) for Np(V) complexation with acetate. They obtained a complexation constant at zero ionic strength $\log \beta_0$ and $\Delta \epsilon$ values for the 1:1 NpO_2^+ -acetate complex similar to the values for propionate derived in this work, with NaCl ($\log \beta_0 = 1.28 \pm 0.04$ and $\Delta \epsilon = -0.24 \pm$

0.02) and NaClO₄ (log β₀ = 1.27 ± 0.02 and Δε = -0.08 ± 0.01) used as background electrolyte. At 298.15 K and [NaClO₄] = 1.05 m, (Rao et al., 2010) determined Δ_rH_m⁰ = 18.1 ± 1.8 kJ mol⁻¹ and Δ_rS_m⁰ = 75 ± 6 J mol⁻¹ K⁻¹, which are comparable to our present results for the propionate system. In general, positive Δ_rH_m⁰ and Δ_rS_m⁰ are found for actinide complexes with monocarboxylic ligands, for example, Cm(III)(Prop)²⁺ (Δ_rH_m⁰ = 5.7 ± 1.8 kJ mol⁻¹ and Δ_rS_m⁰ = 84 ± 5 J mol⁻¹ K⁻¹ (Fröhlich et al., 2013); (Δ_rH_m⁰ = 6 ± 2 kJ mol⁻¹ and Δ_rS_m⁰ = 79 ± 8 J mol⁻¹ K⁻¹ (Fröhlich et al., 2014) or U(VI)(Acetate)⁺ (Δ_rH_m⁰ = 14.5 ± 1.5 kJ mol⁻¹ and Δ_rS_m⁰ = 104 ± 6 J mol⁻¹ K⁻¹ (Sladkov, 2014). For all these actinides, the magnitude of Δ_rS_m⁰ is comparable because both acetate and propionate coordinate mainly in a bidentate fashion, replacing two water molecules in the first coordination shell of the actinide.

Table 17: Thermodynamic parameters specific ion interaction coefficients (Δε) of neptunium (V) complex formation with acetate, propionate and lactate (in NaCl solution), according to the reaction: NpO₂⁺ + L⁻ = NpO₂L.

Complex	Method	log β ₀ (25°C)	Δ _r H _m ⁰ (kJ M ⁻¹)	Δ _r S _m ⁰ (J K ⁻¹ M ⁻¹)	Δε	
NpO ₂ Ac ⁻	spec, cal	1.28±0.04	18.1±1.8*	75±6*	-0.24±0.02	a [§]
		1.27±0.02			-0.08±0.01	a [§]
		1.46±0.22			Pitzer	f
NpO ₂ Prop	lle	1.32±0.05	16.3±3.0	77±9	-0.14±0.03	pw
	spec	1.26 ± 0.03	10.9 ± 1.2	62 ± 4	-0.17±0.03	b
NpO ₂ Lact	lle	2.07±0.01	-5.4±1.4	19±4	-0.10±0.01	pw
	lle	1.97			Pitzer	e
	lle	1.70			unknown	e
	lle	1.10±0.08 ^{&}				c
	spec	1.75±0.02 [#]				j
NdLact ²⁺	cal	2.57 ± 0.09*	-2.02±0.22	43±1	-	d
	spec	2.58 ± 0.05*				d
CmAc ²⁺	spec	3.18 ± 0.34	6 ± 2	79 ± 8	-0.17±0.01	h
CmProp ²⁺	spec	3.24 ± 0.17	5.7 ± 1.8	84 ± 5	-0.11±0.02	g
UO ₂ Ac ⁺	CE	2.94 ± 0.08	14.5 ± 1.5	104 ± 6	-0.14	i

a: (Rao et al., 2010); b: (Vasiliev et al., 2015); c: (Eberle and Schaefer, 1969); d: (Tian et al., 2010); e: (Moore et al., 1999); f: (Novak et al., 1996); g: (Fröhlich et al., 2013); h: (Fröhlich et al., 2014); i: (Sladkov, 2014); j: (Inoue and Tochiyama, 1983).

[#]: 0.01 M NaClO₄; *: 1.05 m NaClO₄; [§]: in NaCl solution; [§]: in NaClO₄ solution; [&]: 1 M NaClO₄
spec: spectroscopy, cal: calorimetry; lle: liquid-liquid extraction; CE : capillary electrophoresis

Np(V)-propionate/lactate complexation at environmentally relevant concentrations

Preliminary calculations are made for pH = 9, in 0.1 M NaCl and at T = 25° C using the presently obtained Np(V)-propionate complexation parameters to illustrate the impact of propionate on Np speciation in environmentally relevant conditions. The percentage of Np(V) complexed to propionate versus log [Prop]_{tot} is shown in Figure 50 ([Np(V)]_{tot} = 10⁻⁹ M). At ligand concentrations up to 0.01 M, less than 1% occurs as propionate complex, because propionate is a weak ligand for Np(V) at these conditions. In natural clay rocks porewater (e.g. OPA/COx), where propionate is present at lower concentration (≤ 27 μM (Courdouan et al., 2007a; Courdouan et al., 2007b)) and where Np(V) is in competition with other cations, propionate complexation is expected to have a minor impact on Np(V) speciation. The lactate complexation is more pronounced than the propionate, but reaches not more than 10% at 0.01 M lactate concentration. However, the lactate concentration in environmental pore waters is also very low compared to other inorganic and organic ligands and surface species. The concentration found in OPA pore waters is ≤ 9 μM (Courdouan et al., 2007a; Courdouan et al., 2007b). We conclude, that the lactate complexation is also expected to have a minor impact on the Np(V) speciation in clay formations comparable to OPA.

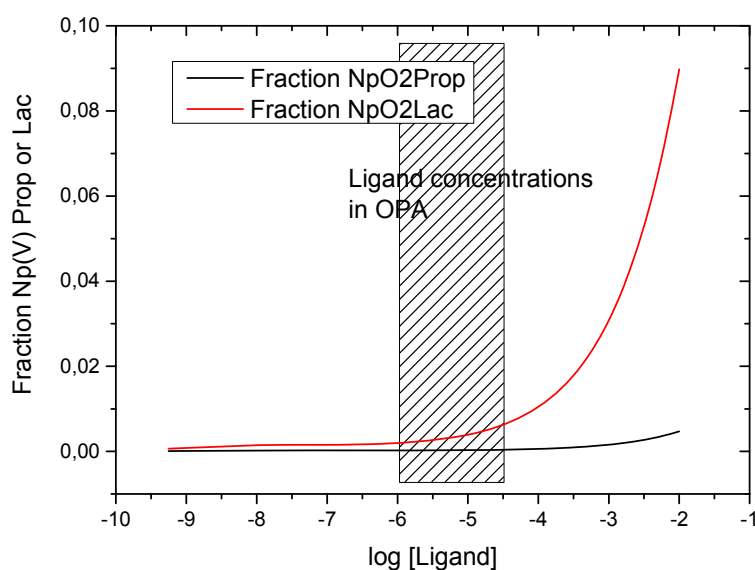


Figure 50: Chemical equilibrium diagram for Np(V) propionate and lactate complexation at pH 9 and 0.1 M NaCl (T= 25 °C). The box represents propionate and lactate concentrations found in OPA pore water and various extracts (Courdouan et al., 2007a; Courdouan et al., 2007b).

4.1.3 Conclusions

In present study, liquid-liquid extraction was successfully applied and distribution ratio for Np(V)-propionate and Np(V)-lactate was calculated.

The present study shows that the stability constant for the formation of 1:1 NpO_2^{+} -propionate/lactate complex, clearly identified as the dominant species under the investigated conditions with $\log \beta_0 (25^\circ\text{C}) = 1.32 \pm 0.05$ for Np(V) propionate and $\log \beta_0 (25^\circ\text{C}) = 2.07 \pm 0.01$ for Np(V) lactate. Both complex formation constants increase with ionic strength ($0.5 < \text{NaCl} < 2.5 \text{ m}$) and temperature ($20 < T < 60^\circ\text{C}$). The complex formation reaction is endothermic for propionate complexation and entropy driven, as evidenced in the present work with $\Delta_r H_m^0 = 16.3 \pm 3.0 \text{ kJ mol}^{-1}$ and $\Delta_r S_m^0 = 77 \pm 9 \text{ J mol}^{-1} \text{ K}^{-1}$. The magnitude of $\Delta_r S_m^0$ is consistent with a bidentate coordination mode (Rao et al., 2010; Sladkov, 2014), which is also shown by spectroscopic results (Lucks et al., 2012). The results are in a good agreement with literature (Rao et al., 2010; Vasiliev et al., 2015). However, the lactate complex formation reaction is exothermic and entropy driven, evidenced by $\Delta_r H_m^0 = -5.4 \pm 1.4 \text{ kJ mol}^{-1}$ and $\Delta_r S_m^0 = 19 \pm 4 \text{ J mol}^{-1} \text{ K}^{-1}$. This could be caused by the influence of the α -hydroxy group in the lactate molecules. The role of the α -hydroxy group was also well reported in the literature for complexation of Nd(III) with lactate (Tian et al., 2010).

With the new set of thermodynamic data ($\Delta_r H_m^0$, $\Delta_r S_m^0$, $\log \beta_0(T)$) for the Np(V) propionate and lactate complexation, it becomes possible to predict the impact of small clay organics - including respective ionic strength and temperature effects - on the geochemical behavior of Np(V) . Our predictions indicate that these small clay organic molecules has a minor impact on Np(V) speciation in environmentally relevant clay organic concentrations as found for OPA.

4.2 Humic acid complexes at high ionic strengths

4.2.1 Stabilization of polynuclear plutonium(IV) species by humic acid

Humic colloids such as humic acids (HA) are ubiquitous in natural waters and present a high binding capacity for dissolved metal ions. Although Pu(IV) was considered as rather immobile due to its low solubility, it shows a colloid-facilitated transport in presence of humic colloids (Artinger et al., 2003). Several studies have shown that the interaction of strongly hydrolysable elements with HA (e.g. Fe(III)) (Gustafsson et al., 2007; Karlsson and Persson, 2010) can lead to the stabilization of small polynuclear species, although the experiments were performed below the saturation index of relevant solid phases. Pu(IV) has an intrinsic tendency to form a great variety of dissolved polynuclear species (Walther et al., 2009). Furthermore, it was previously shown by spectroscopy (Dardenne et al., 2009), at relatively high Pu concentration, that HA can inhibit its precipitation by forming small polynuclear species.

Although the formation of tetravalent plutonium (Pu(IV)) polymers with natural organic matter was previously observed by spectroscopy, there is no quantitative evidence of

such reaction in batch experiments. In the present study, published in (Marsac et al., 2014). Pu(IV) interaction with humic acid (HA) was investigated at pH 1.8, 2.5 and 3, as a function of HA concentration and for Pu total concentration equal to 6×10^{-8} M. The finally measured Pu(IV) concentrations ($[Pu(IV)]_{eq}$) are below Pu(IV) solubility limit.

Pu(IV)–HA interaction can be explained by the complexation of Pu(IV) monomers by HA up to $[Pu(IV)]_{eq} \sim 10^{-8}$ M. However, the slope of the log–log Pu(IV)–HA binding isotherm changes from ~ 0.7 to ~ 3.5 for higher $[Pu(IV)]_{eq}$ than $\sim 10^{-8}$ M and at any pH. This result suggests the stabilization of hydrolyzed polymeric Pu(IV) species by HA, with a 4:1 Pu:HA stoichiometry. This confirms, for the first time, previous observations made by spectroscopy in concentrated systems. The humic ion binding model, Model VII, was introduced into the geochemical speciation program PHREEQC and was used to simulate Pu(IV) monomers binding to HA. The simulations are consistent with other tetravalent actinides–HA binding data from literature.

The stabilization of a Pu tetramer $[Pu_4(OH)_8]^{8+}$ by HA was proposed to illustrate the present experimental results for $[Pu(IV)]_{eq} > 10^{-8}$ M. Predictive simulations of Pu(IV) apparent solubility due to HA show that the chosen Pu(IV)-polymer has no impact for $pH > 4$. However, the comparison between these predictions and recent spectroscopic results suggest that more hydrolyzed polymeric Pu(IV) species can be stabilized by HA at $pH > 4$. Polymeric Pu(IV)–HA species might significantly enhance Pu(IV) apparent solubility due to humics, which support a colloid-facilitated transport of this low solubility element.

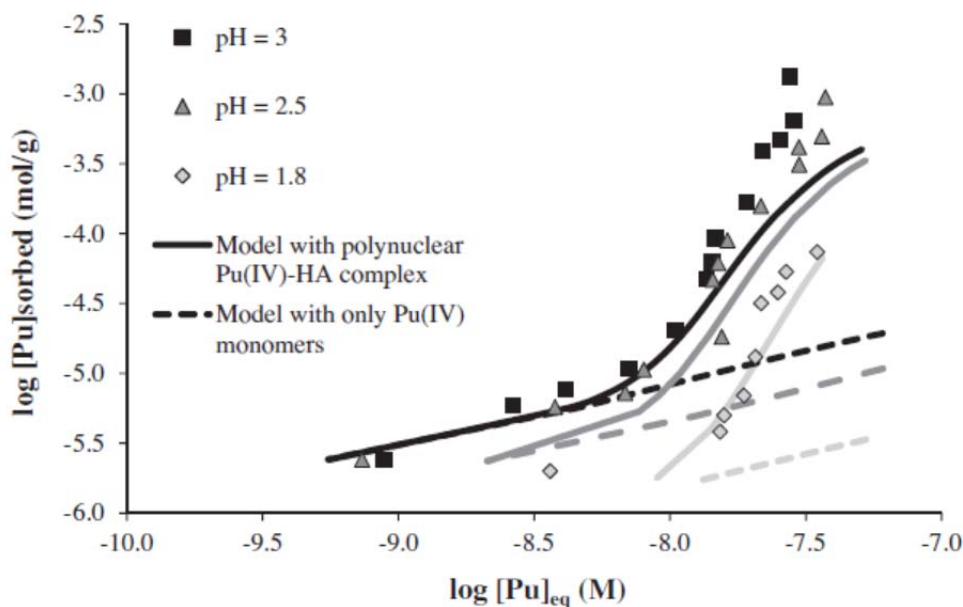


Figure 51: Comparison between experimental and modeling results of Pu(IV)–HA binding considering with or without stabilization of Pu(IV) tetramer by HA.

4.2.2 Conclusions

The present study on Pu(IV) humate complexation at $\text{pH} < 3$ yields evidence for the complexation of both mono and polynuclear Pu(IV) species to HA, at conditions where no Pu(IV) precipitation is expected. Model VII is used to simulate Pu(IV) monomers binding to HA. The simulations are consistent with other tetravalent actinides–HA binding data from literature (Reiller et al., 2008). The stabilization of a Pu tetramer $[\text{Pu}_4(\text{OH})_8^{8+}]$ by HA is proposed to illustrate Pu(IV)–HA interaction in conditions where polynuclear Pu(IV)–HA species are formed. Although a robust model considering both the formation of mono- and polynuclear Pu(IV) complexes with HA cannot be derived from the present and previous studies, such polynuclear species are expected to have an impact under relevant conditions in the environment. They significantly increase the Pu(IV) apparent solubility due to HA complexation, more than by humate complexation of monomeric Pu(IV) species. Due to their similar chemical properties, comparable mechanisms are also expected for other tetravalent actinides, such as U(IV) and Np(IV). Such a mechanism of humate or fulvate complexation strongly supports a transport of An(IV) as a humic colloid-borne species as observed in migration experiments (Artinger et al., 2003). Therefore, further studies should be dedicated to the colloidal stability of An(IV)–HA (i.e. mono- and polynuclear) complexes. More generally, the stabilization of polynuclear cations by HA seems to be a relevant mechanisms at least for cations presenting a high tendency for hydrolysis such as An(IV), Al(III) (Browne and Driscoll, 1993; Sutheimer and Cabaniss, 1997) or Fe(III) (Gustafsson et al., 2007; Karlsson and Persson, 2010). This might impact the fate of these elements in the environment but might also affect other elements through the competition for organic matter binding sites.

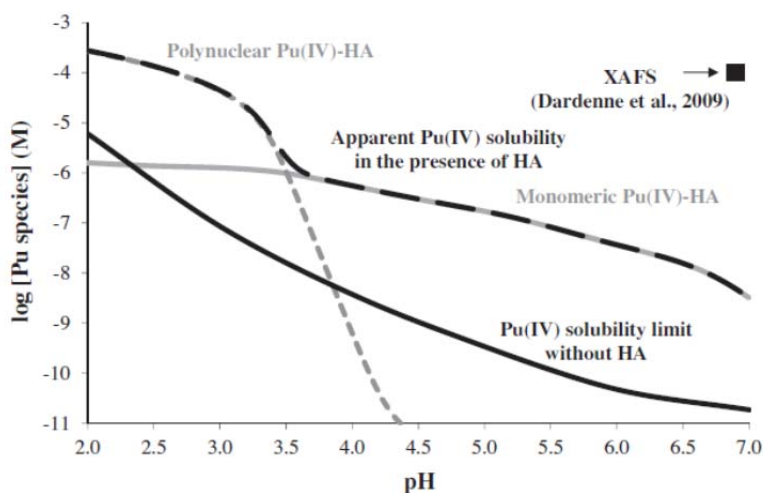


Figure 52: Simulated Pu(IV) solubility versus pH in a 0.1M of NaCl solution containing 140 mg L^{-1} of HA or no HA. The experimental condition studied by XAFS (Dardenne et al., 2009), where polynuclear Pu(IV)–HA species were evidenced, is also shown for comparison.

4.3 Investigations on the stability of humic substances at elevated ionic strengths

To predict the long term safety of a nuclear waste repository, the behaviour of the organic matter (OM), amongst with the humic substances, has to be examined under relevant and specific conditions. In case of regarding i) salt rock formation, ii) the Jurassic and lower Cretaceous clay rock layers in Northern Germany or iii) sedimentary layers like in Canada for a repository host rock, the potential impact of high ionic strength media have to be considered. A crucial point is to determine how it influences the stability of the colloidal organic matter and its metal ions binding properties. In recent investigations (Bouby and Buckau, 2012) in perchlorate media it was shown that even up to 3 M the destabilization of the humic acids (HAs) tested was not complete.

The aim of this work is to examine the stability of fulvic acids (FA) as representative of small size OM (smaller than humic acid) in chloride media of high ionic strengths (IS). The study uses two natural FAs extracted from two ground waters sampled in the Gorleben Site, Lower Saxony, Germany.

The results are completed with those obtained by using i) one synthetic fulvic acid (SFA), ii) one of the two groundwater as received and, iii) a lignin derivative. The OM colloidal suspensions are prepared in NaCl, CaCl₂, MgCl₂, FeCl₃ and HCl for ionic strengths varying from 10⁻² M up to 6.5 M. Evolution of the suspensions is followed by UV-Visible spectrophotometry and TOC analysis before and after centrifugation. To complete the observation of an eventual flocculation, the size variations of the organic matter under those conditions are inspected by using the SEC/UV-Vis technique.

4.3.1 Material and methods

Gorleben groundwater Gohy-532

This natural groundwater is pumped from a bore-hole (number 532) which gives its name to the sample (Gohy-532). Characterization details can be found in previous works of Artinger, Buckau, Schäfer et al. (Artinger et al., 1996; Artinger et al., 1999; Artinger et al., 2000; Buckau et al., 2000b; Buckau et al., 2000d; Buckau et al., 2000c; Buckau et al., 2000a; Schafer et al., 2003; Schäfer et al., 2005).

Fulvic acids (FA): FA-573 & FA-532

These two fulvic acids are isolated, purified and characterized from the corresponding natural Gorleben ground waters pumped out from the bore – hole numbers 573 and 532. For more details on the isolation and purification processes see (Artinger et al., 2000; Wolf et al., 2004). To obtain a stock solution, a small amount of the final products

is dissolved in NaOH 0.1 mol.L⁻¹ (ultrapure, Merck) and then diluted with ultrapure water. The dissolved organic carbon content is measured with a TOC analyzer (TOC-5000, Shimadzu). The FA concentrations are respectively 512 mg/L (FA-573) and 139 mg/L (FA-532). The FA stock solutions are stored at 4°C in a fridge prior to use.

Synthetic (SFA-1)

The synthetic fulvic acid used (SFA-1) is kindly provided by A.K. Kiprop (present address Chemistry Department, Moi University, P.O Box 3900-30100, Eldoret, Kenya). The synthesis was done in the frame of his PhD work in the laboratory UMR 7566 G2R, Nancy Université CNRS, France. Briefly, it consists in an auto polymerisation reaction of cathecol at constant stirring (3000 rpm) and pH during 1 month followed by dialysis at various molecular weight cut-off (MWCO), deep freezing, lyophilization and grounding. More details can be found in (Kiprop, 2009; Kiprop et al., 2013). A stock solution is prepared following the protocol described in the paragraph just above. The SFA concentration is 214 mg/L (SFA-1).

Lignosulfonic acids sodium salt (LS-NA)

Lignosulfonic acid is a lignin-derived poly anionic macromolecule. The commercial product is provided by Sigma-Aldrich. The MWCO is 52 kDa. The salt is used as received. A small amount is dispersed in a mixture ultrapure water/NaOH at pH 10 to obtain a stock solution which is kept in the fridge prior to use. The concentration is 1264 mg/L.

Electrolytes

The NaCl (6.5 M), CaCl₂ (2.3 M) and MgCl₂ (2.1 M) electrolyte solutions are prepared from the salts (Merck, P.A.) dissolved in ultrapure water. A FeCl₃ electrolyte (0.43 M) is prepared in HCl (2M). A 4 M HCl solution is prepared by diluting a calibrated standard volume (Merck, ultrapure, p.a.) in 250 mL instead of 1 L. A 2-(N-morpholino)-ethanesulfonic acid (MES) buffer stock solution (1 M) is freshly prepared in ultrapure water.

OM suspension preparation and ionic strength effect study

The final suspensions (15 mL) are prepared by mixing the appropriate volumes of the different stock solutions together. The MES concentration is 10⁻³ M in all the samples. The final OM concentrations are 25 mg/L for FA-573, SFA-1 and LS-NA and 11.6 mg/L for FA-532 and Gohy-532. The final ionic strengths are 0.01 M, 3 M and 5 M in NaCl, 3 M in CaCl₂ and MgCl₂, 3 M in HCl and 4.58 M in FeCl₃/HCl.

The pH are only indicative as no correction is applied to take into account the salt effect. They are all adjusted after the mixing at 6.5 ± 0.2 . They remain constant 24 h later. (Note: the pH are not measured for the electrolyte HCl 3M and FeCl₃/HCl).

The DOC concentration is checked in each sample before centrifugation and after (30 min at 4000 rpm, Megafuge 2.0 R, Thermo Scientific, Heraeus Instrument) for each supernatant. All the suspensions prepared in NaCl 0.01 M are measured by UV-Vis. spectrophotometry prior to and after the centrifugation. The supernatants of all the other samples are only measured after centrifugation by UV-Vis. spectrophotometry.

UV-Vis spectrophotometry

UV-Vis spectroscopy is commonly used for the characterization of humic substances (Artinger et al., 2000; MacCarthy, 1985; Schnitzer, 1978). The spectra are recorded on a UV-Visible spectrophotometer (Cary 50 Conc, Varian) over the range 900-199 nm after placing some mL of the solutions to be analyzed in quartz cuvettes (precision cells, quartz Suprasil® 300, QX 10.0 mm, HELLMA).

Size Exclusion Chromatography

The general principle of the Size Exclusion Chromatography has been described in details elsewhere, see e.g (Conte and Piccolo, 1999; Pelekani et al., 1999; Perminova, IV et al., 2003; Piccolo, 2001; Striegel et al., 2009). Very briefly, in SEC, the compounds are primarily separated on the basis of their hydrodynamic molecular size. Molecules that are larger than the pore size of the packing material are excluded and elute first at the exclusion/void volume. Smaller molecules can penetrate throughout the porous infrastructure and are then retarded leading to an elution at higher retention time.

In this study, we use a Bio-Silect® SEC250-5 (300*7.8 mm, 5 µm particle size, 250 Å pore size, Bio-Rad Laboratories, California, USA) size exclusion column to perform the separation. A degasser (1100 series, model G1322A, Hewlett-Packard, Waldbronn, Germany) and an isocratic pump (model G1310A, Hewlett-Packard, Waldbronn, Germany) are used to deliver the eluent through the chromatographic column. The eluent consisted of ultra pure water with tris-buffer at $1 \cdot 10^{-2}$ M and $5 \cdot 10^{-3}$ M NaCl. The elution flow rate is fixed at $1 \text{ ml} \cdot \text{min}^{-1}$. The injections are made via a 6-ports/2-channels injection valve (Knauer, Germany) and a PEEK sample loop of 100 µL (Rheodyne, USA). Connections and other tubing are made of PEEK as well. From the SEC column, the eluent solution is directed through an UV-Vis detector (Postnova analytics, Germany) recording the signal at 225 nm. An additional injection valve with a PEEK sample loop of 100 µL is added before the UV-Vis detector for direct injection and recovery measurement. SEC data handling are performed by using the Clarity™ GPC software (Data Apex, the Czech Republic). The calibration is performed with PSS reference standards (Polysciences, Eppelheim, Germany) of various molecular weight (0.891, 1.67, 3.42,

6.43, 15.8, 33.5 kDa). The main characteristics of the column are its total permeation volume and its exclusion volume determined from the total permeation time (498 s) and exclusion time (312 s) and are respectively: 8.27 mL and 5.35 mL, under the present experimental conditions.

4.3.2 Results and discussion

DOC

The DOC concentrations do not vary drastically (not more than 5-10 %) and without any trend. It is not associated to a specific electrolyte neither to an ionic strength value. It could thus be considered to be in the analytical error range. Nevertheless, this absence of significant variation is the first indication that the small organic matter (macro)molecules investigated present a high stability; i.e. it remains suspended even at high ionic strength.

Electrolytes absorption spectra.

The respective contributions of the electrolytes (see Figure 53) to the UV-Vis absorption spectra has been subtracted. Actually, the absorption of the NaCl (5 M), CaCl₂ (3 M), and MgCl₂ (3 M) electrolytes is significant in the range 200-230 nm (Figure 53). The HCl (3 M) absorption is evident over a more extended range (200-300 nm). Note that the absorption of the FeCl₃ (0.4 M) / HCl (2 M) solution is above the limit of the detection and thus cannot be subtracted properly. Accordingly, the nevertheless corrected UV-Vis spectra in that electrolyte cannot be considered. But, as said above, the DOC does not vary significantly in that electrolyte even if a flocculation is visible by eye. It suggests either a rather high stability of the OM at that IS (4.6 M) and in presence of iron and chloride ions.

FA-573 behavior in high ionic strength electrolytes: UV-Vis. absorption spectra variations and chromatograms

The FA-573-UV-Vis absorption spectra in the different electrolytes are presented Figure 54. The evolution of the UV-Vis absorption spectra are presented hereafter for all the suspensions after subtraction of the electrolyte contribution: FA-573 (Figure 54), FA-532 (Figure 56), Gohy-532 (Figure 57), SFA-1 (Figure 58), and LS-Na (Figure 59).

Humic compounds are complex macromolecular polymers consisting of 120 to 150 aliphatic and aromatic compounds intermingled in such a manner that they have lost their individual identities (Rashid, 1985). The resulting biopolymer is composed of an aromatic core (i.e. (poly-)phenols, (poly-) aromatics), linked with aliphatic side chains (i.e. carbohydrates, proteins, organic acids, fatty acids by-products of transformation), in various configurations and cross-linked in random fashions. Humic compounds contain

a variety of functional groups (constituting about 20 to 30 % of the molecule), such as aliphatic and aromatic carboxyls, phenolic hydroxyls, alcoholic hydroxyls, carbonyls, quinones, methoxyls and amino groups.

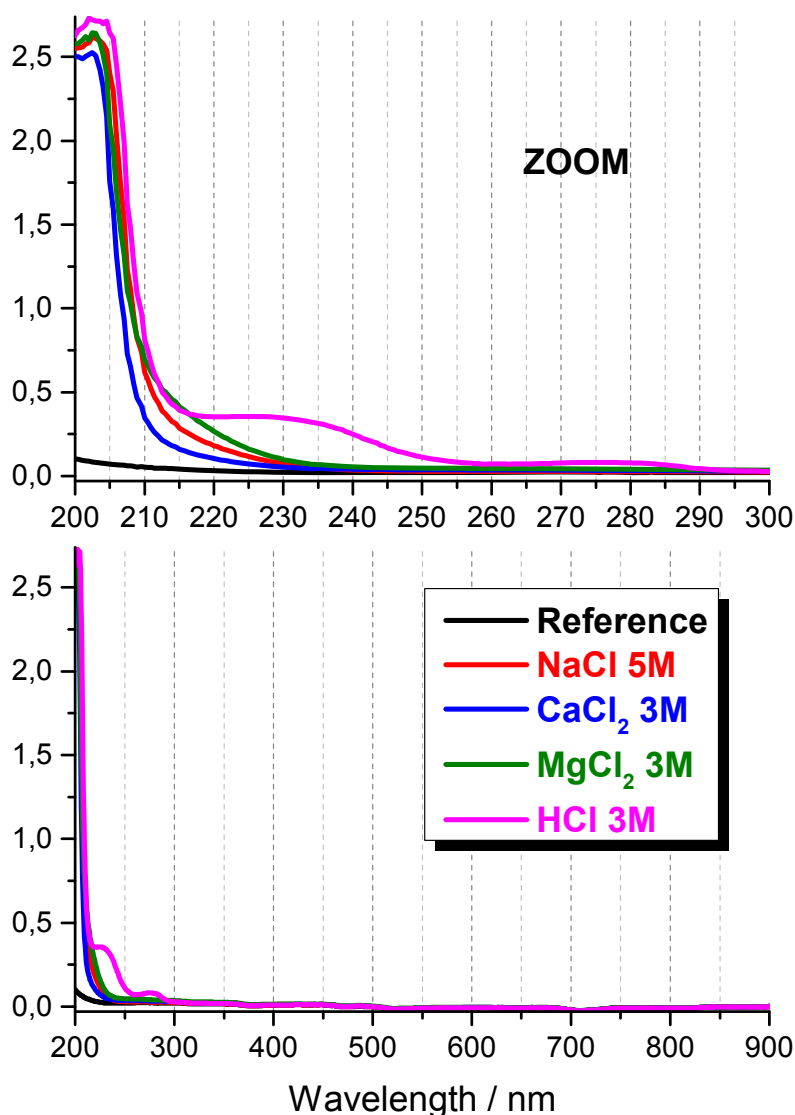


Figure 53: UV-Vis spectra of the electrolytes used to fix the ionic strength.

Humic compounds absorb light over a wide range of wavelength due to the presence of the vast majority of the chromophores that absorb in the UV region (< 400 nm) i.e. the aromatic groups with various degrees and types of substitution, including mono- and polysubstituted phenols and various aromatic acids (Korshin et al., 1997). The spectra of humic substances are frequently described in the literature by an increasing absorption with decreasing wavelength without characteristic feature. This is due to the high number of chromophore types without any possessing a unique and distinguishable absorption spectrum, combined with internal vibration and rotation of the molecules and inter-molecular interactions which broaden the absorption peaks in the UV-spectrum (Korshin et al., 1997).

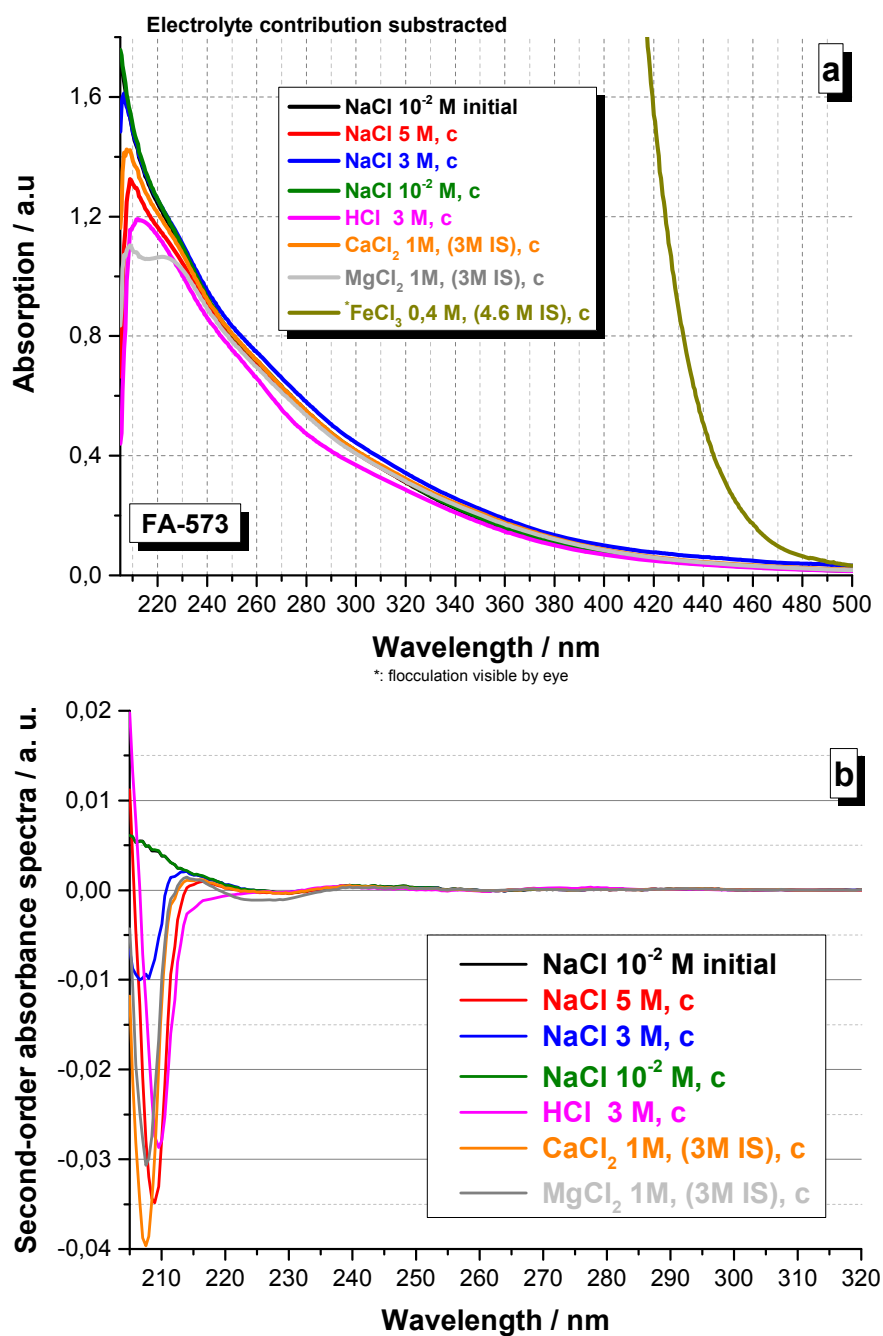


Figure 54: a) FA-573 UV-Vis spectra (range 210-500 nm) in different electrolytes and thus ionic strengths (IS) obtained after centrifugation. The electrolyte contributions have been subtracted. [FA-573]= 25 mg.L⁻¹. b) Second-order derivatives exemplary shown in the range 205-320 nm.

Thus not surprisingly, the fulvic acid FA-573 (Figure 54a, black line – overlain by the green line!) UV-Vis absorption spectrum present the same pattern as that frequently reported in the literature (see (Baes and Bloom, 1990) for example and references cited) with an inflection point at ~ 230 nm. The centrifugation has no effect on this organic matter, as seen on the corresponding UV-Vis spectrum strictly identical (Figure 54a).

At 3 M NaCl (Figure 54a, blue line), the absorption spectrum differs from the one obtained in 10^{-2} M NaCl, an effect clearly accentuated at 5 M NaCl (Figure 54a, red line). A change is observed as well in CaCl_2 1 M (i.e. 3 M IS). At a first look the absorption spectra pre-cited remain quasi featureless. Clear changes appear at the opposite at 1 M MgCl_2 (i.e. 3 M IS) and at 3 M HCl. The absence of significant DOC variations is a strong indication of the FA-573 stability in the different electrolytes and thus at these high ionic strengths but it does not say anything about the conformation of the organic molecule. To obtain more information the spectra variations are further examined based on data treatment proposed in the literature.

Unfortunately, the UV spectrum deconvolution into the constituent spectra of individual chromophore is impossible (Korshin et al., 1997). A more precise characterization is often made by considering the specific absorption at one wavelength or the absorption ratio at two wavelengths (i.e. for example the E4/E6 absorbance ratio at 465 nm and 665 nm) for a qualitative description of the curvature of the absorption continuum and mainly to determine the nature of the organic matter investigated. Actually, an increase in the specific absorption and a decrease in the absorption ratio are indicative of an increasing humification, aromaticity and molecular weight of humic substances (Chin et al., 1994).

Another characterization consists in modeling the UV spectra as a combination of three Gauss-shaped bands in analogy to benzene (Korshin et al., 1997) which presents three bands at 180 nm, 203 nm and 253 nm. It was proposed to attribute absorbance at wavelengths $< \sim 190$ nm to the local excitation (LE) band, absorbance between 190 nm and 240 nm to the benzenoid (Bz) band and absorbance at wavelength > 240 nm to the electron-transfer (ET) transition. Despite overlapping, it is thought that the composite LE, Bz and ET band in natural organic matter do not lose their identity and may be extracted from the UV spectra. Some authors have already applied this protocol successfully to describe the fractionation of humic substances in contact with mineral surface (Claret et al., 2008).

Presently, the same approach could be used in order to detect any specific subtle change induced by ionic strength on the different band constituents. The idea is, as proposed in (Korshin et al., 1997) and used by (Claret et al., 2008), to fit each absorption spectrum by a sum of three Gaussians using a nonlinear regression fitting procedure. Nevertheless, in a first approach, the convergence of the fits was difficult to obtain. Consequently, the next idea has been to use the derivative (differential) spectroscopy (Perkampus, 1992) to better isolate and thus determine the specific wavelength (band peak maximum) where any absorption spectra variation takes place and to see if there is an ionic strength influence (i.e. an eventual shift of this band peak maximum).

Table 18: Band peak maxima positions (± 0.5 nm) as obtained after differential spectroscopy (see text for details). a: initial, b: after centrifugation, c: not clearly determined.

	NaCl 0.01 M ^a	NaCl 0.01 M ^b	NaCl 5 M ^b	NaCl 3M ^b	HCl 3M ^b	CaCl ₂ 3M ^b	MgCl ₂ 3 M ^b
FA-573	-	-	208.7	207.4	209.7	207.6	207.8
	229.9	230.4	229.8	229.1	-	229.8	226.1
	261.6	261.7	261.5	262.1	261.9	261.1	261.0
	311.0	310.5	310.9	311.3	318.6	311.3	311.7
FA-532	-	-	208.4	204	208.9	207.1	207.4
	229.7	229.8	229.9	227.8	-	229.2	225.6
	264.4	266.3	263.7	264.8	260.6	262.3	262.8
	311.3	311.4	318.5	311.6	318.7	318.9	318.8
Gohy-532	-	-	208.1	204.7	208.9-	207.0	207.3
	-	-	-	-	216.8	-	-
	(231.3) ^c	(230.3) ^c	(230.5) ^c	-	229.9	230.5	229.8
	266.1	266.4	262.5	261.4	260.7	266.1	265.9
	311.1	311.0	318.6	311.9	318.8	318.9	318.8
SFA-1	-	-	208.9	204.5	209.5	207.1	206.7
	231.3	230.9	-	229.9	229.9	230.5	225.8
	287.6	286.4	287.7	287.6	283.7	285.3	285.5
	327.3	327.4	327.5	326.9	328.3	327.4	327.8
LS-Na	-	-	208.6	207.9	209.5	207.9	207.8
	236.6	233.7	234.0	235.0	234.7	232.5	232.2
	285.7	286.1	285.7	286.0	285.9	286.6	286.1
	(327.6) ^c	(327.9) ^c	(318.2) ^c	(326.6) ^c	(327.1) ^c	(318.4) ^c	(318.0) ^c

Derivative spectroscopy is the representation of the first- and second-derivative as well as higher-order derivatives of a normal (or zero-order) spectrum with respect to wavelength (or wavenumber). It emphasizes subtle spectral features. This enables better resolution of multicomponent samples to be obtained. Numerous examples of applications are reported nowadays as it has become a useful analytical/data processing technique to extract qualitative and quantitative information from spectra consisting of unresolved and/or greatly overlapping bands (see (Bosch Ojeda and Sanchez Rojas, 2013; Pavón et al., 2012) for details). Amongst the firsts (Cieslewicz and Gonet, 2004), Hur et al. (Hur et al., 2006) used this method to obtain valuable dissolved organic matter (DOM) discrimination indices. Similarly to (Hur et al., 2006), we used the method of Savitsky and Golay in the present study (Savitzky and Golay, 1964). The process involved a stepwise interval smoothing of the original zero-order spectra using a constrained second order polynomial function to obtain the second derivative (i.e. $d^2A(\lambda)/d\lambda^2$). We tested a smoothing using 5, 10, 15 or 20 points by using the Origin 9.1 Software (Microcal Software, Inc.). The results are exemplary shown Figure 54b for the range 205-320 nm. The minimum obtained are the band peak maxima of the UV-Vis. spectra. The results are summarized Table 18.

For FA-573, 3 band peak maxima can be isolated at ~ 230 nm, ~ 262 nm, ~ 311 nm and in addition one at ~207-209 nm for the highest ionic strength. No change occurs after the centrifugation (3 peaks detected), confirming the visual spectral observation. It is presently difficult to state on the significance of the slight peaks shifts observed for the bands located at ~ 230 nm, ~ 260 nm and ~ 311 nm for increasing ionic strength with maybe an exception in MgCl₂ (peak at ~226 nm instead of 230 nm initially) and in HCl 3M (peak at ~319 nm instead of 311 nm initially). Nevertheless, a clear effect of the ionic strength is detected with the appearance of an additional peak located at 207-210 nm in each electrolyte.

(Baes and Bloom, 1990) recorded the UV-Vis spectra of some fulvic acids and they noted shoulders in the 260-290 nm and 310-330 nm range. The pH-dependent behavior of these bands make them suggest that the relevant chromophoric systems are –OH and –COOH-substituted benzene rings. In addition, they attributed the very strong absorbance at very short wavelengths (e.g., 210 nm) to the benzenoid bands of the carboxyphenols. This opened somehow the way to the analogy with the benzene proposed later by (Korshin et al., 1997) as benzene presents 3 bands at 180 nm, 203 nm and 253 nm, or one may think eventually as well to an analogy with the benzoic acid, the simplest aromatic carboxylic acid which presents 3 bands centered near 190 nm, 230 nm and 280 nm (Baum and McClure, 1979)

In the present case, for the fulvic acid FA-573, one can attribute similarly the peaks located at ~ 207~209 nm and at ~ 230 nm to the Bz band, the peaks at ~ 262 nm and ~ 311 nm to the ET band. This kind of groups (aromatic with or without substitution like –OH and –COOH-substituted benzene rings or carboxyphenols) could thus be thought as the ones affected by an increase of the ionic strength. The variations observed would reflect a change in their environment. Nevertheless, many other functional groups (Liu and Ryan, 1997) could have been affected.

Maybe of interest is to remember few studies done in the 60's to correlate changes in protein structure from denaturation or proteolysis with alterations of their UV absorption spectra in the wavelength range 200 to 320 nm (Donovan, 1969; Glazer and Smith, 1960; Martin and Bhatnagar, 1966; Móra and Elöudi, 1968). It was first proposed that the spectral changes in the 220-250 nm region may be due to peptide chromophore undergoing an helix-coil transition (Glazer and Smith, 1960). Later, the absorption changes observed near 230 nm were attributed primarily to environmental effect on the aromatic chromophore (Martin and Bhatnagar, 1966; Móra and Elöudi, 1968) (e.g. indol and phenol for globular protein compared to the helix to coil transition of the amide group (Donovan, 1969)). According to these pioneer works and due to the presence of a band at 230 nm, it appeared interesting to follow the size evolution of the fulvic acids as a function of the ionic strength. This has been done by using the SEC-UV-Vis equipment. (Note: Due to the low pH of the suspension in HCl 3M, it was not analyzed by SEC).

The SEC chromatograms after injection of the FA-573 suspensions prepared in NaCl 10^{-2} M are similar before or after the centrifugation (see Figure 55). It confirms that the centrifugation has thus no effect. The UV-FA-573-chromatograms present peak maxima at ~6 min and a shoulder at ~7 min which, according to the calibration done with Na-PSS standards, indicate that the size of the main FA-573 fraction is comprised between 1.5 and 2 nm (hydrodynamic diameter) with a residual fraction below 1 nm (see Table 19). The chromatograms are drastically different for increasing ionic strengths with the appearance of an additional peak after the total permeation time (see Figure 55).

Table 19: SEC-hydrodynamic diameter values (in nm).

	FA-573	FA-532	SFA-1	LS-Na
1st (main) Fraction	1,5-2	< 1.5	< 1,5	3,0
2nd(minor) Fractions	< 1 nm	< 1 nm	< 1 nm	< 1 nm

In 5M NaCl, the FA-573 peak is broader and the elution peak maximum is detected at ~ 5.7 min. This is attributed to intramolecular electrostatic interactions. Adding NaCl to increase the ionic strength at 5 M may have shielded the internal electrostatic repulsive forces that act to expand the FA-573. The result is a more compact FA-573 shape with an outer layer of Na⁺ ions. This finally increases the hydrodynamic volume occupied by the fulvic acids. This results in earlier elution volumes (times) with respect to those observed in the absence of high NaCl concentration. This has been already reported in the literature (Striegel et al., 2009). In CaCl₂ 3M (IS), the chromatograms are less reproducible. Nevertheless, it is clear that the FA-573 peak is shifted but this time towards later elution times (~ 6.2 min). This might be due to a Ca²⁺-induced bridging effect on the FA-573 molecule resulting in a more compacted (and thus smaller) molecule. The same remarks can be done for the chromatograms obtained in MgCl₂ 3M (IS), which are very reproducible. In that electrolyte, the peak shift is even more pronounced (elution at ~ 7 min). This means that the compaction could be even more pronounced. This might be as well related to the more pronounced shift of the UV band initially measured at 230 nm which occurs at ~226 nm in MgCl₂ (see Table 18). Accordingly, a variation of this band peak maximum could be considered as a conformation change indicator as proposed in the past for the proteins (Donovan, 1969; Glazer and Smith, 1960; Martin and Bhatnagar, 1966; Móra and Elöudi, 1968).

here Na^+ , Ca^{2+} , Mg^{2+}) experience a preferential diffusion into the pores of the packing material to balance the difference between the stagnant and the flowing mobile phase. This so-called *ion inclusion effect* (Striegel et al., 2009) may result in later elution as those presently observed.

In conclusion, the FA-573 fulvic acids are stable in high ionic strength chloride electrolyte media nevertheless they experience variable conformation (size) changes as a function of the counterions (Na^+ , Ca^{2+} or Mg^{2+}). The following ordering might be proposed concerning the hydrodynamic diameters: MgCl_2 (3M IS) < NaCl (10^{-2} M IS) < MgCl_2 (3M IS) < NaCl (5M IS) < 2 nm.

FA-532 and Gohy-532 behavior in high ionic strength electrolytes: UV-Vis absorption spectra variations and chromatograms

The UV-Vis. absorption spectra are presented Figure 56 (FA-532) and Figure 57 (Gohy-532). Note that the fulvic acids FA-532 are isolated, extracted and purified from the original Gohy-532 ground water sample. Accordingly, and in agreement with literature, the FA-573, FA-532 and Gohy 532 UV-Vis. absorption spectra present similar patterns in NaCl 10^{-2} M.

The variations observed in Figure 56 for the fulvic acids FA-532 are rather comparable to the ones described for the fulvic acids FA-573. On the opposite, the variations are more pronounced on the absorption spectra of the original Gohy-532 ground water. This might be due to the fact that the Gohy-532 ground water contains other constituents more affected by the ionic strength than its fulvic acids fraction. One can emit the hypothesis that this is mainly the fulvic acids fraction which remains rather unaffected and in suspension.

The same data treatment has been applied and the results are similar to those previously described. The same absorption bands can be isolated at ~ 230 nm, ~ 264 nm and 311 nm initially, with an additional one for increasing ionic strength at ~ 204-209 nm. The peak shifts of the band at 260 nm and 311 nm might be more significant than for the FA-573 (see Table 18).

Accordingly the same conclusion can be proposed: the ionic strength affects more specifically some kind of groups (aromatic with or without substitution like $-\text{OH}$ and $-\text{COOH}$ -substituted benzene rings or carboxyphenols), this is accompanied by conformation (size) changes as visible by SEC-UV-Vis. analysis (data not shown) leading to the following hydrodynamic diameter ordering for FA-532: MgCl_2 (3M IS) < NaCl (10^{-2} M IS) < CaCl_2 (3M IS) < NaCl (5M IS) < 1,7 nm. The initial FA-532 hydrodynamic diameter of the main fraction in NaCl 10^{-2} M is estimated < 1.5 nm (see Table 19).

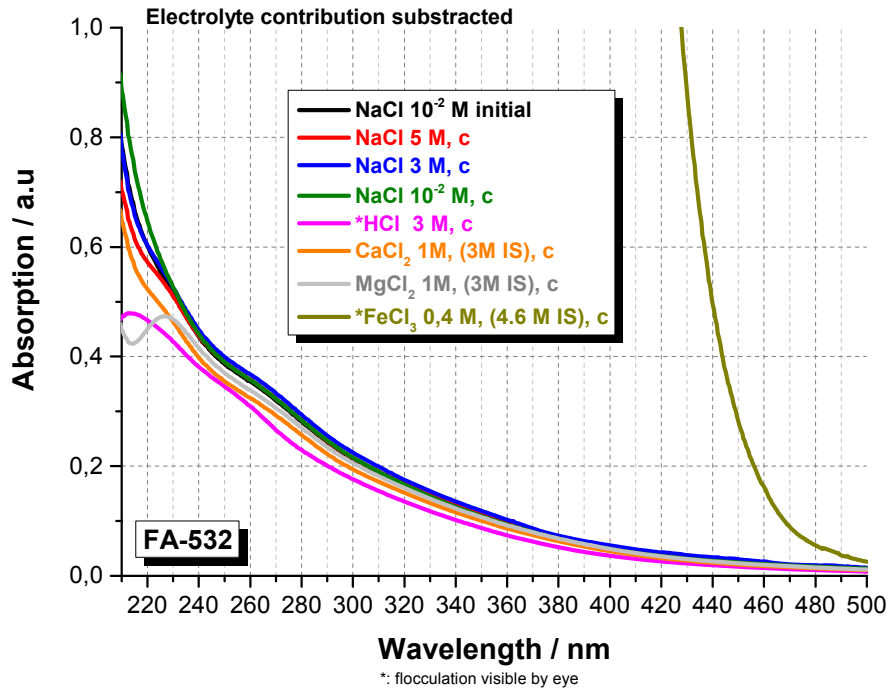


Figure 56: FA-532 UV-Vis spectra (range 210-500 nm) in different electrolytes and thus ionic strengths (IS) obtained after centrifugation. The electrolyte contributions have been subtracted. [FA-532]= 12 mg.L⁻¹.

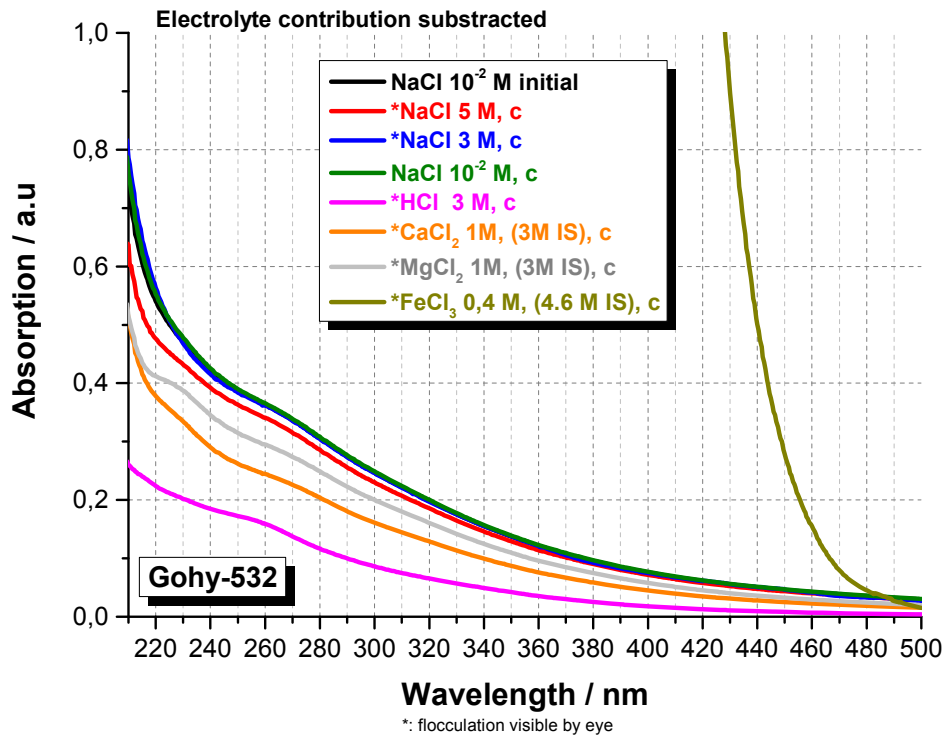


Figure 57: Gohy-532 UV-Vis. spectra (range 210-500 nm) in different electrolytes and thus ionic strengths (IS) obtained after centrifugation. The electrolyte contributions have been subtracted. [Gohy-532]= 12 mg L⁻¹.

SFA-1 behavior in high ionic strength electrolytes: UV-Vis. absorption spectra variations and chromatograms

The absorption spectra of the synthetic fulvic acids SFA-1-UV-Vis in different electrolytes are presented Figure 58. The pattern in NaCl 10^{-2} M is similar to the one reported in literature for natural fulvic acids. It is consistent with the UV-Vis absorption spectra recorded after its synthesis (Kiprop, 2009) showing clearly three broad bands at ~ 228 nm, 278 nm and 362 nm. In the present work, the data analysis by differential spectroscopy indicate the presence of three bands as well but located at ~231 nm, ~ 288 nm and 327 nm. The last band is thus shifted compared to estimation done by the raw visual inspection of the UV-spectra (Kiprop, 2009). The results are nevertheless in good agreement. A last band at ~ 484 nm was proposed but not presently clearly detected.

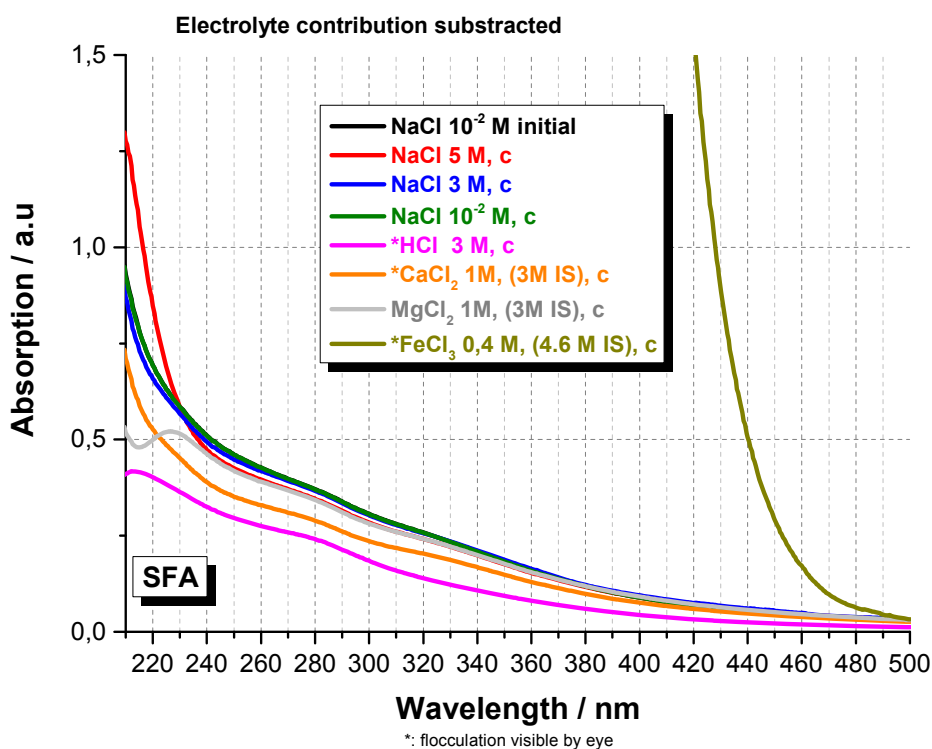


Figure 58: SFA-1 UV-Vis spectra (range 210-500 nm) in different electrolytes and thus ionic strengths (IS) obtained after centrifugation. The electrolyte contributions have been subtracted. [SFA-1]= 25 mg L⁻¹.

A noticeable effect of the ionic strength is seen (Figure 58) especially above 3 M IS and in HCL electrolyte. At high ionic strength, a fourth band can be isolated from the data treatment (see Table 18) located at ~205-210 nm, similarly to the natural fulvic acids.

This synthetic fulvic acid is obtained from the polymerization of catechol. The molecular structure determined from ATR-FTIR spectroscopy (Kiprop, 2009) consists of several

aromatic rings linked to each other through aryl-aryl and ether bonds, each aromatic ring may bear up to five substitutional groups. The first (~ 231 nm) and second band (~ 288 nm) are assigned to the aromatic bands. The slight variations of the peak maxima of these bands for increasing ionic strength may indicate its specific effect on these substituted (or not) aromatic groups.

SEC-UV-Vis analysis was performed (data not shown). The hydrodynamic diameter of the main size fractions are listed in Table 19. The variations of the SFA-1-chromatograms present great similarities with the chromatograms of the natural fulvic acids. The following size sequence effects can be proposed: MgCl_2 (3M IS) < NaCl (10^{-2} M IS) \leq CaCl_2 (3M IS) < NaCl (5M IS) < 3.8 nm. Note that this is a much bigger size than observed for the natural fulvic acids.

LS-Na behavior in high ionic strength electrolytes: UV-Vis. absorption spectra variations and chromatograms

The LS-Na-UV-Vis absorption spectra of this lignin-derived poly anionic macromolecule in the different electrolytes are presented Figure 59. This compound was under investigation for its use as plasticizer in cement composition, reason for why its study could be of interest.

The UV-Vis spectra present a clear feature at 280 nm which is accordingly one of the band clearly detected by differential spectroscopy (see Table 18). The centrifugation has apparently an effect as noted by a decrease of the absorption at wave length below 230 nm. This leads to a shift in the peak maximum position detected by differential spectroscopy (see Table 18).

This organic macromolecule is affected by increasing ionic strength as seen by the variation of the absorption spectra, especially below 230 nm, and as reflected by the shift of this band peak maxima values and the detection of an additional band with a peak maximum value at ~ 208-209 nm. Again it might be seen as a specific IS effect on substituted (or not) aromatic groups.

Some conformation (size) changes have been seen by SEC-UV analysis (data not shown). The hydrodynamic diameter of the main size fractions are specified in Table 19. Nevertheless, in that case only a clear shift towards bigger size (elution at earlier retention time) is noticeable. The following size sequence effects can be proposed: NaCl (10^{-2} M IS) < MgCl_2 (3M IS) < 2.7 nm < CaCl_2 (3M IS) & NaCl (5M IS) much bigger as eluted at the exclusion time limit (i.e. the size cannot be estimated).

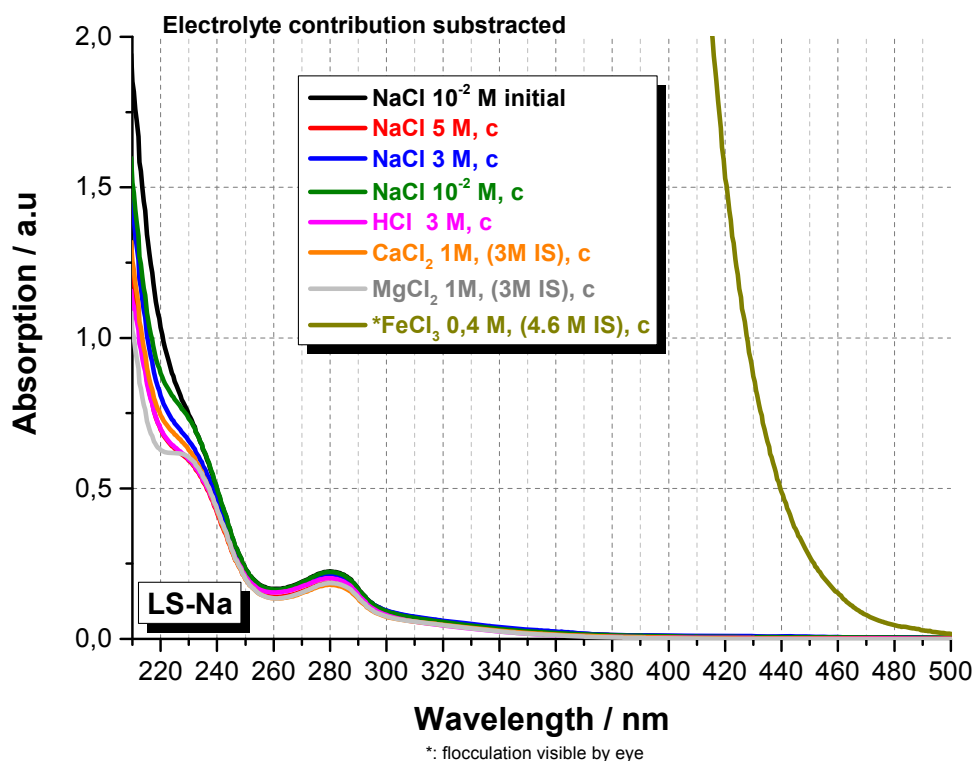


Figure 59: LS-Na UV-Vis. spectra (range 210-500 nm) in different electrolytes and thus ionic strengths (IS) obtained after centrifugation. The electrolyte contributions have been subtracted. [LS-Na]= 25 mg L⁻¹.

4.3.3 Conclusions

The first results indicate a high stability of the small sized organic matter under the present conditions: the DOC varies by less than 5-10%. No effect is noticeable up to 3 M IS in NaCl. At 5 M IS NaCl or 3 M IS CaCl₂/MgCl₂ and HCl some variations are noticeable on the absorption spectra.

The fulvic acids (FA-573 and FA-532) isolated from the respective Gorleben ground waters (Gohy-573 and Gohy-532) behave similarly. The synthetic fulvic acids (SFA-1) react as the natural ones but its final conformation appears more expanded. This synthetic product might be a good analogue for natural fulvic acids with the advantage of a better known (controlled) composition;

A refined analysis of the absorption spectra by differential spectroscopy evidence various band which can be attributed to the local excitation band (LE), to the benzenoid band (Bz) and to the electron-transfer transition band (ET). The shifts of the corresponding band peak maxima (if considered significant enough) suggest that an increase of the ionic strength affects more specifically some kind of groups (aromatic with or without substitution like -OH and -COOH-substituted benzene rings or carboxyphenols). This would reflect a change in their close environment;

Conformation (size) changes are qualitatively evidenced by SEC-UV-Vis analysis. For the fulvic acids, natural or synthetic, the NaCl addition (> 3 M) results in an expansion of the hydrodynamic molecular volume due to intramolecular electrostatic interactions (even more pronounced for the synthetic FA), while the addition of CaCl₂ or MgCl₂ results in a compaction of the macromolecule certainly due to a divalent cation-induced bridging effect (the Mg²⁺ being more efficient). The maximum hydrodynamic diameter values estimated from SEC data are respectively 2 nm, 1.7 nm and 3.8 nm for FA-573, FA-532, and SFA-1, respectively. The natural fulvic acids can thus certainly preserve their mobility in natural media of high ionic strength. For the lignin-derived macromolecule, the ionic strength increase results in an expansion of the hydrodynamic molecular volume whatever the electrolytes up to ~ 2.7 nm (MgCl₂, 3M IS) and more (no quantification possible) for CaCl₂ (3M IS) and NaCl (5M). Here, the mobility cannot be guaranteed.

These conclusions are restricted to the experimental time frame of the present work, i.e. 24 hours. More work is necessary to state on their long term stability in high ionic strength electrolyte media. The fulvic acids seem to preserve their stability even in high ionic strength media even if they experience conformational change. This is certainly due to their low molecular weight and density close to the one of the solvent. It does not mean that they preserve their complexation properties as the functional groups are affected in their environment, a point which call for further investigations.

5 Solubility of Actinides in presence of borate and at high ionic strengths

The interaction of borate with lanthanides (III) and actinides (III, IV, V, VI) is investigated in dilute to concentrated saline solutions. Boron can be present as component of the emplaced waste in a nuclear waste repository. In certain rock salt formations, high boron concentrations can also occur in the intruding brine solutions. In this framework, it is very relevant to understand the impact of borate in the chemical behaviour of actinides (e. g. complexation, solubility phenomena or redox processes) under repository relevant conditions. In spite of this, only a limited number of studies on the interaction of borate with lanthanides and actinides are reported in the literature. This is also reflected by the absence of any thermodynamic data selection for actinide–borate aqueous complexes or solid compounds in the current NEA–TDB reviews. In order to gain a better understanding of the processes taking place in the Ln(III)– and An(III, IV, V, VI)–borate systems, comprehensive solubility experiments in combination with spectroscopic studies and a detailed solid phase characterization were performed under repository-relevant conditions.

In the present work, the interaction of borate with actinide (III, IV, V, VI) is investigated in diluted to concentrated saline solutions with a combination of solubility experiments, spectroscopic methods (including TRLFS, EXAFS and UV–Vis/NIR) and comprehensive solid phase characterization (accomplished with XRD, XPS, SEM–EDS, XANES/EXAFS). The work comprises experimental conditions relevant for different concepts of radioactive waste disposal, and thus different background electrolytes (NaCl, MgCl₂ and CaCl₂) as well as a broad pH-range ($6 \leq \text{pHm} \leq 13$) are considered. The main objectives of this work are:

- The solubility of Nd(III) is studied in dilute to concentrated NaCl, CaCl₂ and MgCl₂ solutions with varying pH and boron concentration. Focus is given to the possible formation of Nd(III)–borate compounds and their eventual role on the immobilization of An(III). Thus a comprehensive solid phase characterization is performed using XRD, XPS and SEM–EDS. Additional TRLFS experiments with Cm(III) give information on the aqueous speciation of An(III)/Ln(III) in the presence of borate. With these data, a first thermodynamic description is proposed for the system Ln(III)/Cm(III)-Na⁺-Mg²⁺-Ca²⁺-H⁺-Cl⁻-B(OH)₄⁻ at 25°C.
- The solubility of Np(V) is studied in dilute to concentrated NaCl and MgCl₂ solutions with varying pH and boron concentration. Focus is given to the possible formation of Np(V)–borate compounds and their possible impact on the Np source term. Solid phase characterization is accomplished using XRD, SEM–EDS, XPS and EXAFS techniques. The aqueous speciation of Np under increasing concentrations of borate is investigated using UV–Vis/NIR. The combination of solubility data, spectroscopic results and solid phase characterization is aimed at deriving a first thermodynamic description for the system Np(V)- Na⁺-Mg²⁺-Ca²⁺-H⁺-Cl⁻-B(OH)₄⁻ at 25°C.

- Because of their stronger hydrolysis and the expectedly weaker interaction with borate, the solubility of Th(IV) and U(VI) is exemplarily investigated in dilute to concentrated NaCl and MgCl₂ solutions and at various boron concentrations. Solubility measurements are complemented with solid phase characterization using XRD. The system Pu(III)–Pu(IV) is considered to gain insight on the effect of borate on the chemical behavior of redox sensitive actinides and allow a better assessment of the plutonium source term.

5.1 Experimental

Details of the experimental parameters and applied methods can be find in (Hinz, 2015; Hinz et al., 2015). This report contains only a brief summary.

5.1.1 Chemicals

All chemicals used in the experiments were obtained from Merck or specifically prepared at INE and were not further purified. All solutions were prepared with purified water from a Milli-Q-academic apparatus (Millipore, 18.2 MΩ) purged with Argon before use. The long-lived curium isotope ²⁴⁸Cm ($t_{1/2} = 3.4 \times 10^5$ years) was used for the TRLFS measurements. The stock solution used in the experiments (2×10^{-5} M Cm(III) in 0.1 M HClO₄) had an isotopic composition of 89.7% ²⁴⁸Cm, 9.4% ²⁴⁶Cm, 0.4% ²⁴³Cm, 0.3% ²⁴⁴Cm and 0.1% ²⁴⁷Cm. A ²³⁷Np stock solution was previously prepared with 2.5 g of ²³⁷Np ($t_{1/2} = 2.14 \cdot 10^6$ years), which was purified from trace impurities of Pu and Am using an ion exchange method. The resulting Np solution (0.32 M ²³⁷Np in 0.01 M HCl) was characterized by gamma spectrometry, liquid scintillation counting (LSC), UV–Vis/NIR and alpha spectrometry, which confirmed both the chemical and radiochemical purity of the ²³⁷Np stock solution. Pu solubility experiments were performed with ²⁴²Pu with the exact isotopic composition of ²⁴²Pu (99.4%), ²³⁹Pu (0.58%), ²³⁸Pu (0.005%) and ²⁴¹Pu (0.005%). Since the main isotope is ²⁴²Pu ($t_{1/2} = 375000$ years), no radiolysis effects, occurring by the decay of short lived Pu isotopes in concentrated chloride solutions are expected.

5.1.2 pH measurement in saline solutions

In solutions with $I \geq 0.1$ m, ion interaction processes affect the activity coefficient of H⁺ (γ_{H^+}) and the liquid junction potential. To determine pH in high salinity no longer the activity of H⁺ but the concentration of H⁺ are used (Knauss et al., 1990):

$$pH_m = -\log(m_{H^+}) \text{ and } pH_c = -\log(c_{H^+})$$

Where pH_m and pH_c are the negative logarithm of the molal and molar concentration of H⁺, respectively.

The values pH_m and pH_c can be calculated from the operationally measured pH_{exp} and an empirical correction factor (A) where liquid junction potential and the activity coefficient of H^+ are included.

$$pH_m = pH_{exp} + A_m \quad \text{and} \quad pH_c = pH_{exp} + A_c$$

with

$$A_m = \log m \gamma_{H^+} + \Delta E_j F / RT \ln(10)$$

and

$$A_c = \log c \gamma_{H^+} + \Delta E_j F / RT \ln(10)$$

The correction factor A is experimentally determined for the respective salt system and concentration with a set of reference solutions with known proton concentration.

For pH measurements in this work, a combination glass pH electrode (type ROSS, Orion), freshly calibrated against dilute standard pH buffers (pH 7–13, Merck), was used to determine the molar or molal H^+ concentration, $[H^+]$ and m_{H^+} , respectively. Whenever needed, pH adjustments were performed with HCl-NaCl-NaOH, HCl-MgCl₂ and HCl-CaCl₂ solutions of proper ionic strength. Alkaline solutions in MgCl₂ and CaCl₂ were adjusted with Mg(OH)₂(s) and Ca(OH)₂(s), respectively. All “A” factors used in this work for NaCl, CaCl₂ and MgCl₂ solutions were previously reported by Altmaier et al (Altmaier et al., 2003a; Altmaier et al., 2008) and are summarized in Table 20. The pH_m measurements performed following this approach are assigned with an uncertainty of ± 0.04 pH units. Note that the impact of borate on the background electrolyte is not corrected for the determination of pH. Nonetheless, it cannot be excluded that high boron concentrations ($[B]_{tot} = 0.4$ M) might have impact on pH measurements in this work. The uncertainty of pH measurements in these specific cases is considered ± 0.1 pH units.

Table 20: A_c - and A_m values used in this work for the quantification of pH_c and pH_m , respectively.

Salt system	Concentration	A_c	A_m
NaCl	0.1 M	-0.08	-0.08
NaCl	1.0 M	0.09	0.08
NaCl	5.0 M	0.95	0.9
CaCl ₂	0.25 M	0	-0.01
CaCl ₂	1.0 M	0.34	0.33

CaCl ₂	3.5 M	1.77	1.71
MgCl ₂	0.25 M	0.03	0.03
MgCl ₂	1.0 M	0.4	0.4
MgCl ₂	3.5 M	1.98	1.93

5.1.3 Speciation of boron in aqueous saline solutions

¹¹B-NMR in NaCl, CaCl₂ and MgCl₂ solutions: ¹¹B-NMR spectra were recorded with a Bruker NMR-spectrometer (Avance III, 400 MHz) with a field strength of 9.4 T and a corresponding ¹¹B resonance frequency of 128.4 MHz with a broadband observe probe. The ¹¹B chemical shifts (δ) are referenced externally with respect to BF₃ etherate in CDCl₃. All spectra were evaluated with the software Top Spin (Bruker). For all spectra a pulse sequence with a very short delay time (100 μ s) was used. The ¹¹B-NMR measurements were performed under atmospheric conditions in teflon liners (Rototec-Spintec, PTFE-FEB-NMR Tube Liner 8", 5 mm) filled with 400 μ L sample solution and mixed with 40 μ L D₂O at 25°C. Table 21 summarizes the samples prepared in dilute and concentrated NaCl, MgCl₂ and CaCl₂ with 0.04-0.4 M total boron concentration with varying pH_m.

Table 21: Experimental conditions in the system investigated by ¹¹B-NMR

System	Concentration of background electrolyte	[B] _{tot}	pH _m
NaCl	0.1 M	0.04 M, 0.16 M	8; 12
NaCl	5.0 M	0.04 M, 0.16 M	2.6; 8; 12
CaCl ₂	0.25 M	0.04 M	8; 12
CaCl ₂	3.5 M	0.04 M	8; 12
MgCl ₂	0.25 M	0.04 M, 0.16 M, 0.4 M	8
MgCl ₂	3.5 M	0.04 M, 0.16 M, 0.4 M	8

5.1.4 Determination of total metal concentration and aqueous speciation techniques used for Ln(III) and An(III/IV/V/VI) in solution

The total aqueous concentration of Nd, Th and U was measured by ICP-MS after phase separation by 10 kD ultrafiltration (~1.5 nm, Pall Life Sciences) (Thermo scientific X-Series II for Nd(III) and Perkin Elmer Elan 6100 for Th(IV) and U(VI)).

LSC measurements were performed to determine concentrations of Np and Pu and the measurement has been done in PP vials (20 mL, Zinsser Analytic). After 10 kD ultrafiltration (~1.5 nm, Pall Life sciences), a small aliquot of the sample was mixed with 10 mL LSC cocktail (Ultima Gold XR, Fa. Perkin-Elmer). Samples were measured for 30 minutes with a Perkin Elmer 1220 Quantulus. The Quantulus apparatus used in this work provides a pulse shape analyzer (PSA) to perform a simultaneous alpha/beta gross counting, which allows the distinction between alpha and beta pulses, and hence, the distinction between ^{237}Np and its daughter ^{233}Pa .

In this work the Pu concentration in solution was determined using the low energetic β -emitter ^{241}Pu , because alpha peaks of ^{242}Pu , ^{239}Pu , ^{238}Pu , and ^{241}Am (daughter from the ^{241}Pu) cannot be separated by LSC.

Cm(III) concentrations and speciation was performed by time resolved laser fluorescence spectroscopy (TRLFS). Experiments were performed with $1 \cdot 10^{-7}$ M Cm(III) per sample in dilute to concentrated NaCl, CaCl₂ and MgCl₂ solution. Total boron concentrations ranged from 0.004 M to 0.4 M. Spectra in NaCl and MgCl₂ systems were collected at $\text{pH}_m = 8.0 \pm 0.1$, whereas spectra in CaCl₂ were collected at $\text{pH}_m = 8.0 \pm 0.1$ and 12.0 ± 0.1 . Cm(III)-TRLFS spectra in NaCl and CaCl₂ solutions with freshly prepared borate solutions ($[\text{B}]_{\text{tot}} \geq 0.04$ M) showed very pronounced kinetic effects. Therefore, sufficiently long equilibration times (~ two weeks) were allowed for all matrix solutions used in the TRLFS experiments shown in this work. After this equilibration time, the Cm(III) was spiked to the matrix solutions. The samples were measured within 2 hours after the Cm(III) addition. Measurements with longer equilibration times (up to 2 days) did not show any relevant kinetic effect on the fluorescence spectra.

The speciation of Np(V) was done by absorption spectroscopy. Absorption spectra of Np(V) were collected with a Varian UV-Vis spectrometer (Cary 5E) against a reference solution with the same background electrolyte and borate concentration as the measured sample. Spectra were recorded in the range $\lambda = 850 - 1250$ nm with a step width of 0.2 nm. All measurements were performed with ~3 mL of sample solution in quartz cuvettes with $d = 1$ cm.

5.1.5 Solid phase characterization (XRD, XPS, SEM-EDS, EXAFS)

Solid phases from the Nd, Pu, Np and U solubility experiments were characterized by XRD, XPS and SEM-EDS after a given equilibrium time. Selected solid phases from the Np(V) solubility experiments were also investigated by EXAFS.

5.1.6 Ln(III)/An(III/IV/V/VI) solubility experiments

Nd(III) and An(III/IV/V/VI) solid phase preparation

Amorphous Nd(III) hydroxide used in the solubility experiments was prepared by hydration of crystalline neodymium hydroxide ($\text{Nd}_2\text{O}_3(\text{cr})$, Merck) in Milli-Q water under an argon atmosphere (Neck et al., 2009). The complete transformation of the oxide into the hydroxide phase was confirmed by XRD (JCPDF file No: 70-0214, JCPDS 2001). $\text{Nd}[\text{B}_9\text{O}_{13}(\text{OH})_4](\text{cr})$ was prepared by the group of Dr. Evgeny Alekseev at the research center Jülich (FZJ).

To prepare $\text{Pu}^{\text{IV}}\text{O}_2(\text{am,hyd})$, a purified $^{242}\text{Pu}(\text{VI})$ stock solution was added to a pH-buffered (25 mM MES) and redox-buffered (1.5 mM hydroquinone) solution leading to an immediate formation of aqueous Pu(V) and a slow “reductive precipitation” of $\text{Pu}^{\text{IV}}\text{O}_2(\text{am,hyd})$. The mild in situ “reductive precipitation” leads to a microcrystalline solid phase which is less affected to aging effects than “fresh” $\text{Pu}^{\text{IV}}\text{O}_2(\text{am,hyd})$ prepared by addition of NaOH to an acidic Pu(IV) solution.

$\text{Th}(\text{OH})_4(\text{am})$ was prepared under argon atmosphere by titration of thorium chloride stock solution with carbonate-free NaOH up to pH ~ 10 . The precipitate was washed with Milli-Q water several times before further use in the solubility experiments.

$\text{NpO}_2\text{OH}(\text{am,fresh})$ was prepared under argon atmosphere by titration of a (radiochemically pure) acidic $^{237}\text{Np}(\text{V})$ stock solution with carbonate-free NaOH. The resulting precipitate ($\text{NpO}_2\text{OH}(\text{am,fresh})$) was separated from the solution by centrifugation and washed several times with water before use in the solubility experiments.

Metaschoepite $\text{UO}_3 \cdot 2\text{H}_2\text{O}(\text{cr})$ was prepared under argon atmosphere by a very slow titration of an acidic uranium(VI) chloride stock solution with carbonate-free NaOH. In the precipitation process, the pH was checked regularly and kept always below 5 to avoid the transformation of $\text{UO}_3 \cdot 2\text{H}_2\text{O}(\text{cr})$ into sodium uranate or other Na–U(IV)–OH ternary phases.

Sodium uranate, $\text{Na}_2\text{UO}_2\text{O}_7 \cdot \text{H}_2\text{O}(\text{cr})$, was prepared by transformation of initial metaschoepite in 2.5 M NaCl solution at $\text{pH}_m \sim 12$ for several months. The new formed solid was separated and washed before use in the solubility experiments.

Sample preparation

All experiments were prepared and carried out at 22 ± 2 °C in Ar-gloveboxes under exclusion of $\text{O}_2(\text{g})$ and $\text{CO}_2(\text{g})$. Solubility samples in NaCl, MgCl_2 and CaCl_2 solutions were prepared from undersaturation conditions of the respective Ln/An hydroxide. A detailed list of all prepared samples for $\text{Nd}(\text{OH})_3(\text{am})$, $\text{PuO}_2(\text{am,hyd})$, $\text{Th}(\text{OH})_4(\text{am})$, $\text{NpO}_2\text{OH}(\text{am,fresh})$, $\text{UO}_3 \cdot 2\text{H}_2\text{O}(\text{cr})$ and $\text{Na}_2\text{U}_2\text{O}_7 \cdot \text{H}_2\text{O}(\text{cr})$ is given in Table 22 to Table

27. Boron concentrations ($[B]_{tot}$) in $MgCl_2$, $NaCl$ and $CaCl_2$ solutions were restricted to 0.4 M, 0.16 M and 0.04 M, respectively. The limitations in solubility observed for these systems are likely related with the formation of stable Mg-, Na- and Ca-borate solid phases [85]. Preliminary spectroscopic experiments (Cm(III)–TRLFS) conducted with freshly prepared borate solutions showed Cm(III)-borate complex formation with pronounced kinetic effects, which decreased notably with the pre-equilibration of borate in the corresponding saline solution. Consequently, the boron containing saline solutions were equilibrated for at least 2 weeks before the addition of the Ln/An hydroxide phase. Solubility experiments with $PuO_2(am,hyd)$ were performed in 0.1 M $NaCl$ solution and $[B]_{tot} = 0.16$ M in the present of 2 mM $Na_2S_2O_4$ and hydroquinone as reducing system. Ln/An concentrations, pH and Eh (Pu experiments) were determined at regular time intervals for up to 860 days. The concentration of Ln/An(III) was quantified after phase separation by 10 kD ultrafiltration (~ 1.5 nm, Pall Life Sciences) by ICP-MS and LSC.

Table 22: Experimental conditions in the solubility study with $Nd(OH)_3(am)$.

System	Concentration of background electrolyte	$[B]_{tot}$	pHm	Equilibration time
NaCl	0.1 M	0.004 M; 0.04 M; 0.16 M	7-13	7-142 days
NaCl	5.0 M	0.004 M; 0.04 M; 0.16 M	8-13	7-142 days
$CaCl_2$	0.25 M	0.004 M; 0.04 M	8-12	7-142 days
$CaCl_2$	3.5 M	0.004 M; 0.04 M	8-12	7-142 days
$MgCl_2$	0.25 M	0.004 M; 0.04 M; 0.16 M; 0.4 M	8-12	7-72 days
$MgCl_2$	3.5 M	0.004 M; 0.04 M; 0.16 M; 0.4 M	8-12	7-72 days

Table 23: Experimental conditions in the solubility study with $Nd[B_9O_{13}(OH)_4](cr)$.

System	Concentration of background electrolyte	$[B]_{tot}$	pHm	Equilibration time
NaCl	0.1 M; 5.0 M	0.16 M	6-9	7-48 days
$MgCl_2$	0.25 M; 3.5 M	0.16 M	6-9	7-48 days

Table 24: Experimental conditions in the solubility study with $PuO_2(am,hyd)$.

System	Concentration of background electrolyte	$[B]_{tot}$	Reducing chemical	pHm	Equilibration time
NaCl	0.1 M	0.16 M	$Na_2S_2O_4$	7.5; 9	14-300 days
NaCl	0.1 M	0.16 M	Hydroquinone	7.5; 9	14-300 days

Table 25: *Experimental conditions in the solubility study with Th(OH)₄(am).*

System	Concentration of background electrolyte	[B] _{tot}	pH _m	Equilibration time
NaCl	0.1 M	0 M; 0.16 M	7; 9; 11	14-860 days
NaCl	5.0 M	0 M; 0.16 M	8; 9; 11	14-860 days
MgCl ₂	0.25 M	0 M; 0.16 M	7.5; 9	14-860 days
MgCl ₂	3.5 M	0 M; 0.16 M	7.5; 9	14-860 days

Table 26: *Experimental conditions in the solubility study with NpO₂OH(am, fresh).*

System	Concentration of background electrolyte	[B] _{tot}	pH _m	Equilibration time
NaCl	0.1 M	0.04 M; 0.16 M	8-9	14-300 days
NaCl	5.0 M	0.04 M; 0.16 M	8-9	14-300 days
MgCl ₂	0.25 M	0.04 M; 0.16 M	8-9	14-300 days
MgCl ₂	3.5 M	0.04 M; 0.16 M	8-9	14-300 days

Table 27: *Experimental conditions in the solubility study with UO₃·2 H₂O(cr) and Na₂U₂O₇·H₂O(cr).*

System	Concentration of background electrolyte	[B] _{tot}	pH _m	Equilibration time
NaCl	0.1 M	0 M; 0.04 M; 0.16 M	7; 9; 11	14-138 days
NaCl	5.0 M	0 M; 0.04 M; 0.16 M	8; 9; 11	14-138 days
MgCl ₂	0.25 M	0 M; 0.04 M; 0.16 M	7.5; 9	14-138 days
MgCl ₂	3.5 M	0 M; 0.04 M; 0.16 M	7.5; 9	14 138 days

5.2 ¹¹B-NMR in NaCl, CaCl₂ and MgCl₂ solutions

In this work, ¹¹B-NMR spectra were collected in dilute to concentrated NaCl and MgCl₂ solutions within $2.6 \leq \text{pH}_m \leq 12$ and $0.04 \text{ M} \leq [\text{B}]_{\text{tot}} \leq 0.4 \text{ M}$ with the aim of gaining further insight on the speciation of boron, especially under the poorly investigated highly

saline conditions. An introduction about the boron chemistry as well as interpretation of recorded NMR spectra can be found in (Hinz, 2015).

5.2.1 ^{11}B -NMR studies in NaCl solutions

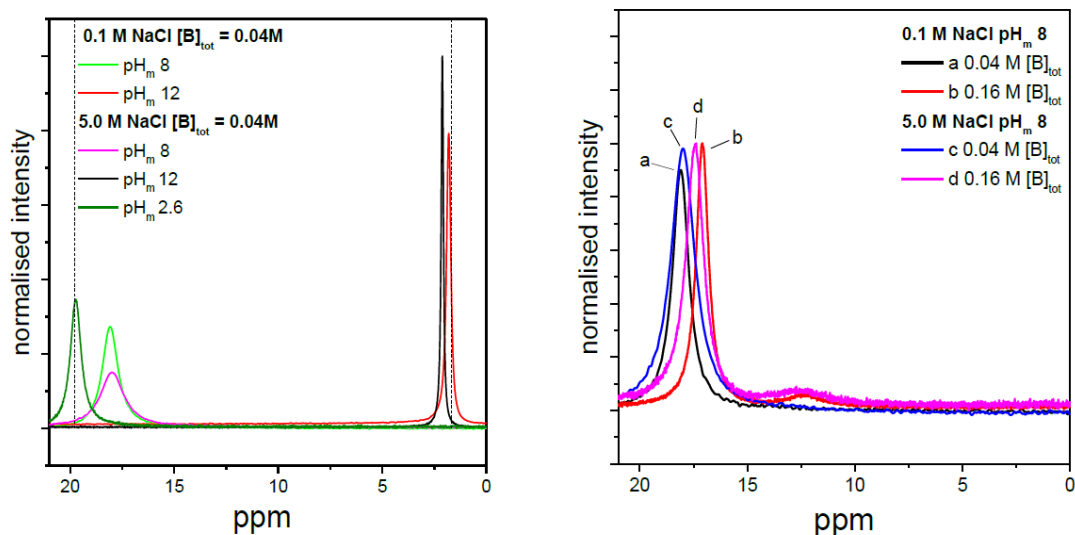


Figure 60: ^{11}B -NMR spectra collected in 0.1 M and 5.0 M NaCl solutions: (left) spectra with $2.6 \leq \text{pH}_m \leq 12$ and $[\text{B}]_{\text{tot}} = 0.04 \text{ M}$, (right) spectra with $\text{pH}_m = 8$ and a) 0.04 M $[\text{B}]_{\text{tot}}$ b) 0.16 M $[\text{B}]_{\text{tot}}$ in 0.1 M NaCl and c) 0.04 M $[\text{B}]_{\text{tot}}$ d) 0.16 M $[\text{B}]_{\text{tot}}$ in 5.0 M NaCl.

^{11}B -NMR spectra were collected for 0.1 M and 5.0 M NaCl solutions with $0.04 \text{ M} \leq [\text{B}]_{\text{tot}} \leq 0.16 \text{ M}$ at $\text{pH}_m = 2.6, 8$ and 12 are shown in Figure 60. A single reference signal corresponding to the exchange peak of the monomeric species $\text{B}(\text{OH})_3(\text{aq})\text{--B}(\text{OH})_4^-$ is observed in all systems with $[\text{B}]_{\text{tot}} \leq 0.04 \text{ M}$. At this $[\text{B}]_{\text{tot}}$ no (or very few) polyborates are present in solution. In the NaCl system at $\text{pH}_m = 2.6$, the peak at $\sim 20 \text{ ppm}$ can be unequivocally assigned to $\text{B}(\text{OH})_3(\text{aq})$. In dilute and concentrated NaCl systems and $\text{pH}_m = 8$, the peak observed 17–18 ppm indicates the predominance of $\text{B}(\text{OH})_3(\text{aq})$ in the solution. For the same pH a broad second peak can be observed at $[\text{B}]_{\text{tot}} = 0.16 \text{ M}$. According to studies in KCl, NaCl and LiCl solutions this broad peak at $\sim 12\text{--}14 \text{ ppm}$ can be assigned to the triborate species $\text{B}_3\text{O}_3(\text{OH})_4^-$ (Hertam, 2011; Salentine, 1983). At $\text{pH}_m = 12$, the chemical shift observed at 0–3 ppm agrees very well with the expected predominance of $\text{B}(\text{OH})_4^-$ in the solution at high pH_m . The results in NaCl solutions are in good agreement with data from Borkowski and co-workers measured in water at comparable $[\text{B}]_{\text{tot}}$ (Borkowski et al., 2011).

5.2.2 ^{11}B -NMR studies in CaCl_2 and MgCl_2 solutions

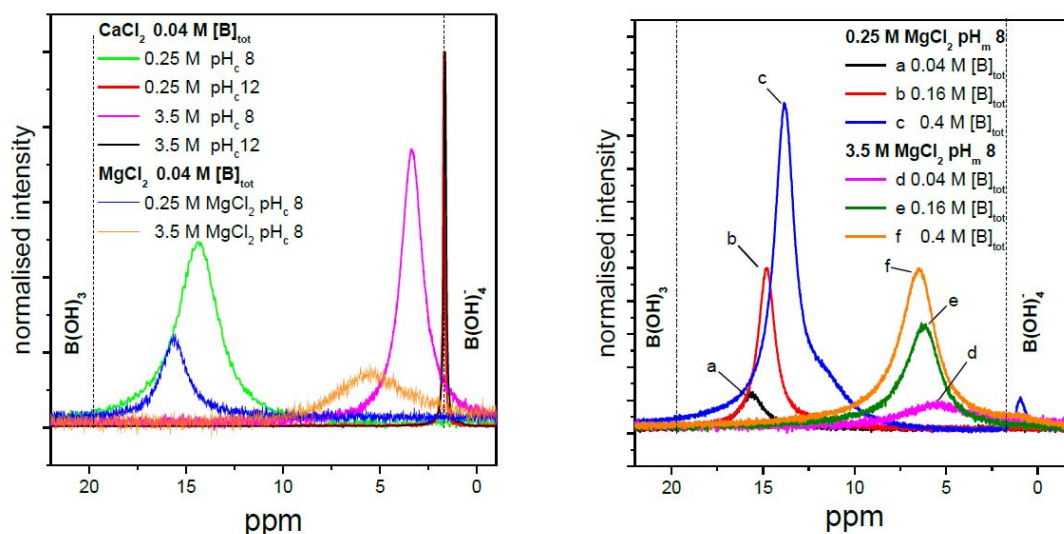


Figure 61: ^{11}B -NMR spectra collected in 0.25 M and 3.5 M CaCl_2 and MgCl_2 solutions: (left) spectra with $8 \leq \text{pH}_c \leq 12$ and $[\text{B}]_{\text{tot}} = 0.04 \text{ M}$, (right) spectra with $\text{pH}_m = 8$ and a) 0.04 M $[\text{B}]_{\text{tot}}$ b) 0.16 M c) 0.4 M $[\text{B}]_{\text{tot}}$ in 0.25 M MgCl_2 and d) 0.04 M $[\text{B}]_{\text{tot}}$ e) 0.16 M $[\text{B}]_{\text{tot}}$ f) 0.4 M $[\text{B}]_{\text{tot}}$ in 3.5 M MgCl_2 .

^{11}B -NMR spectra were collected for 0.25 M and 3.5 M CaCl_2 with $[\text{B}]_{\text{tot}} = 0.04 \text{ M}$ at $\text{pH}_m = 8$ and 12, and collected for 0.25 M and 3.5 M MgCl_2 with $0.04 \text{ M} \leq [\text{B}]_{\text{tot}} \leq 0.4 \text{ M}$ at $\text{pH}_m = 8$ are shown in Figure 61. For comparison purposes, peak positions for $\text{B}(\text{OH})_3(\text{aq})$ and $\text{B}(\text{OH})_4^-$ in NaCl solutions are shown as dashed lines. Analogously to the NaCl system, a single resonance peak is visible in the spectra collected for samples in CaCl_2 and MgCl_2 solutions with $[\text{B}]_{\text{tot}} = 0.04 \text{ M}$. Nevertheless, significantly broader peaks are detected in these salt solutions compared to the NaCl system. At $\text{pH}_m = 8$, the peak at $\sim 17\text{--}18 \text{ ppm}$ observed in the NaCl system and indicating the predominance of $\text{B}(\text{OH})_3(\text{aq})$ is shifted to lower ppm in CaCl_2 and MgCl_2 solution. Note further that the peak broadening and peak shift are more pronounced in concentrated MgCl_2 and CaCl_2 solutions for the same pH ($\text{pH}_m = 8$) and boron concentration ($[\text{B}]_{\text{tot}} = 0.04 \text{ M}$). This observation can be likely explained by the complexation of Mg/Ca with B , as presented in the thermodynamic calculations shown in Figure 62 conducted using the thermodynamic and activity models reported by Felmy and co-workers on the system Mg^{2+} - $\text{B}(\text{OH})_4^-$ - Cl^- - H_2O (Felmy and Weare, 1986).

In 0.25 M MgCl_2 solutions with $\text{pH}_m = 8$, the peak position is shifted from $\sim 16 \text{ ppm}$ to $\sim 13 \text{ ppm}$ when increasing $[\text{B}]_{\text{tot}}$ from 0.04 M to 0.4 M. The observed peak at $[\text{B}]_{\text{tot}} = 0.4 \text{ M}$ is very broad and shows a pronounced shoulder at $\sim 12 \text{ ppm}$ and a second small peak at 0.7 ppm. The shoulder and the additional peak indicate the presence of more than one boron species present in the investigated solution. A significant peak broadening is also observed in 3.5 M MgCl_2 solutions. The fraction diagram shown in Figure 62 shows the predominance of $\text{B}(\text{OH})_3(\text{aq})$ and $\text{MgB}(\text{OH})_4^-$ species, and thus the observed peak broadening cannot be attributed to the presence of polyborate species. In

contrast to the NaCl system, no peak assignment is possible in CaCl₂ and MgCl₂ systems at pH_m 8 due to the lack of literature data.

At pH_m = 12 in CaCl₂ systems the peak position at ~ 2 ppm indicates B(OH)₄⁻ as main borate species similar to observations made in NaCl systems. In contrast to systems at lower pH values, no broadening of this peak is observed at increased CaCl₂ concentration. No further information on aqueous boron speciation in saline solution can be drawn from the measured NMR spectra.

5.2.3 Conclusions

¹¹B-NMR studies conducted in NaCl, CaCl₂ and MgCl₂ solutions at pH_m = 2.6, 8 and 12 give insight in the complex borate speciation in saline solutions. Spectra measured in NaCl solutions are similar to spectra collected in water with the same pH_m and comparable [B]_{tot}. According to the collected spectra and consistently with literature data, the speciation of boron is only weakly influenced by the presence of monovalent cations like Na⁺, K⁺ and Li⁺ (Hertam, 2011; Salentine, 1983). Based on the reported literature data, the detected peaks can be correctly assigned to the expected boron species, although no quantitative analysis of the spectra is possible.

In contrast to the NaCl systems, very broad peaks are observed in CaCl₂ and MgCl₂ solutions. At pH_m = 8 the peak position in both CaCl₂ and MgCl₂ systems is significantly shifted compared to peaks at same pH_m and [B]_{tot} measured in NaCl solutions, indicating the formation of Ca/Mg–borate complex. This is in good agreement with thermodynamic calculations indicating the formation of the complex MgB(OH)₄⁺. For more specific information on the boron speciation in presence of high NaCl, CaCl₂ and MgCl₂ concentrations, additional comprehensive experiments are needed.

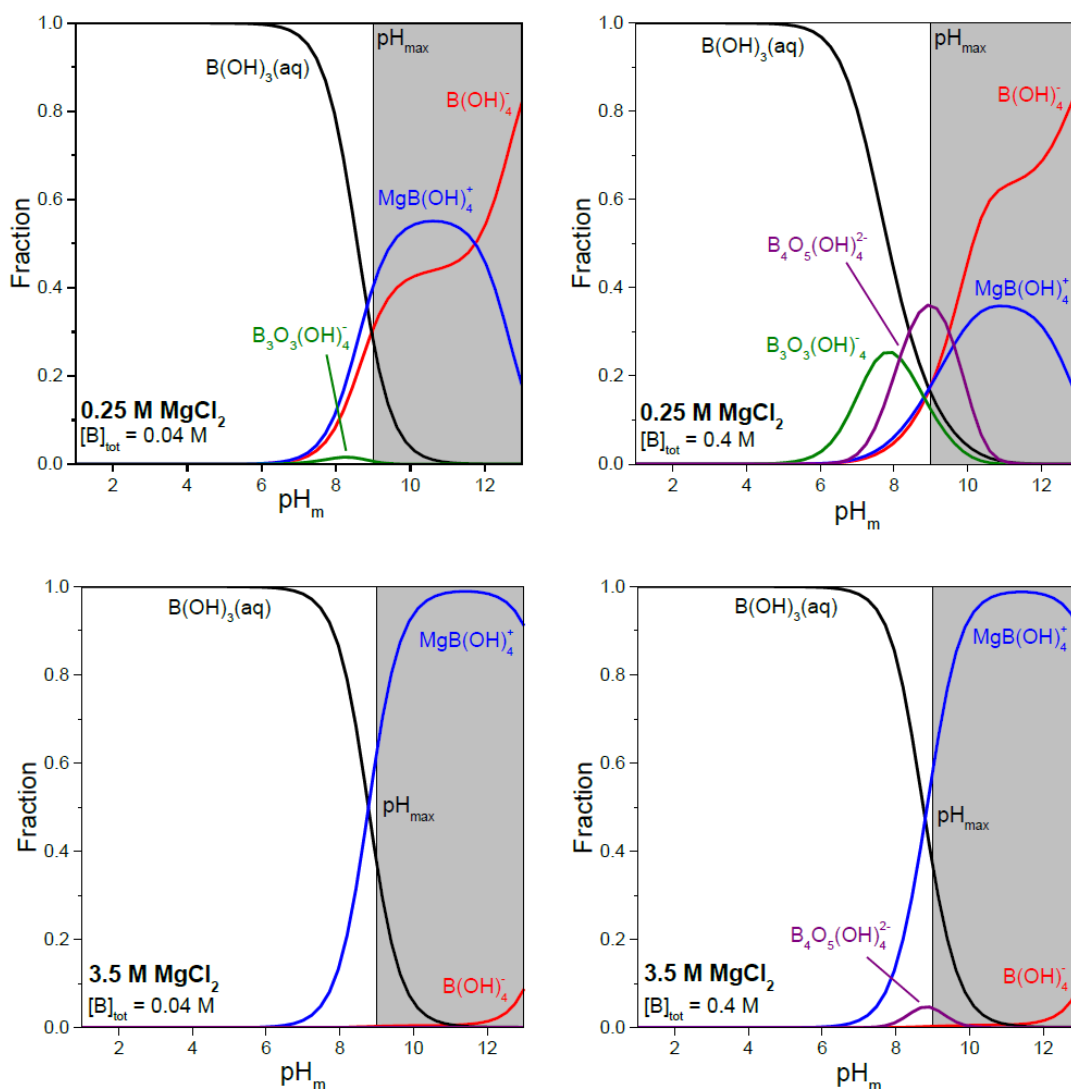


Figure 62: Fraction diagram of aqueous borate species in 0.25 M and 3.5 M MgCl_2 as calculated with the thermodynamic and activity models reported in (Felmy and Weare, 1986). The highest pH in dilute to concentrated MgCl_2 solutions is limited to $\text{pH}_{\text{max}} \sim 9$ by the precipitation of $\text{Mg}(\text{OH})_2(\text{s})$ or $\text{Mg}-\text{OH}-\text{Cl}$ phases, and thus calculations above this pH represent only a modelling exercise giving insight on the possible interaction Ca -borate in CaCl_2 systems (where $\text{pH}_{\text{max}} \sim 12$) under the assumption of a comparable complexation behavior of Ca^{2+} and Mg^{2+} .

5.3 Interaction of Ln(III)/An(III) with borate

The interaction of Ln(III)/An(III) with borate was investigated from undersaturation conditions with $\text{Nd}(\text{OH})_3(\text{am})$ in dilute to concentrated NaCl , CaCl_2 and MgCl_2 solutions with $0.04 \text{ M} \leq [\text{B}]_{\text{tot}} \leq 0.4 \text{ M}$ at $6 \leq \text{pH}_m \leq 13$. Samples were equilibrated for up to 142 days, and pH_m and $[\text{Nd}(\text{III})]$ were monitored at regular time intervals. After attaining equilibrium conditions, selected solid phases were characterized by XPS, SEM-EDS and XRD. For comparison purposes, additional solubility experiments with a well-

defined Nd(III) borate solid phase, $\text{Nd}[\text{B}_9\text{O}_{13}(\text{OH})_4](\text{cr})$, were performed in NaCl and MgCl_2 solutions with $[\text{B}]_{\text{tot}} = 0.16 \text{ M}$. The aqueous phase was further investigated by TRLFS with 10^{-7} M Cm(III) in $0.1 - 5.0 \text{ M}$ NaCl, $0.25 - 3.5 \text{ M}$ MgCl_2 and $0.25 - 3.5 \text{ M}$ CaCl_2 with $0.004 \text{ M} \leq [\text{B}]_{\text{tot}} \leq 0.4 \text{ M}$ and $\text{pH}_m = 8$. Additional Cm(III) TRLFS spectra were collected at $\text{pH}_m = 12$ for CaCl_2 systems.

5.3.1 Solubility of Nd(III) in NaCl, CaCl_2 and MgCl_2 solutions

The experimental solubility data of Nd(III) determined in $0.1 \text{ M} - 5.0 \text{ M}$ NaCl and $0.25 \text{ M} - 3.5 \text{ M}$ MgCl_2 and CaCl_2 solutions in the presence of $0.004 \text{ M} \leq [\text{B}]_{\text{tot}} \leq 0.4 \text{ M}$ are shown in Figure 63 to Figure 68. Note that only data corresponding to thermodynamic equilibrium (constant pH_m and $[\text{Nd}(\text{III})]$) are presented in the figures. For comparison purposes, the figures also show the experimental solubility data and calculated solubility curves for $\text{Nd}(\text{OH})_3(\text{am})$ as reported by Neck et al. in the absence of borate under analogous pH_m and ionic strength conditions (Neck et al., 2009). In the figures of 0.1 M , 5.0 M NaCl and 0.25 M , 3.5 M MgCl_2 systems undersaturation solubility data obtained with $\text{Nd}[\text{B}_9\text{O}_{13}(\text{OH})_4](\text{cr})$ and $[\text{B}]_{\text{tot}} = 0.16 \text{ M}$ are also provided.

No significant effect of borate on Nd(III) solubility is observed in near neutral to slightly alkaline pH_m values ($7 \leq \text{pH}_m \leq 9$) and $[\text{B}]_{\text{tot}} \leq 0.04 \text{ M}$ (dilute salt systems: 0.1 and 1.0 M NaCl; 0.25 M MgCl_2) or $[\text{B}]_{\text{tot}} \leq 0.004 \text{ M}$ (concentrated salt systems: 5.0 M NaCl; 1.0 and 3.5 M MgCl_2). Under these conditions, the concentration of Nd(III) is in good agreement with borate-free solubility data obtained under analogous pH_m and ionic strength conditions (Neck et al., 2009).

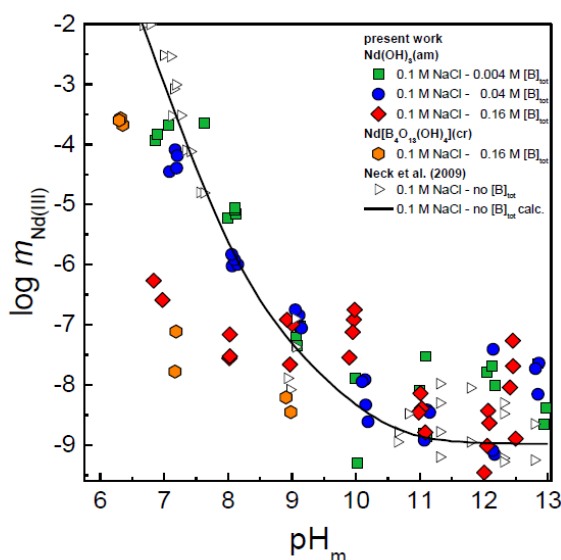


Figure 63: Solubility of $\text{Nd}(\text{OH})_3(\text{am})$ and $\text{Nd}[\text{B}_9\text{O}_{13}(\text{OH})_4](\text{cr})$ in the presence of $0.004 \text{ M} \leq [\text{B}]_{\text{tot}} \leq 0.16 \text{ M}$ in 0.1 M NaCl solutions. Comparison with experimental (open symbols, black) and calculated (solid line) solubility data in the absence of borate as reported in (Neck et al., 2009).

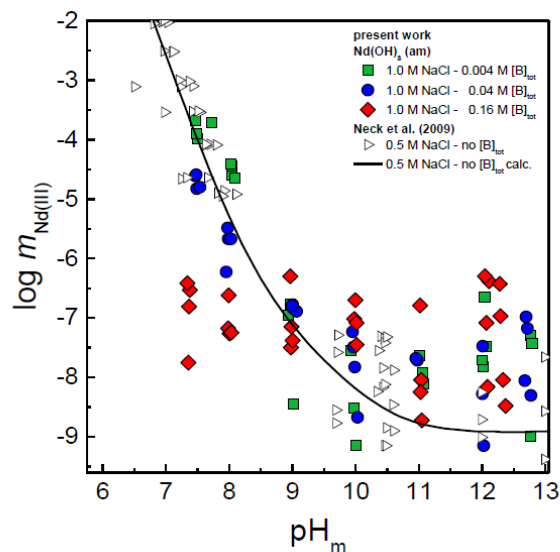


Figure 64: Solubility of $\text{Nd}(\text{OH})_3(\text{am})$ in the presence of $0.004 \text{ M} \leq [\text{B}]_{\text{tot}} \leq 0.16 \text{ M}$ in 1.0 M NaCl solutions. Comparison with experimental (open symbols, black) and calculated (solid line) solubility data in the absence of borate as reported in (Neck et al., 2009).

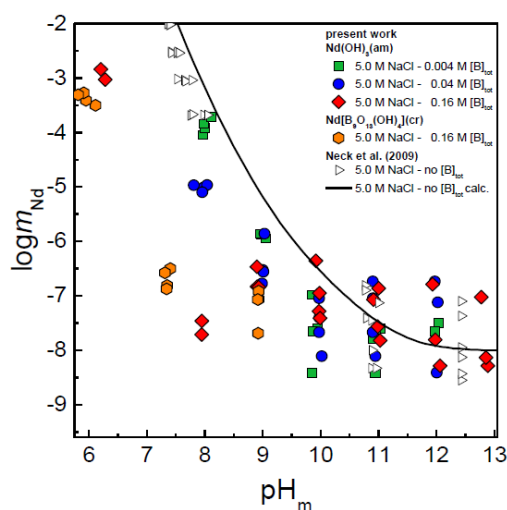


Figure 65: Solubility of $\text{Nd}(\text{OH})_3(\text{am})$ and $\text{Nd}[\text{B}_9\text{O}_{13}(\text{OH})_4](\text{cr})$ in the presence of $0.004 \text{ M} \leq [\text{B}]_{\text{tot}} \leq 0.16 \text{ M}$ in 5.0 M NaCl solutions. Comparison with experimental (open symbols, black) and calculated (solid line) solubility data in the absence of borate as reported in (Neck et al., 2009).

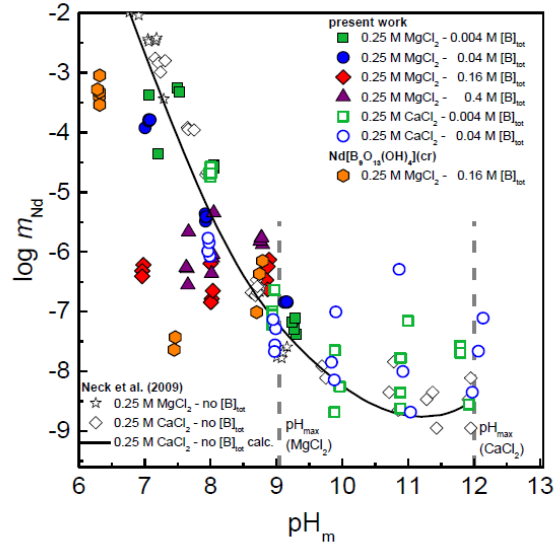


Figure 66: Solubility of $\text{Nd}(\text{OH})_3(\text{am})$ and $\text{Nd}[\text{B}_9\text{O}_{13}(\text{OH})_4](\text{cr})$ in the presence of $0.004 \text{ M} \leq [\text{B}]_{\text{tot}} \leq 0.4 \text{ M}$ in 0.25 M MgCl_2 and CaCl_2 solutions. Comparison with experimental (open symbols, black) and calculated (solid line) solubility data in the absence of borate as reported in (Neck et al., 2009).

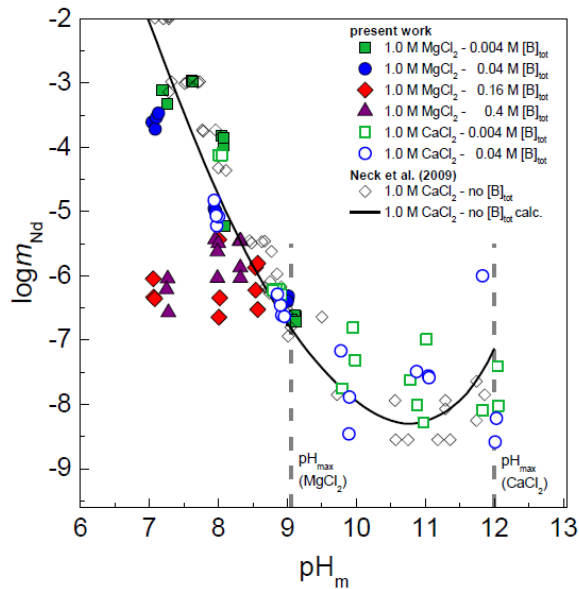


Figure 67: Solubility of $\text{Nd}(\text{OH})_3(\text{am})$ in the presence of $0.004 \text{ M} \leq [\text{B}]_{\text{tot}} \leq 0.4 \text{ M}$ in 1.0 M MgCl_2 and CaCl_2 solutions. Comparison with experimental (open symbols, black) and calculated (solid line) solubility data in the absence of borate as reported in (Neck et al., 2009).

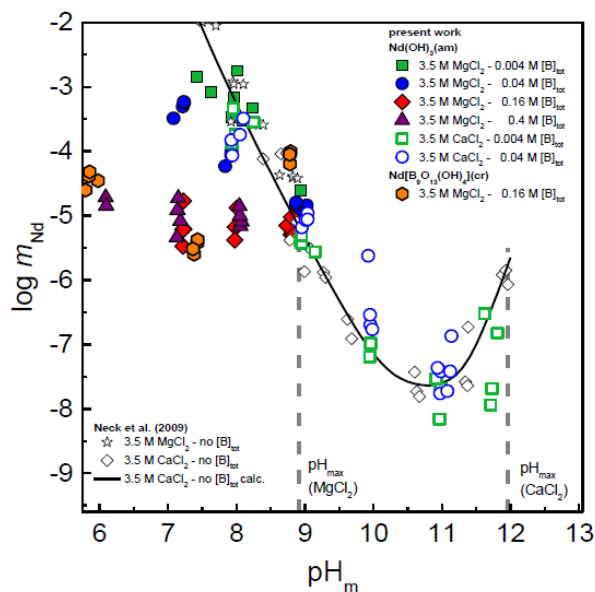


Figure 68: Solubility of $\text{Nd}(\text{OH})_3(\text{am})$ and $\text{Nd}[\text{B}_9\text{O}_{13}(\text{OH})_4](\text{cr})$ in the presence of $0.004 \text{ M} \leq [\text{B}]_{\text{tot}} \leq 0.4 \text{ M}$ in 3.5 M MgCl_2 and CaCl_2 solutions. Comparison with experimental (open symbols, black) and calculated (solid line) solubility data in the absence of borate as reported in (Neck et al., 2009).

At enhanced $[\text{B}]_{\text{tot}} \geq 0.16 \text{ M}$, a significant decrease in the $\text{Nd}(\text{III})$ concentration occurs for all NaCl and MgCl_2 systems evaluated. The drop in solubility at $[\text{B}]_{\text{tot}} \sim 0.16\text{--}0.4 \text{ M}$ is accompanied with a changed slope of the solubility curve from -2 to approximately 0 . This observation clearly indicates the transformation of $\text{Nd}(\text{OH})_3(\text{am})$ into a new solubility controlling borate-bearing solid phase. After an equilibration time of 72 to 142 days (depending upon salt system), the measured $\text{Nd}(\text{III})$ concentrations remain constant at $\square 10\text{--}6.5 \text{ M}$ (in 0.25 M MgCl_2) to $10\text{--}5 \text{ M}$ (in 3.5 M MgCl_2). These solubility limits are more than three orders of magnitude lower than those observed in the absence of borate (Hinz, 2015). The decrease in $\text{Nd}(\text{III})$ solubility in NaCl solutions is similar, although the overall solubility is slightly lower indicating that increasing MgCl_2 concentrations and resulting high ionic strength enhances significantly the solubility of $\text{Nd}(\text{III})$ in the presence of borate as it is also the case in borate-free systems. No (or very limited) effect of borate on $\text{Nd}(\text{III})$ solubility is observed in CaCl_2 solutions in contrast to NaCl and MgCl_2 systems, very likely due to the lower boron solubility in this background electrolyte ($[\text{B}]_{\text{tot}} \leq 0.04 \text{ M}$).

Solid phase characterization

Solid phases of selected solubility experiments were investigated after attaining equilibrium conditions by XRD, SEM-EDS and XPS. Very distinct XRD pattern are observed for this solid phase, confirming that none of the solubility experiments initiated with $\text{Nd}(\text{OH})_3(\text{am})$ led to the formation of this solid phase (above the detection limit of XRD, $\square 5\%$). In contrast to XRD, XPS analyses of the solid phases from solubility samples with $[\text{B}]_{\text{tot}} \geq 0.16 \text{ M}$ confirm the presence of a newly formed borate-bearing secondary

phase on the surface of $\text{Nd}(\text{OH})_3(\text{am})$ indicating the formation of a new solubility controlling borate-bearing solid phase. This mechanism is confirmed by SEM–EDS technique, which suggest that the formation of a Nd(III)-borate solid phase takes place as a coating on an unreacted $\text{Nd}(\text{OH})_3(\text{am})$ core (for details see in (Hinz, 2015)).

5.3.2 Cm(III) aqueous speciation in the presence of borate: TRLFS

Fluorescence emission spectra of Cm(III) were measured with $0.004 \text{ M} \leq [\text{B}]_{\text{tot}} \leq 0.4$ in 0.1 M – 5.0 M NaCl and 0.25 M – 3.5 M CaCl_2 and MgCl_2 solutions at $\text{pH}_m = 8$. The normalised spectra in 0.1 M and 5.0 M NaCl solution are presented in Figure 69. Spectra at $\text{pH}_m = 8$ in 0.25 M and 3.5 M MgCl_2 solutions are presented in Figure 70. In CaCl_2 solutions additional spectra with $0.004 \leq [\text{B}]_{\text{tot}} \leq 0.04 \text{ M}$ at $\text{pH}_{\text{max}} \sim 12$ were taken and are shown in Figure 71. Furthermore, fluorescence decay measurements were performed for Cm(III) in NaCl, CaCl_2 and MgCl_2 solutions with $0.004 \text{ M} \leq [\text{B}]_{\text{tot}} \leq 0.4$ at $\text{pH}_m = 8$. Note that boron concentrations in NaCl and CaCl_2 solutions were restricted due to the precipitation of Na- and Ca-borate solid phases, to 0.16 M and 0.04 M , respectively. The resulting fluorescence lifetimes are presented in Table 28.

Cm(III) TRLFS studies in NaCl solutions

In the near neutral pH_m region ($\text{pH}_m = 8$) in the absence of borate, several Cm(III) species are expected to be present in solution simultaneously. Their relative contribution depends on the ionic strength and electrolyte composition of the respective solution. Besides the free Cm^{3+} aquo ion, also Cm(III) complexes such as CmCl_2^{2+} , CmCl_2^+ , $\text{Cm}(\text{OH})_2^{2+}$ and $\text{Cm}(\text{OH})_2^+$ can be present in different proportions. At very low $[\text{B}]_{\text{tot}} = 0.004 \text{ M}$ no significant influence of borate on Cm(III) aqueous speciation can be observed in all investigated samples (Figure 69). The peak maximum, located at $\sim 603 \text{ nm}$ of the scattered spectra in 0.1 M NaCl solution can be associated mainly with the $\text{Cm}(\text{OH})_2^+$ complex.. In the absence of complexing ligands other than hydroxide, generally a strong decrease in aqueous Cm(III) concentration at higher pH_m ($\text{pH}_m \geq 8$) is observed due to sorption on surfaces and precipitation as hydroxide. This explains the low intensities and spectral scattering observed for these measured spectra at very low $[\text{B}]_{\text{tot}}$.

In 5.0 M NaCl and $[\text{B}]_{\text{tot}} = 0.004 \text{ M}$ two peaks with maxima at 594 nm and 604 nm can be found. The first peak can be attributed to the Cm(III) aquo ion (with small contributions of chloro complexes very likely present in higher NaCl concentrations), the second peak can be assigned to the second hydrolysis species $\text{Cm}(\text{OH})_2^+$, as expected at $\text{pH}_m = 8$. The measured spectra with low $[\text{B}]_{\text{tot}}$ in NaCl solutions are in good agreement with the corresponding solubility data (Figure 63 and Figure 65).

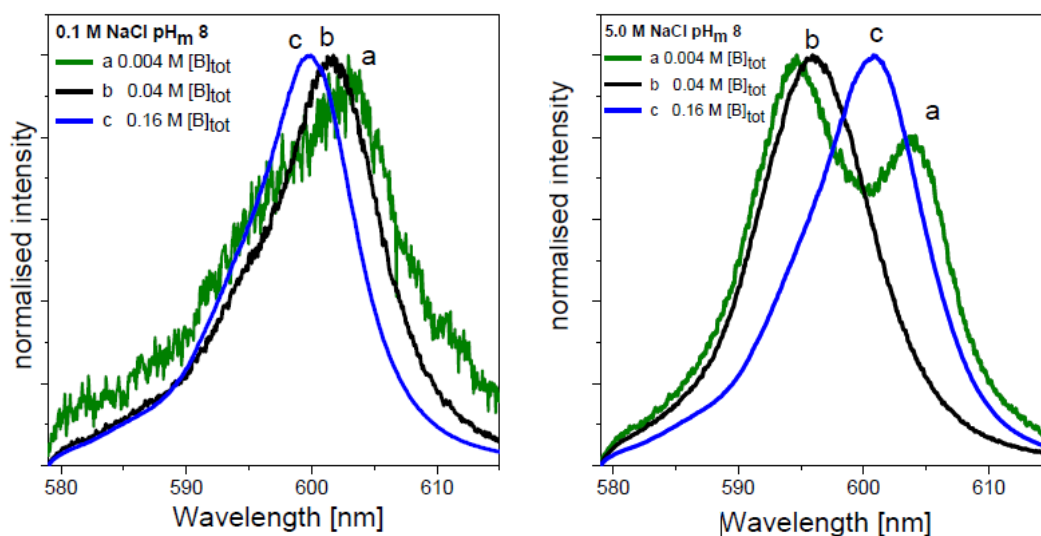


Figure 69: TRLFS emission spectra of Cm(III) in 0.1 M and 5.0 M NaCl solutions at $\text{pH}_m = 8$ and various borate concentrations.

With increasing $[\text{B}]_{\text{tot}}$ ($[\text{B}]_{\text{tot}} > 0.004\text{M}$), an effect of borate on the Cm(III) speciation is observed in 0.1 M NaCl solutions with a peak shift to shorter wavelengths in combination with an increased fluorescence intensity of the spectra. At $[\text{B}]_{\text{tot}} = 0.16\text{ M}$ the competition between borate complexation and hydrolysis leads to a suppression of the Cm(III) hydrolysis species and the formation of a borate containing Cm(III) complex with a peak maximum at $\sim 600\text{ nm}$. A very short fluorescence lifetime ($\tau = 59\ \mu\text{s}$) at $[\text{B}]_{\text{tot}} = 0.16\text{ M}$ is observed in 0.1 M NaCl solutions. This decrease in the fluorescence lifetime together with a clear shift in the emission spectra in comparison to the Cm(III) aquo ion cannot be explained at the moment. The presence of Cm(III) containing colloids by precipitation of a Cm(III) borate solid, in accordance to the analogue Nd(III)-solubility experiments (Figure 63), could lead to a decrease in the fluorescence lifetime.

The double peak observed in 5.0 M NaCl solution and at $[\text{B}]_{\text{tot}} = 0.004\text{ M}$ indicates that the Cm(III) hydrolysis at $\text{pH}_m = 8$ is less pronounced compared to 0.1 M NaCl and considerable amounts of uncomplexed Cm^{3+} are still present. By increase of $[\text{B}]_{\text{tot}}$ to 0.04 M, the peak maximum assigned to the second hydrolysis species at $\sim 604\text{ nm}$ disappears due to competition with borate and a broad peak with a peak maximum at $\sim 596\text{ nm}$ can be detected consisting of contributions of Cm^{3+} and a new formed Cm(III) borate component. Further increase of $[\text{B}]_{\text{tot}}$ up to 0.16 M leads to a decrease of the Cm(III) aquo ion contribution, the fluorescence peak is shifted to $\sim 601\text{ nm}$ which can be explained only by the formation of a Cm(III)–borate complex. At the same time an increase of the corresponding fluorescence lifetime from $77\ \mu\text{s}$ at $[\text{B}]_{\text{tot}} = 0.04\text{ M}$ to $108\ \mu\text{s}$ at $[\text{B}]_{\text{tot}} = 0.16\text{ M}$ is measured. The fluorescence decay curves in all investigated systems show a single averaged exponential decay for all spectra, caused by a faster ligand exchange than the lifetime of the excited state. According to the relation of (Kimura et al., 1996), 4 H_2O molecules are removed from the first hydration sphere of the Cm(III) complex at $[\text{B}]_{\text{tot}} = 0.16\text{ M}$. Note that no influence of high ionic strength on this linear relation is considered. The peak positions ($\sim 600\text{-}601\text{ nm}$) at $[\text{B}]_{\text{tot}} = 0.16\text{ M}$ for

both 0.1 M and 5.0 M NaCl solutions are very similar implying that similar Cm–borate species are formed.

Cm(III) TRLFS studies in CaCl₂ and MgCl₂ solutions

In contrast to NaCl systems, no Cm(III) hydroxide species are found in dilute to concentrated MgCl₂ solutions under near neutral pH_m conditions (pH_m = 8) and absence of borate (Herm, 2012). Note that these findings are in contrast to studies with Nd(OH)₃(am) in MgCl₂ solutions, where hydrolysis species of Nd(III) species are prevailing at this pH (Neck et al., 2009). In MgCl₂ solutions spectra with high boron concentrations up to 0.4 M [B]_{tot} could be measured and allow a systematic investigation of the Cm(III) borate complexation. A broad emission peak at ~597 nm at [B]_{tot} = 0.04 M can be observed for both investigated MgCl₂ concentrations. The shift of the peak maximum compared to the borate-free system indicates the complexation of Cm(III) with borate. The corresponding fluorescence lifetimes (77 μs – 87 μs, depending upon salt system and ionic strength) are significantly increased compared to the fluorescence lifetime of the Cm(III) aquo ion with 64 μs ± 3 μs.

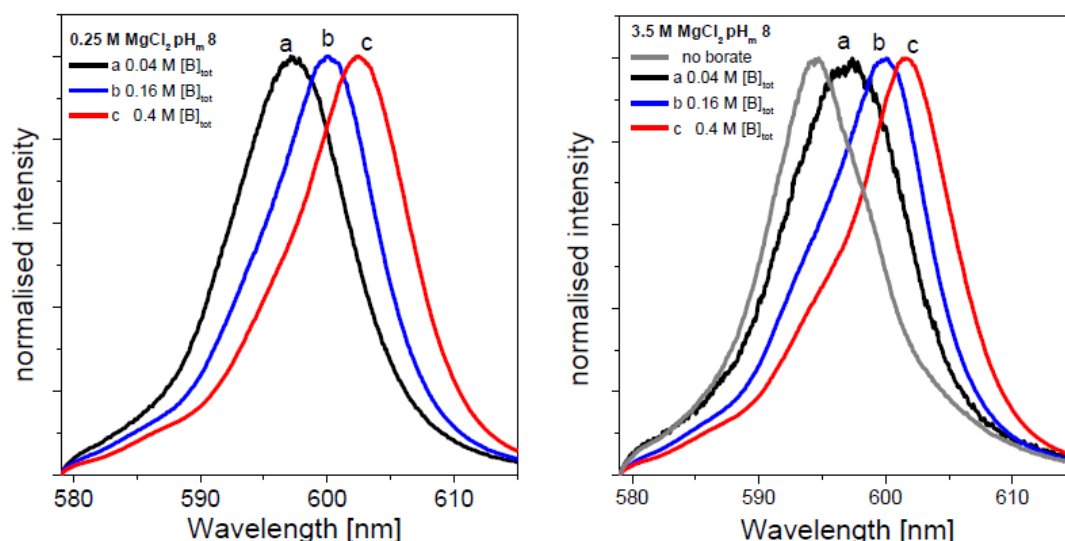


Figure 70: TRLFS emission spectra of Cm(III) in 0.25 M and 3.5 M MgCl₂ solutions at pH_m = 8 and various [B]_{tot}. Comparison with a spectrum in the absence of borate.

With increasing [B]_{tot}, the peak maxima of the fluorescence emission bands are further shifted to higher wavelengths, clearly indicating the formation of Cm(III) complexes with borate. These pronounced bathochromic peak shifts support the assumption that more than one Cm(III)–borate complexes exist under these conditions, as also proposed for the NaCl system. The bathochromic peak shift of the Cm(III) emission with increasing [B]_{tot} is accompanied with an increase of the fluorescence lifetimes up to 121 μs for 3.5 M MgCl₂ and [B]_{tot} = 0.4 M (see Table 28).

Table 28: Fluorescence lifetimes (τ) and peak maxima (λ_{\max}) in NaCl, CaCl₂ and MgCl₂ solutions at $\text{pH}_m = 8$ and various $[\text{B}]_{\text{tot}}$.

Background electrolyte	0.004 M $[\text{B}]_{\text{tot}}$		0.04 M $[\text{B}]_{\text{tot}}$		0.16 M $[\text{B}]_{\text{tot}}$		0.4 M $[\text{B}]_{\text{tot}}$	
τ [μs]	λ_{\max} [nm]	τ [μs]	λ_{\max} [nm]	τ [μs]	λ_{\max} [nm]	τ [μs]	λ_{\max} [nm]	
0.1 M NaCl	–	603	77 ± 5	601	59 ± 5	600	–	–
5.0 M NaCl	85 ± 5	604	77 ± 5	596	108 ± 5	601	–	–
0.25 M CaCl ₂	72 ± 5	594	78 ± 5	597	–	–	–	–
3.5 M CaCl ₂	73 ± 5	595	77 ± 5	596	–	–	–	–
0.25 M MgCl ₂	–	–	85 ± 5	597	96 ± 5	600	114 ± 7	603
3.5 M MgCl ₂	–	–	87 ± 5	597	95 ± 5	600	121 ± 7	602

According to the Kimura equation (Kimura et al., 1996), 3 H₂O molecules are removed in the Cm(III) complexes found in 0.25 M and 3.5 M MgCl₂ with $[\text{B}]_{\text{tot}} = 0.16$ M, and 4 to 4.5 H₂O molecules for 0.25 M MgCl₂ and 3.5 M MgCl₂ with $[\text{B}]_{\text{tot}} = 0.4$ M, respectively. The formation of Cm(III)–borate species in weakly alkaline MgCl₂ solutions shows no clear dependence on ionic strength of the solution within the uncertainty limits of the technique, as already observed in NaCl systems.

Under highly alkaline conditions ($\text{pH}_m = 12$), no influence of borate on the emission spectra can be observed in CaCl₂ solutions and $[\text{B}]_{\text{tot}} \leq 0.04$ M (Figure 71). The measured spectra and corresponding fluorescence lifetimes in presence of borate in both 0.25 M and 3.5 M CaCl₂ solutions are in good agreement with the borate-free system (Rabung et al., 2008). As already discussed for the Nd(III) solubility data, borate is a weak ligand that can only compete with hydrolysis under near-neutral pH conditions and relatively high $[\text{B}]_{\text{tot}}$, but cannot outcompete hydrolysis under hyperalkaline conditions.

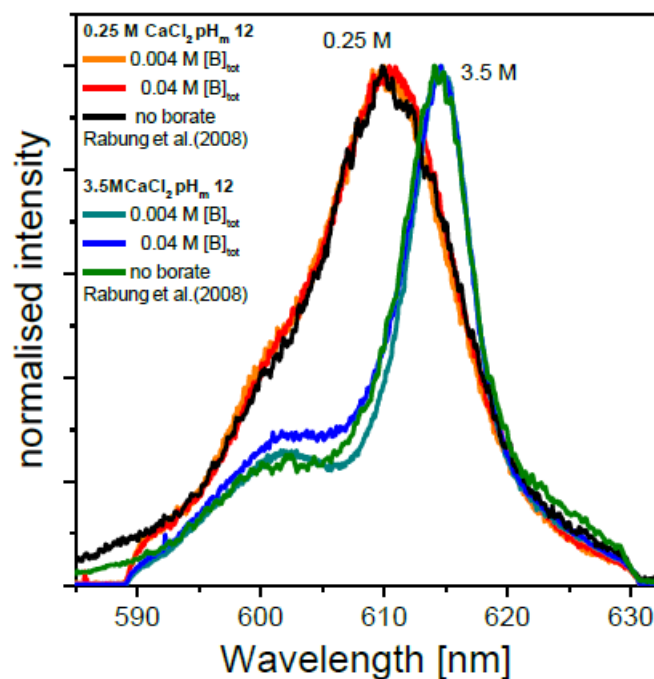


Figure 71: TRLFS emission spectra of Cm(III) in 0.25 M and 3.5 M CaCl₂ at pH_m = 12 and various borate concentrations in comparison with borate-free literature data.

5.3.3 Conclusions

Solubility studies with Nd(OH)₃(am) and TRLFS investigations with Cm(III) confirm the formation of aqueous complexes of Ln(III) and An(III) with borate in dilute to concentrated NaCl, MgCl₂ and CaCl₂ solutions under near-neutral pH_m conditions and [B]_{tot} ≥ 0.04 M. At [B]_{tot} ≥ 0.16 M and near-neutral pH_m (pH_m = 8), Cm(III)–borate aqueous species outcompete hydrolysis and become predominant. TRLFS indicates that (at least) two Cm(III)–borate species (maybe 1:1 and 1:2) form in NaCl and MgCl₂ solutions, although the exact stoichiometry of the complexation reaction remains unknown. A similar trend can be found in UV-Vis studies with Np(V) in MgCl₂ solutions with comparable [B]_{tot}. Despite the clear formation of Ln(III)/An(III)–borate aqueous species in near neutral pH_m conditions, no significant increase in solubility is observed for Nd(OH)₃(am) in the presence of [B]_{tot} ≤ 0.4 M in all investigated systems.

Conversely, a clear drop in the Nd(III) solubility of 2–3 orders of magnitude occurs at 6 ≤ pH_m ≤ 9, indicating the formation of a new solubility controlling borate-bearing solid phase. This mechanism is confirmed by XPS and SEM–EDS technique (Hinz, 2015), which suggest that the formation of a Nd(III)-borate solid phase takes place as a coating on an unreacted Nd(OH)₃(am) core. Unlike solubility studies with NpO₂(OH)(am), no complete transformation of the initial Nd(III) solid occurred in samples with [B]_{tot} ≥ 0.16 M. The significant decrease observed in the Ln(III)/An(III) solubility at pH_m < 9 related to the formation of secondary An(III)–borate alteration phases represents a hither-

to unknown actinide retention mechanism in repository systems. A thermodynamic evaluation and model of the Ln(III)/An(III) interactions in the presence of borate in NaCl, CaCl₂ and MgCl₂ systems is proposed in chapter **Fehler! Verweisquelle konnte nicht gefunden werden.**

5.4 Solubility of Th(IV) in the presence of borate

Figure 72 and Figure 73 show the solubility of Th(OH)₄(am) determined in 0.1 M – 5.0 M NaCl and 0.25 M – 3.5 M MgCl₂ solutions with [B]_{tot} = 0 and 0.16 M and varying pH_m. Data points below the detection limit were set to log $m_{\text{Th}} = -10$ for dilute (0.1 M NaCl and 0.25 M MgCl₂) and -9 and -8.5 for concentrated (5.0 M NaCl and 3.5 M MgCl₂) solutions, respectively, due to the different dilution steps needed in each case for ICP–MS measurements. For comparison purposes, the figures also show the calculated solubility of Th(OH)₄(am) (both for fresh and aged phases) in dilute NaCl and MgCl₂ systems in the absence of borate. Under these boundary conditions and provided the predominance of the neutral species Th(OH)₄(aq) over the complete pH-range investigated in this work, no significant effect of ionic strength is foreseen according with thermodynamic calculations.

The solubility of Th(OH)₄(am) remains largely unaffected by borate in dilute NaCl and MgCl₂ solutions over the entire pH_m range considered in this work. However, a slight increase in the solubility of Th(IV) compared to borate-free systems can be claimed for samples with [B]_{tot} = 0.16 M, both in concentrated NaCl and MgCl₂ solutions at pH_m ~8–9. Although Th(IV)–borate complexation appears unlikely considering the strong tendency of Th(IV) towards hydrolysis, this hypothesis cannot be completely ruled out in view of the experimental data gained in this work. Large scattering of the measured data is observed in all samples. A similar behavior in this pH_m region (pH_m > 6) has been reported for Nd(III) and Th(IV) in the absence of boron. This observation can be likely explained by the tendency of neutral aqueous species to sorb (*i.e.* Th(OH)₄(aq)), the presence of colloidal nanoparticles not removed from the solution by ultrafiltration and the very low concentrations of Th(IV) in solution (close to the detection limit of ICP–MS) (Altmaier et al., 2004; Neck et al., 2009). Note further that especially tetravalent actinides tend to form stable colloids in saline solution. In the case of thorium, these have been reported to increase the total concentration in solution 2–3 orders of magnitude (Altmaier et al., 2004).

The difficulties in evaluating the aquatic chemistry of Th(IV) within this pH region are also reflected on the quality (*i.e.* associated uncertainty) of the thermodynamic data available for this system in the absence of borate. This fact is discussed in more detail in (Hinz, 2015).

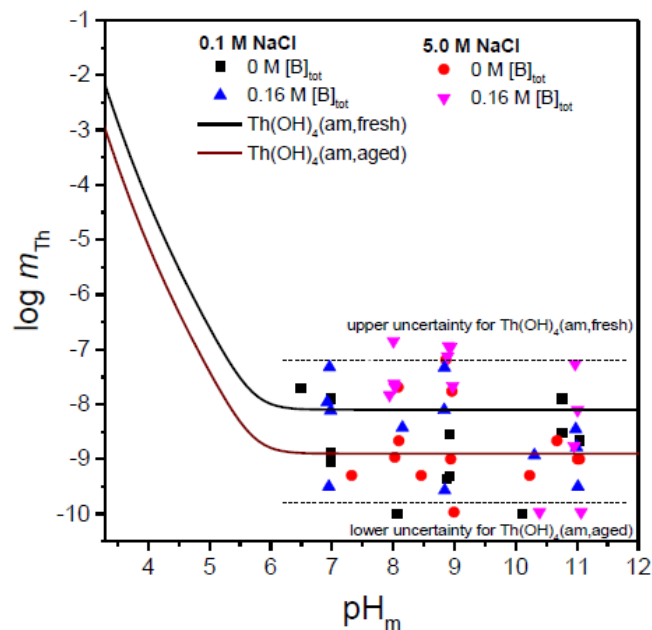


Figure 72: Solubility of Th(OH)₄(am), experimentally determined in the presence of 0 M ≤ [B]_{tot} ≤ 0.16 M in 0.1 M and 5.0 M NaCl solutions. Comparison with solubility of Th(OH)₄(am, fresh) and Th(OH)₄(am, aged), as calculated for 0.1 M NaCl using the NEA-TDB thermodynamic selection.

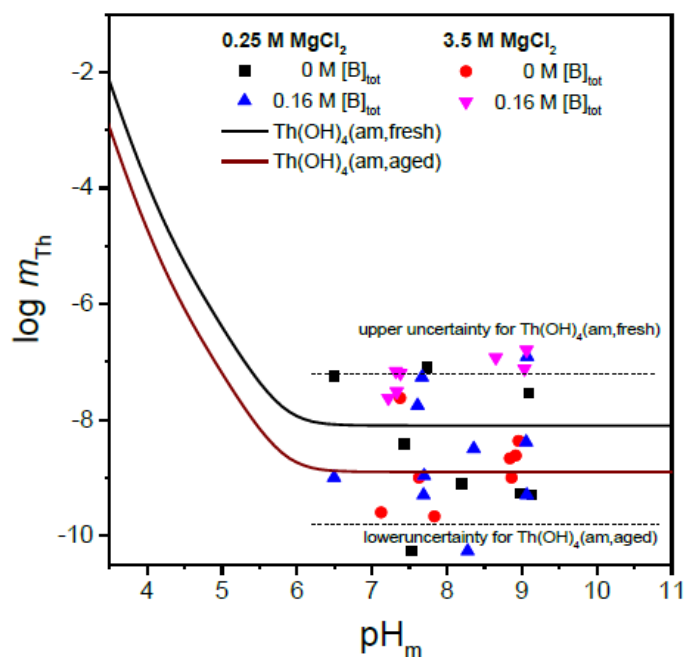


Figure 73: Solubility of Th(OH)₄(am) experimentally determined in the presence of 0 M ≤ [B]_{tot} ≤ 0.16 M in 0.25 M and 3.5 M MgCl₂ solutions. Comparison with solubility of Th(OH)₄(am, fresh) and Th(OH)₄(am, aged), as calculated for 0.25 M MgCl₂ using the NEA-TDB thermodynamic selection.

5.4.1 Conclusions

In contrast to Ln(III)/An(III), An(V) and An(VI) systems investigated in this work, no significant effect of borate on the Th(IV) solubility was observed in dilute NaCl and MgCl₂ systems within $6.5 \leq \text{pH}_m \leq 11$ and $[\text{B}]_{\text{tot}} = 0.16 \text{ M}$. A slight increase in the solubility of Th(IV) could be claimed for both concentrated NaCl and MgCl₂ systems at $\text{pH}_m = 7.5\text{--}9$, which may hint towards a weak Th(IV)–borate complexation in this pH_m region under these experimental conditions. Further experimental evidences would be needed to confirm this possibility. The weaker Th(IV)–borate interaction compared to Ln(III)/An(III), An(V) and An(VI) is in good agreement with the strong hydrolysis tendency of tetravalent actinides, which significantly outcompetes the formation of weaker complexes. The sparingly soluble Th(IV) oxy-hydroxide phase controlling the solubility in the conditions of this experiment retains very low Th(IV) concentrations in solution, and thus prevents the formation of any secondary phase in the presence of borate. The large scattering in the solubility data observed both in the absence and presence of borate is attributed to the predominance of the neutral aqueous species $\text{Th}(\text{OH})_4(\text{aq})$ and the possible formation of polymeric/colloidal Th(IV) species (Altmaier et al., 2004), and reflects also the large uncertainty associated to the thermodynamic data available for Th(IV) aqueous species and solid compounds forming in these conditions.

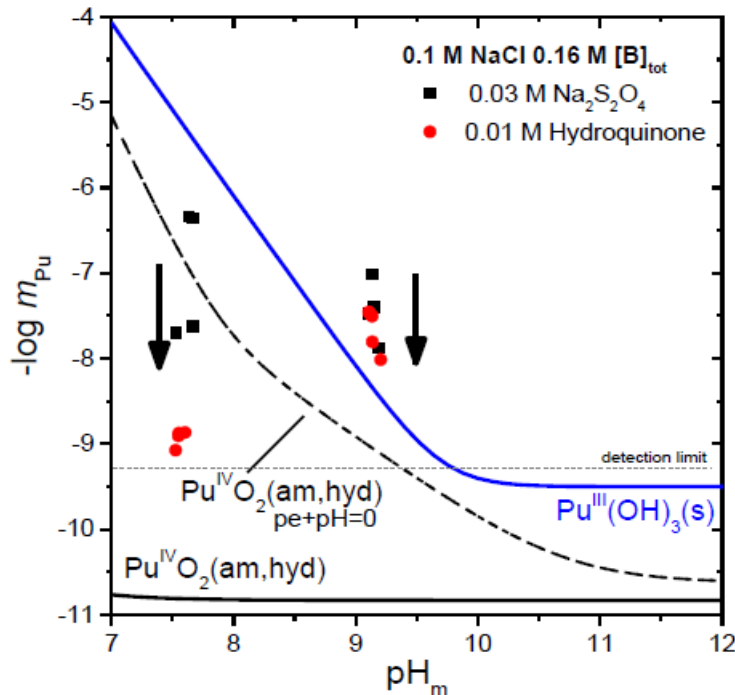


Figure 74: Solubility of $\text{Pu}^{\text{IV}}\text{O}_2(\text{am,hyd})$ in the presence of $[\text{B}]_{\text{tot}} = 0.16 \text{ M}$ with $0.03 \text{ M Na}_2\text{S}_2\text{O}_4$ and 0.01 M hydroquinone in 0.1 M NaCl solutions. Comparison with calculated solubility data for $\text{Pu}^{\text{IV}}\text{O}_2(\text{am,hyd})$ (black solid line) and $\text{Pu}^{\text{III}}(\text{OH})_3(\text{s})$ (blue solid line) and the calculated equilibrium of $\text{Pu}^{\text{III}}(\text{aq})$ with $\text{Pu}^{\text{IV}}\text{O}_2(\text{am,hyd})$ with $\text{pe} + \text{pH} = 0$ (dashed line) in the absence of borate as reported in NEA-TDB.

5.5 Interaction of Pu(III/IV) with borate

The solubility of $\text{Pu}^{\text{IV}}\text{O}_2(\text{am,hyd})$ in 0.1 M NaCl solution with $[\text{B}]_{\text{tot}} = 0.16 \text{ M}$ in the presence of $\text{Na}_2\text{S}_2\text{O}_4$ and hydroquinone at $\text{pH}_m = 7.5$ and 9.0 is presented in Figure 74. Experimental Eh and pH values of the samples are displayed in the Pu Pourbaix diagram (Figure 75).

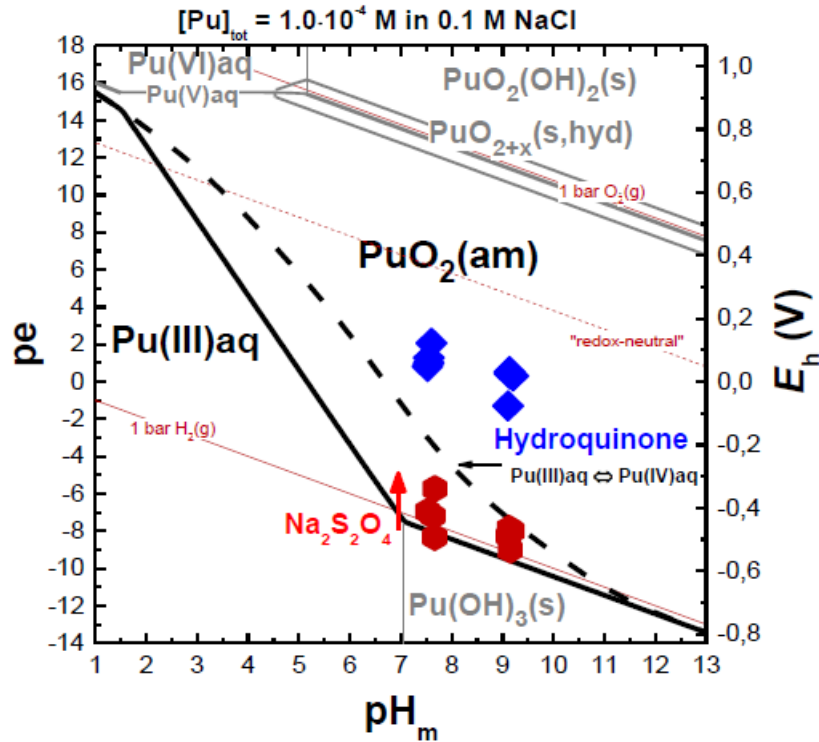


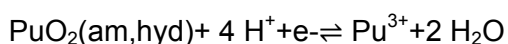
Figure 75: Pourbaix diagram calculated for $[\text{Pu}]_{\text{tot}} = 10^{-4} \text{ M}$ in 0.1 M NaCl and absence of borate. Dashed and solid lines represent the calculated borderlines for the individual Pu redox species (Guillaumont et al., 2003; Neck et al., 2007). pe and pHm values are shown for the solubility samples in the presence of hydroquinone (blue) and $\text{Na}_2\text{S}_2\text{O}_4$ (red).

Measured Eh values for the two samples with hydroquinone are in the stability field of $\text{Pu}^{\text{IV}}\text{O}_2(\text{am,hyd})$. The experimental Pu(IV) solubility at $\text{pH}_m \sim 7.5$ is at the detection limit for LSC, i.e. $1 \cdot 10^{-9} \text{ M}$. This upper limit value is consistent with the expected $\text{Pu}^{\text{IV}}\text{O}_2(\text{am,hyd})$ solubility. XPS analysis confirm $\text{Pu}^{\text{IV}}\text{O}_2(\text{am,hyd})$ as solubility controlling phase. In conclusion, no significant effect of borate on the Pu(IV) aqueous and solid phase speciation is observed at $\text{pH}_m = 7.5$ in slightly reducing solutions, which is consistent with the results obtained for Th(IV) (chapter 5.4). At $\text{pH}_m = 9.0$ the experimental $\text{Pu}^{\text{IV}}\text{O}_2(\text{am,hyd})$ solubility is significantly enhanced compared to the Pu solubility expected for the measured (pe + pH) conditions ($\log [\text{Pu}(\text{IV})] = -10.8$) (Figure 74). In the first two measurements ($t \leq 14 \text{ d}$), $[\text{Pu}]$ was at $\sim 10^{-7} \text{ M}$ and slowly decreased to $\sim 10^{-8} \text{ M}$ within 300 days. Thus, no stable conditions were reached indicating that strong kinetics affect the equilibration process. Note that no change in the oxidation state of Pu in the solid phase was detected by XPS (see (Hinz, 2015)), although the

low concentrations in solution prevent the accurate characterization of the redox state in the aqueous phase. Although the complexation of Pu(IV) with borate was considered unlikely due to the very strong tendency of An(IV) towards hydrolysis in alkaline solutions (Rai et al., 1999; Yamaguchi et al., 1994), the experimental observations gained in this work could be explained properly on the basis of this hypothesis. Note that a similar increase in solubility is found for Th(OH)₄(am) in concentrated NaCl and MgCl₂ solutions at pH_m = 9, thus indicating that the complexation of Pu(IV) and Th(IV) with borate cannot be completely ruled out (chapter 5.4). Note however that no Th(IV) solubility increase in these conditions was found for dilute NaCl solutions. The enhanced [Pu] can hardly be attributed to the initial presence of Pu(III) as the redox conditions (pe + pH) are clearly in the stability field of Pu(IV) (the hydroquinone sample at pH_m = 7.5 is even closer to the stability field of Pu(III), but does not show any indication for the presence of Pu(III)). More experimental data in the investigated conditions with longer equilibration times are needed to completely understand the observed processes.

Redox conditions in the two samples with Na₂S₂O₄ are very close to the borderline of Pu^{IV}O₂(am,hyd)/Pu(OH)₃(s). At pH_m = 7.5, fast transformation of the initial Pu^{IV}O₂(am,hyd) into a dark solid phase occurred within one week. The main oxidation state of the latter is Pu(III) as confirmed by XPS analysis after 300 days. The peak shape and position of the 4f_{3/2} and 4f_{7/2} transitions are in agreement with Pu(III) reference spectra (Larson and Haschke, 1981; Larson and Motyl, 1990). The experimental Pu solubility within the first two measurements (~ 5·10⁻⁷ M) is clearly above the Pu(IV) solubility curve, but slightly lower than expected for Pu(OH)₃(s) according to the data from NEA. The solubility constant log *K[°]_{s,0}{Pu(OH)₃(s)} = 15.8 ± 1.5 is reported with a large uncertainty of 1.5 log-units which can explain the deviations (Guillaumont et al., 2003). Recent results from Fellhauer further suggest a lower value for the solubility constant of ~ log *K[°]_{s,0}{Pu(OH)₃(s)} = 14.35 (Fellhauer, 2013). Therefore it is likely that the solubility for t ≤ 14 d is controlled by Pu(OH)₃(s). For t > 14 d (i.e. in the last two measurements) pe-values are slightly increasing, and [Pu]_{tot} decreasing to ~2 10⁻⁸ M. Note that Na₂S₂O₄ is only metastable in neutral pH conditions (Holman and Bennett, 1994; Munchow and Steudel, 1994). The slightly increasing pe values for the sample at pH_m = 7.5 points to slow decomposition of Na₂S₂O₄. While the measured (pe + pH) values suggest a solubility control by the reductive dissolution equilibrium (see below; implying a quantitative re-oxidation of Pu(OH)₃(s) to PuO₂(am,hyd)), XPS clearly revealed the presence of a rather oxidation state pure Pu(III) solid phase. Therefore, the decrease in [Pu]_{tot} for t > 14 d is likely caused by the formation of a Pu(III) borate coating or borate containing Pu(III) solid phase similar to the findings in Nd(III) solubility studies.

For the sample at pH_m = 9 (Na₂S₂O₄), XPS analysis indicates the presence of both Pu(III) and Pu(IV) in the solid phase after t = 300 d (see (Hinz, 2015)). The measured [Pu]_{tot} at pH_m = 9 after short equilibration time is enhanced compared to the solubility expected under these pe + pH conditions, i.e. *the reductive dissolution equilibrium*:



As the experimental [Pu] is even higher than that of $\text{Pu}(\text{OH})_3(\text{s})$ in borate-free systems, the formation of Pu(III) borate complexes has to be considered, analogously to the Cm(III) borate complexes observed under comparable experimental conditions. In solubility studies with $\text{Nd}(\text{OH})_3(\text{am})$, the increase in [Nd(III)] in 0.1 M and 1.0 M NaCl at $\text{pH}_m = 9$ and 10 in presence of $[\text{B}]_{\text{tot}} \geq 0.16 \text{ M}$ is attributed to Nd(III)-borate complexes (see chapter 5.3). The initial [Pu] decreased with time (by ~ 1 order of magnitude after $t = 300 \text{ d}$) indicates that no equilibrium has been attained. As for the sample at $\text{pH}_m = 7.5$ ($\text{Na}_2\text{S}_2\text{O}_4$), the decrease of initial [Pu] (i.e. [Pu(III)]) is consistent with the formation of a Pu(III) borate coating or borate containing Pu(III) solid phase as reported for Nd(III) in chapter 5.3.

5.5.1 Conclusions

Solubility studies with $\text{Pu}^{\text{IV}}\text{O}_2(\text{am,hyd})$ under mildly reducing conditions controlled by hydroquinone and with $[\text{B}]_{\text{tot}} = 0.16 \text{ M}$ show a differential behavior at $\text{pH}_m = 7.5$ and $\text{pH}_m = 9.0$. Hence, the very low solubility determined at $\text{pH}_m = 7.5$ is in good agreement with the reported solubility of Pu(IV) in equilibrium with $\text{u}^{\text{IV}}\text{O}_2(\text{am,hyd})$ in the absence of borate. The solubility increase observed at $\text{pH}_m = 9$ could be explained by a possible Pu(IV)-borate interaction, similar to observations made with Th(IV) in concentrated NaCl and MgCl_2 solutions at same pH. Note however that a Pu(IV)-borate complexation leading to an increased Pu(IV) solubility was considered unlikely on the basis of the strong tendency of Pu(IV) towards hydrolysis, and thus additional experiments evidences are needed to clarify the influence of borate on the Pu(IV) solubility and speciation in this pH_m region. The slow decrease of the measured Pu concentration at this pH_m with time clearly indicates that no equilibrium conditions are reached after 300 days. XPS analysis of the alteration phases in the presence of hydroquinone and $[\text{B}]_{\text{tot}} = 0.16 \text{ M}$ showed no reduction of the initial Pu(IV) solid, as expected under the measured $\text{pe} + \text{pH}$ conditions.

In the presence of $\text{Na}_2\text{S}_2\text{O}_4$, a complete ($\text{pH}_m = 7.5$) and partial ($\text{pH}_m = 9$) reduction of the initial $\text{Pu}^{\text{IV}}\text{O}_2(\text{am,hyd})$ to a Pu(III) solid phase occurs according to XPS analyses. At $\text{pH}_m = 7.5$, the measured Pu solubility at short equilibration times ($t \leq 14 \text{ d}$) are in agreement with a solubility control by $\text{Pu}(\text{OH})_3(\text{s})$. The continuous decrease in $[\text{Pu}]_{\text{tot}}$ (i.e. [Pu(III)]) with time and the XPS results at the end of the solubility experiments are consistent with the formation of a Pu(III) borate coating or formation of a Pu(III)-borate solid phase similar to observations gained for Nd(III) under analogues experimental conditions. At $\text{pH}_m = 9$, the formation of Pu(III)-complexes likely occurs slightly enhancing the Pu(III) solubility compared to the borate-free system. The latter agrees with the findings for Cm(III) and Np(V) at this pH_m with comparable $[\text{B}]_{\text{tot}}$ in NaCl media. In most samples, no stable Pu(III/IV) concentrations are measured clearly indicating that longer equilibration times than 300 days are needed. Additional experimental efforts are

needed to gain a conclusive insight on the impact of borate on the Pu solubility and redox chemistry under weakly alkaline reducing conditions.

5.6 Solubility of Np(V) in the presence of borate

The system Np(V) – borate was intensively studied by Hinz and the results are described and discussed in detail in her Ph.D. thesis (Hinz, 2015). Here, only the most important findings of this study are summarized.

The solubility of Np(V) with borate was investigated from undersaturation conditions using $\text{NpO}_2\text{OH(am)}$ as starting material. Experiments were performed in NaCl and MgCl_2 solutions with $0.04 \text{ M} \leq [\text{B}]_{\text{tot}} \leq 0.16 \text{ M}$ at $6 \leq \text{pH}_m \leq 9$. $[\text{Np(V)}]$ and pH_m were monitored at regular time intervals for up to 270 days. After reaching equilibrium conditions, solid phases from selected samples were characterized by XPS, SEM–EDS, XRD, XANES and EXAFS. The interaction of Np(V) with borate in the aqueous phase was further investigated in an independent batch series with $\sim 10^{-4} \text{ M}$ Np(V) in 0.25 M and 3.5 M MgCl_2 with $0.04 \text{ M} \leq [\text{B}]_{\text{tot}} \leq 0.16 \text{ M}$ and $\text{pH}_m = 8$ and 9 by UV-VIS/NIR spectroscopy.

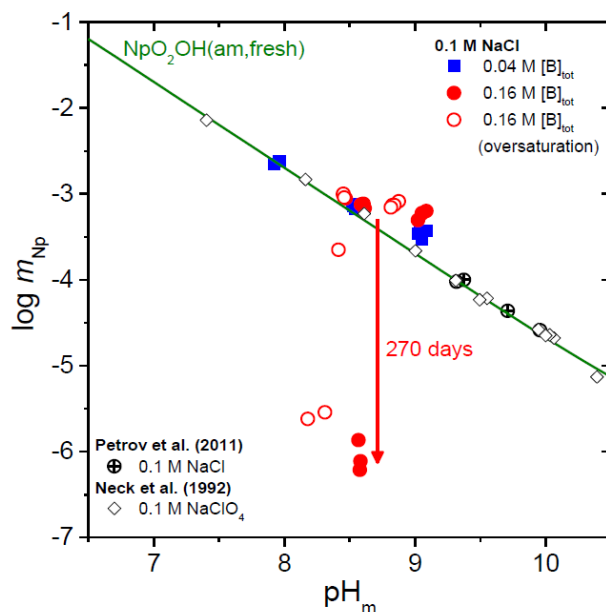


Figure 76: Solubility of Np(V) in the presence of $0.04 \text{ M} \leq [\text{B}]_{\text{tot}} \leq 0.16 \text{ M}$ in 0.1 M NaCl solutions (blue and red symbols). Comparison with experimental (open symbols, black) solubility data in the absence of borate as reported by (Neck et al. 1992) and (Petrov et al. 2011). Solid line corresponding to the solubility of $\text{NpO}_2\text{OH(am, fresh)}$ in 0.1 M NaCl calculated according to the NEA– TDB selection.

5.6.1 Solubility of Np(V) in NaCl and MgCl₂ solutions

The experimental solubility data of Np(V) in 0.1 M NaCl, 5.0 M NaCl, 0.25 M MgCl₂ and 3.5 M MgCl₂ solutions in the presence of $0.04 \text{ M} \leq [\text{B}]_{\text{tot}} \leq 0.16 \text{ M}$ are shown in Figure 76 to Figure 79. The figures also show experimental and calculated solubility of Np(V) in the absence of borate as reported by Petrov et al., Neck et al. and the NEA-TDB (Guillaumont et al., 2003; Neck et al., 1992; Petrov et al., 2011).

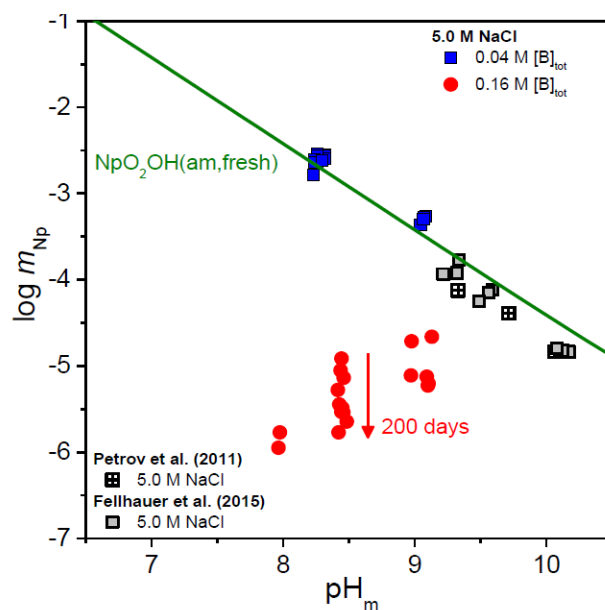


Figure 77: Solubility of Np(V) in the presence of $0.04 \text{ M} \leq [\text{B}]_{\text{tot}} \leq 0.16 \text{ M}$ in 5.0 M NaCl solutions (blue and red symbols). Comparison with experimental (open symbols, black) solubility data in the absence of borate as (Fellhauer et al., 2015) and (Petrov et al., 2011). Solid line corresponding to the solubility of $\text{NpO}_2\text{OH}(\text{am}, \text{fresh})$ in 5.0 M NaCl calculated according to the NEA-TDB selection. Arrow indicates that the decrease in the concentration of Np for the same solubility sample was only completed after 270 days

Within the timeframe of this study, low boron concentrations ($[\text{B}]_{\text{tot}} = 0.04 \text{ M}$) show no significant effect on the solubility of Np(V) in 5.0 M NaCl and 0.25 M and 3.5 M MgCl₂ solutions with $8 \leq \text{pH}_m \leq 9$. The experimentally measured Np(V) solubility in these systems is in good agreement with Np(V) solubility data in the absence of borate (Fellhauer, 2015; Neck et al., 1992; Petrov et al., 2011). A slight increase in the Np(V) solubility is observed in 0.1 M NaCl solutions with $\text{pH}_m = 9$ and $[\text{B}]_{\text{tot}} \geq 0.04 \text{ M}$, indicating the possible formation of Np(V)–borate complexes in solution. Similar to observations made for Nd(III) (see chapter 5.3), a distinct decrease in solubility occurs in 0.1 M and 5.0 M NaCl solutions with higher boron concentration ($[\text{B}]_{\text{tot}} = 0.16 \text{ M}$) and $\text{pH}_m \leq 9$ (Figure 76 and Figure 77). The drop in the solubility is accompanied by a transformation of the initial greenish $\text{NpO}_2\text{OH}(\text{am})$ into a white-grayish solid phase. The solid phase transformation was fast in 5.0 M NaCl (~2 weeks), but slower in 0.1 M NaCl where it occurred only for $\text{pH}_m \leq 8.5$. Note that samples prepared from oversaturation conditions in 0.1 M NaCl and $[\text{B}]_{\text{tot}} = 0.16 \text{ M}$ result in very similar experimental observations than samples

prepared from undersaturation conditions: a slight increase of Np(V) concentration at $\text{pH}_m \sim 8.8$ and a drop in the Np(V) solubility at $\text{pH}_m \leq 8.5$ together with a slow transformation of the solid phase. In both cases, the concentration of Np(V) in equilibrium with the newly formed solid phase is approximately three orders of magnitude lower than the solubility of $\text{NpO}_2\text{OH}(\text{am}, \text{fresh})$. The transformation is tentatively faster at lower pH_m values, see Figure 76 to Figure 79. It is therefore likely that the non-occurrence of a solid phase transformation in 0.1 M NaCl and $\text{pH}_m > 8.5$ is due to insufficient equilibration time.

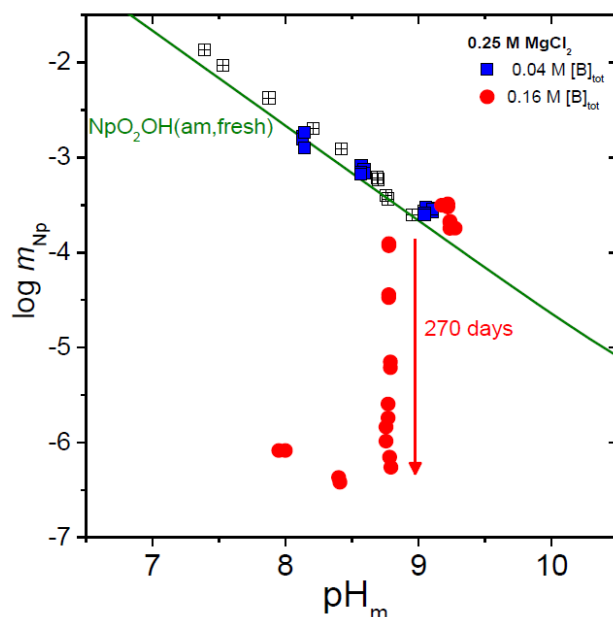


Figure 78: Solubility of Np(V) in the presence of $0.04 \text{ M} \leq [\text{B}]_{\text{tot}} \leq 0.16 \text{ M}$ in 0.25 M MgCl_2 solutions (blue and red symbols). Comparison with experimental (open symbols, black) solubility data in the absence of borate as reported by (Petrov et al., uhhuj 2011). Solid line corresponding to the solubility of $\text{NpO}_2\text{OH}(\text{am}, \text{fresh})$ in 0.25 M MgCl_2 calculated according to the NEA–TDB selection.

A comparable decrease in Np(V) solubility accompanied by a transformation of the initial greenish $\text{NpO}_2\text{OH}(\text{am})$ into a newly formed white–gray solid phase occurs in dilute MgCl_2 systems at $\text{pH}_m < 9$ and $[\text{B}]_{\text{tot}} = 0.16 \text{ M}$ (Figure 78). Similarly to the dilute NaCl system the solubility of Np(V) decreased slowly and attained a constant value ($\sim 10^{-6.5} \text{ M}$) only after 270 days. In 3.5 M MgCl_2 solutions with $[\text{B}]_{\text{tot}} = 0.16 \text{ M}$ only a minor decrease in Np(V) solubility is observed after 270 days. As observed in Nd(III), Cm(III) and U(VI) solubility studies (see chapters 5.3 and 5.7) actinide borate interactions in MgCl_2 solutions are less pronounced than in NaCl solutions at comparable pH_m and ionic strength conditions. As discussed in chapter 5.2 based on the ^{11}B -NMR data gained in this work in combination with the thermodynamic model reported by Felmy and co-workers (Felmy and Weare, 1986), the formation of Mg–borate complexes decreases the concentration of free borate and outcompetes the formation of An–borate aqueous complexes and solid phases.

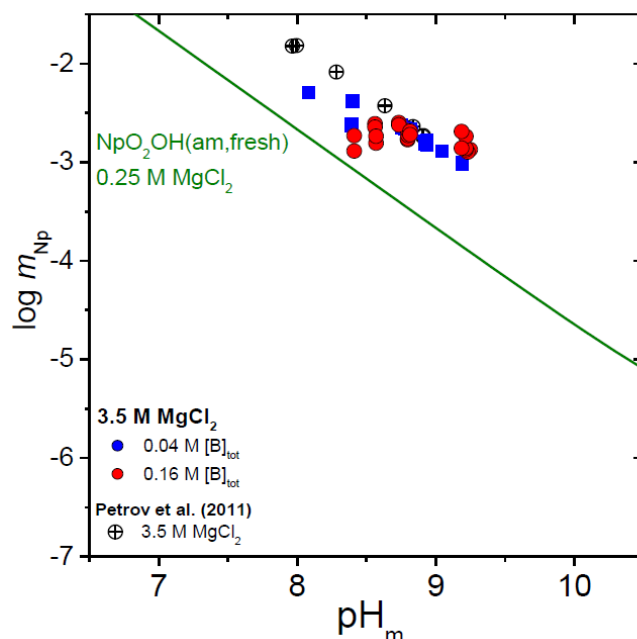


Figure 79: Solubility of Np(V) in the presence of $0.04 \text{ M} \leq [\text{B}]_{\text{tot}} \leq 0.16 \text{ M}$ in 3.5 M MgCl_2 solutions (blue and red symbols). Comparison with experimental (open symbols, black) solubility data in the absence of borate as reported by (Petrov et al., 2011). Solid line corresponding to the solubility of $\text{NpO}_2\text{OH}(\text{am}, \text{fresh})$ in 0.25 M MgCl_2 calculated according to the NEA–TDB selection. Calculations were restricted to 0.25 M MgCl_2 due to a lack of ion interaction parameters for high concentrated MgCl_2 systems.

Solid phase characterization by XRD, XPS and SEM-EDS

Solid phases of selected solubility experiments in 0.1 M , 5.0 M NaCl and 0.25 M MgCl_2 with $[\text{B}]_{\text{tot}} = 0.16 \text{ M}$ were investigated after attaining equilibrium conditions by XRD, SEM–EDS and XPS. Np–L_{III} XANES and EXAFS spectra were also acquired for the alteration phases formed in 0.25 M MgCl_2 , 0.1 M NaCl and 5.0 M NaCl , all of them with $[\text{B}]_{\text{tot}} = 0.16 \text{ M}$ and $\text{pH}_m \sim 8.5$. Spectra were collected at the INE–Beamline for Actinide Research at ANKA.

In contrast to the initial X-ray amorphous $\text{NpO}_2\text{OH}(\text{am}, \text{fresh})$, XRD diffractograms of the transformed solid phases show a series of sharp peaks, indicating the crystalline character of the newly formed solid phase (Figure 80). Although with certain similarities, the diffractograms obtained for the solid phases formed in NaCl and MgCl_2 solutions are markedly different, indicating that the cation of the background electrolyte participates (or at least influences) in the formation of the secondary solid phase. Note that the collected diffractograms gave no positive match with any of the existing borate entries in the JCPDS database. Note further that, in spite of the several washing steps

with ethanol, all diffractograms collected for Np(V) secondary phases formed in 5.0 M NaCl solutions showed only very strong reflexes corresponding to NaCl (data not shown in Figure 80).

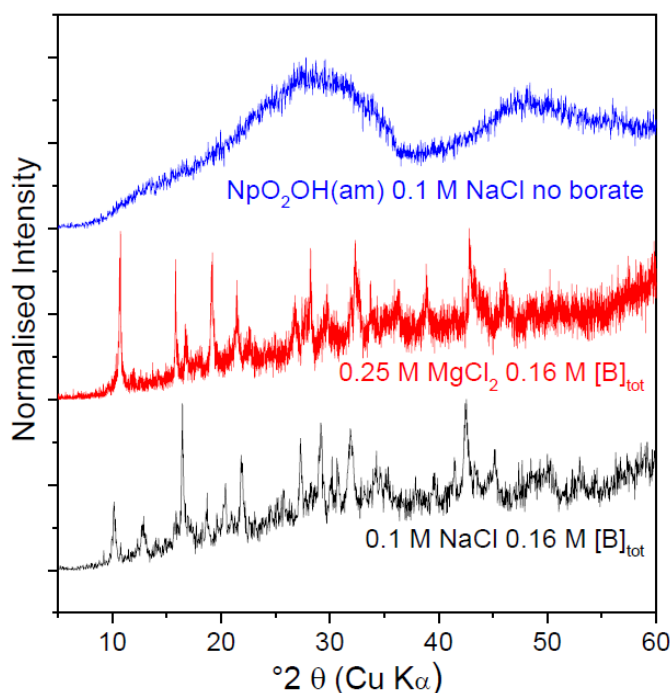


Figure 80: Diffractograms of the solubility-controlling Np(V) solid phases in the absence and presence of borate ($[B]_{tot} = 0.16$ M) in 0.1 M NaCl and 0.25 M $MgCl_2$ solutions at $pH_m \sim 8.5$.

XPS analyses of the Np(V) secondary phases formed in dilute NaCl and $MgCl_2$ solutions confirm the stoichiometric presence of boron and Na^+/Mg^{2+} . The composition of the newly formed solid phases hint towards the formation of solid phases with stoichiometry $NpO_2[B_5O_6(OH)_4] \cdot 2NaOH$ and $(NpO_2)_2[B_5O_6(OH)_4]_2 \cdot 3Mg(OH)_2(cr)$, respectively (Hinz, 2015).

SEM images of the surface of the Np(V)–borate solid phases formed in NaCl and $MgCl_2$ solutions are shown in Figure 81. Solid phases collected from samples in 0.1 M NaCl (Figure 81 a) and 0.25 M $MgCl_2$ solutions (Figure 81 b) show a homogeneous transformation and distribution of Np(V) in the entire investigated area. The sample equilibrated in 0.1 M NaCl contains very thin (~ 20 nm) hexagonal platelets with a diameter of ~ 500 nm. The structure of the sample equilibrated in 0.25 M $MgCl_2$ looks similar in shape but appears more amorphous. The investigation of the Np(V)–borate solid phase formed in 5.0 M NaCl (Figure 81 c and d) clearly shows the co-existence of two phases. Hence, massive, crystalline hexagonal blocks appear surrounded by an amorphous phase. EDS analyses indicated the predominance of Na and Cl in the block structures, whereas the amorphous phase would correspond to the newly formed Np(V)–borate phase. The identification of NaCl and presence of an amorphous Np(V) phase is consistent with the observations collected by XRD, where only the pattern of

NaCl could be identified and no additional peaks of a newly formed Np(V)–borate solid phase were observed.

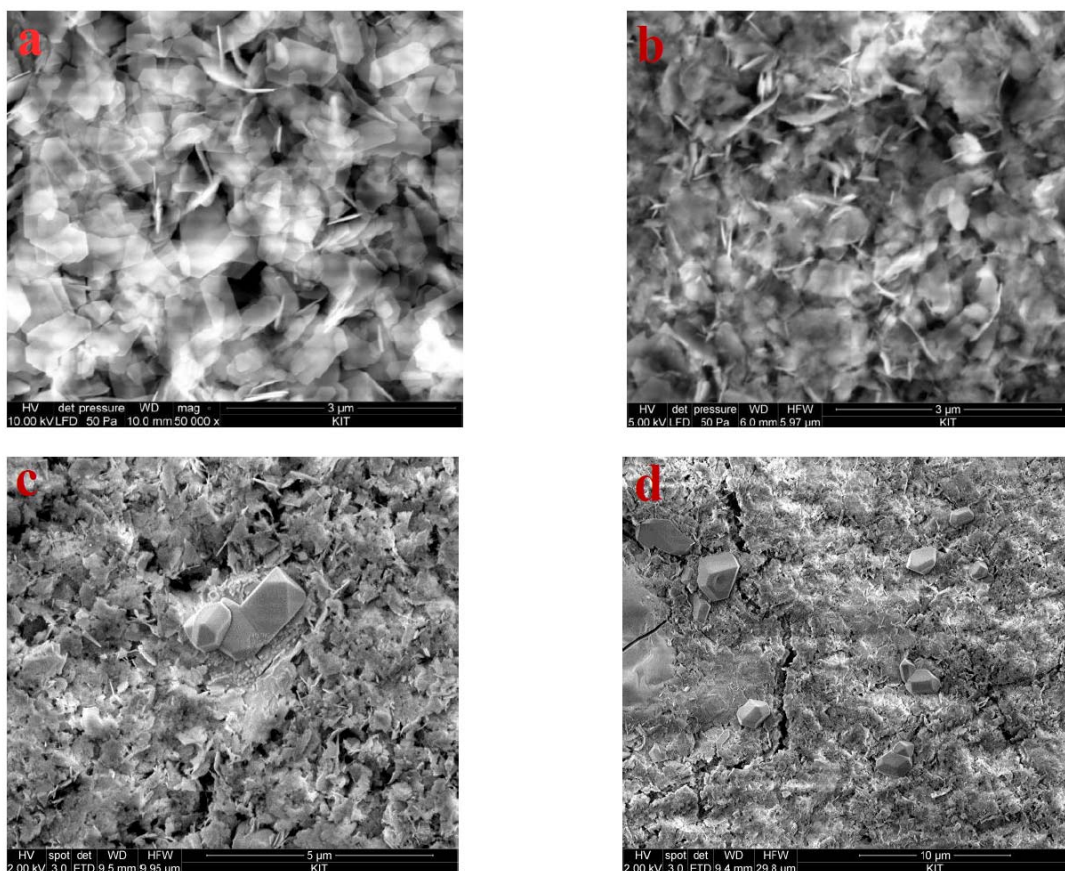


Figure 81: SEM-images of the new formed solubility-controlling Np(V) solid phases in the presence of borate ($[B]_{\text{tot}} = 0.16 \text{ M}$) in 0.1 M NaCl (a) and 0.25 M MgCl_2 (b) and 5.0 M NaCl (c, d).

EXAFS investigations (Hinz, 2015) confirmed the Np(V)–borate compound formed in 0.1 M NaCl as the most stable and well crystallized structure, whereas the structures formed in 5 M NaCl and in 0.25 M MgCl_2 are less stable and undefined probably consisting of a mixture of different phases. Note that EXAFS analyses are in good agreement with the findings obtained by XRD and SEM–EDS techniques.

5.6.2 Conclusions

Solubility studies with $\text{NpO}_2\text{OH}(\text{am})$ combined with accurate solid phase characterization and UV-Vis/NIR investigations (not shown here, see (Hinz, 2015)) confirm that the presence of borate strongly affects both the aqueous and solid speciation of Np(V) in dilute to concentrated NaCl and MgCl_2 solutions at $\text{pH}_m = 8$ and 9 and $[B]_{\text{tot}} \geq 0.04 \text{ M}$. UV–Vis/NIR investigations confirm the formation of at least one Np(V)–borate complex in MgCl_2 solutions. A much weaker interaction is observed in concentrated MgCl_2 solu-

tions, as a result of the competition between Mg^{2+} and NpO_2^+ for borate complexation. The evaluation of the spectroscopic data collected suggests $\text{B}(\text{OH})_4^-$ as most probable complexing borate species in the aqueous phase, although the exact stoichiometry of the complexation reaction and the determination of a formation constant was not feasible in this work. A similar trend in borate complexation was observed for Cm(III) in NaCl, CaCl_2 and MgCl_2 solutions with comparable $[\text{B}]_{\text{tot}}$ using TRLFS (see chapter 5.3).

In spite of the clear formation of Np(V)–borate aqueous species in solution at moderate pH_m , no significant increase in the solubility of $\text{NpO}_2\text{OH}(\text{am}, \text{fresh})$ is observed in the presence of $[\text{B}]_{\text{tot}} \leq 0.4 \text{ M}$. On the contrary and similarly to Nd(III), a clear drop in the Np(V) solubility occurs in borate-bearing NaCl and MgCl_2 solutions with $\text{pH}_m \leq 9$. The drop in solubility is accompanied by a visible change of the initial solid (from green to white-gray), confirming the formation of a new solid phase. The formation of this previously unreported Np(V)–borate solid phase is further confirmed by XRD, XPS, SEM–EDS and EXAFS analysis (details are found in (Hinz, 2015)). This solid phase transformation constitutes a previously unreported retention mechanism for the highly mobile Np(V).

5.7 Solubility of U(VI) in the presence of borate

The system U(VI) – borate was studied by Hinz and the experiments and results are described and discussed in detail in her Ph.D. thesis (Hinz, 2015).

The solubility of U(VI) was studied from undersaturation conditions in the presence of $0 \text{ M} \leq [\text{B}]_{\text{tot}} \leq 0.16 \text{ M}$ with $4.5 \leq \text{pH}_m \leq 9.3$ in 0.1 M and 5.0 M NaCl and 0.25 and 3.5 M MgCl_2 solutions. Samples in 0.1 M and 5.0 M NaCl systems with $\text{pH}_m \geq 7.5$ were prepared with $\text{Na}_2\text{U}_2\text{O}_7 \cdot \text{H}_2\text{O}(\text{cr})$ as initial solid phase. In all samples in 0.25 and 3.5 M MgCl_2 systems and in 0.1 M and 5.0 M NaCl systems with $\text{pH}_m < 7.5$ freshly prepared meta-schoepite $\text{UO}_3 \cdot 2\text{H}_2\text{O}(\text{cr})$ was added as initial solid phase. For comparison purposes, samples with U(VI) in the same pH_m and ionic strength conditions but without borate were prepared and measured following the same experimental approach. The U(VI) concentration was regularly quantified in combination with the measurement of pH_m for up to 380 days. Solid samples from selected solubility experiments were characterized by XRD after attaining equilibrium conditions.

5.7.1 Solubility of U(VI) in NaCl and MgCl_2 solutions

The solubility of U(VI) in 0.1 M, 5.0 M NaCl, 0.25 M MgCl_2 and 3.5 M MgCl_2 solutions with $0 \text{ M} \leq [\text{B}]_{\text{tot}} \leq 0.16 \text{ M}$ is shown in Figure 82 and Figure 83. The figures also show the solubility of $\text{UO}_3 \cdot 2\text{H}_2\text{O}(\text{cr})$ and $\text{Na}_2\text{U}_2\text{O}_7 \cdot \text{H}_2\text{O}(\text{cr})$ in NaCl and MgCl_2 solutions as calculated using the thermodynamic and (SIT) activity models.

No effect of borate on the solubility of U(VI) is observed in dilute to concentrated NaCl solutions at $\text{pH}_m \leq 6.5$ (solubility control by $\text{UO}_3 \cdot 2\text{H}_2\text{O}(\text{cr})$). The weak complexation capacity of borate is not sufficient to outcompete the cationic hydrolysis species of U(VI) prevailing in this pH region. Note also that in this pH_m region the non-complexing $\text{B}(\text{OH})_3(\text{aq})$ species is dominating the aqueous chemistry of boron. These data are also in excellent agreement with the solubility of $\text{UO}_3 \cdot 2\text{H}_2\text{O}(\text{cr})$ as calculated in the absence of borate. In 0.1 M and 5.0 M NaCl solutions at $\text{pH}_m \geq 7.5$, a solubility increase with increasing $[\text{B}]_{\text{tot}}$ is observed. This effect is more pronounced in 5.0 M NaCl solution with an increase in U(VI) solubility of about 1.5 orders of magnitude, rather than in 0.1 M NaCl solution where a slight increase of $\sim \frac{1}{2}$ order of magnitude is seen. This solubility increase unequivocally hints towards the formation of U(VI)–borate aqueous complexes within the pH-range 7.5–9. Lucchini et al. investigated the solubility of U(VI) in a synthetic brine solution (2.2–4.2 M NaCl and ~ 0.01 M $[\text{B}]_{\text{tot}}$) and found no effect of borate on the U(V) solubility at $\text{pH}_m \sim 8.9$ but the used $[\text{B}]_{\text{tot}}$ are significantly lower compared to the present experiments (Lucchini et al., 2007).

In contrast to the observations made for Nd(III) and Np(V), no decrease in the solubility of U(VI) is observed in NaCl solutions within the timeframe of the experiment (380 days). Hence, in spite of the observed U(VI)–borate interaction in the aqueous phase, such interaction did not progress further towards the formation of a secondary U(VI)–borate solid phase. It is worth mentioning that $[\text{U}(\text{VI})]$ in equilibrium with $\text{Na}_2\text{U}_2\text{O}_7 \cdot \text{H}_2\text{O}(\text{cr})$ at $\text{pH}_m = 7.5$ is significantly lower than the solubility-limit set by $\text{Nd}(\text{OH})_3(\text{am})$ and $\text{NpO}_2\text{OH}(\text{am})$, and thus that the solubility product of a potentially-forming U(VI)–borate solid phase is not exceeded. Although not evaluated in the present work, the formation of a U(VI)–borate solid phase at $\text{pH}_m \sim 9$ and absence of Na^+ ($I \rightarrow 0$) cannot be completely ruled out. In these conditions, $\text{UO}_3 \cdot 2\text{H}_2\text{O}(\text{cr})$ allows significantly higher $[\text{U}(\text{VI})]$ in solution compared to $\text{Na}_2\text{U}_2\text{O}_7 \cdot \text{H}_2\text{O}(\text{cr})$ (1 to 2 log-units difference, see dashed lines in Figure 82), which may lead to the formation of a secondary U(VI)–borate solid phase.

In contrast to the observations made for Nd(III) and Np(V), no decrease in the solubility of U(VI) is observed in NaCl solutions within the timeframe of the experiment (380 days). Hence, in spite of the observed U(VI)–borate interaction in the aqueous phase, such interaction did not progress further towards the formation of a secondary U(VI)–borate solid phase. It is worth mentioning that $[\text{U}(\text{VI})]$ in equilibrium with $\text{Na}_2\text{U}_2\text{O}_7 \cdot \text{H}_2\text{O}(\text{cr})$ at $\text{pH}_m = 7.5$ is significantly lower than the solubility-limit set by $\text{Nd}(\text{OH})_3(\text{am})$ and $\text{NpO}_2\text{OH}(\text{am})$, and thus that the solubility product of a potentially-forming U(VI)–borate solid phase is not exceeded. Although not evaluated in the present work, the formation of a U(VI)–borate solid phase at $\text{pH}_m \sim 9$ and absence of Na^+ ($I \rightarrow 0$) cannot be completely ruled out. In these conditions, $\text{UO}_3 \cdot 2\text{H}_2\text{O}(\text{cr})$ allows significantly higher $[\text{U}(\text{VI})]$ in solution compared to $\text{Na}_2\text{U}_2\text{O}_7 \cdot \text{H}_2\text{O}(\text{cr})$ (1 to 2 log-units difference, see dashed lines in Figure 82), which may lead to the formation of a secondary U(VI)–borate solid phase.

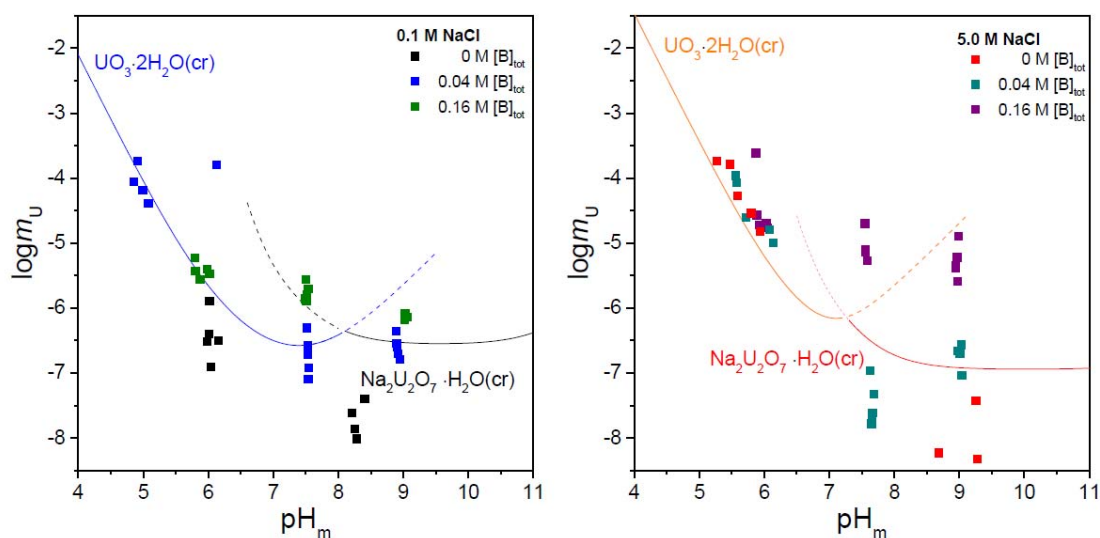


Figure 82: Solubility of $\text{UO}_3 \cdot 2\text{H}_2\text{O}(\text{cr})$ and $\text{Na}_2\text{U}_2\text{O}_7 \cdot \text{H}_2\text{O}(\text{cr})$ in the presence of $0 \text{ M} \leq [\text{B}]_{\text{tot}} \leq 0.16 \text{ M}$ in 0.1 M and 5.0 M NaCl solutions. Comparison with calculated solubility of $\text{UO}_3 \cdot 2\text{H}_2\text{O}(\text{cr})$ (blue line) and $\text{Na}_2\text{U}_2\text{O}_7 \cdot \text{H}_2\text{O}(\text{cr})$ (black line) in the absence of borate as reported in Altmaier et al. (Altmaier et al., 2003b).

A weaker effect of borate (compared to the NaCl system) on the $\text{U}(\text{VI})$ solubility can be observed for dilute to concentrated MgCl_2 systems. This effect is especially visible at $\text{pH}_m = 7.5$ and $[\text{B}]_{\text{tot}} = 0.16 \text{ M}$. As already observed in the $\text{Np}(\text{V})$ solubility studies, actinide borate interactions in MgCl_2 solutions are less pronounced than in NaCl solutions at comparable pH_m and ionic strength conditions. This effect is likely caused by a changed boron speciation in MgCl_2 media due to an interaction of Mg^{2+} with borate species in solution. This effect was also hinted in ^{11}B -NMR experiments (see chapter 5.2).

In MgCl_2 systems, the solubility data in the borate-free systems is partly scattered and lower than the expected solubility reported in the literature (Altmaier et al., 2003b). The lower solubility is likely caused by differences in the crystallinity and particle size of the initial solid phase controlling the solubility of $\text{U}(\text{VI})$.

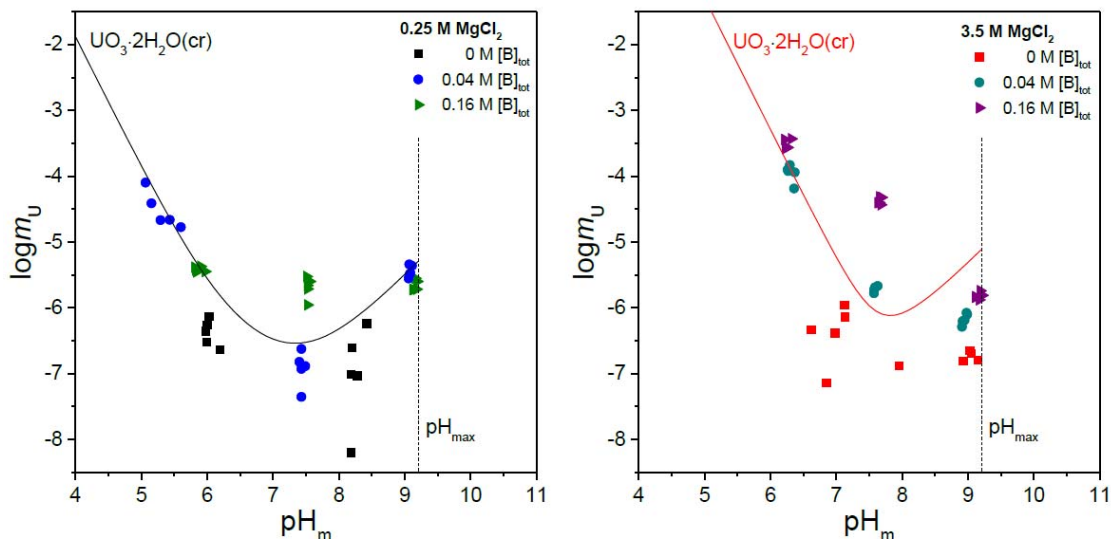


Figure 83: Solubility of $\text{UO}_3 \cdot 2\text{H}_2\text{O}(\text{cr})$ in the presence of $0 \text{ M} \leq [\text{B}]_{\text{tot}} \leq 0.16 \text{ M}$ in 0.25 M and 3.5 M MgCl_2 solutions. Comparison with calculated solubility of $\text{UO}_3 \cdot 2\text{H}_2\text{O}(\text{cr})$ in the absence of borate (solid line) as reported in Altmaier et al. (Altmaier et al., 2003b).

5.7.2 Solid phase characterization

XRD diffractograms obtained for selected solid phases are shown in Figure 84. In all cases the measured patterns agree very well with those reported for $\text{UO}_3 \cdot 2\text{H}_2\text{O}(\text{cr})$ JCPDF file No: 43-0364 and $\text{Na}_2\text{U}_2\text{O}_7 \cdot \text{H}_2\text{O}(\text{cr})$ (Altmaier et al., 2003b), indicating that the bulk U(VI) controlling solid phase in all investigated samples is not affected by the presence of borate.

5.7.3 Conclusions

Experimental data from U(VI) solubility studies in the presence of borate showed an increase in U(VI) solubility in NaCl systems at $7.5 \leq \text{pH}_m \leq 9$ for $[\text{B}]_{\text{tot}} \geq 0.04 \text{ M}$ likely caused by the formation of aqueous U(VI)-borate complexes. A weaker effect of borate is observed in dilute to concentrated MgCl_2 solutions, where a slight solubility increase at $\text{pH}_m = 7.5$ and $[\text{B}]_{\text{tot}} = 0.16 \text{ M}$ can be seen. No drop in U(VI) solubility caused by the transformation of the initial solid phase as observed in Nd(III) (see chapter 5.3) and Np(V) systems (see chapter 5.6) is found in NaCl and MgCl_2 solutions under the investigated conditions. This behavior is likely related with the very low uranium concentration imposed by $\text{Na}_2\text{U}_2\text{O}_7 \cdot \text{H}_2\text{O}(\text{cr})$ as solubility controlling-phase in NaCl media under weakly alkaline conditions, although it could also be due to slow kinetics. In very dilute systems (absence of Na^+), the higher uranium concentrations under weakly alkaline conditions set by $\text{UO}_3 \cdot 2\text{H}_2\text{O}(\text{cr})$ may lead to the formation of secondary U(VI)-borate

solid phases. The observations collected in this work allow neither confirming nor rejecting the latter hypothesis, and thus provide space for additional studies.

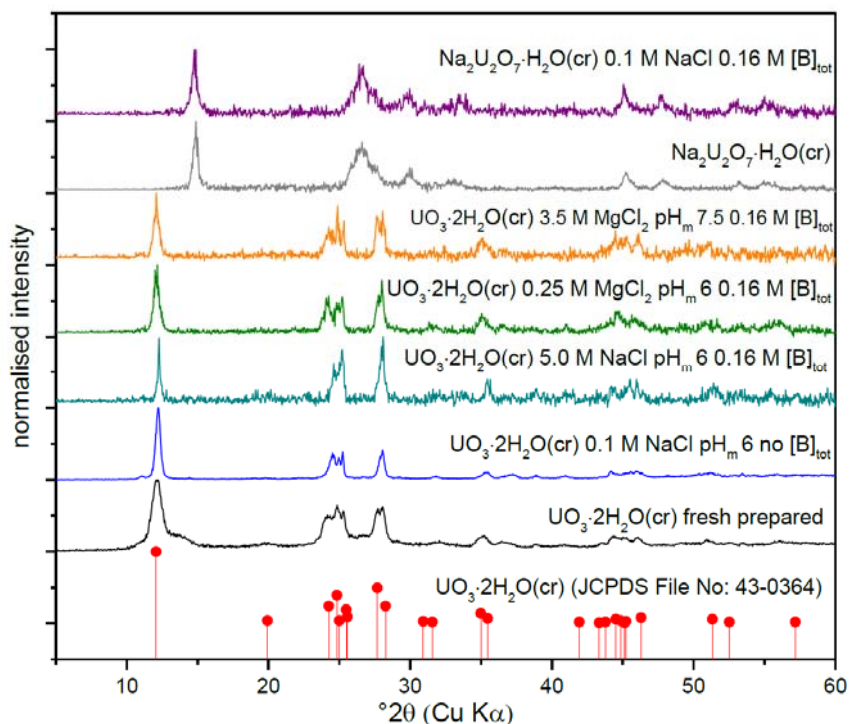


Figure 84: XRD pattern of freshly prepared initial $UO_3 \cdot 2H_2O(cr)$, $UO_3 \cdot 2H_2O(cr)$ reference [137] and $UO_3 \cdot 2H_2O(cr)$ alteration phases from solubility experiments in NaCl and MgCl₂ systems with $0 M \leq [B]_{tot} \leq 0.16 M$ at pH_m 6–7.5 and initial Na₂U₂O₇·H₂O (cr) and Na₂U₂O₇·H₂O (cr) alteration phases from solubility experiment in 0.1 M NaCl and [B]_{tot} = 0.16 M.

List of Tables

Table 1: Formation constants for hydrolysis and chloride complexation at infinite solution used for Eu in the sorption modeling. Data are from the NEA-TDB (Guillaumont et al., 2003)	3
Table 2: Cation exchange capacities (CEC) and surface hydroxyl group densities for SWy-2 and Illite du Puy (Bradbury and Baeyens, 2006, 2009a).....	4
Table 3: Protolysis of Eu(III) surface species to model Eu sorption on illite with the 2SPNE SC/CE model and SWy-2 for comparison reasons (Bradbury and Baeyens, 2006, 2009a)	4
Table 4: Cation exchange reaction of illite (IdP) and SWy at infinite dilution to model Eu sorption on illite with the 2SPNE SC/CE model and SWy-2 for comparison reasons (Bradbury and Baeyens, 2006, 2009a), (Schnurr, 2015).	4
Table 5: Thermodynamic equilibrium parameters at infinite dilution to model Eu sorption on illite (IdP) with the 2SPNE SC/CE model (Bradbury and Baeyens, 2009b).	5
Table 6: Calculation of the relative occupation of cation exchange sites ($[X_{\text{gesamt}}] = 4.5 \times 10^{-4} \text{ M}$) in experiments with various NaCl/CaCl ₂ ratios in solution (Bradbury and Baeyens, 2009a), (Schnurr, 2015).	13
Table 7: Reactions and respective thermodynamic constants used in the present modeling section.	25
Table 8: Thermodynamic constants at zero ionic strength used in the present study (Guillaumont et al., 2003). The missing hydrolysis constants for Pu are taken from the corresponding analogues (in brackets). Surface complexation constants for Pu(III, IV, V, VI) are obtained assuming that the experimental uptake data of Am(III), Th(IV), Np(V) and U(VI) by kaolinite are representative for the uptake of the corresponding Pu redox states. (*) Exchange and surface complexation constants have been determined by (Tertre et al., 2008). Some constants could not be determined since no appropriate experimental data were available. According to (Tertre et al., 2006; Tertre et al., 2008), the surface area of kaolinite is 10 m ² /g, site density for ≡SOH and exchange sites are 1.66 and 3.70 μmol/m ² , respectively.	32

Table 9: Relevant aqueous reaction for the calculations of Pu sorption and speciation in the present study. Thermodynamic constants are taken from the NEA-TDB ¹ and refer to the value at infinite dilution. Ternary Pu(IV)-hydroxo-carbonato complexes formation constants are taken for THEREDA ² . In case of gaps in the available database for Pu, data for analogues are used (i.e. Eu/Am(III), Np(IV), Np(V) and U(VI) for the respective Pu redox states). Although available for Pu, the formation constants for PuOH ²⁺ and Pu(OH) _{4(aq)} are taken from Eu/Am(III) and Np(IV) to ensure the consistency between aqueous speciation and surface complexation modeling, i.e. to avoid additional corrections of the literature parameters for the 2 SPNE SC/CE model.	36
Table 10: Surface complexation and cation exchange parameters for the 2 SPNE SC/CE model are taken from the literature ^{3,4,5} and for Pu(IV) (determined in the present study). The surface complexing site density is $[\equiv S]_{\text{tot}} = 2 \times 10^{-3}$ mol/kg. The cation exchange capacity is $[X]_{\text{tot}} = 0.225$ eq/kg. “na” refers to non-available values. Only the relevant reactions and constants for the present calculations are tabulated.	37
Table 11: SIT parameters ($\epsilon(i,k)$) used in the present study, taken from the NEA-TDB ¹ for Pu or the corresponding analogue (as in Table S1). “na” refers to non-available values (set equal to 0).	38
Table 12: Thermodynamic equilibrium parameters ($\log K_{\text{SC}}$) at infinite dilution to model U(VI) sorption on illite (IdP) with the 2SPNE SC/CE model (Bradbury and Baeyens, 2009b)	50
Table 13: Summary of D_e ($\text{m}^2 \text{s}^{-1}$) and α (-) values for HTO and ³⁶ Cl in Na-illite at a bulk dry density (p _{db}) of $\sim 1700 \text{ kg m}^{-3}$ together with literature data ((Glaus et al., 2010), unpublished data from SCK-CEN and PSI).....	57
Table 14: Thermodynamic data and interaction parameters according SIT for Np(V) propionate complex formation in NaCl solution determined in the present study. Uncertainties are reported at $\pm 1\sigma$ confidence level. Individual $\epsilon(i,k)$ values are estimated based on $\epsilon(\text{Na}^+; \text{acetate}^-)$ value.....	72
Table 15: Conditional complex formation constants of neptunium (V) acetate, propionate, and lactate formation at 25 ± 1 °C.....	78
Table 16: Conditional stability constants of neptunium (V) complex formation at different temperatures.	79

Table 17: Thermodynamic parameters specific ion interaction coefficients ($\Delta\varepsilon$) of neptunium (V) complex formation with acetate, propionate and lactate (in NaCl solution), according to the reaction: $\text{NpO}_2^+ + \text{L}^- = \text{NpO}_2\text{L}$	81
Table 18: Band peak maxima positions (± 0.5 nm) as obtained after differential spectroscopy (see text for details). a: initial, b: after centrifugation, c: not clearly determined.....	93
Table 19: SEC-hydrodynamic diameter values (in nm).....	95
Table 20: A_c - and A_m values used in this work for the quantification of pH_c and pH_m , respectively.....	105
Table 21: Experimental conditions in the system investigated by ^{11}B -NMR.....	106
Table 22: Experimental conditions in the solubility study with $\text{Nd}(\text{OH})_3(\text{am})$	109
Table 23: Experimental conditions in the solubility study with $\text{Nd}[\text{B}_9\text{O}_{13}(\text{OH})_4](\text{cr})$	109
Table 24: Experimental conditions in the solubility study with $\text{PuO}_2(\text{am,hyd})$	109
Table 25: Experimental conditions in the solubility study with $\text{Th}(\text{OH})_4(\text{am})$	110
Table 26: Experimental conditions in the solubility study with $\text{NpO}_2\text{OH}(\text{am,fresh})$	110
Table 27: Experimental conditions in the solubility study with $\text{UO}_3 \cdot 2 \text{H}_2\text{O}(\text{cr})$ and $\text{Na}_2\text{U}_2\text{O}_7 \cdot \text{H}_2\text{O}(\text{cr})$	110
Table 28: Fluorescence lifetimes (τ) and peak maxima (λ_{max}) in NaCl, CaCl_2 and MgCl_2 solutions at $\text{pH}_m = 8$ and various $[\text{B}]_{\text{tot}}$	122

List of Figures

- Figure 1: Eu(III) sorption on Illit du Puy (IdP) plotted as sorbed % against pH_c in NaCl (0.09 M) ; S :L = 2 g/L, $[Eu]_{total} = 2.0 \times 10^{-7}$ M..... 6
- Figure 2: Eu(III) sorption on Illit du Puy (IdP) plotted as log K_D against pH_c at different NaCl concentrations (0.09, 0.90, 3.60 M) ; S :L = 2 g/L, $[Eu]_{total} = 2.0 \times 10^{-7}$ M. The data from TRLFS measurements of Cm(III) sorption and data from literature (Bradbury and Baeyens, 2009a, 2015) are additionally shown. 7
- Figure 3: Modeling (solid lines) of the Eu(III) sorption data (symbols) plotted as log K_D against pH_c at different NaCl concentrations (0.09, 0.90, 3.60 M) ; S :L = 2 g/L, $[Eu]_{total} = 2.0 \times 10^{-7}$ M. The 2SPNE SC/NE model with detailed sorption species distribution at I = 0.09 M was used..... 8
- Figure 4: Comparison of Eu(III) sorption on Illite in NaCl (0.09 M), $CaCl_2$ (0.06 M) and $MgCl_2$ (0.06 M) solutions. 9
- Figure 5: Distribution coefficients log K_d of Eu(III) sorption on illite ($[Eu]_{total} = 2.0 \cdot 10^{-7}$ M, solid:liquid = 2 g/L) as a function of pH_c in $MgCl_2$ and $CaCl_2$ solutions with various concentrations (0.06, 0.60, 2.00 M). 10
- Figure 6: Eu(III) sorption ($[Eu]_{total} = 2.0 \cdot 10^{-7}$ M) an IdP (S:L = 2 g/L) plotted as log K_D against pH_c values at various $MgCl_2$ und $CaCl_2$ concentrations (0.06, 0.60, 2.00 M). The lines are the modelled values by 2SPNE SC/CE modell including detailed sorption speciation at I = 0.18 M..... 11
- Figure 7: Speciation of Eu(III) in aqueous $CaCl_2$ solutions ($[Eu]_{total} = 2.0 \cdot 10^{-7}$ M) in $CaCl_2$ ($[CaCl_2] = 0.06, 0.6, 2.0$ and 4.0 M). 12
- Figure 8: Eu(III) sorption ($[Eu]_{gesamt} = 2.0 \cdot 10^{-7}$ M) on IdP (S :L = 2 g/L) plotted as log K_d against the pH_c in different NaCl – $CaCl_2$ mixtures (I = 1 M). 13
- Figure 9: Eu(III) sorption ($[Eu]_{total} = 2.0 \cdot 10^{-7}$ M) on illite (IdP) (S:L = 2 g/L) plotted as log K_D against the pH_c value in various NaCl - $CaCl_2$ mixtures (I = 1 M). The curves were generated by predictions with the 2SPNE SC/CE model. 14
- Figure 10: pH_c dependence of the TRLFS spectra (peak area normed) $[Cm]_{Total} = 2.0 \cdot 10^{-7}$ M, $[NaCl] = 0.1$ M, IdP, S:L = 0.25 g/L. 15

Figure 11: (a) Na-illite, (b) Na-SWy-2: Pure component spectra derived from peak deconvolution of measured fluorescence spectra obtained at each ionic strength (0.10, 4.0 M (0.10 and 4.37 m))	16
Figure 12: Cm(III) fluorescence spectra of solution containing IdP (0.25 g/L), different amounts of Si(IV) (0, $1 \cdot 10^{-5}$, $1 \cdot 10^{-4}$, $1 \cdot 10^{-3}$ M), and 0.1 M NaCl at $\text{pH}_c = 9$.	18
Figure 13: Eu(III) sorption on OPA clay fraction (OPA-CF) and IdP in NaCl (0.09, 0.90 und 3.60 M) and in CaCl_2 (0.06, 0.6, and 2.00 M) plotted as $\log K_d$ against pH_c ($[\text{Eu}]_{\text{total}} = 2.0 \cdot 10^{-7}$ M, S:L = 2 g/L).	20
Figure 14: Np sorption to illite (R_d , in L/kg) versus pH measured for different reaction times (7, 21, 35, 63 days) and a Np total concentration of (a) 10^{-6} M and (b) 3×10^{-8} M. (c) Results obtained for $\text{pH} = 7.2 \pm 0.2$ are plotted as $\log R_d$ versus $[\text{Np}]_{\text{tot}}$.	22
Figure 15: (a) Np L3-XANES measured for a Np-illite sample prepared at $\text{pH} = 7.4$ and 9.6 ($[\text{Np}]_{\text{tot}} = 3 \times 10^{-4}$ M, $m/V = 20\text{g/L}$, $E_h = 0.40 \pm 0.05$ V). Reference XANES of aqueous Np(IV) and Np(V) in 1M HClO_4 from (Gaona et al., 2012) are shown for comparison. Arrows highlight a Np(V) reduction to Np(IV) process in the present study. The area between 17610 and 17670 eV is enlarged in (b).	24
Figure 16: Experimental $\log R_d$ (black circles) and the corresponding calculated values (white circles) with the fitted surface complexation constants for Np(IV) with illite versus pH for $[\text{Np}]_{\text{tot}} = 10^{-6}$ (a), 10^{-7} (b) and 3×10^{-8} M (c). The corresponding redox (pH-pe/Eh plot) conditions are shown on the right side with the predominance diagram for aqueous Np species (d) (e) (f). Lines represent calculations made for constant pH+pe (bold line) ± 0.8 (lower limit: bold dashed line; upper limit: thin dashed line).	26
Figure 17: pH-pe (or Eh on the secondary scale) diagram of Neptunium in 0.1 M NaCl solution (black lines) and superimposed Np predominance diagram calculated at the illite surface (grey lines). It shows that the Np(V)/Np(IV) borderline at the illite surface is between 3 and 5 pe units (0.18-0.30 V), depending on the pH, higher than the corresponding one in solution. Experimental pH-pe values are also plotted (without error bars for clarity, s. also (Marsac et al., 2015a)), showing that in the present batch experiments, Np(V) prevails in solution whereas and Np(IV) prevails at the surface, explaining the stronger Np-illite sorption observed compared with literature, under aerobic condition.	28

Figure 18: Experimental sorption data (K_d , in L/kg) on kaolinite versus pH for actinides with different redox states (Am(III)/Th(IV)/Np(V); data from (Amayri et al., 2011; Banik et al., 2007; Buda et al., 2008) for 0.1 M NaClO₄. Data for U(VI) are taken from (Křepelová, 2007) for 0.1 M NaClO₄ in the presence of CO₂ (closed diamonds; pH < 8) and 0.01 M NaClO₄ in the absence of CO₂ (open diamonds). The elements are considered as chemical analogues for Pu(III/IV/V/VI). Pu(IV) data are recalculated from the sorption data and Pu redox state analysis of (Banik, 2006) using eq. 17 (two large white circles). Curves represent the modeled result for each Pu redox state..... 30

Figure 19: (a) Percentage uptake of Pu and Th by kaolinite ($[Pu]_{tot} = 6.6 \times 10^{-9}$ M / $[Th]_{tot} = 6.6 \times 10^{-13}$ M; 0.1 M NaClO₄; S/V = 4 g/L; either under ambient air below pH = 8 or argon atmosphere) experimentally obtained by (Banik et al., 2007) and calculated for pH+pe = 16.2, considering (bold line) or not (bold dashed line) the precipitated PuO_{2(am)} to be removed from the aqueous phase with the kaolinite. The model sensitivity to pe is illustrated applying ± 0.5 uncertainty on the pe: pH+pe = 15.7 (dashed line) and 16.7 (dashed-dotted line); precipitated PuO_{2(am)} is considered to have been removed with kaolinite. (b) Predominance diagram for the aqueous solution plotting pH+pe versus pe to visualize constant redox conditions horizontally. The legend is valid for (a) and (b). 31

Figure 20: (a) Pu sorption to illite (R_d in L kg⁻¹) in 0.1 M NaCl as a function of the pH for $[Pu]_{tot} = 8 \times 10^{-11}$ M after 1 week and 1 year contact time. (b) Pu-illite sorption isotherms for pH = 4.3, 6.2 and 9.3 after 1 year contact time..... 39

Figure 21 (a) Predominance pH-pe diagram for Pu in 0.1 M NaCl. Measured pH-pe values in the Pu-illite (present work) and Np-illite (Marsac et al., 2015a) suspensions in 0.1 M NaCl are shown as symbols. The bold red lines show the estimated (on the basis of chemical analogues; dashed line) and presently determined (solid line) Pu(IV)/Pu(III) borderline at the illite surface (see text for more details). (b) Pu and Eu(III) uptake data on illite (R_d in L kg⁻¹) as a function of pH compared with the predicted Eu/Am(III) (green bold line), Np(IV) (dashed black line) and the present model for Pu(IV) (blue bold line) based on the 2 SPNE SC/CE framework. Thin dashed lines correspond to the uncertainty associated to the surface complexation constants for Np(IV). 40

Figure 22: The experimental results for Pu sorption to illite (R_d in L kg⁻¹) as a function of pH are compared with overall log R_d calculated for pH+pe

= 11.8 ± 1.0 (bold line; lower and upper values: dashed and dashed-dotted lines).....	42
Figure 23: Experimental results for Pu sorption to illite (R_d in $L\ kg^{-1}$) versus pH after 1 year and 1 week (for pH = 10) in the absence of calcite, and after 1 week in the presence of calcite. The lines are model predictions of log R_d values for Pu (bold line) and the total inorganic carbon concentration ([DIC], in mM; dashed line) in the case of the Na-illite in contact equilibrium with calcite.....	44
Figure 24: U(VI) sorption on IdP (S:L = 2 g/L) plotted as log K_d versus pH_c values at different NaCl concentrations. Opened quadratic symbols are data from (Bradbury and Baeyens, 2009b). $[U]_{total} = 4.0 \times 10^{-7}$ M.	45
Figure 25: U(VI) sorption on IdP: Comparison between experimental data (symbols) and modelling by the 2SPNE SC/CE model (curves). The species distribution is exemplary shown for 0.1 M NaCl. $[U]_{total} = 4.0 \times 10^{-7}$ M; IdP: S/L = 2 g/L.	46
Figure 26: U(VI) sorption on IdP in NaCl solution: Comparison between experimental data (symbols) and modelling (lines) by the 2SPNE SC/CE model including the species $SO-UO_2Cl(OH)_2^{2-}$ (green dashed curve). The species distribution is exemplary shown for 0.1 M NaCl. $[U]_{total} = 4.0 \times 10^{-7}$ M; IdP: S/L = 2 g/L.....	47
Figure 27: U(VI) sorption ($[U]_{total} = 4.0 \cdot 10^{-7}$ M) an IdP (S:L = 2 g/L) plotted as % sorbed against pH_c value in $MgCl_2$ (black, open), $CaCl_2$ (black, closed, 0.06 M) and NaCl (red, 0.10 M) solutions.....	48
Figure 28: : U(VI) sorption on IdP (S:L = 2 g/L) in $Ca/MgCl_2$ solution plotted as log K_d versus pH_c values at different $MgCl_2$ (open symbols) and $CaCl_2$ (closed symbols) concentrations.....	48
Figure 29: U(VI) sorption on IdP (S:L = 2 g/L) in 0.06 M $Ca/MgCl_2$ solution; comparison between experimental log K_D values (symbols) and calculation (curves) by the 2SPNE SC/CE model using the log K_{SC} for Na-IdP (black) and Ca-IdP (blue) from Table 12 (column 2 and 4).....	49
Figure 30: U(VI) sorption on IdP (S:L = 2 g/L) in $Ca/MgCl_2$ solution at various concentrations; comparison between experimental log K_D values (symbols) and calculation (curves) by the 2SPNE SC/CE model including sorption species distribution at 0.18 M salt concentration. The log K_{SC} used for the modelling is listed in Table 12 (column 5).....	50

Figure 31: U(VI) sorption on IdP (S:L = 2 g/L) in Ca/MgCl ₂ solution at various concentrations; Calculation of the sorption including the surface species SO-UO ₂ Cl(OH) ₂ ²⁻ (green dashed curve). Modelling with the 2SPNE SC/CE model and log K _{SC} listed in Table 12 (column 5).	51
Figure 32: X-ray diffractogram of the sample Nd-GR and of the sample after different washing procedures, with comparison to the database.	52
Figure 33: SEM micrographs of the sample Nd-GR before (left) and after (right) washing and aging overnight. Both samples exhibit a layered structure.	53
Figure 34: XPS Fe 2p (left) and Am 4f (right) spectra of the GR and magnetite containing Am(III). The indium line comes from the substrate	54
Figure 35: Raman spectra of Am-GR (top) and Am-Magn recorded at two wavelengths. Only magnetite is detected.....	55
Figure 36: Diffusion of HTO (a) and ³⁶ Cl ⁻ (b) in compacted Na-illite (ρ _{db} ~1700 kg m ⁻³) at pH 5.5 and 0.1 M NaCl as mass flux in the low concentration reservoir (J) and evolution of the source reservoir concentration.	58
Figure 37: Schematic illustration of the two Np diffusion experiments NP1 and NP2.	60
Figure 38: Np flux and break through cumulated activity of experiment Np1 (stainless steel filter, black and red points) and Np2 (peek supporting plate plus filter membrane, dark and light brown points) as a function of time.	61
Figure 39: Diffusion of fulvic acid (FA) in compacted Na-illite at pH 5 and NaCl as back electrolyte: cumulated activity of ³ H-FA in LCR and flux of FA as a function of time.....	62
Figure 40: (a) Np(V) absorption spectra for various propionate concentrations (0–0.1 M) at [Np(V)] _{tot} = 5.94 × 10 ⁻⁵ M, I = 0.51 m; T = 23 °C. (b) Example of a deconvoluted spectrum ([Prop] = 0.1 m; I = 0.51 m; pH _c = 5.0, T = 23 °C.)	66
Figure 41: Slope analysis of the Np(V) propionate complex formed at 23 and 85 °C for [NaCl] = 0.51 m, and 23 °C for [NaCl] = 3.2 m. Slopes ≈ 1 (1.05 ± 0.05 and 0.99 ± 0.11 for both T, respectively, 1.04 ± 0.15 for I = 3.2 m) indicate the formation of the 1:1 complex. Log β (conditional) increases both with the temperature and the ionic strength (from 1.04 ± 0.06 to 1.36 ± 0.13).....	68

Figure 42: SIT plot of the equilibrium reaction $\text{NpO}_2^+ + \text{Prop}^- \rightleftharpoons \text{NpO}_2(\text{Prop})$ in NaCl, yielding $\log \beta_0 = 1.26 \pm 0.03$. The white symbol ($[\text{NaCl}] = 4.37$ m) shows data outside the recommended applicability of the SIT (data not used in the regression). The dotted line shows the extrapolation of the results obtained for lower I to 4.37 m.....	69
Figure 43: Np(V)-propionate complexation constant extrapolated to zero ionic strength ($\log \beta_0$) versus the reciprocal of the temperature (K^{-1}).	70
Figure 44: Calculated percentage of the Np(V)-propionate complex ($[\text{Np(V)}]_{\text{tot}} = 10^{-10}$ m) versus $\log[\text{Prop}]_{\text{tot}}$ for pHc = 7 and I = 0.1 or 3 m and T = 20 or 85 °C using thermodynamic parameters determined in this study.....	71
Figure 45: Distribution ratios of Np(V) upon extraction by $1 \cdot 10^{-3}$ M TTA and $5 \cdot 10^{-4}$ M 1,10-phenanthroline in the absence of complex forming ligands at 23 °C with two ionic strength 0.5 m and 2.6 m NaCl.	75
Figure 46: Distribution ratios of Np(V) upon extraction by $1 \cdot 10^{-3}$ M TTA and $5 \cdot 10^{-4}$ M 1,10-phenanthroline in the absence of complex forming ligands at varying temperature and at 0.5 m NaCl.	75
Figure 47: Representative plot of D_0/D versus free ligand concentration. Aqueous phase: 0.5 m NaCl. Organic phase: 0.001 m TTA + 0.0005 m 1,10-phenanthroline.	76
Figure 48: SIT plot of the equilibrium reaction $\text{NpO}_2^+ + \text{L}^- \rightleftharpoons \text{NpO}_2(\text{L})$ in NaCl, yielding $\log \beta_0 = 1.32 \pm 0.03$ for propionate and $\log \beta_0 = 2.07 \pm 0.03$ for lactate. The white symbol ($[\text{NaCl}] = 2.5$ m) shows data outside the recommended applicability of the SIT (data not used in the regression). The dotted line shows the extrapolation of the results obtained for lower I to 2.5 m.....	77
Figure 49: Np(V) complexation constants corrected to zero ionic strength ($\log \beta_0$) versus the reciprocal of the temperature (K^{-1}).....	80
Figure 50: Chemical equilibrium diagram for Np(V) propionate and lactate complexation at pH 9 and 0.1 M NaCl (T= 25 °C). The box represents propionate and lactate concentrations found in OPA pore water and various extracts (Courdouan et al., 2007a).	82
Figure 51: Comparison between experimental and modeling results of Pu(IV)–HA binding considering with or without stabilization of Pu(IV) tetramer by HA.	84

Figure 52: Simulated Pu(IV) solubility versus pH in a 0.1M of NaCl solution containing 140 mg L ⁻¹ of HA or no HA. The experimental condition studied by XAFS (Dardenne et al., 2009), where polynuclear Pu(IV)-HA species were evidenced, is also shown for comparison.....	85
Figure 53: UV-Vis spectra of the electrolytes used to fix the ionic strength.....	90
Figure 54: a) FA-573 UV-Vis spectra (range 210-500 nm) in different electrolytes and thus ionic strengths (IS) obtained after centrifugation. The electrolyte contributions have been subtracted. [FA-573]= 25 mg.L ⁻¹ . b) Second-order derivatives exemplary shown in the range 205-320 nm.	91
Figure 55: FA-573-UV-chromatograms obtained after injection of the FA-573 suspensions prepared in different electrolytes, 100 µL injected, 2 measurements.	96
Figure 56: FA-532 UV-Vis spectra (range 210-500 nm) in different electrolytes and thus ionic strengths (IS) obtained after centrifugation. The electrolyte contributions have been subtracted. [FA-532]= 12 mg.L ⁻¹	98
Figure 57: Gohy-532 UV-Vis. spectra (range 210-500 nm) in different electrolytes and thus ionic strengths (IS) obtained after centrifugation. The electrolyte contributions have been subtracted. [Gohy-532]= 12 mg L ⁻¹	98
Figure 58: SFA-1 UV-Vis spectra (range 210-500 nm) in different electrolytes and thus ionic strengths (IS) obtained after centrifugation. The electrolyte contributions have been subtracted. [SFA-1]= 25 mg L ⁻¹	99
Figure 59: LS-Na UV-Vis. spectra (range 210-500 nm) in different electrolytes and thus ionic strengths (IS) obtained after centrifugation. The electrolyte contributions have been subtracted. [LS-Na]= 25 mg L ⁻¹	101
Figure 60: ¹¹ B-NMR spectra collected in 0.1 M and 5.0 M NaCl solutions: (left) spectra with 2.6 ≤ pH _m ≤ 12 and [B] _{tot} = 0.04 M, (right) spectra with pH _m = 8 and a) 0.04 M [B] _{tot} b) 0.16 M [B] _{tot} in 0.1 M NaCl and c) 0.04 M [B] _{tot} d) 0.16 M [B] _{tot} in 5.0 M NaCl.....	111
Figure 61: ¹¹ B-NMR spectra collected in 0.25 M and 3.5 M CaCl ₂ and MgCl ₂ solutions: (left) spectra with 8 ≤ pH _m ≤ 12 and [B] _{tot} = 0.04 M, (right) spectra with pH _m = 8 and a) 0.04 M [B] _{tot} b) 0.16 M c) 0.4 M [B] _{tot} in 0.25 M MgCl ₂ and d) 0.04 M [B] _{tot} e) 0.16 M [B] _{tot} f) 0.4 M [B] _{tot} in 3.5 M MgCl ₂	112

Figure 62: Fraction diagram of aqueous borate species in 0.25 M and 3.5 M MgCl ₂ as calculated with the thermodynamic and activity models reported in (Felmy and Weare, 1986). The highest pH in dilute to concentrated MgCl ₂ solutions is limited to pH _{max} ~9 by the precipitation of Mg(OH) ₂ (s) or Mg–OH– Cl phases, and thus calculations above this pH represent only a modelling exercise giving insight on the possible interaction Ca–borate in CaCl ₂ systems (where pH _{max} ~12) under the assumption of a comparable complexation behavior of Ca ²⁺ and Mg ²⁺	114
Figure 63: Solubility of Nd(OH) ₃ (am) and Nd[B ₉ O ₁₃ (OH) ₄](cr) in the presence of 0.004 M ≤ [B] _{tot} ≤ 0.16 M in 0.1 M NaCl solutions. Comparison with experimental (open symbols, black) and calculated (solid line) solubility data in the absence of borate as reported in (Neck et al., 2009).	115
Figure 64: Solubility of Nd(OH) ₃ (am) in the presence of 0.004 M ≤ [B] _{tot} ≤ 0.16 M in 1.0 M NaCl solutions. Comparison with experimental (open symbols, black) and calculated (solid line) solubility data in the absence of borate as reported in (Neck et al., 2009).	116
Figure 65: Solubility of Nd(OH) ₃ (am) and Nd[B ₉ O ₁₃ (OH) ₄](cr) in the presence of 0.004 M ≤ [B] _{tot} ≤ 0.16 M in 5.0 M NaCl solutions. Comparison with experimental (open symbols, black) and calculated (solid line) solubility data in the absence of borate as reported in (Neck et al., 2009).	116
Figure 66: Solubility of Nd(OH) ₃ (am) and Nd[B ₉ O ₁₃ (OH) ₄](cr) in the presence of 0.004 M ≤ [B] _{tot} ≤ 0.4 M in 0.25 M MgCl ₂ and CaCl ₂ solutions. Comparison with experimental (open symbols, black) and calculated (solid line) solubility data in the absence of borate as reported in (Neck et al., 2009).	117
Figure 67: Solubility of Nd(OH) ₃ (am) in the presence of 0.004 M ≤ [B] _{tot} ≤ 0.4 M in 1.0 M MgCl ₂ and CaCl ₂ solutions. Comparison with experimental (open symbols, black) and calculated (solid line) solubility data in the absence of borate as reported in (Neck et al., 2009).	117
Figure 68: Solubility of Nd(OH) ₃ (am) and Nd[B ₉ O ₁₃ (OH) ₄](cr) in the presence of 0.004 M ≤ [B] _{tot} ≤ 0.4 M in 3.5 M MgCl ₂ and CaCl ₂ solutions. Comparison with experimental (open symbols, black) and calculated (solid line) solubility data in the absence of borate as reported in (Neck et al., 2009).	118

Figure 69: TRLFS emission spectra of Cm(III) in 0.1 M and 5.0 M NaCl solutions at pH _m = 8 and various borate concentrations.	120
Figure 70: TRLFS emission spectra of Cm(III) in 0.25 M and 3.5 M MgCl ₂ solutions at pH _m = 8 and various [B] _{tot} . Comparison with a spectrum in the absence of borate.....	121
Figure 71: TRLFS emission spectra of Cm(III) in 0.25 M and 3.5 M CaCl ₂ at pH _m = 12 and various borate concentrations in comparison with borate-free literature data.	123
Figure 72: Solubility of Th(OH) ₄ (am), experimentally determined in the presence of 0 M ≤ [B] _{tot} ≤ 0.16 M in 0.1 M and 5.0 M NaCl solutions. Comparison with solubility of Th(OH) ₄ (am,fresh) and Th(OH) ₄ (am,aged), as calculated for 0.1 M NaCl using the NEA-TDB thermodynamic selection.	125
Figure 73: Solubility of Th(OH) ₄ (am) experimentally determined in the presence of 0 M ≤ [B] _{tot} ≤ 0.16 M in 0.25 M and 3.5 M MgCl ₂ solutions. Comparison with solubility of Th(OH) ₄ (am,fresh) and Th(OH) ₄ (am,aged), as calculated for 0.25 M MgCl ₂ using the NEA-TDB thermodynamic selection.	125
Figure 74: Solubility of Pu ^{IV} O ₂ (am,hyd) in the presence of [B] _{tot} = 0.16 M with 0.03 M Na ₂ S ₂ O ₄ and 0.01 M hydroquinone in 0.1 M NaCl solutions. Comparison with calculated solubility data for Pu ^{IV} O ₂ (am,hyd) (black solid line) and Pu(OH) ₃ (s) (blue solid line) and the calculated equilibrium of Pu(III)(aq) with Pu ^{IV} O ₂ (am,hyd) with pe + pH = 0 (dashed line) in the absence of borate as reported in NEA-TDB.	126
Figure 75: Pourbaix diagram calculated for [Pu] _{tot} = 10 ⁻⁴ M in 0.1 M NaCl and absence of borate. Dashed and solid lines represent the calculated borderlines for the individual Pu redox species (Guillaumont et al., 2003; Neck et al., 2007). pe and pH _m values are shown for the solubility samples in the presence of hydroquinone (blue) and Na ₂ S ₂ O ₄ (red).	127
Figure 76: Solubility of Np(V) in the presence of 0.04 M ≤ [B] _{tot} ≤ 0.16 M in 0.1 M NaCl solutions (blue and red symbols). Comparison with experimental (open symbols, black) solubility data in the absence of borate as reported by (Neck et al. 1992) and (Petrov et al. 2011). Solid line corresponding to the solubility of NpO ₂ OH(am,fresh) in 0.1 M NaCl calculated according to the NEA– TDB selection.....	130

Figure 77: Solubility of Np(V) in the presence of $0.04 \text{ M} \leq [\text{B}]_{\text{tot}} \leq 0.16 \text{ M}$ in 5.0 M NaCl solutions (blue and red symbols). Comparison with experimental (open symbols, black) solubility data in the absence of borate as (Fellhauer et al, 2015) and (Petrov et al., 2011). Solid line corresponding to the solubility of NpO ₂ OH(am, fresh) in 5.0 M NaCl calculated according to the NEA–TDB selection. Arrow indicates that the decrease in the concentration of Np for the same solubility sample was only completed after 270 days	131
Figure 78: Solubility of Np(V) in the presence of $0.04 \text{ M} \leq [\text{B}]_{\text{tot}} \leq 0.16 \text{ M}$ in 0.25 M MgCl ₂ solutions (blue and red symbols). Comparison with experimental (open symbols, black) solubility data in the absence of borate as reported by (Petrov et al., 2011). Solid line corresponding to the solubility of NpO ₂ OH(am, fresh) in 0.25 M MgCl ₂ calculated according to the NEA–TDB selection.	132
Figure 79: Solubility of Np(V) in the presence of $0.04 \text{ M} \leq [\text{B}]_{\text{tot}} \leq 0.16 \text{ M}$ in 3.5 M MgCl ₂ solutions (blue and red symbols). Comparison with experimental (open symbols, black) solubility data in the absence of borate as reported by (Petrov et al., 2011). Solid line corresponding to the solubility of NpO ₂ OH(am, fresh) in 0.25 M MgCl ₂ calculated according to the NEA–TDB selection. Calculations were restricted to 0.25 M MgCl ₂ due to a lack of ion interaction parameters for high concentrated MgCl ₂ systems.....	133
Figure 80: Diffractograms of the solubility-controlling Np(V) solid phases in the absence and presence of borate ($[\text{B}]_{\text{tot}} = 0.16 \text{ M}$) in 0.1 M NaCl and 0.25 M MgCl ₂ solutions at pH _m ~8.5.	134
Figure 81: SEM-images of the new formed solubility-controlling Np(V) solid phases in the presence of borate ($[\text{B}]_{\text{tot}} = 0.16 \text{ M}$) in 0.1 M NaCl (a) and 0.25 M MgCl ₂ (b) and 5.0 M NaCl (c, d).	135
Figure 82: Solubility of UO ₃ ·2H ₂ O(cr) and Na ₂ U ₂ O ₇ ·H ₂ O (cr) in the presence of $0 \text{ M} \leq [\text{B}]_{\text{tot}} \leq 0.16 \text{ M}$ in 0.1 M and 5.0 M NaCl solutions. Comparison with calculated solubility of UO ₃ ·2H ₂ O(cr) (blue line) and Na ₂ U ₂ O ₇ ·H ₂ O (cr) (black line) in the absence of borate as reported in Altmaier et al. (Altmaier et al., 2003b).	138
Figure 83: Solubility of UO ₃ ·2H ₂ O(cr) in the presence of $0 \text{ M} \leq [\text{B}]_{\text{tot}} \leq 0.16 \text{ M}$ in 0.25 M and 3.5 M MgCl ₂ solutions. Comparison with calculated solubility of UO ₃ ·2H ₂ O(cr) in the absence of borate (solid line) as reported in Altmaier et al. (Altmaier et al., 2003b).....	139

Figure 84: XRD pattern of freshly prepared initial $\text{UO}_3 \cdot 2\text{H}_2\text{O}(\text{cr})$, $\text{UO}_3 \cdot 2\text{H}_2\text{O}(\text{cr})$ reference [137] and $\text{UO}_3 \cdot 2\text{H}_2\text{O}(\text{cr})$ alteration phases from solubility experiments in NaCl and MgCl_2 systems with $0 \text{ M} \leq [\text{B}]_{\text{tot}} \leq 0.16 \text{ M}$ at pHm 6–7.5 and initial $\text{Na}_2\text{U}_2\text{O}_7 \cdot \text{H}_2\text{O}(\text{cr})$ and $\text{Na}_2\text{U}_2\text{O}_7 \cdot \text{H}_2\text{O}(\text{cr})$ alteration phases from solubility experiment in 0.1 M NaCl and $[\text{B}]_{\text{tot}} = 0.16 \text{ M}$ 140

6 References

- Altmaier, M., Metz, V., Neck, V., Müller, R., Fanghanel, T., 2003a. Solid-liquid equilibria of $\text{Mg}(\text{OH})_2(\text{cr})$ and $\text{Mg}_2(\text{OH})_3\text{Cl} \cdot 4\text{H}_2\text{O}(\text{cr})$ in the system Mg-Na-H-OH-O-Cl-H₂O at 25 degrees C. *Geochimica et Cosmochimica Acta* 67 (19), 3595–3601.
- Altmaier, M., Neck, V., Fanghanel, T., 2008. Solubility of Zr(IV), Th(IV) and Pu(IV) hydrous oxides in CaCl_2 solutions and the formation of ternary Ca-M(IV)-OH complexes. *Radiochimica Acta* 96 (9-11), 541–550.
- Altmaier, M., Neck, V., Fanghanel, T., 2004. Solubility and colloid formation of Th(IV) in concentrated NaCl and MgCl_2 solution. *Radiochimica Acta* 92 (9-11), 537–543.
- Altmaier, M., Neck, V., Metz, V., Müller, R., Schlieker, M., Fanghanel, T., 2003b. The solubility of U(VI) in NaCl and MgCl_2 solution, in: 9th International Conference on Chemistry and Migration Behavior of Actinides and Fission Products in the Geosphere. Migration '03, Gyeongju, Korea. 21. - 26.09.2003, Yuseong, Daejeon, Korea, p. 46.
- Amayri, S., Jermolajev, A., Reich, T., 2011. Neptunium(V) sorption on kaolinite. *Radiochimica Acta* 99 (6), 349–357.
- Artinger, R., Buckau, G., Geyer, S., Fritz, P., Wolf, M., Kim, J.I., 2000. Characterization of groundwater humic substances: influence of sedimentary organic carbon. *Applied Geochemistry* 15 (1), 97–116.
- Artinger, R., Buckau, G., Kim, J.I., 1996. Influence of sedimentary organic matter on dissolved fulvic acids in groundwater: Significance for groundwater dating with C-14 in dissolved organic matter, in: IAEA (Ed.), *Isotopes in Water Resources Management. Proceedings of a Symposium on Isotopes in Water Resources Management organized in Co-Operation with the United Nations Educational, Scientific and Cultural Organization and Held in Vienna, 20 - 24 March 1995*, IAEA-SM-336/26.
- Artinger, R., Buckau, G., Kim, J.I., Geyer, S., 1999. Characterization of groundwater humic and fulvic acids of different origin by GPC with UV/Vis and fluorescence detection. *Fresenius' Journal of Analytical Chemistry* 364 (8), 737–745.
- Artinger, R., Buckau, G., Zeh, P., Geraedts, K., Vancluysen, J., Maes, A., Kim, J.I., 2003. Humic colloid mediated transport of tetravalent actinides and technetium. *Radiochimica Acta* 91 (12), 743–750.
- Baes, A.U., Bloom, P.R., 1990. Fulvic acid ultraviolet-visible spectra. Influence of solvent and pH. *Soil Science Society of America Journal* 54 (5), 1248–1254.

- Baeyens, B., Bradbury, M.H., 2004. Cation exchange capacity measurements on illite using the sodium and cesium isotope dilution technique: Effects of the index cation, electrolyte concentration and competition: modeling. *Clays Clay Miner.* 52 (4), 421–431.
- Banik, N.I., Marsac, R., Luetzenkirchen, J., Diascorn, A., Bender, K., Marquardt, C.M., Geckeis, H., 2016. Sorption and Redox Speciation of Plutonium at the Illite Surface. *Environmental Science & Technology* 50 (4), 2092–2098.
- Banik, N.L., 2006. Speciation of tetravalent plutonium in contact with humic substances and kaolinite under environmental conditions. PhD thesis, Mainz, Germany.
- Banik, N.L., Buda, R.A., Buerger, S., Kratz, J.V., Trautmann, N., 2007. Sorption of tetravalent plutonium and humic substances onto kaolinite. *Radiochimica Acta* 95 (10), 569–575.
- Baum, J.C., McClure, D.S., 1979. Ultraviolet transitions of benzoic acid - 1. Interpretation of the singlet absorption spectrum. *J Am Chem Soc* 101 (9), 2335–2339.
- Begg, J.D., Zavarin, M., Zhao, P., Tumey, S.J., Powell, B., Kersting, A.B., 2013. Pu(V) and Pu(IV) sorption to montmorillonite. *Environmental Science and Technology* 47 (10), 5146–5153.
- Bertrand, P.A., Choppin, G.R., 1982. Separation of actinides in different oxidation states by solvent extraction. *Radiochimica Acta* 31 (3-4), 135–138.
- Borkowski, M., Richmann, M., Kalanke, S., Reed, D. T., 2011. Borate chemistry and interactions with Actinides in high ionic strength solutions at moderate pH.: Proceedings of the international workshop ABC-Salt in Karlsruhe (Germany), (2011). Karlsruhe Institut für Technologie (KIT), Karlsruhe.
- Bosch Ojeda, C., Sanchez Rojas, F., 2013. Recent applications in derivative ultraviolet/visible absorption spectrophotometry: 2009-2011. A review. *Microchemical Journal* 106, 1–16.
- Bouby, M.G., Buckau, G., 2012. Ionic strength and complexation induced humic agglomeration study: Humic acid agglomeration study as a function of ionic strength and metal ion loading, in: Altmaier, M., Kienzler, B., Metz, V., Reed, D.T. (Eds.), *Proceedings of the International Workshop ABC-Salt (II) and HiTAC 2011*, Karlsruhe.
- Bradbury, M.H., Baeyens, B., 1997. A mechanistic description of Ni and Zn sorption on Na-montmorillonite Part II: Modelling. *Journal of Contaminant Hydrology* 27 (3-4), 223–248.

- Bradbury, M.H., Baeyens, B., 2002. Sorption of Eu on Na- and Ca-montmorillonites: Experimental investigations and modelling with cation exchange and surface complexation. *Geochimica et Cosmochimica Acta* 66 (13), 2325–2334.
- Bradbury, M.H., Baeyens, B., 2005. Modelling the sorption of Mn(II), Co(II), Ni(II), Zn(II), Cd(II), Eu(III), Am(III), Sn(IV), Th(IV), Np(V) and U(VI) on montmorillonite: Linear free energy relationships and estimates of surface binding constants for some selected heavy metals and actinides. *Geochimica et Cosmochimica Acta* 69 (4), 875–892.
- Bradbury, M.H., Baeyens, B., 2006. Modelling sorption data for the actinides Am(III), Np(V) and Pa(V) on montmorillonite. *Radiochimica Acta* 94 (9-11), 619–625.
- Bradbury, M.H., Baeyens, B., 2009a. Sorption modelling on illite Part I: Titration measurements and the sorption of Ni, Co, Eu and Sn. *Geochimica et Cosmochimica Acta* 73 (4), 990–1003.
- Bradbury, M.H., Baeyens, B., 2009b. Sorption modelling on illite. Part II: Actinide sorption and linear free energy relationships. *Geochimica et Cosmochimica Acta* 73 (4), 1004–1013.
- Bradbury, M.H., Baeyens, B., 2011. Predictive sorption modelling of Ni(II), Co(II), Eu(III), Th(IV) and U(VI) on MX-80 bentonite and Opalinus Clay: A "bottom-up" approach. *Applied Clay Science* 52 (1-2), 27–33.
- Bradbury, M.H., Baeyens, B., 2015. unpublished data, Sorption data of Eu(III) on Illite.
- Bradbury, M.H., Marques, M.M., 2013. Private communication about Phase separation.
- Browne, B.A., Driscoll, C.T., 1993. pH-dependent binding of aluminum by a fulvic acid. *Environmental Science and Technology* 27 (5), 915–922.
- Buckau, G., Artinger, R., Fritz, P., Geyer, S., Kim, J.I., Wolf, M., 2000a. Origin and mobility of humic colloids in the Gorleben aquifer system. *Applied Geochemistry* 15 (2), 171–179.
- Buckau, G., Artinger, R., Geyer, S., Wolf, M., Fritz, P., Kim, J.I., 2000b. C-14 dating of Gorleben groundwater. *Applied Geochemistry* 15 (5), 583–597.
- Buckau, G., Artinger, R., Geyer, S., Wolf, M., Fritz, P., Kim, J.I., 2000c. Groundwater in-situ generation of aquatic humic and fulvic acids and the mineralization of sedimentary organic carbon. *Applied Geochemistry* 15 (6), 819–832.

- Buckau, G., Artinger, R., Kim, J.I., Geyer, S., Fritz, P., Wolf, M., Frenzel, B., 2000d. Development of climatic and vegetation conditions and the geochemical and isotopic composition in the Franconian Albvorland aquifer system. *Applied Geochemistry* 15 (8), 1191–1201.
- Buda, R.A., Banik, N.L., Kratz, J.V., Trautmann, N., 2008. Studies of the ternary systems humic substances - Kaolinite - Pu(III) and Pu(IV). *Radiochimica Acta* 96 (9-11), 657–665.
- Chin, Y.P., Aiken, G., O'Loughlin, E., 1994. Molecular weight, polydispersity, and spectroscopic properties of aquatic humic substances. *Environmental Science and Technology* 28 (11), 1853–1858.
- Choppin, G.R., 1997. Inner versus outer sphere complexation of f-elements. *Journal of Alloys and Compounds* 249 (1-2), 9–13.
- Ciavatta, L., 1980. The Specific Interaction Theory in Evaluating Ionic Equilibria. *Annali di Chimica* 70 (11-1), 551–567.
- Cieslewicz, J., Gonet, S.S., 2004. Properties of humic acids as biomarkers of lake catchment management. *Aquatic Sciences* 66 (2), 178–184.
- Claret, F., Schaefer, T., Brevet, J., Reiller, P.E., 2008. Fractionation of Suwannee River Fulvic Acid and Aldrich Humic Acid on alpha-Al₂O₃: Spectroscopic Evidence. *Environmental Science & Technology* 42 (23), 8809–8815.
- Conte, P., Piccolo, A., 1999. High pressure size exclusion chromatography (HPSEC) of humic substances: Molecular sizes, analytical parameters, and column performance. *Chemosphere* 38 (3), 517–528.
- Courdouan, A., Christl, I., Meylan, S., Wersin, P., Kretzschmar, R., 2007a. Characterization of dissolved organic matter in anoxic rock extracts and in situ pore water of the Opalinus Clay. *Applied Geochemistry* 22 (12), 2926–2939.
- Courdouan, A., Christl, I., Meylan, S., Wersin, P., Kretzschmar, R., 2007b. Isolation and characterization of dissolved organic matter from the Callovo-Oxfordian formation. *Applied Geochemistry* 22 (7), 1537–1548.
- Dardenne, K., Seibert, A., Denecke, M.A., Marquardt, C.M., 2009. Plutonium(III,IV,VI) speciation in Gorleben groundwater using XAFS. *Radiochimica Acta* 97 (2), 91–97.
- Dong, W., Brooks, S.C., 2006. Determination of the formation constants of ternary complexes of uranyl and carbonate with alkaline earth metals (Mg²⁺, Ca²⁺, Sr²⁺,

- and Ba²⁺) using anion exchange method. *Environmental Science and Technology* 40 (15), 4689–4695.
- Donovan, J.W., 1969. Changes in ultraviolet absorption produced by alteration of protein conformation. *Journal of Biological Chemistry* 244 (8), 1961–1967.
- Eberle, S.H., Schaefer, J.B., 1969. Stabilitätskonstanten der Komplexe des neptunyl(V)-ions mit α -hydroxykarbonsäuren. *Journal of Inorganic and Nuclear Chemistry* 31 (5), 1523–1527.
- Fellhauer, D., 2013. Untersuchungen zur Redoxchemie und Löslichkeit von Neptunium und Plutonium. Ph.D. Thesis, Heidelberg.
- Fellhauer, D., 2015. Solubility of Np(V) in 5 M NaCl. Private communication.
- Felmy, A.R., Weare, J.H., 1986. The prediction of borate mineral equilibria in natural waters: Application to Searles Lake, California. *Geochimica et Cosmochimica Acta* 50 (12), 2771–2783.
- Fröhlich, D.R., Skerencak-Frech, A., Morkos, M.L., Panak, P.J., 2013. A spectroscopic study of Cm(III) complexation with propionate in saline solutions at variable temperatures. *New Journal of Chemistry* 37 (5), 1520–1528.
- Fröhlich, D.R., Skerencak-Frech, A., Panak, P.J., 2014. A spectroscopic study on the formation of Cm(III) acetate complexes at elevated temperatures. *Dalton Transactions* 43 (10), 3958–3965.
- Fuger, J., Parker, V.B., Hubbard, W., Oetting, F.L., 1983. The chemical thermodynamics of actinide elements and compounds: Part 8. The actinide halides, Vienna.
- Gaona, X., Tits, J., Dardenne, K., Liu, X., Rothe, J., Denecke, M.A., Wieland, E., Altmaier, M., 2012. Spectroscopic investigations of Np(V/VI) redox speciation in hyperalkaline TMA-(OH, Cl) solutions. *Radiochimica Acta* 100 (10), 759–770.
- Glaus, M.A., Frick, S., Rosse, R., van Loon, L.R., 2010. Comparative study of tracer diffusion of HTO, Na-22(+) and Cl-36(-) in compacted kaolinite, illite and montmorillonite. *Geochimica et Cosmochimica Acta* 74 (7), 1999–2010.
- Glazer, A.N., Smith, E.L., 1960. Effect of Denaturation on the Ultraviolet Absorption Spectra of Proteins. *Journal of Biological Chemistry* 235 (10), PC43-PC44.
- Gorgeon, L., 1994. Contribution à la modélisation physico-chimique de la rétention de radioéléments à vie longue par des matériaux argileux. Ph.D. thesis, Paris.

- Gouder, T., Oppeneer, P.M., Huber, F., Wastin, F., Rebizant, J., 2005. Photoemission study of the electronic structure of Am, AmN, AmSb, and Am₂O₃ films. *Physical Review B* 72 (115122), 1–7.
- Guillaumont, R., Fanghänel, T., Fuger, J., Grenthe, I., Neck, V., Palmer, D.A., Rand, M.H., 2003. Update on the Chemical Thermodynamics of Uranium, Neptunium, Plutonium, Americium and Technetium. Nuclear Energy Agency Organisation for Economic Co-Operation and Development, Issy-les-Moulineaux (France).
- Gustafsson, J.P., Persson, I., Kleja, D.B., van Schaik, J.W.J., 2007. Binding of iron(III) to organic soils: EXAFS spectroscopy and chemical equilibrium modeling. *Environmental Science & Technology* 41 (4), 1232–1237.
- Hartmann, E., Geckeis, H., Rabung, T., Luetzenkirchen, J., Fanghaenel, T., 2008. Sorption of radionuclides onto natural clay rocks. *Radiochimica Acta* 96 (9-11), 699–707.
- Herm, M., 2012. Untersuchung der Löslichkeit und Speziation von drei- und sechswertigen Actiniden in nitrathaltigen salinaren Lösungen. Diploma Thesis, Karlsruhe.
- Hertam, A., 2011. ¹¹B-NMR spektroskopische Untersuchungen zum Lösungszustand von Boraten in konzentrierten Salzlösungen. Diploma Thesis, Freiberg, Germany.
- Hinz, K., 2015. Interaction of Ln(III) and An(III/IV/V/VI) with borate in dilute to concentrated NaCl, CaCl₂ and MgCl₂ solutions. Ph.D. Thesis, Karlsruhe, 157 pp.
- Hinz, K., Altmaier, M., Gaona, X., Rabung, T., Schild, D., Richmann, M., Reed, D.T., Alekseev, E.V., Geckeis, H., 2015. Interaction of Nd(III) and Cm(III) with borate in dilute to concentrated alkaline NaCl, MgCl₂ and CaCl₂ solutions: solubility and TRLFS studies. *New Journal of Chemistry* 39 (2), 849–859.
- Hixon, A.E., Arai, Y., Powell, B.A., 2013. Examination of the effect of alpha radiolysis on plutonium(V) sorption to quartz using multiple plutonium isotopes. *Journal of Colloid and Interface Science* 403, 105–112.
- Hixon, A.E., Powell, B.A., 2014. Observed Changes in the Mechanism and Rates of Pu(V) Reduction on Hematite As a Function of Total Plutonium Concentration. *Environmental Science & Technology* 48 (16), 9255–9262.
- Holman, D.A., Bennett, D.W., 1994. A multicomponent kinetics study of the anaerobic decomposition of aqueous sodium dithionite. *Journal of Physical Chemistry* 98 (50), 13300–13307.

- Huber, F., Schild, D., Vitova, T., Rothe, J., Kirsch, R., Schaefer, T., 2012. U(VI) removal kinetics in presence of synthetic magnetite nanoparticles. *Geochimica et Cosmochimica Acta* 96, 154–173.
- Huittinen, N., Rabung, T., Schnurr, A., Hakanen, M., Lehto, J., Geckeis, H., 2012. New insight into Cm(III) interaction with kaolinite - Influence of mineral dissolution. *Geochimica et Cosmochimica Acta* 99, 100–109.
- Hur, J., Williams, M.A., Schlautman, M.A., 2006. Evaluating spectroscopic and chromatographic techniques to resolve dissolved organic matter via end member mixing analysis. *Chemosphere* 63 (3), 387–402.
- Inoue, Y., Tochiyama, O., 1982. Solvent extraction of neptunium (v) by thenoyltrifluoroacetone and 1,10-phenanthroline or tri-n-octylphosphine oxide. *Radiochimica Acta* 31 (3-4), 193–196.
- Inoue, Y., Tochiyama, O., 1983. Study of the complexes of Np(V) with organic ligands by solvent extraction with TTA and 1, 10-phenanthroline. *Polyhedron* 2 (7), 627–630.
- Karlsson, T., Persson, P., 2010. Coordination chemistry and hydrolysis of Fe(III) in a peat humic acid studied by X-ray absorption spectroscopy. *Geochimica et Cosmochimica Acta* 74 (1), 30–40.
- Keizer, M.G., van Riemsdijk, W.H., 1999. ECOSAT - A computer Program for the calculation of speciation and Transport in soil-water systems, Version 4.8. Wageningen University, Wageningen, Netherlands.
- Kimura, T., Choppin, G.R., Kato, Y., Yoshida, Z., 1996. Determination of the hydration number of Cm(III) in various aqueous solutions. *Radiochimica Acta* 72 (2), 61–64.
- Kinniburgh D. G., Cooper D. M., 2009. PhreePlot: Creating graphical output with PHREEQC.
- Kiprop, A.K., 2009. Synthesis and characterization of fulvic acids in the C-H-O, C-H-O-N and C-H-O-N-S systems. UV-Visible spectroscopic investigations of uranyl(VI)-fulvate complexation as a function of pH at 25°C and 1 bar. Ph.D. Thesis, UMR 7566 G2R, Nancy (France).
- Kiprop, A.K., Coumon, M.-C.J., Pourtier, E., Kimutai, S., Kirui, S., 2013. Synthesis of Humic and Fulvic Acids and their Characterization using Optical Spectroscopy (ATR-FTIR and UV-Visible). *International J. Appl. Sci. Technol.* Vol. 3 (No. 8).

- Knauss, K.G., Wolery, T.J., Jackson, K.J., 1990. A new approach to measuring pH in brines and other concentrated electrolytes. *Geochimica et Cosmochimica Acta* 54 (5), 1519–1523.
- Korshin, G.V., Li, C.W., Benjamin, M.M., 1997. Monitoring the properties of natural organic matter through UV spectroscopy: A consistent theory. *Water Research* 31 (7), 1787–1795.
- Křepelová, A., 2007. Influence of humic acid on the sorption of uranium(VI) and americium(III) onto kalonite. Dissertation, Dresden, Germany.
- Larson, D.T., Haschke, J.M., 1981. XPS-AES characterization of plutonium oxides and oxide carbide. The existence of plutonium monoxide. *Inorganic Chemistry* 20 (7), 1945–1950.
- Larson, D.T., Motyl, K.M., 1990. Detection of plutonium hydride using X-ray photoelectron spectroscopy. *Journal of Electron Spectroscopy and Related Phenomena* 50 (1), 67–76.
- Liu, X., Ryan, D.K., 1997. Analysis of fulvic acids using HPLC/UV coupled to FT-IR spectroscopy. *Environmental Technology* 18 (4), 417–423.
- Lucchini, J.-F., Borkowski, M., Richmann, M.K., Ballard, S., Reed, D.T., 2007. Solubility of Nd³⁺ and UO₂²⁺ in WIPP brine as oxidation-state invariant analogs for plutonium. *Journal of Alloys and Compounds* 444, 506–511.
- Lucks, C., Rossberg, A., Tsushima, S., Foerstendorf, H., Scheinost, A.C., Bernhard, G., 2012. Aqueous Uranium(VI) Complexes with Acetic and Succinic Acid: Speciation and Structure Revisited. *Inorganic Chemistry* 51 (22), 12288–12300.
- MacCarthy, P., 1985. Spectroscopic methods (other than NMR) for determining functionality in humic substances, in: Aiken, R., McKnight, D.M., Wershaw, R.L., MacCarthy, P. (Eds.), *Humic substances in soil, sediment and water: Geochemistry, isolation and characterization*. Wiley - Interscience, New York, NY, pp. 527–559.
- Marquardt, C.M., Seibert, A., Artinger, R., Denecke, M.A., Kuczewski, B., Schild, D., Fanghanel, T., 2004. The redox behaviour of plutonium in humic rich groundwater. *Radiochimica Acta* 92 (9-11), 617–623.
- Marques Fernandes, M., Baeyens, B., Bradbury, M.H., 2008. The influence of carbonate complexation on lanthanide/actinide sorption on montmorillonite. *Radiochimica Acta* 96 (9-11), 691–697.

- Marques Fernandes, M., Baeyens, B., Daehn, R., Scheinost, A.C., Bradbury, M.H., 2012. U(VI) sorption on montmorillonite in the absence and presence of carbonate: A macroscopic and microscopic study. *Geochimica et Cosmochimica Acta* 93, 262–277.
- Marsac, R., Banik, N.I., Luetzenkirchen, J., Marquardt, C.M., Dardenne, K., Schild, D., Rothe, J., Diascorn, A., Kupcik, T., Schaefer, T., Geckeis, H., 2015a. Neptunium redox speciation at the illite surface. *Geochimica et Cosmochimica Acta* 152, 39–51.
- Marsac, R., Banik, N.I., Marquardt, C.M., Kratz, J.V., 2014. Stabilization of polynuclear plutonium(IV) species by humic acid. *Geochimica et Cosmochimica Acta* 131, 290–300.
- Marsac, R., Banik, N.L., Luetzenkirchen, J., Buda, R.A., Kratz, J.V., Marquardt, C.M., 2015b. Modeling plutonium sorption to kaolinite: Accounting for redox equilibria and the stability of surface species. *Chemical Geology* 400, 1–10.
- Martin, C.J., Bhatnagar, G.M., 1966. Unfolding reactions of proteins. I. Kinetic and equilibrium measurements of diisopropylphosphorylchymotrypsin and chymotrypsinogen in urea. *Biochemistry* 5 (4), 1230–1241.
- Moore, R.C., Borkowski, M., Bronikowski, M.G., Chen, J.F., Pokrovsky, O.S., Xia, Y.X., Choppin, G.R., 1999. Thermodynamic modeling of actinide complexation with acetate and lactate at high ionic strength. *Journal of Solution Chemistry* 28 (5), 521–531.
- Móra, S., Elöudi, P., 1968. Investigation of the Near and Far Ultraviolet Denaturation Difference Spectra of Dehydrogenases. *European Journal of Biochemistry* 5 (4), 574–582.
- Mullet, M., Guillemin, Y., Ruby, C., 2008. Oxidation and deprotonation of synthetic Fe-II-Fe-III (oxy)hydroxycarbonate Green Rust: An X-ray photoelectron study. *Journal of Solid State Chemistry* 181 (1), 81–89.
- Munchow, V., Steudel, R., 1994. The Decomposition of Aqueous Dithionite and its Reactions with Polythionates SNO₆²⁻ (N = 3-5) Studied by Ion-Pair Chromatography. *Zeitschrift für Anorganische und Allgemeine Chemie* 620 (1), 121–126.
- Neck, V., Altmaier, M., Fanghänel, T., 2007. Solubility of plutonium hydroxides/hydrous oxides under reducing conditions and in the presence of oxygen. *Comptes Rendus Chimie* 10 (10-11), 959–977.
- Neck, V., Altmaier, M., Rabung, T., Lützenkirchen, J., Fanghänel, T., 2009. Thermodynamics of trivalent actinides and neodymium in NaCl, MgCl₂, and CaCl₂ solutions:

- Solubility, hydrolysis, and ternary Ca-M(III)-OH complexes. *Pure and Applied Chemistry* 81 (9), 1555–1568.
- Neck, V., Kim, J.I., Kanellakopoulos, B., 1992. Solubility and Hydrolysis Behaviour of Neptunium(V). *Radiochimica Acta* 56 (1), 25–30.
- Nitsche, H., Roberts, K., Xi, R.H., Prussin, T., Becraft, K., Almahamid, I., Silber, H.B., Carpenter, S.A., Gatti, R.C., Novak, C.F., 1994. Long-term Plutonium Solubility and Speciation Studies in a Synthetic Brine. *Radiochimica Acta* 66-7, 3–8.
- Novak, C.F., Borkowski, M., Choppin, G.R., 1996. Thermodynamic Modeling of Neptunium(V)-Acetate Complexation in Concentrated NaCl Media. *Radiochimica Acta* 74, 111–116.
- Parkhurst, D.L., Appelo, C., 1999. User's guide to PHREEQC (Version 2): A computer program for speciation, batch-reaction, one-dimensional transport, and inverse geochemical calculations. *Water-Resources Investigations Report* 99-4259.
- Pavón, J.C., de Torres, A.G., Ojeda, C.B., Rojas, F.S., Alonso, E.I., 2012. Derivative Techniques in Molecular Absorption, Fluorimetry and Liquid Chromatography as Tools for Green Analytical Chemistry, in: , *Handbook of Green Analytical Chemistry*, pp. 245–259.
- Pearson, F.J., Tournassat, C., Gaucher, E.C., 2011. Biogeochemical processes in a clay formation in situ experiment: Part E - Equilibrium controls on chemistry of pore water from the Opalinus Clay, Mont Terri Underground Research Laboratory, Switzerland. *Applied Geochemistry* 26 (6), 990–1008.
- Pelekani, C., Newcombe, G., Snoeyink, V.L., Hepplewhite, C., Assemi, S., Beckett, R., 1999. Characterization of natural organic matter using high performance size exclusion chromatography. *Environmental Science & Technology* 33 (16), 2807–2813.
- Perkampus, H.-H., 1992. *UV-VIS Spectroscopy and Its Applications*. Springer Berlin Heidelberg, Berlin, Heidelberg, 1 online resource.
- Perminova, IV, Frimmel, F.H., Kudryavtsev, A.V., Kulikova, N.A., Abbt-Braun, G., Hesse, S., Petrosyan, V.S., 2003. Molecular weight characteristics of humic substances from different environments as determined by size exclusion chromatography and their statistical evaluation. *Environmental Science & Technology* 37 (11), 2477–2485.
- Petrov, V.G., Kalmykov, S.N., Altmaier, M., 2011. Solubility and phase transformations of Np(V) hydroxide in solutions with different ionic strengths. *Moscow University Chemistry Bulletin* 66 (2), 107–115.

- Piccolo, A., 2001. The supramolecular structure of humic substances. *SOIL SCIENCE* 166 (11), 810–832.
- Poinsot, C., Baeyens, B., Bradbury, M.H., 1999. Experimental and modelling studies of caesium sorption on illite. *Geochimica et Cosmochimica Acta* 63 (19-20), 3217–3227.
- Pokrovsky, O.S., Choppin, G.R., 1997. Neptunium(V) Complexation by Acetate, Oxalate and Citrate in NaClO₄ Media at 25°C. *Radiochimica Acta* 79 (3), 167–171.
- Powell, B.A., Fjeld, R.A., Di Kaplan, Coates, J.T., Serkiz, S.M., 2005. Pu(V)O₂(+) adsorption and reduction by synthetic hematite and goethite. *Environmental Science & Technology* 39 (7), 2107–2114.
- Rabung, T., Altmaier, M., Neck, V., Fanghänel, T., 2008. A TRLFS study of Cm(III) hydroxide complexes in alkaline CaCl₂ solutions. *Radiochimica Acta* 96 (9-11), 551–559.
- Rabung, T., Pierret, M.C., Bauer, A., Geckeis, H., Bradbury, M.H., Baeyens, B., 2005. Sorption of Eu(III)/Cm(III) on Ca-montmorillonite and Na-illite. Part 1: Batch sorption and time-resolved laser fluorescence spectroscopy experiments. *Geochimica et Cosmochimica Acta* 69 (23), 5393–5402.
- Rai, D., Hess, N.J., Felmy, A.R., Moore, D.A., Yui, M., Vitorge, P., 1999. A thermodynamic model for the solubility of PuO₂(am) in the aqueous K⁺-HCO₃⁻-CO₃²⁻-OH⁻-H₂O system. *Radiochimica Acta* 86 (3-4), 89–99.
- Rao, L., Tian, G., Srinivasan, T.G., Zanonato, P., Di Bernardo, P., 2010. Spectrophotometric and calorimetric studies of Np(V) complexation with acetate at various temperatures from T=283 to 343 K. *Journal of Solution Chemistry* 39 (12), 1888–1897.
- Rao, L.F., Srinivasan, T.G., Garnov, A.Y., Zanonato, P.L., Di Bernardo, P., Bismondo, A., 2004. Hydrolysis of neptunium(V) at variable temperatures (10-85 degrees C). *Geochimica et Cosmochimica Acta* 68 (23), 4821–4830.
- Rashid, M.A., 1985. *Geochemistry of Marine Humic Compounds*. Springer New York, New York, NY, 300 pp.
- Reiller, P.E., Evans, N.D.M., Szabo, G., 2008. Complexation parameters for the actinides(IV)-humic acid system: a search for consistency and application to laboratory and field observations. *Radiochimica Acta* 96 (6), 345–358.

- Runde, W., 2011. Effect of chloride on actinyl(V) and (VI) speciation and solubility: the formation of ternary complexes.: Book of abstracts. 13th International Conference on the Chemistry and Migration Behaviour of Actinides and Fission Products in the Geosphere, Beijing, China, September, 18-23, 2011,, 2011, Beijing.
- Salentine, C.G., 1983. High-field ^{11}B NMR of alkali borates. Aqueous polyborate equilibria. *Inorganic Chemistry* 22 (26), 3920–3924.
- Savitzky, A., Golay, M.J.E., 1964. Smoothing and Differentiation of Data by Simplified Least Squares Procedures. *Anal. Chem.* 36 (8), 1627–1639.
- Schafer, T., Hertkorn, N., Artinger, R., Claret, F., Bauer, A., 2003. Functional group analysis of natural organic colloids and clay association kinetics using C(1s) spectromicroscopy. *Journal de Physique IV* 104, 409–412.
- Schäfer, T., Buckau, G., Artinger, R., Kim, J.I., Geyer, S., Wolf, M., Bleam, W.F., Wirick, S., Jacobsen, C., 2005. Origin and mobility of fulvic acids in the Gorleben aquifer system: Implications from isotopic data and carbon/sulfur XANES. *Organic Geochemistry* 36 (4), 567–582.
- Schäfer, T., Claret, F., Bauer, A., Griffault, L., Ferrage, E., Lanson, B., 2003. Natural organic matter (NOM)-clay association and impact on Callovo-Oxfordian clay stability in high alkaline solution: Spectromicroscopic evidence. *Journal de Physique IV* 104, 413–416.
- Schnitzer, M., 1978. Humic substances chemistry and reactions, in: Schnitzer, M., Khan, S.U. (Eds.), *Soil Organic of Soils*. Elsevier, Amsterdam (The Netherlands), pp. 1–64.
- Schnurr, A., 2015. Untersuchungen zur Radionuklidsorption an Tonmineraloberflächen bei hohen Ionenstärken. Dissertation, Karlsruhe, 161 pp.
- Schnurr, A., Marsac, R., Rabung, T., Luetzenkirchen, J., Geckeis, H., 2015. Sorption of Cm(III) and Eu(III) onto clay minerals under saline conditions: Batch adsorption, laser-fluorescence spectroscopy and modeling. *Geochimica et Cosmochimica Acta* 151, 192–202.
- Seibert, A., Mansel, A., Marquardt, C.M., Keller, H., Kratz, J.V., Trautmann, N., 2001. Complexation behaviour of neptunium with humic acid. *Radiochimica Acta* 89 (8), 505–510.
- Sladkov, V., 2014. Interaction of uranyl with acetate in aqueous solutions at variable temperatures. *Journal of Chemical Thermodynamics* 71, 148–154.

- Striegel, A.M., Yau, W.W., Kirkland, J.J., Bly, D.D., 2009. Modern Size-Exclusion Liquid Chromatography: Practice of Gel Permeation and Gel Filtration Chromatography: Second Edition, in: , Modern Size-Exclusion Liquid Chromatography: Practice of Gel Permeation and Gel Filtration Chromatography: Second Edition, pp. 1–494.
- Sutheimer, S.H., Cabaniss, S.E., 1997. Aluminum binding to humic substances determined by high performance cation exchange chromatography. *Geochimica et Cosmochimica Acta* 61 (1), 1–9.
- Tertre, E., Castet, S., Berger, G., Loubet, M., Giffaut, E., 2006. Surface chemistry of kaolinite and Na-montmorillonite in aqueous electrolyte solutions at 25 and 60 degrees C: Experimental and modeling study. *Geochimica et Cosmochimica Acta* 70 (18), 4579–4599.
- Tertre, E., Hofmann, A., Berger, G., 2008. Rare earth element sorption by basaltic rock: Experimental data and modeling results using the "Generalised Composite approach". *Geochimica et Cosmochimica Acta* 72 (4), 1043–1056.
- Tian, G., Martin, L.R., Rao, L., 2010. Complexation of lactate with neodymium(III) and europium(III) at variable Temperatures: Studies by potentiometry, microcalorimetry, optical absorption, and luminescence spectroscopy. *Inorganic Chemistry* 49 (22), 10598–10605.
- Vasiliev, A.N., Banik, N.L., Marsac, R., Froehlich, D.R., Rothe, J., Kalmykov, S.N., Marquardt, C.M., 2015. Np(V) complexation with propionate in 0.5–4 M NaCl solutions at 20–85 degrees C. *Dalton Transactions* 44 (8), 3837–3844.
- Walther, C., Rothe, J., Brendebach, B., Fuss, M., Altmaier, M., Marquardt, C.M., Buechner, S., Cho, H.-R., Yun, J.-I., Seibert, A., 2009. New insights in the formation processes of Pu(IV) colloids. *Radiochimica Acta* 97 (4-5), 199–207.
- Wolf, M., Buckau, G., Geyer, S., 2004. Isolation and characterisation of new batches of GoHy-573 humic and fulvic acids, in: Buckau, G. (Ed.), Humic substances in performance assessment of nuclear waste disposal: Actinide and iodine migration in the far-field., pp. 111–124.
- Yamaguchi, T., Sakamoto, Y., Ohnuki, T., 1994. Effect of the complexation on solubility of Pu(IV) in aqueous carbonate system. *Radiochimica Acta* 66-7, 9–14.
- Zavarin, M., Powell, B.A., Bourbin, M., Zhao, P., Kersting, A.B., 2012. Np(V) and Pu(V) Ion Exchange and Surface-Mediated Reduction Mechanisms on Montmorillonite. *Environmental Science & Technology* 46 (5), 2692–2698.

Zavarin, M., Roberts, S.K., Hakem, N., Sawvel, A.M., Kersting, A.B., 2005. Eu(III), Sm(III), Np(V), Pu(V), and Pu(IV) sorption to calcite. *Radiochimica Acta* 93 (2), 93–102.